Study of low temperature processes for non-reactive elimination of tars from the producer gas

Rita Harb

PSL UNIVERSITÉ PARIS

THÈSE DE DOCTORAT
DE L'UNIVERSITÉ PSL

Préparée à MINES ParisTech

Etude des procédés à basse température en vue de l'élimination non réactive des goudrons contenus dans le gaz produit

Study of low temperature processes for non-reactive elimination of tars from the producer gas

Soutenue par

Rita HARB

Le 9 décembre 2021

Ecole doctorale n° 621

Ingénierie des systèmes, matériaux, mécanique, énergétique

Spécialité

Energétique et génie des procédés

Composition du jury :

Jean-Philippe, PASSARELLO Professeur, Université Sorbonne Paris Nord	*Président*
Guillain, MAUVIEL Professeur, Université de Lorraine	*Rapporteur*
Olivier, AUTHIER HDR, EDF	*Rapporteur*
Carolina, FONT PALMA Senior Lecturer, University of Hull	*Rapporteur*
Rodrigo, RIVERA-TINOCO Docteur, Pentair	*Examinateur*
Chakib, BOUALLOU Professeur, MINES ParisTech	*Directeur de thèse*

MINES ParisTech | PSL

Acknowledgements

This manuscript compiles the work of three years of research completed between the Centre for Energy efficiency of Systems (CES) and the Holy Spirit University of Kaslik (USEK).

I would like to begin by thanking Dr. Maroun Nemer, the director of the Centre for Energy efficiency of Systems, who helped me in defining the boundaries of my thesis during the first year and for his constructive criticism.

My sincere gratitude is also addressed to Dr. Barbar Zeghondy who was the first one to believe in me and encouraged me to accomplish a PhD by establishing the link between me, the Holy Spirit University of Kaslik and the Centre for Energy efficiency of Systems. I also extend my sincere gratitude to the Dean of the School of Engineering Dr. Joseph El Assad.

I extend my sincere gratitude to my PhD director Prof. Chakib Bouallou for guiding me during my journey, for his advices and for his confidence in me.

I would like to express my deepest gratitude to my PhD co-supervisor Dr. Rodrigo Rivera-Tinoco who supported me throughout my PhD. I would like to thank him for having continuously supervised my research activities, for the patience he has shown towards me and for his help and support during this thesis. I would also like to thank him not only for being an advisor but also for being a friend and for all the laughs and the tears that we shared during this journey.

I would like to thank the jury members Prof. Jean-Philippe Passarello, Prof. Guillain Mauviel, Dr. Olivier Authier and Dr. Carolina Font-Palma for the time they have spent reading the thesis, for their valuable comments and for accepting to participate in the defense.

I would like to thank my colleagues and my friends in the CES for their encouragement, support, help and for the good times that we have spent together, especially for Ghiwa, Joëlle and Samer. I would like to thank Ghiwa for hosting me multiple times during my stay in France and most importantly for spending the first quarantine with me.

Special thanks goes for my fiancé Eddy who stood by my side from the beginning of the thesis and helped me in completing my thesis emotionally and academically. This work would not have been completed without his support during the difficult times.

Finally yet importantly, I would like to thank my family, especially my father Hamid, my mother Souzy, my sister Nisrine, my brother Tony and my niece Tali for their kindness, support and for believing in me. Without their continuous support, my career would not have resulted in this thesis.

Table of Content

LIST OF FIGURES..... VII

LIST OF TABLES..... XII

NOMENCLATURE XIV

GENERAL INTRODUCTION 1

CHAPTER 1 : STATE-OF-THE-ART OF BIOMASS GASIFICATION AND TAR TREATMENT METHODS. 7

1.1. USES OF BIOMASS IN THE WORLD AND IN FRANCE 7
1.2. CONVERSION PATHWAYS 9
1.3. GASIFICATION 11
1.3.1. Gasifier stages and main reactions 11
1.3.2. Gasifier types 12
1.3.3. Producer gas composition 14
1.4. TAR PROPERTIES 15
1.4.1. Tar composition 15
1.4.2. Tar classification 16
1.4.3. Tar content limits 16
1.5. TAR TREATMENT 18
1.5.1. Primary methods 18
1.5.2. Secondary methods 18
1.5.2.1 Physical/ Mechanical methods 19
1.5.2.2 Simulations of oil-based scrubbers 22
1.5.2.3 Thermal treatment 27
1.5.3. Catalytic cracking 28
1.6. METHANATION REQUIREMENTS 33
1.7. BIOMETHANE PRODUCTION PLANTS BASED ON BIOMASS GASIFICATION 35
1.8. CONCLUSION 37

CHAPTER 2 : PHASE EQUILIBRIUM FOR TAR-PRODUCER GAS MIXTURES AND WATER SCRUBBING FOR THE REMOVAL OF THE HEAVY FRACTION TAR. 47

2.1. PROCESS DESCRIPTION 47
2.2. PHASE EQUILIBRIUM DEVELOPMENT FOR TAR COMPONENTS – PRODUCER GAS MIXTURES 49
2.2.1. Assumptions and methodology 50
2.2.1.1 Tar representative components 50
2.2.1.2 Producer gas composition 51
2.2.1.3 Saturation and constant relative concentration lines 52
2.2.1.4 Saturation enthalpy and isenthalpic lines 53
2.2.2. Results and discussion 54
2.2.2.1 Solid – gas equilibrium 54
2.2.2.2 Tar dew point 55
2.2.2.3 Psychrometric charts 57
2.3. REMOVAL OF THE HEAVY TAR FRACTION BY TWO WATER SCRUBBERS PLACED IN SERIES. 61
2.3.1. Liquid to gas ratio 63
2.3.1.1 First scrubber: collector 63
2.3.1.2 Second scrubber: absorber 64

2.3.2. Water temperature ... *65*
2.3.3. Results analysis ... *67*
2.3.4. Regeneration of the scrubbing liquid ... *69*
2.4. PHASE DISTRIBUTION FUNCTION OF TEMPERATURE ... 70
2.5. CONCLUSION ... 72

CHAPTER 3 : CONDENSATION OF TARS AT LOW TEMPERATURE OVER COLD PLATES ... 81

3.1. MODEL APPROACH FOR TAR AND WATER CONDENSATION ... 81
3.2. TAR DEPOSITION MODELLING ... 82
3.2.1. Model presentation ... *84*
3.2.2. Main assumptions ... *85*
3.2.3. Governing equations ... *86*
3.2.3.1 Producer gas stream ... 86
3.2.3.2 Frost Surface ... 87
3.2.3.3 Interface between the benzene and the ice frost layers ... 88
3.2.3.4 Frost layer ... 88
3.2.3.5 Liquid toluene film ... 89
3.2.3.6 Refrigerant side ... 89
3.2.4. The modelling approach: Finite volume method ... *90*
3.2.4.1 Middle cells ... 92
3.2.4.2 Boundary cells ... 92
3.2.5. Boundary and initial conditions ... *93*
3.2.6. Gas Thermophysical properties ... *94*
3.2.7. Effective thermal conductivity ... *95*
3.2.8. Diffusion and effective diffusion coefficients ... *97*
3.2.9. Saturation mass fraction ... *100*
3.2.10. Heat transfer coefficient ... *101*
3.2.11. Mass transfer coefficient ... *102*
3.3. CARBON DIOXIDE FROSTING ... 102
3.4. MODEL VALIDATION ... 104
3.4.1. One-dimensional: water vapor frosting from humid air ... *104*
3.4.2. Two-dimensional ... *106*
3.4.2.1 Water vapor frosting from humid air ... 106
3.4.2.2 CO_2 frosting from CO_2-N_2 mixture ... 108
3.5. MODEL RESULTS AND DISCUSSION ... 110
3.5.1. Single plate ... *111*
3.5.1.1 Gas temperature ... 112
3.5.1.2 Benzene and toluene remaining content ... 113
3.5.1.3 Frost thickness ... 116
3.5.1.4 Mass flux of the condensable components ... 119
3.5.1.5 Frost density ... 121
3.5.1.6 Effective thermal conductivity ... 123
3.5.1.7 Heat fluxes ... 125
3.5.2. Several plates placed in series ... *126*
3.5.2.1 Gas temperature ... 127
3.5.2.2 Benzene and toluene remaining content ... 127
3.5.2.3 Frost thickness ... 128

3.5.2.4 Mass flux of the condensable components 129
3.5.2.5 Benzene frost density 130
3.5.2.6 Thermal diffusivity 131
3.5.2.7 Heat fluxes 132
3.6. REGENERATION OF THE PLATES 133
3.7. CONCLUSION 134

CHAPTER 4 : ECONOMIC ASSESSMENT 149

4.1. REFERENCE PROCESS 149
4.2. METHODOLOGY 150
4.3. SCRUBBERS 151
4.3.1. Investment cost 151
4.3.2. Operating cost 152
4.3.2.1 Oil-based scrubbers 152
4.3.2.2 Water-based scrubbers 153
4.4. LOW TEMPERATURE PROCESS 155
4.4.1. Studied configurations of refrigeration utilities 155
4.4.2. Thermodynamic analysis 160
4.4.2.1 Energy Analysis 160
4.4.2.2 Exergy analysis 161
4.4.3. Economic analysis 163
4.4.3.1 Investment cost 163
4.4.3.2 Operating cost 164
4.4.4. Environmental analysis: CO_2 emissions 164
4.4.5. Design parameters 165
4.4.6. Results and discussion 166
4.4.6.1 Producer gas temperature 166
4.4.6.2 Coefficient of performance (COP) 171
4.4.6.3 Total cost calculation 172
4.4.6.4 Exergy destruction 176
4.4.7. Optimal configuration 177
4.5. SCALE FACTOR 178
4.6. CONCLUSION 181

GENERAL CONCLUSION AND PERSPECTIVES 194

REFERENCES 199

APPENDICES 210

List of Figures

Figure 0-1: Overall process for the reduction of the tar content to 1 mg.Nm^{-3}. 2
Figure 1-1: The ten leading countries in the production of renewable energy in 2018 [12]. 7
Figure 1-2: Percentage of primary production of renewable energy by sector in 2020 in metropolitan France [12] 8
Figure 1-3 : Conversion pathways of biomass into bioenergy [14]..... 9
Figure 1-4 : Schematic illustration of gasification steps [5]..... 11
Figure 1-5 : Updraft gasifier (left) vs. downdraft gasifier (right) [23]. 13
Figure 1-6: Illustration of A) Bubbling Fluidized Bed (BFB), B) Circulating Fluidized Bed (CFB), and C) Dual Fluidized Bed (DFB) gasifiers [29]. 14
Figure 1-7 : Example of the composition of the tar produced from biomass gasification [5]..... 15
Figure 1-8 : Scheme of tar formation [38]..... 15
Figure 1-9 : Description of primary, secondary and tertiary tar classification. 16
Figure 1-10 : Different tar classes dew point according to their concentration [39,40]. 17
Figure 1-11: Dry and wet tar removal methods. 19
Figure 1-12: Flowsheet of the OLGA process [46]. 20
Figure 1-13 : Comparison between the remaining tar concentrations for different treatment absorption – adsorption methods [48]. 22
Figure 1-14: Schematic diagram of the scrubbing process for tar removal, using Aspen Plus. 23
Figure 1-15: Variation of the cleaned gas temperature (°C) and content (mg.Nm^{-3}) of phenol, m/p-xylene, o-xylene + styrene, indene and naphthalene, as function of the L/G ratio in the absorber for a scrubbing liquid temperature of 60°C. 24
Figure 1-16: Variation of the cleaned gas temperature (°C) and content (mg.Nm^{-3}) of phenol, m/p-xylene, o-xylene + styrene, indene and naphthalene, as function of the scrubbing liquid temperature fed to the absorber, for a L/G ratio of 1.82x10^{-3} m^3.m^{-3}. 25
Figure 1-17 : Tar conversion by class in A) oil scrubber B) dolomite bed catalyst [66]. 29
Figure 1-18: 1-MN conversion percentage for different catalyst after 10 hours of operation [67]. 30
Figure 1-19 : Effect of the catalytic cracking, for a residence time of 0.3 second on A) phenol at 700°C with an initial concentration of 8-12 g.Nm^{-3} B) naphthalene at 900°C with an initial concentration of 40 g.Nm^{-3} and 90 g.Nm^{-3} [69]. 31
Figure 1-20 : Stages of catalyst deactivation function of the reaction time [77]..... 33
Figure 1-21: Impact of the gasification agent on H_2/CO and H_2/CO_2 ratios. 35
Figure 1-22: Process flow diagram of the full GoBiGas plant. Labels: 1&2) gasification and combustion, 3) cyclone, 4) post-combustion, 5) cooler, 6) filter, 7) scrubber, 8) AC beds, 9) flue gas recovery heat exchanger, 10) biomass feed, 11) compressor, 12) olefins hydrogenation, 13) carbonyl sulfide hydrolyzer, 14) hydrogen sulphides removal, 15) guard bed, 16) water gas shift 17) pre-methanation, 18) carbon dioxide removal, 19) methanation and 20) drying [84]..... 36
Figure 1-23: Block flow diagram of the biomethane production process from wood gasification using Milena and OLGA [86]. 37
Figure 2-1: BFD showing one possible configuration for producing biomethane, based on biomass gasification. 48
Figure 2-2: Illustration of the constant enthalpy line calculations. 54
Figure 2-3: Comparison between the experimental VP and the calculated ones based on Aspen for A) fluoranthene [101], B) naphthalene [102], C) phenol [103] and D) benzene [104] at temperatures lower than their triple point. 55

Figure 2-4: Dew point of A) fluoranthene, B) naphthalene, C) indene, D) phenol, E) toluene and F) benzene in producer gas mixtures for different compositions. 56
Figure 2-5: Psychrometric charts of fluoranthene-raw gas mixture. 58
Figure 2-6: Psychrometric charts of naphthalene-raw gas mixture. 58
Figure 2-7: Psychrometric charts of indene-raw gas mixture. 59
Figure 2-8: Psychrometric charts of phenol-raw gas mixture. 59
Figure 2-9: Psychrometric charts of toluene-raw gas mixture. 60
Figure 2-10: Psychrometric charts of benzene-raw gas mixture. 60
Figure 2-11: Process Flow Diagram (PFD) for tar removal from producer gas. 62
Figure 2-12: Variation of the remaining content of phenol, naphthalene, indene and fluoranthene, and variation of the temperature of the gas stream leaving the first scrubber (stream 16), function of the L/G ratio in the collector, for a water temperature of 25°C. 63
Figure 2-13: Variation of the remaining contents of phenol, naphthalene, indene and fluoranthene, and variation of the temperature of the gas stream leaving the second scrubber (stream 17), function of the L/G ratio in the absorber, for a water temperature of 20°C. 64
Figure 2-14: Variation of the benzene and toluene contents remaining in the gas phase, function of the L/G ratio in the collector for a temperature of 25°C (a) and in the absorber for a temperature of 20°C (b). 65
Figure 2-15: Variation of the remaining content of phenol, naphthalene, indene and fluoranthene, and variation of the temperature of the gas stream leaving the second scrubber (stream 17), function of the water temperature, for a L/G ratio of $2.57x10^{-3}$ $m^3.m^{-3}$. 66
Figure 2-16: Variation of the benzene and toluene contents remaining in the gas phase, function of the scrubbing liquid temperature after the absorber, for a L/G ratio of $2.57x10^{-3}$ $m^3.m^{-3}$. 66
Figure 2-17: Comparison between the elementary tar removal efficiencies obtained by using methyl-oleate and water as scrubbing mediums, in the collector and the absorber. 67
Figure 2-18: Variation of the mass percentage of the condensable components (tars and water) in the condensate, function of the gas temperature. 71
Figure 2-19: Freezing temperature for each tar component. 71
Figure 2-20: Variation of the phase distribution in the condensed phase, function of the gas temperature. 72
Figure 3-1: Cold plates placed in series, targeting the tar condensation. 81
Figure 3-2: Frosting and condensation process diagram. 85
Figure 3-3: Physical representation of the system with a counter-current refrigerant flow (not to scale). 90
Figure 3-4: Schematic illustration of the cell arrangement in a two-dimensional Cartesian coordinate system. 91
Figure 3-5: Schematic illustration of the top boundary cell of the ice frost layer. 92
Figure 3-6: Variation of the gas a) thermal conductivity in $W.m^{-1}.K^{-1}$, b) density in $kg.m^{-3}$, c) molar heat capacity in $J.kmol^{-1}.K^{-1}$, and d) viscosity in $N.s.m^{-2}$, function of the temperature in °C. 94
Figure 3-7: Variation of the solid benzene thermal conductivity (k_{benz}) function of the temperature based on three different correlations. 96
Figure 3-8: Variation of the effective thermal conductivities of the a) ice and b) benzene frost layers, function of the average frost densities, for the main correlations. 97
Figure 3-9: Variation of the diffusion coefficients of the benzene (a), toluene (b) and water vapor (c) in the producer gas, function of the temperature, for the two calculation methods [130,143]. 99
Figure 3-10: Variation of the diffusion resistance factor for several correlations, function of the average frost density. 100
Figure 3-11: Carbon dioxide phase diagram [151]. 103

Figure 3-12: Validation of the 1D frost growth model for the variation of the frost layer thickness over time, based on a comparison with Lee et al. [121]. 105
Figure 3-13: Validation of the 1D frost growth model for the variation of the frost surface temperature over time, based on a comparison with Lee et al. [121]. 105
Figure 3-14: Validation of the 1D frost growth model for the variation of the average frost layer density over time, based on a comparison with Lee et al. [121]. 105
Figure 3-15: Validation of the 1D frost growth model for the variation of the heat flux over time for Case 2 in Table 3-4, based on a comparison with Lee et al. [121]. 106
Figure 3-16: Validation of the 2D frost growth model: frost density and frost thickness obtained by the proposed model (a) and by Lee et al. [120] (b). 107
Figure 3-17: Validation of the 2D frost growth model based on a comparison with Lee et al. [120], for the variation of the frost surface temperature over time. 108
Figure 3-18: Validation of the 2D frost growth model based on a comparison with Lee et al. [120], for the variation of the heat flux over time. 108
Figure 3-19: Validation of the 2D frost growth model based on a comparison with Shchelkunov et al [153], for the variation of the CO_2 average frost density over the time. 109
Figure 3-20: Validation of the 2D frost growth model based on a comparison with Shchelkunov et al [153], for the variation of the CO_2 average frost layer thickness over the time. 110
Figure 3-21: Schematic representation of the considered procedure to solve the mathematical model on Dymola. 111
Figure 3-22 : Variation of the gas temperature function of the plate length and the time, for different initial conditions. 113
Figure 3-23: Variation of the benzene mass fraction remaining in the gas phase, function of the plate length and the time, for different initial conditions. 114
Figure 3-24: Variation of the toluene mass fraction remaining in the gas phase, function of the plate length and the time, for different initial conditions. 115
Figure 3-25: Variation of the benzene frost thickness function of the plate length and the time, for different initial conditions. 116
Figure 3-26 : Variation of the ice frost thicknesses function of the plate length and the time, for different initial conditions. 118
Figure 3-27: Variation of the average (a) benzene and (b) ice frost thicknesses function of time, for different initial conditions. 119
Figure 3-28 : Variation of benzene, ice and toluene condensable mass fluxes function of time, for different initial conditions. 121
Figure 3-29: Variation of the average (a) benzene and (b) ice frost densities function of time, for different initial conditions 122
Figure 3-30 :Variation of the benzene frost density along the plate length and the frost thickness, at t=60 min. 123
Figure 3-31 : Variation of the ice frost density along the plate length and the frost thickness, at t=60 min. 123
Figure 3-32 : Variation of the benzene effective thermal conductivity along the plate length and the frost thickness, at t=60 min. 124
Figure 3-33: Variation of the ice effective thermal conductivity along the plate length and the frost thickness, at t=60 min. 124
Figure 3-34 : Variation of the total heat flux, sensible heat flux and latent heat fluxes of water vapor frosting, benzene frosting and toluene condensation function of time, for different initial conditions. 125

Figure 3-35: Variation of the total heat flux, sensible heat flux and latent heat fluxes of water vapor frosting, benzene frosting and toluene condensation function of the plate length and the time, for case 7. 126
Figure 3-36 : Two different views of the gas temperature variation function of the plate length and the time, for the six plates placed in series. 127
Figure 3-37: Variation of the mass fraction of benzene (a) and toluene (b) remaining in the gas phase, function of the plate length and the time, for the six plates placed in series. 128
Figure 3-38: Variation of the benzene frost thickness function of the plate length and the time, for the six plates placed in series. 128
Figure 3-39: Variation of the ice frost thickness function of the plate length and the time, for the six plates placed in series. 129
Figure 3-40 : Variation of benzene, ice and toluene mass fluxes function of time, for plates 2 to 6 placed in series. 130
Figure 3-41: Variation of the benzene frost density along the plate length and the frost thickness at t=60min, for the six plates placed in series. 131
Figure 3-42: Variation of the benzene frost layer thermal diffusivity for the six plates, function of the plate length after 1 min, 10 min, 30 min and 60 min of operation. 132
Figure 3-43 : Variation of the ice frost layer thermal diffusivity for the six plates, function of the plate length after 1 min, 10 min, 30 min and 60 min of operation. 132
Figure 3-44 : Variation of the total heat flux, sensible heat flux, and latent heat fluxes of water vapor frosting, benzene frosting, toluene condensation and CO_2 frosting, function of time, for plates 1 to 6. 133
Figure 4-1: Variation of the utilities cost in oil-based scrubbers process, function of a) the L/G ratio in the absorber at 60°C b) the scrubbing liquid temperature fed to the absorber for a L/G ratio of 1.82×10^{-3} $m^3.m^{-3}$. 153
Figure 4-2: Variation of the utilities cost in the water scrubbers process, function of a) the L/G ratio in the collector, for a water temperature of 25°C, b) the L/G in the absorber, for a water temperature of 20°C and c) the water temperature, for a L/G ratio of 2.57×10^{-3} $m^3.m^{-3}$. 154
Figure 4-3: Simple refrigeration cycle with heat integration formed of a compressor followed by a cooler or a condenser, then a throttle valve and finally a heater or an evaporator. 156
Figure 4-4: Schematic diagram of the refrigeration cycle “Conf1” (a), P-h diagrams of nitrogen (b) and methane (c). 157
Figure 4-5: Refrigeration cycles of the pre-cooling unit based on single stage (a) and two-stages (b) semi-hermetic reciprocating compressors, in addition to their application limits for the R404A refrigerant [168]. 158
Figure 4-6: Schematic diagram of the refrigeration cycle “Conf2” (a), and P-h diagrams of nitrogen (b). 159
Figure 4-7: Schematic diagram of the refrigeration cycle “Conf3”. 160
Figure 4-8: Variation of the temperature of the clean producer gas leaving the evaporator ($\boldsymbol{T9}$), for the different considered cases in $\boldsymbol{Conf1}$, while using nitrogen as a refrigerant. 168
Figure 4-9: Variation of the temperature of the clean producer gas leaving the evaporator ($\boldsymbol{T9}$), for the different considered cases in $\boldsymbol{Conf1}$, while using methane and the mixture of nitrogen and methane as refrigerants. 169
Figure 4-10: Variation of the temperature of the clean producer gas leaving the evaporator ($\boldsymbol{T9}$), for the different cases considered for $\boldsymbol{Conf2}$, while using nitrogen as a refrigerant. 170
Figure 4-11: Variation of the temperature of the clean producer gas leaving the evaporator ($\boldsymbol{T6}$), for the different cases considered for $\boldsymbol{Conf3}$, while using nitrogen as a refrigerant. 171

Figure 4-12: $\boldsymbol{COP}$ variation, function of the different considered cases in $\boldsymbol{Conf1}$, $\boldsymbol{Conf2}$ and $\boldsymbol{Conf3}$. 172
Figure 4-13: Variation of $\boldsymbol{ZInv}$, $\boldsymbol{Zop}$, $\boldsymbol{Zenv}$ and $\boldsymbol{Ztot}$ function of the different considered cases in $\boldsymbol{Conf1}$, $\boldsymbol{Conf2}$ and $\boldsymbol{Conf3}$. 173
Figure 4-14: $\boldsymbol{Zinv}$ distribution of (a) $\boldsymbol{Conf1}$, (b) $\boldsymbol{Conf2}$ and (c) $\boldsymbol{Conf3}$. 174
Figure 4-15: Distribution of $\boldsymbol{Zop}$ of (a) $\boldsymbol{Conf1}$, (b) $\boldsymbol{Conf2}$ and (c) $\boldsymbol{Conf3}$..... 175
Figure 4-16: Comparison between the $\boldsymbol{ExD}$values in the different refrigeration system components of Conf1, Conf2 and Conf3. 176
Figure 4-17: Comparison between the $\boldsymbol{ZInv,spec}$ variation of the tar removal by adsorption, with that of (a) Conf1, (b) Conf2 and (c) Conf3, function of the biomethane production capacity. 179
Figure 4-18: Variation of $\boldsymbol{Zop}$function of $\boldsymbol{Celec}$, for the three studied configurations. 180
Figure 4-19: Comparison between the variation of $\boldsymbol{ZInv + Zop}$ of the optimal case for each configuration, function of the biomethane production capacity. 181
Figure B.1: Two stages water gas shift reaction [179]. 213
Figure B.2: Variation of K_p and $X_{CO,eq}$, function of temperature. 214
Figure C.1: Comparison between the variation of A) frost density, B) frost thickness and C) frost surface temperature function of time for different values of M. 216
Figure D.1: P-h diagram of nitrogen [151]. 217
Figure D.2: P-h diagram of methane [151]. 218

List of Tables

Table 1-1 : Main characteristics of thermo-chemical conversion processes (combustion, pyrolysis, gasification and hydrothermal liquefaction) [17–20]. 10
Table 1-2: Main reactions of the biomass gasification process [15,16,23,26]. 12
Table 1-3 : Typical producer gas composition for multiple gasifiers and gasification agents [30–35]. 14
Table 1-4 : Tar classification with respect to its molecular weight [4,5,8] 16
Table 1-5 : Tar concentration in product gas limits for different applications [3,4]. 17
Table 1-6 : Efficiencies of dry and wet tar and particles removal methods [4,8]..... 19
Table 1-7: Absorption efficiencies of tar components by different absorbents (%) [47]. 21
Table 1-8: Producer gas composition considered in the OLGA process simulation [53]. 23
Table 1-9: Main operating conditions and stream variables considered in Aspen Plus for simulating OLGA process using two different RME compositions. 24
Table 1-10: Tar content in the different gas streams for methyl-oleate and RME absorbents at a mass flow rate of 5500 $kg.h^{-1}$ and for an initial scrubbing liquid temperature of 60°C. 26
Table 1-11: Performance of nickel and non-nickel metal catalysts..... 32
Table 1-12: Specifications for the injection of the Synthetic Natural Gas (SNG) in the grid in France [79]. 34
Table 2-1: Physical properties of common tar components. 51
Table 2-2: Different raw gas compositions in wet basis used for the tar dew point calculation. 52
Table 2-3: Producer gas mass composition obtained from a wood-based biomass dual fluidized bed gasifier, operating with steam as gasifying agent (Thunman et al. 2018b). 62
Table 2-4: Main operating conditions and stream variables considered in water scrubbers. 62
Table 2-5: The selected optimal operating conditions for methyl-oleate and water scrubbers. 67
Table 2-6: Producer gas mass composition after the water-based collector and absorber, at the selected optimal operating conditions. 69
Table 2-7: Content of the tar representative components in the different producer gas streams. 69
Table 2-8: Temperature and composition of the streams entering and leaving the regeneration column. 70
Table 3-1: Summary of the approximated effective thermal conductivities and derivatives at the boundary cell faces of the ice frost layer. 93
Table 3-2: Diffusion coefficients, in $m^2.s^{-1}$, of the different components in the air at atmospheric pressure..... 98
Table 3-3: Summary of the convection correlations. 101
Table 3-4: Operating conditions used in the experiments of Lee et al. [121]. 104
Table 3-5: Operating conditions for the experiments conducted by Shchelkunov et al. [153]. 109
Table 3-6: Inlet conditions of the first plate. 111
Table 3-7: Selected wall temperature for the different plates. 127
Table 3-8: Brief description of the different thermal defrosting methods. 134
Table 4-1: Investment and operating costs of the tar treatment system of the GoBiGas plant [85].... 149
Table 4-2: Values of the CEPCI, from 2001 to 2021 [160]. 150
Table 4-3: Values of the economical parameters of eqs. (4-4) and (4-5). 151
Table 4-4: Pricing of the different process utilities. 152
Table 4-5: Functions for estimating the capital cost of the different components in the refrigeration cycle [159,173,174]. 163
Table 4-6: The different cases considered to analyze the impact of $\boldsymbol{LP}$, $\boldsymbol{HP}$, $\boldsymbol{T7}$ and $\boldsymbol{mr}$, on the refrigeration cycle design of $\boldsymbol{Conf1}$, for nitrogen and methane. 167

Table 4-7: The different cases considered to analyze the impact of $\boldsymbol{LP}$, $\boldsymbol{HP}$, $\boldsymbol{T7}$ and $\boldsymbol{mr}$, on the refrigeration design of $\boldsymbol{Conf2}$, for nitrogen. 169
Table 4-8: The different cases considered to analyze the impact of $\boldsymbol{LP}$, $\boldsymbol{HP}$ and $\boldsymbol{mr}$ on the refrigeration design of $\boldsymbol{Conf3}$, for nitrogen. 171
Table 4-9: Optimum case for each configuration. 177
Table 4-10: Scale factors of the different equipment [85] 178
Table A.1: Computational mass content (w) and concentration (C) at temperature (T) and atmospheric pressure for the mixture of fluoranthene in raw gas. 210
Table A.2: Computational mass content (w) and concentration (C) at temperature (T) and atmospheric pressure for the mixture of indene in raw gas. 210
Table A.3: Computational mass content (w) and concentration (C) at temperature (T) and atmospheric pressure for the mixture of naphthalene in raw gas. 211
Table A.4: Computational mass content (w) and concentration (C) at temperature (T) and atmospheric pressure for the mixture of phenol in raw gas. 211
Table A.5: Computational mass content (w) and concentration (C) at temperature (T) and atmospheric pressure for the mixture of toluene in raw gas. 212
Table A. 6: Computational mass content (w) and concentration (C) at temperature (T) and atmospheric pressure for the mixture of benzene in raw gas. 212
Table B.1: Initial gas composition for each case expressed in mole fraction. 214
Table B.2: Variation of H_2/CO and H_2/CO_2 ratios, function of the temperature and the initial gas composition. 214

Nomenclature

Acronyms

AC	Activated Carbon
BTX	Benzene, Toluene, Xylene
BFB	Bubbling Fluidized Bed
BFD	Block Flow Diagram
CEPCI	Chemical Engineering Plant Cost Index
CFB	Circulating Fluidized Bed
CFD	Computational Fluid Dynamic
CFS	Coagulation Flocculation Sludge
CHP	Combined Heat and Power
COP	Coefficient Of Performance
CR	Catalytic steam Reforming
CRF	Capital Recovery Factor
DD	Thermal Decomposition
DFB	Dual Fluidized Bed
DWC	Dropwise condensation
ECN	Energy research Centre of the Netherlands
ER	Equivalence Ratio
FLH	Full Load Hour
FT	Fischer-Tropsch
FVM	Finite Volume Method
FW	Food Waste
FWC	Filmwise condensation
GC	Gas Chromatography
GR	Gasifying Ratio
GWP	Global Warming Potential
HDS	Hydro-DeSulfurization
HP	High Pressure
HT	High Temperature
HTL	Hydro-Thermal Liquefaction
HX	Heat exchanger
L/G	Liquid to Gas
LMTD	Log Mean Temperature Difference
LP	Low Pressure
LT	Low Temperature
PAH	Polycyclic Aromatic Hydrocarbons

PCR	Plasma enhanced Catalytic steam Reforming
PD	Plasma-assisted Decomposition
PFD	Process Flow Diagram
RME	Rapeseed Methyl Ester
S/B	Steam/Biomass
SEK	Swedish krona
SF	Scale Factor
SNG	Synthetic Natural Gas
UWP	Used Wood Pellets
VF	Vapor Fraction
WGS	Water-Gas Shift
WGSR	Water-Gas Shift Reaction

Nomenclature

A	Heat transfer area	m^2
C_{CO2}	Penalty cost rate of CO_2 emissions	€.kg^{-1}_{CO2}
C_{CW}	Cooling Water Cost	€.m^{-3}
C_{elec}	Electrical Cost	€.kWh^{-1}
C_p	Specific heat capacity	kJ.kg^{-1}.K^{-1} or J.kg^{-1}.K^{-1}
$C_{p,m}$	Molar specific heat capacity	J.$kmol^{-1}$.K^{-1}
C_{tar}	Tar concentration	mg.Nm^{-3}
D	Mass diffusion coefficient	m^2.s^{-1}
D_h	Hydraulic diameter	m
$\Delta H^0_{r\,25°C,1atm}$	Enthalpy of the reaction at 25°C and 1 atm	kJ.mol^{-1}
$\dot{ex}$	Exergy	kJ.kg^{-1}
$\dot{Ex}$	Exergy transfer rate	kW
$\dot{Ex}_D$	Exergy destruction	kW
$\dot{Ex}^Q$	Exergy transfer rate accompanying the heat transfer	kW
$\dot{Ex}^W$	Exergy transfer rate associated with the work	kW
h	Enthalpy	J.kg^{-1} or kJ.kg^{-1}
h_c	Convective heat transfer coefficient	W.m^{-2}.K^{-1}
h_{fg}	Latent Heat of Vaporization	kJ.kg^{-1}
h_p	Plate height	m
i	interest rate	-
k	Thermal conductivity	W.m^{-1}.K^{-1}
k_m	Mass transfer coefficient	m.s^{-1}
K_p	Equilibrium constant	-
Le	Lewis Number	-
L_H	Hydrodynamic entrance length	m

L_p	Plate length	m
L_{sv}	Latent heat of sublimation	$J.kg^{-1}$
L_{vap}	Latent heat of evaporation	$J.kg^{-1}$
$\dot{m}$	Mass flow rate	$kg.s^{-1}$
m”	Mass Flux	$kg.s^{-1}.m^{-2}$
M	Molecular weight	$kg.kmol^{-1}$
M_c	Number of meshes along the x-axis	-
N	Expected equipment lifetime	years
N_c	Number of meshes along the y-axis	-
n	number of cycles	-
Nu	Nusselt number	-
P	Production Capacity	MW
Pr	Prandtl number	-
P_{Sat}	Saturation pressure	Pa
P_V	Vapor pressure	Pa
$\dot{Q}$	Heat transfer rate	W or kW
Q”	Heat flux	$W.m^{-2}$
Re	Reynolds number	-
RH	Relative Humidity	-
S	Gas side heat transfer area	m^2
s	Entropy	$kJ.kg^{-1}.K^{-1}$
S_l	Liquid saturation	-
Sh	Sherwood number	-
S/B	Steam to biomass ratio	-
T	Temperature	°C
t	Time	s
to	Evaporating temperature	°C
tc	Condensing temperature	°C
U	Overall heat transfer coefficient	$W.m^{-2}.K^{-1}$
V	Volume	m^3
v	Volume fraction	-
V_g	Gas velocity	$m.s^{-1}$
VP	Vapor pressure	Pa
w	Mass fraction	-
w_p	Plate width	m
w_t	Tar content	$kg_t.kg_{t.f.}^{-1}$ producer gas
$\dot{W}$	Work	kW
x	Mole fraction	-
X	Mass fraction	
$X_{CO,eq}$	Equilibrium conversion of CO	-
y	Gas phase mole fraction	-

Z	Cost	€
$\dot{Z}$	Cost rate	€.s^{-1}

Greek Letters

μ	Diffusion resistance factor	-
μ_{CO2}	Emission conversion factor	$kg.kWh^{-1}$
μ_g	Gas dynamic viscosity	Pa.s
α	Absorption rate	$kg.m^{-3}.s^{-1}$
α_{air}	Thermal diffusivity of air	-
α_{gas}	Thermal diffusivity of gas	-
δ	Frost thickness	m
ε	Porosity	-
ρ	Density	$kg.m^{-3}$
τ	Tortuosity	-
υ	Atomic diffusion volume	-
η	Efficiency	%
φ	Maintenance factor	-
ϕ	Relative Concentration	-

Subscript

0	Reference state
a	Amorphous coke
avg	Average
benz	Benzene
comp	Compressor
cond	Conductivity
cnd	Condenser
CW	Cooling Water
DB	Dry Bulb
DP	Dew Point
eff	Effective
elec	Electrical
env	Environment
evap	Evaporator
f	Filamentous coke
fr	Frost
g	Gas
HCV	Higher Calorific Value
i	Component i
int	Interface

Inv	Investment
isen	Isentropic
lat	Latent
op	Operating
pre-coo	Pre-cooler
r	Refrigerant
ref	Reference
s	Surface
sat	Saturation
sens	Sensible
spec	Specific
t	Tar
t.f.	Tar free
tar	Tar product
tol	Toluene
tot	Total
turb	Turbine
TV	Throttle Valve
vap	Vapor
wat	Water

General introduction

With the growing interest in fighting against global warming and carbon dioxide emissions, researchers are looking to replace fossil fuels by renewable energy sources. Biomass is one of these energy sources, which is carbon neutral since the carbon dioxide released during its thermo-chemical degradation is equal to that absorbed during its growth through photosynthesis. Biomass includes agricultural crops, residues, part of municipal organic wastes and forestry residues. Among other renewable energy technologies, such as wind power and solar energy, biomass is the only one enabling to directly produce liquid fuels [1].

Physical, biochemical, and thermo-chemical processes are used to convert biomass into bioenergy, the latter being the most applied one. Thermo-chemical conversion includes pyrolysis, gasification and combustion. Biomass gasification gained the highest interest among them. Gasification process converts organic matter into a mixture of gas, tar and char using steam, oxygen, or air as a gasifying agent. The gas contains carbon monoxide (CO), carbon dioxide (CO_2), hydrogen (H_2), steam (H_2O), nitrogen (N_2) and methane (CH_4) in addition to tar vapors and some other impurities [2]. This gas mixture is known as producer gas and its composition depends on the used gasification agent as well as on the gasifier type. The end-use of the producer gas is limited due to the formation of multiple by-products, such as NO_x, SO_x, fly ashes and tars within the gasification process [3]. Among the pollutants and contaminants, tar removal remains the hardest one to deal with, being the main drawback of biomass gasification [4].

The first scientific objective relies on analyzing the limitations of the existing tar removal methods and proposing a new method for tar treatment that allows a larger biomethane production. Therefore, defining the frontiers of the study by classifying biomass thermal decomposition processes and tar treatment methodologies that are compatible with methanation is of great importance. For this purpose, Chapter 1 presents a description of the gasification processes followed by tar characteristics. Then, the different existing methods for tar removal as well as the processes of methanation based on wood gasification are presented. The allowable tar content, remaining in the producer gas after its treatment, is defined by the desired application [3,5]. Lower restrictions on tar concentration are set for the combined heat and power production (CHP), while much stricter limitations are defined for chemical synthesis processes involving a catalyst, such as Fischer-Tropsch, methanation and methanol synthesis. As for CHP, it is enough to reduce the dew point of the tar to a temperature below the lowest one in the process to avoid its deposition. While for chemical synthesis, the catalyst is easily deactivated due to the presence of tar even at low concentrations. At temperatures lower than 1100°C, tar and light hydrocarbons are decomposed into coke that deactivates catalysts [6].

Biomass conversion into biofuels and biogas is a promising way for energy and heat generation. Lately, research works focused on the production of biomethane based on biomass gasification, followed by methanation as an alternative to fossil natural gas. This process gained great interest after a study carried out in France aiming at shifting the gas system entirely into renewable gas by 2050. The challenge of this process remains in the intensive gas cleaning and the required tar removal. To ensure a proper operation, the tar content remaining in the producer gas prior to the methanation step should be less than 1 $mg.Nm^{-3}$ [7].

Tar properties, composition and classification should be well studied to ensure its treatment. Otherwise tar will condense in the downstream equipment leading to the blockage and fouling of engines, filters and turbines [8]. Up to now, many tar removal methods have been developed. They are classified between primary and secondary. Primary methods are based on reducing tar formation within the

gasification process, while secondary ones rely on tar removal after its formation. However, few researchers were able to reach the acceptable tar limit for the methanation.

A second scientific objective of this thesis is to assess the condensing temperatures of tars and other condensable compounds in the producer gas. In order to study tar removal from the producer gas downstream biomass gasification, solid–vapor and liquid–vapor equilibrium must be known for different tar concentrations. To assess tar removal by condensation at low temperatures, psychrometric charts are developed in the first part of Chapter 2. Since the composition of tar is complex, benzene, toluene, phenol, indene, naphthalene and fluoranthene are selected as tar representative components. Each component is studied separately in four different producer gas compositions. Methods for calculating saturation, isenthalpic and constant relative concentration lines are presented. Psychrometric charts of the different tar components are finally plotted at atmospheric pressure. Results show that a temperature of -110°C is required to reduce the tar content to 1 mg.Nm^{-3}.

One of the possible routes suggested for tar removal from the producer gas is their condensation over cold surfaces. However, treating the tar directly after the gasifier with cold surfaces is costly, requires high energy for cooling the gas and leads to the formation of a very thick deposit layer that should be removed after a very short operating time. Thus, a first stage is required to remove the condensable tar fraction at temperatures higher than the ambient. Moreover, previous research works have mentioned the possibility of valorizing the remaining fraction of benzene, toluene and xylene present in the producer gas by condensation at low temperature. Therefore, the multi-component deposition/condensation of the remaining tar content is suggested as a suitable method for tar removal. Figure 0-1 illustrates the described process combination for tar removal.

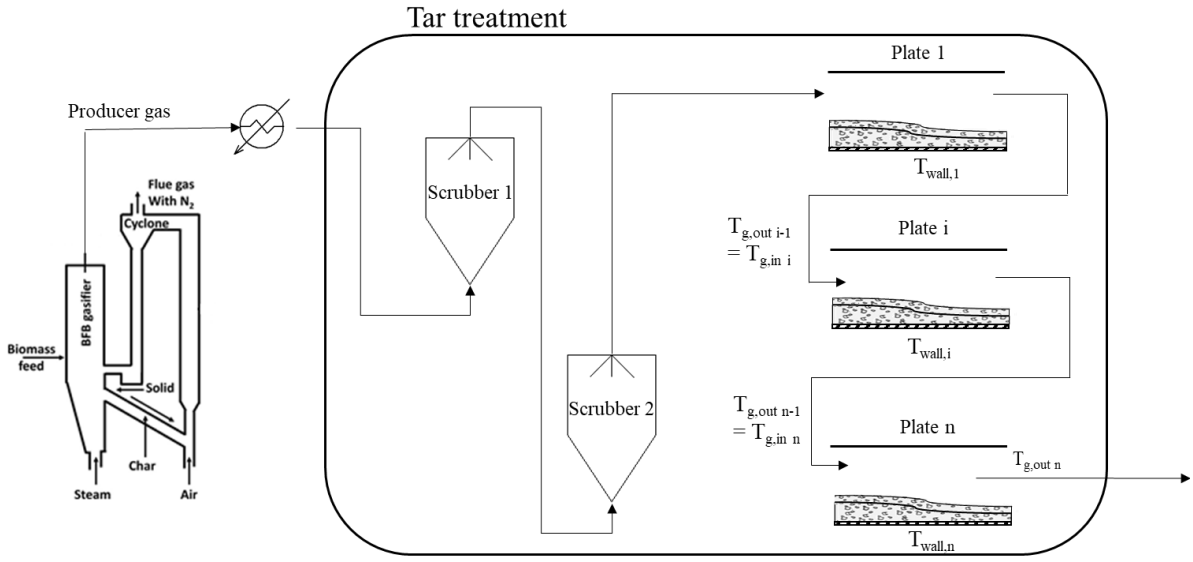

Figure 0-1: Overall process for the reduction of the tar content to 1 mg.Nm^{-3}.

The second part of Chapter 2 includes simulations of water-based scrubbers as a pre-treatment step prior to the low temperature process of tar removal. Those simulations define the inlet gas and tar composition for the cold plates as well as the most convenient operating conditions to recover the light tar fraction.

Chapter 3 highlights the third scientific objective that targets developing mathematical models for the simultaneous multi-phase deposition/condensation over cold surfaces. The tar composition that is going to be treated by the low temperature process is known and is formed of benzene and toluene. In addition to those two components, water vapor remaining in the gas phase after the scrubber will also condense leading to the formation of an additional frost layer. For the operating conditions of the low temperature

process, benzene and water vapor will form two frost layers while toluene will condense as a liquid film for temperatures higher than -94.97°C. Then frost growth and condensation are modeled using Dymola. The model is based on heat and mass transfer equations for the different subdomains. It is validated by comparing the obtained results with published experimental and theoretical data for water vapor in moist air.

Finally, Chapter 4 sheds light on the economic aspect of the proposed process for tar removal. The investment and the operating costs of the water scrubbers followed by the low temperature process are analyzed. Sensitivity analyses for selecting the optimal refrigeration cycle with heat integration are completed. Different configurations for the refrigeration cycle are considered including the use of a throttle valve or a turbine. The cost of the developed process is compared with the cost of existing ones. Moreover, a study to assess the impact of the biomethane production capacity on the developed tar treatment method cost is completed.

Introduction générale

Afin de lutter contre le réchauffement climatique et les émissions de dioxyde de carbone, les chercheurs visent à remplacer les combustibles fossiles par des sources d'énergie renouvelables. La biomasse est l'une de ces sources d'énergie, qui est neutre en carbone puisque le dioxyde de carbone libéré lors de sa dégradation thermochimique est égal à celui absorbé lors de sa croissance par photosynthèse. La biomasse comprend les cultures agricoles, les résidus, une partie des déchets organiques municipaux et les résidus forestiers.

Des procédés physiques, biochimiques et thermochimiques sont utilisés pour convertir la biomasse en bioénergie, cette dernière étant la plus appliquée. Parmi les procédés de conversion, la gazéification de la biomasse a suscité le plus d'intérêt afin de convertir la matière organique en un mélange de gaz (nommé gaz produit), de goudron et de charbon. La conversion est complétée en utilisant un agent de gazéification tel que la vapeur d'eau, l'oxygène ou l'air. L'utilisation finale du gaz produit est limitée en raison de la formation de multiples sous-produits, tels que NO_x, SO_x, cendres volantes et goudron durant la gazéification. Parmi les polluants et contaminants, l'élimination de goudron reste le plus difficile à traiter, étant le principal inconvénient de la gazéification de la biomasse.

Le premier objectif scientifique analyse les limitations des méthodes existantes pour l'élimination de goudron et la propose une nouvelle méthode de traitement permettant une production plus importante de biométhane. Chapitre 1 définit alors les frontières de l'étude en classant les processus de décomposition thermochimique et plus précisément la gazéification de la biomasse et les méthodologies de traitement de goudron y compris ceux qui sont compatibles avec la méthanation. De plus, la teneur en goudron admissible, restant dans le gaz produit après son traitement, est définie par l'application souhaitée. Par exemple, pour la synthèse chimique, y inclus la méthanation, le catalyseur est rapidement désactivé même à de faibles concentrations de goudron suite à leur décomposition en coke pour des températures inférieures à 1100°C.

Récemment, les travaux de recherche se sont concentrés sur la production de biométhane à partir de la gazéification de la biomasse, suivie de la méthanation comme alternative au gaz naturel fossile. Pour assurer un bon fonctionnement, la teneur en goudron restante dans le gaz produit avant l'étape de méthanation doit être réduite à 1 $mg.Nm^{-3}$.

Un deuxième objectif scientifique de cette thèse est d'évaluer les températures de condensation des goudrons et d'autres composants condensables présents dans le gaz produit. Afin d'étudier l'élimination de goudron du gaz produit après la gazéification, l'équilibre solide-vapeur et liquide-vapeur doit être connu pour différentes concentrations de goudron. Par conséquent, des diagrammes psychrométriques pour les composants représentatifs du goudron sont développés dans la première partie du Chapitre 2. Selon ces diagrammes, une température de -110°C est requise afin de réduire la concentration du goudron à 1 $mg.Nm^{-3}$. Du coup, l'élimination des goudrons par condensation/déposition sur des surfaces froides est proposée. Cependant, traiter le goudron directement après le gazéifieur avec des surfaces froides est coûteux, nécessite une énergie élevée pour refroidir le gaz et conduit à la formation d'une couche de dépôt très épaisse qui doit être éliminée après un temps de fonctionnement très court. Ainsi, une première étape est nécessaire pour éliminer la partie condensable de goudron à des températures supérieures à l'ambiante. Par ailleurs, des travaux de recherche antérieurs ont évoqué la possibilité de valoriser la fraction restante de benzène, toluène et xylène dans le gaz produit par condensation à basse température.

La deuxième partie du chapitre 2 comprend des simulations des colonnes d'absorption qui utilisent l'eau comme agent de lavage en tant qu'une étape de prétraitement pour le processus d'élimination du goudron

à basse température. Ces simulations définissent la composition du gaz d'entré et du goudron à traiter par les plaques froides, ainsi que les conditions opératoires initiales.

Chapitre 3 met en évidence le troisième objectif scientifique qui vise à développer des modèles mathématiques pour le dépôt/condensation multiphasique simultané sur des surfaces froides. La composition des goudrons qui vont être traités par le procédé à basse températures est connue et elle est formée de benzène et de toluène. En plus de ces deux composants, la vapeur d'eau restante dans la phase gazeuse après les colonnes d'absorption se condensera également, entraînant à la formation d'une couche de givre supplémentaire. Pour les conditions opératoires du procédé à basse température, le benzène et la vapeur d'eau formeront deux couches de givre tandis que le toluène se condensera sous forme de film liquide pour des températures supérieures à -94,97°C. Ensuite, la croissance du givre et la condensation sont modélisées à l'aide de Dymola.

Enfin, chapitre 4 met en lumière l'aspect économique du procédé proposé pour l'élimination du goudron. Les coûts d'investissement et de fonctionnement des colonnes d'absorption suivis du procédé à basse température sont analysés. Les analyses de sensibilité pour la sélection du cycle de réfrigération optimal avec intégration du froid sont complétées. Différentes configurations pour le cycle de réfrigération sont envisagées dont l'utilisation d'une vanne d'étranglement ou d'une turbine. Le coût du procédé développé est comparé au coût des procédés existants. Par ailleurs, une étude d'évaluation de l'impact de la capacité de production de biométhane sur le coût de la méthode de traitement de goudron développée est achevée.

Chapter 1 : State-of-the-art of biomass gasification and tar treatment methods.

Renewable energy sources include hydropower, geothermal, wind, solar, tidal, wave and biomass. This last is a collective term used to indicate to an organic matter. Biomass is composed of carbon, hydrogen, oxygen and a small amount of nitrogen and sulfur. Wood, agricultural residues and crops, food, industrial or animal wastes present different forms of biomass [9]. Traditional biomass, such as charcoal and wood, has been used since a very long time for cooking and heating. Nowadays, modern biomass has been integrated to produce bioenergy through different conversion processes. Bioenergy uses can be divided into electricity, heat and transport fuels. In 2019, renewable energy supplied around 11% of the total world's primary energy [10]. This chapter presents a description of the gasification process followed by the tar characteristics. Then, the different existing methods for tar removal as well as the methanation processes that are based on biomass gasification are presented.

1.1. Uses of biomass in the world and in France

In 2019, the world primary energy is produced 26.8% from coal, 30.9% from fuel (oil), 23.2% from natural gas, 5% from nuclear energy, 2.5% from hydraulic energy, 9.4% from biofuels and 2.2% from other renewable sources [11]. Figure 1-1 presents the ten leading countries in the production of renewable energy in 2018. China is the world's leading producer of renewable energy in 2018, followed by India and then the European Union (EU). The latter is in the lead when it comes to both biogas and the incineration of renewable waste. Several countries in South Asia or Africa, such as India or Nigeria, stand out in the ranking due to a relatively large population and a significant use of solid biomass, generally outside the commercial channels.

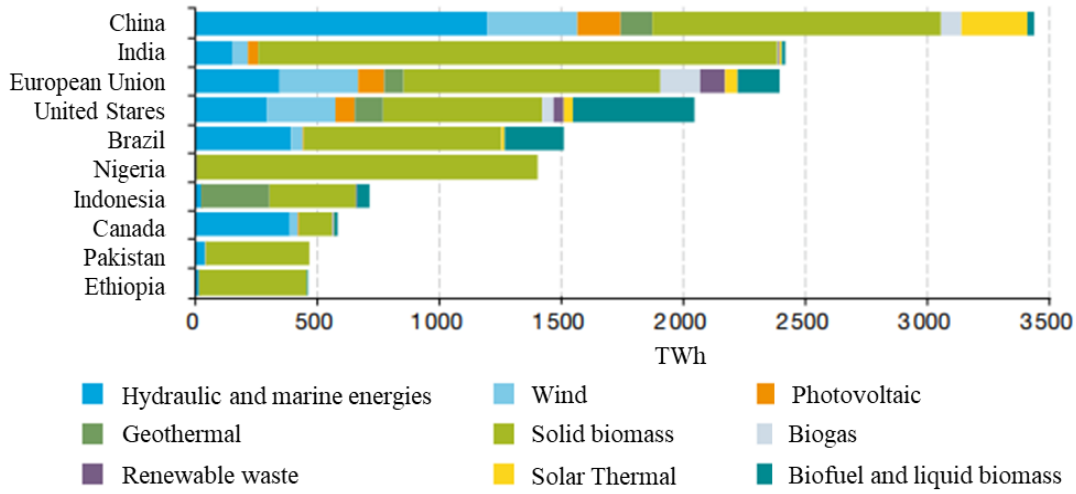

Figure 1-1: The ten leading countries in the production of renewable energy in 2018 [12].

In France, the renewable energy is the fourth source for primary energy after nuclear energy (39.2%), petroleum products (27.5%) and gas (16.9%). The contribution of renewable energy in primary energy consumption increased from 8.3% in 2010 to 13.1% in 2020 in the metropolitan France [12]. Biomass is the primary energy source of renewable energy in France. Biomass can be converted into biogas, biofuels or into energy by direct combustion. Individual wood heating is the largest sector for bioenergy in France, followed by biomass boilers and combined heat and power production (CHP).

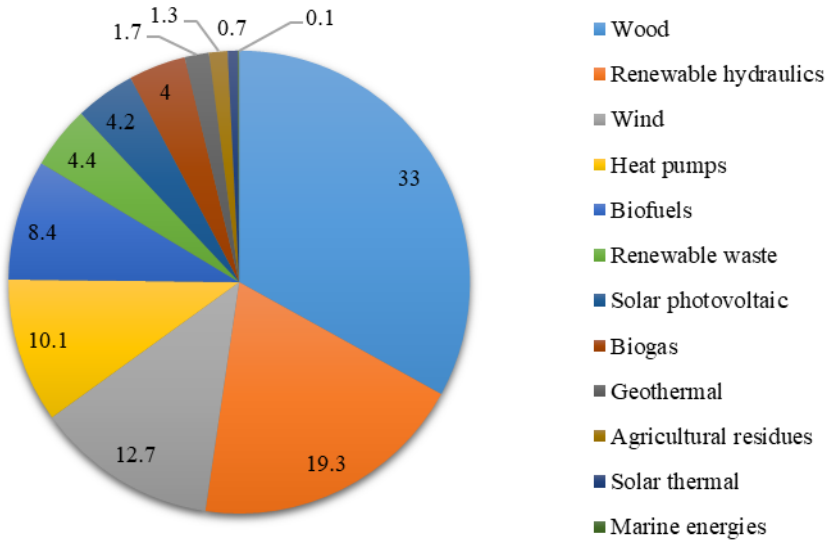

Figure 1-2: Percentage of primary production of renewable energy by sector in 2020 in metropolitan France [12]

The total energy produced from biomass can be broadly defined as the sum of the energy derived from wood, renewable waste, agricultural residues (solid phase), biofuels (liquid phase) and biogas (gas phase). According to Figure 1-2, 50.5% of the primary production of renewable energy in the metropolitan France is based on biomass. The largest contributions for the renewable energy share are solid biomass (wood and agricultural residues) for heating followed by hydraulics for electricity production.

Around 92% of solid biomass (without renewable waste) is used for heating since it has a higher efficiency than when used for electricity production. Renewable waste and biogas are used for generating heat or electricity or both through a combined cycle process. In 2020, 34% of the biogas was used to produce electricity and 42% for heating. The remaining 24% (which was only 2% in 2016) of the biogas is upgraded into biomethane; the latter can be injected into natural gas lines and used for transportation.

A study, carried out by ADEME in collaboration with GRDF and GRT_{gaz} on the gas supply and demand in France [13], aims at checking the feasibility of shifting the gas supply system entirely into renewable gas by 2050 in France. This energy transition helps in reducing carbon dioxide emissions while fostering the implementation of renewable energies. In 2050, theoretically, 460 TWh_{HCV} of injectable renewable gas (bio-methane) could be produced through primary resources. This production potential is capable of covering all the gas demand. Many scenarios exist for predicting the gas demand in 2050. The latter varies from 276 TWh to 361 TWh. The expected bio-methane is produced through three different processes that can be explained as follows:

- Anaerobic Digestion (AD): It is the decomposition of organic matter in absence of oxygen through microorganisms into biogas and digestate. The anaerobic digestion of bio-waste, seaweed and agricultural residues could supply 30% of the injectable renewable gas (140 TWh_{HCV}).
- Pyro-gasification: Thermo-chemical conversion of biomass (wood, refuse-derived fuel and some agricultural residues) into producer gas. It could supply 40% of the injectable renewable gas (180 TWh_{HCV}) by converting the producer gas into biomethane.
- Power to Gas (PtG): The excess of the electricity produced from renewable energy sources (solar and wind) is converted into hydrogen through electrolysis. Then H_2 is converted into CH_4

through methanation in presence of CO_2. It could supply 30% of the injectable renewable gas (140 TWh_{HCV}).

Note that the biomass used in these conversion processes should not be in competition with food usage nor raw materials for biomaterials, wood industry and agriculture. Pyro-gasification followed by methanation seems to be a promising route for renewable gas production. However, combining the two processes together requires intensive producer gas cleaning units after the gasification in order to meet the requirements of the methanation process and ensure its operation. Reducing tar content in the producer gas to the acceptable level forms the main challenge for this route. In this section, a particular attention will be paid to the different biomass conversion processes.

1.2. Conversion pathways

The conversion of biomass into bioenergy can be carried out through physical, thermo-chemical, and biochemical processes as schematized in Figure 1-3. The interest of this thesis falls into the thermo-chemical conversion processes. The latter includes combustion, gasification, pyrolysis and hydrothermal liquefaction of biomass. Thermo-chemical processes are usually faster than other routes of conversion and operate at higher temperatures. They can also handle a larger variety of biomass kinds and sources.

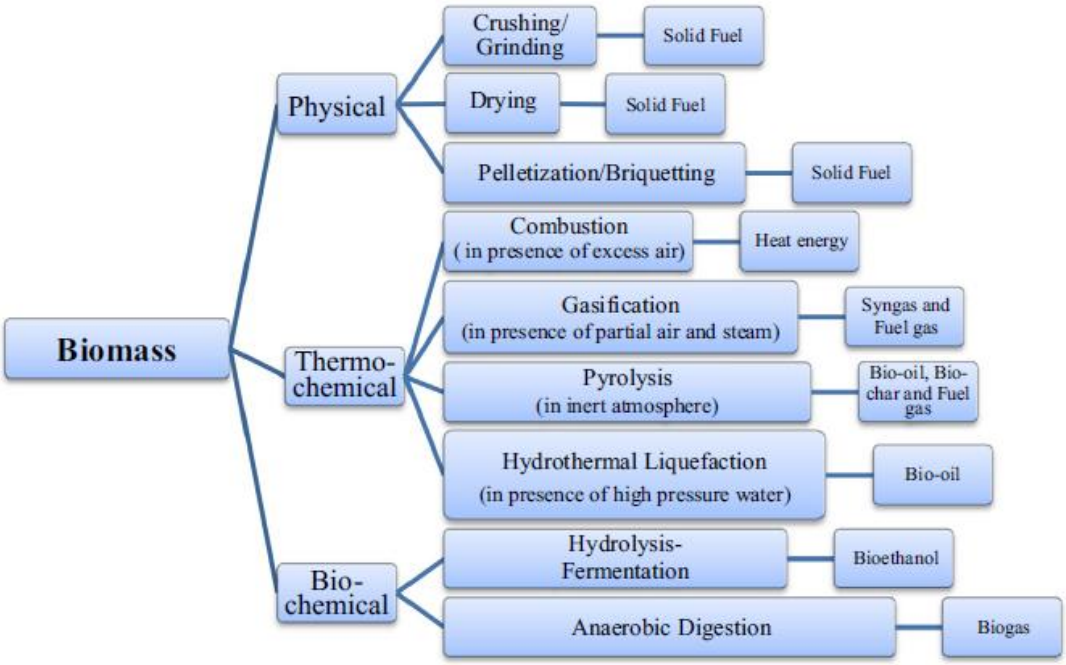

Figure 1-3 : Conversion pathways of biomass into bioenergy [14].

Thermo-chemical decomposition can be performed through different ways by mainly varying the operating conditions, such as temperature, pressure, reactor type and the oxidant used. Table 1-1 presents a summary of the different parameters for each thermo-chemical conversion pathway.

During combustion, biomass is totally oxidized in presence of excess air, into a flue gas composed mainly of N_2, CO_2 and H_2O, having a high temperature and some char. The heat produced during the process is often integrated into domestic heating or electricity production system via a Rankine cycle. In spite of straight forward use of biomass, direct combustion is one of the main industrial source for air pollution since it leads to the formation of pollutants including SO_x, NO_x and particulates that are directly released to the atmosphere [15,16].

Table 1-1 : Main characteristics of thermo-chemical conversion processes (combustion, pyrolysis, gasification and hydrothermal liquefaction) [17–20].

	Combustion	Pyrolysis	Gasification	Hydrothermal liquefaction
Oxidant	Excess of air	None - Inert atmosphere such as nitrogen	Steam or partial air	Water
Temperature	$850℃\ to\ 1200℃$	$300℃\ to\ 600℃$	- Air: $500℃\ to\ 900℃$ - Pure oxygen or steam: $1000℃\ to\ 1600℃$	$250℃\ to\ 375℃$
Pressure	Atmospheric	Atmospheric or higher $(0.1\ to\ 5\ MPa)$	Atmospheric	High $(4\ to\ 22\ MPa)$
Main products	Flue gas and ash	Fuel gas, tar and char	Producer gas and tar	Liquid fuels with low tar yield

Biomass pyrolysis takes place in an inert environment and leads to the formation of gaseous, liquid and solid fractions of fuel gas, bio-oil (tar) and char, respectively. Based on the heating rate and the residence time, the pyrolysis can be divided into fast and slow [21]. On the one hand, the slow pyrolysis corresponds to a low heating rate with a long residence time. The slow pyrolysis enhances the solid phase production and therefore the char formation. On the other hand, fast pyrolysis corresponds to a higher heating rate with a shorter residence time. This process is utilized to maximize the liquid phase formation. Moreover, the yield of the gas produced by slow pyrolysis is higher than that produced by fast pyrolysis [22].

Gasification occurs at higher temperature than pyrolysis. Within the biomass gasification process, several chemical reactions take place leading to the decomposition of the feedstock into a producer gas rich in carbon monoxide, hydrogen in addition to other gas compounds [23]. Several by-products are produced during the gasification process, mainly H_2S, NH_3 and tar. The feedstock decomposition happens in the presence of a controlled gasification agent flow at high temperature. The producer gas can be further integrated in different processes for electricity and heat generation, chemical synthesis and hydrogen production. Moreover, biomass gasification yields a cleaner gas and therefore reduces the amount of pollutants that must be treated before being released to the atmosphere. The composition of the producer gas depends on the biomass composition, the gasification agent and the gasification conditions, such as the equivalence ratio, the pressure and the temperature. The gasification agent can be air, steam or steam/O_2.

Hydrothermal liquefaction (HTL), synonym of hydrous pyrolysis, is the direct conversion of biomass into liquid fuels at temperatures around 350°C and under a high pressure, typically between 4 and 22 MPa in a water environment. At those conditions, the water remains in its liquid phase. HTL is typically used for the thermo-chemical conversion of microalgae since the latter is already present in hydrous environment. This eliminates the need of a drying step. HTL converts the biomass into a mixture of gas, solid, bio-oil and water soluble components such as organic acid and sugar [24]. The main product of the HTL is the bio-oil, which is also known as biocrude. Compared to pyrolysis, HTL yields a lower tar content and a higher energy efficiency [20].

In summary, the combustion produces incombustible gases that cannot be converted into biofuels. The flue gas can only be used for CHP. Fast pyrolysis is mainly used for the production of bio-oil that can be later upgraded into transportation fuel. Slow pyrolysis aims at producing char, which is processed into activated carbon or used as soil amendment. HTL aims at maximizing the production of biocrude.

The latter can be upgraded into petroleum derived fuel products depending on the biomass type [25]. Biomass gasification yields the highest gas fraction. Moreover, the gaseous product is a mixture of combustible components that can be further valorized into bio-fuel through a series of reactions. Therefore, this thesis focuses on the gasification process rather than other processes since it is the most industrially applied one for biomass conversion and shows major relevance on the renewable energy pathway set for the gas supply in France and worldwide.

1.3. Gasification

1.3.1. Gasifier stages and main reactions

As seen in Figure 1-4, the gasification process involves different steps: drying, pyrolysis, combustion or oxidation and reduction or gasification.

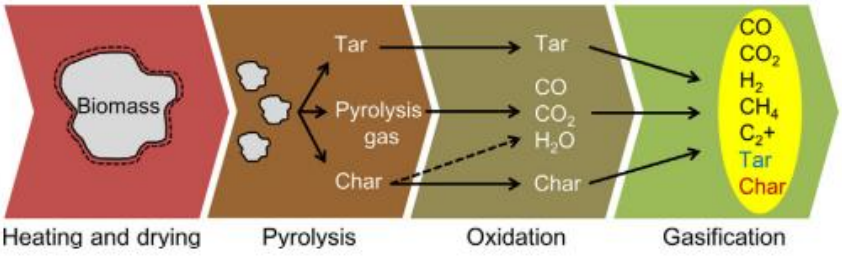

Figure 1-4 : Schematic illustration of gasification steps [5].

As a first step, the biomass is dried, as it approaches the flame zone in the gasifier at temperatures varying between 100°C and 200°C, in order to remove the moisture content from the feedstock:

$$Moist\ feedstock + heat \rightarrow Dry\ feedstock + H_2O \quad (1\text{-}1)$$

The second step is the pyrolysis of the dried biomass that take place in an inert atmosphere at temperature between 300°C and 600°C, known also as devolatilization reaction. It is an endothermic reaction, which converts the biomass into a mixture of solid char, condensable vapors (known as tars) and permanent gases. The required heat for the reaction is ensured either from the partial oxidation that happens in the gasifier or from an external heat source [23]. The products of the pyrolysis reaction will then undergo a series of gasification and combustion reactions due to introducing the gasification agent.

$$\begin{aligned} &Feedstock + heat \\ &\quad \rightarrow Permanent\ gas(H_2 + CO + CO_2 + CH_4 + C_nH_m) + Tar + Char(C) \\ &\quad + Impurities \end{aligned} \quad (1\text{-}2)$$

During the combustion, the gasification agent, present in excess, oxidize the combustible products (tar, char and pyrolysis gases) into carbon dioxide (CO_2) and steam (H_2O). The increase in the temperature during the combustion favors the reduction reactions, and leads to the partial oxidation of the carbon feedstock, into CO, H_2, CH_4 and residual char [4].

The main reactions of the biomass gasification process are summarized in Table 1-2 with the enthalpy of the reaction at 25°C and atmospheric pressure ($\Delta H^0_{r\,25°C,1atm}$). The reactions that take place during oxidation and gasification can be divided into heterogeneous and homogenous reactions. On the first hand, heterogeneous reactions can be defined as the reactions between the solid phase and the gas phase. For instance, heterogeneous reactions cover the reactions between the solid char formed within the biomass pyrolysis step and the gasification agent. Those reactions are presented from eq. (1-3) to eq.

(1-7) in Table 1-2. On the second hand, homogeneous reactions present the reactions in the gaseous phase that take place between the permanent gaseous phase and the gasification agent. Those reactions are presented from eq. (1-8) to eq. (1-14) in Table 1-2. The tar decomposition reaction presented in eq. (1-14) is classified as a homogenous reaction since the decomposition happens in the gaseous phase. This reaction is endothermic, therefore it is favored in high temperature zones. The required heat for the endothermic reactions, such as steam reforming eq. (1-11), is provided from the exothermic reactions, for instance the oxidation and partial oxidation reactions with oxygen.

Table 1-2: Main reactions of the biomass gasification process [15,16,23,26].

Reaction name	Reaction equation	$\Delta H^{0}_{r_{25℃,1atm}}$ $kJ.mol^{-1}$	
Heterogeneous reactions			
Carbon partial oxidation	$C + 1/2\,O_2 \rightarrow CO$	-111	(1-3)
Carbon oxidation	$C + O_2 \rightarrow CO_2$	-394	(1-4)
Carbon steam gasification	$C + H_2O \leftrightarrow CO + H_2$	$+131$	(1-5)
Hydrogasification	$C + 2H_2 \rightarrow CH_4$	-75	(1-6)
Boudouard reaction	$C + CO_2 \leftrightarrow 2CO$	$+172$	(1-7)
Homogeneous reactions			
Hydrogen oxidation	$H_2 + 1/2\,O_2 \rightarrow H_2O$	-242	(1-8)
Carbon monoxide oxidation	$CO + 1/2\,O_2 \rightarrow CO_2$	-283	(1-9)
Water-Gas shift reaction	$CO + H_2O \leftrightarrow CO_2 + H_2$	-41	(1-10)
Steam reforming	$CH_4 + H_2O \leftrightarrow CO + 3H_2$	$+210$	(1-11)
Methane gasification	$CH_4 + 1/2\,O_2 \leftrightarrow CO + 2H_2$	-36	(1-12)
Methane oxidation	$CH_4 + 2O_2 \leftrightarrow CO_2 + 2H_2O$	-803	(1-13)
Tar decomposition	$Tar + heat \rightarrow gas + solid\ carbon$	> 0	(1-14)

Note that the reaction of the impurities, consisting of nitrogen and sulfur, are not presented in Table 1-2 since their content is negligible compared to the rest of the compounds listed in other reactions. The content of sulfur and nitrogen depends on the type of biomass being gasified. In general, the sulfur is converted into sulfur oxides (SO_x) and hydrogen sulfide (H_2S) by oxidation and gasification, respectively. The nitrogen content is converted into nitrogen oxides (NO_x) and nitrogen (N_2) by oxidation and gasification, respectively.

1.3.2. Gasifier types

Different types of gasifiers exist: updraft (counter-current), downdraft (co-current), fluidized bed (bubbling or circulating), indirect and entrained flow gasifiers. The type of the gasifier affects the composition of the producer gas as well as the tar content. Updraft and downdraft gasifiers are both fixed bed gasifiers. As it can be seen in Figure 1-5, for an updraft gasifier, oxidant is fed from the bottom while biomass is fed from the top. This results in a low temperature zone at the top of the gasifier. The producer gas leaves the gasifier at a temperature around 250°C with a high tar content (10-150 $g.Nm^{-3}$) [27]. In a downdraft gasifier, biomass is introduced from the top, while the oxidant is fed at a certain position lower than the top. This eliminates the low temperature zone, and yields a producer gas with low tar content (0.01-6 $g.Nm^{-3}$) at 800°C [23]. Tar yields in a downdraft gasifier are lower than those in an updraft gasifier since the tar produced in a downdraft gasifier passes through a hot zone where primary tars are converted into non-condensable gases as illustrated in Figure 1-5. As stated previously, tar is produced mainly in the pyrolysis zone. In an updraft gasifier, primary tar produced within the pyrolysis zone flows through the drying zone only that operates at low temperatures. While in the downdraft gasifier, tar produced in the pyrolysis will pass through combustion and reduction zones.

Since these zones operate at high temperature, part of the tar produced in the pyrolysis zone will be converted into non-condensable gases.

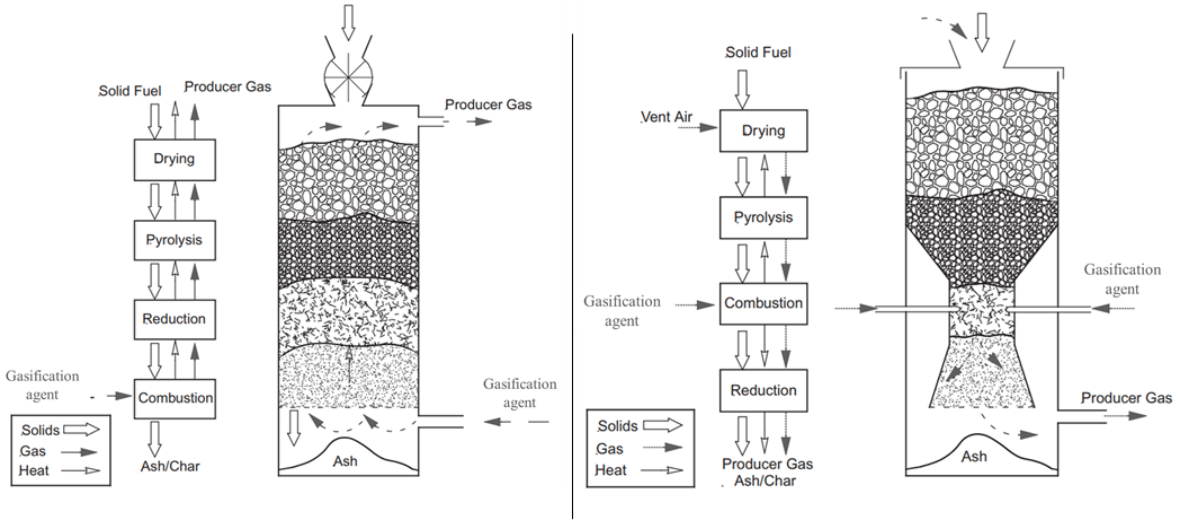

Figure 1-5 : Updraft gasifier (left) vs. downdraft gasifier (right) [23].

Fluidized bed gasifier can be divided into bubbling (Figure 1-6 (A)) and circulating (Figure 1-6 (B)) types. For both, biomass is fluidized by means of the gasification agent injected from the bottom of the gasifier. A velocity of 0.5 $m.s^{-1}$ to 1 $m.s^{-1}$ is needed to create a bubbling medium, while a higher gas velocity of 3.5 $m.s^{-1}$ to 5.5 $m.s^{-1}$ is required for a circulating fluidized bed reactor. The gasification agent can be air, steam, oxygen, or steam/oxygen mixture. A bed material is placed in the fluidized gasifier in order to enhance the heat transfer within it. The bed material can be an inert such as alumina or a catalyst such as dolomite. The typical operation temperature of the fluidized gasifier as well as the gas exit temperature varies between 800°C and 900°C. The tar content in the gas produced in a fluidized bed varies between 1 and 30 $g.Nm^{-3}$.

A new type of gasifier known as Dual Fluidized Bed (DFB) or indirect gasifier is shown in Figure 1-6 (C). Combustion and gasification stages are separated into two fluidized bed chambers. Biomass is fed to the bubbling fluidized bed gasifier where it is gasified in presence of steam (gasification agent) into producer gas and char. Char and the bed material are transferred to the circulating fluidized bed combustion section. Char is burned in the combustion section by air injection, while the heated bed material is recirculated to the gasification chamber to ensure the heat of the endothermic gasification reaction. This type of gasification is considered the most suitable for synthesis application since it yields a non-diluted producer gas by inert. The producer gas leaves the gasification chamber at a temperature near 850°C with an average tar content of 30 $g.Nm^{-3}$ [28].

The last type of gasifiers is the entrained flow gasifier. The fluidization speed should be greater than 6 $m.s^{-1}$ such that the speed of the particles is close to the speed of the gases [27]. The biomass is introduced in pulverized form. The reaction takes place at a very high temperature (between 1200°C and 1500°C), so that a low tar content is present in the producer gas. However, the residence time of the solid in the reactor is very short and does not allow the total conversion of the solid. On the other hand, the small biomass particle size involves significant preparation costs and the technology complexity makes it expensive and difficult to implement.

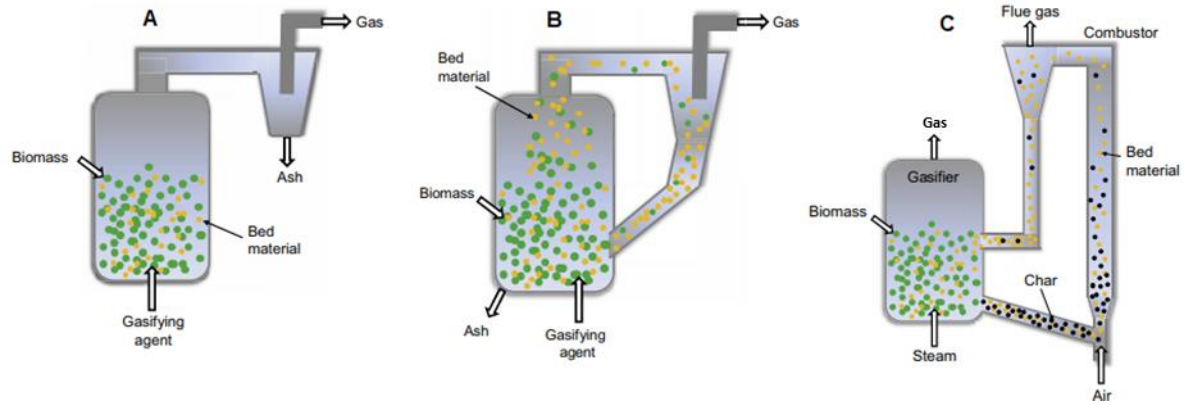

Figure 1-6: Illustration of A) Bubbling Fluidized Bed (BFB), B) Circulating Fluidized Bed (CFB), and C) Dual Fluidized Bed (DFB) gasifiers [29].

The gasification agent used has a high impact on the composition of the producer gas. Oxygen is the less used gasification agent due to its high cost and the need of a distillation unit to separate it from air when large amounts of this agent are needed. Using air as a gasification agent yields a producer gas having high N_2 content (≈ 50 vol%). The presence of an important nitrogen fraction in the producer gas reduces its heating value. Air is usually used as a gasification agent when CHP via internal combustion engines or gas turbines is the desired application for the producer gas. Steam gasification yields a producer gas having a high water content (≈ 30 vol%).

1.3.3. Producer gas composition

The producer gas composition depends on many gasification variables such as the temperature, the gasifier type and the gasification agent. Table 1-3 presents the producer gas composition for the different gasification agents and gasifier types discussed above. Each gasifier has its advantages and disadvantages depending on the application of the producer gas. In the case where methanation is the desired application after the gasification, DBF gasifier is the most suitable one. The latter yields a producer gas with high methane and low inert content. A low nitrogen content could be present in the producer gas. This nitrogen comes from the combustion that takes place in a separated chamber and from the biomass carrier gas. The disadvantage of the DFB gasifier is its high tar yield.

Table 1-3 : Typical producer gas composition for multiple gasifiers and gasification agents [30–35].

Gasification agent	Air			Steam		$Steam/O_2$
Gasifier type	Updraft	Downdraft	BFB	DFB	BFB	Downdraft
H_2 ($vol\%_{wet}$)	10-14	17-20	4.5-11.1	18.6-27.8	12.4-27.8	15.9-19
CO ($vol\%_{wet}$)	15-20	18-21	13.5-18.4	16.7-17.5	5.5-15.9	21-23
CO_2 ($vol\%_{wet}$)	8-10	8-12	13.2-14.9	11.1-13.9	4.2-8.5	16.6-19.2
CH_4 ($vol\%_{wet}$)	2-3	1-3	3.5-4.5	6-7.1	2.3-5.9	1.4-2.5
C_2H_n ($vol\%_{wet}$)	n.d.	n.d.	1.2-1.6	1.6-2.7	0.7-1.1	0.16-0.49
N_2 ($vol\%_{wet}$)	45-52	45-50	41.8-50.1	0.05-3.7	0	0
H_2O ($vol\%_{wet}$)	2-6	0.5-2	8.8-16.2	30.3-42.8	52-60	31-61
Tar ($g.Nm^{-3}$)	10-150	0.01-6	2-30	30-70	37.5-73	2-5.5

In general, biomass contains traces of nitrogen, sulfur and chloride. Therefore, biomass gasification leads to the formation of a producer gas having a certain content of impurities, mainly H_2S, NH_3, and HCl. According to Schmid et al. [36], the mole fraction of those impurities varies with respect to the

type of the gasified biomass. The mole fraction, on dry basis, of H_2S, NH_3, and HCl ranges between $1.24x10^{-3}$ to $2.04x10^{-3}$, $1.81x10^{-3}$ to $7.40x10^{-3}$, and $0.09x10^{-3}$ to $0.46x10^{-3}$, respectively.

One of the main problems related to the gasification is the tar entrainment to the downstream equipment by the hot producer gas. If tars are not treated, they will condense when in contact with cold surfaces forming sticky deposits in the equipment, fouling and blocking engines, fuel lines and filters, and limiting heat transfer in exchangers. Moreover, tar leads to catalytic deactivation in chemical synthesis applications. The tar composition is variable and mainly depends on the gasifier operating conditions and biomass sources. In the sequel, a bibliography on tar compositions and tar removal methods is respectively presented in sections 1.4 and 1.5.

1.4. Tar properties

According to the tar measurement protocol meeting held on 1988 in Brussels [37], tar is defined as hydrocarbons with molecular weight higher than benzene. Tar can be classified in the condensable fraction of the producer gas during thermo-chemical conversion. It is formed of aromatic hydrocarbons having up to five rings [4,8].

1.4.1. Tar composition

It is hard to predict the composition of tar since it depends on many factors such as the type of biomass, the gasifying agent, the reactor type, the temperature and the pressure. Tar is mainly formed during the pyrolysis step where biomass is converted into a mixture of condensable hydrocarbons, including aromatic and polycyclic aromatic compounds (which might be oxygenated compounds), by the decomposition of the lignocellulosic biomass [4]. Figure 1-7 shows an example of the tar composition.

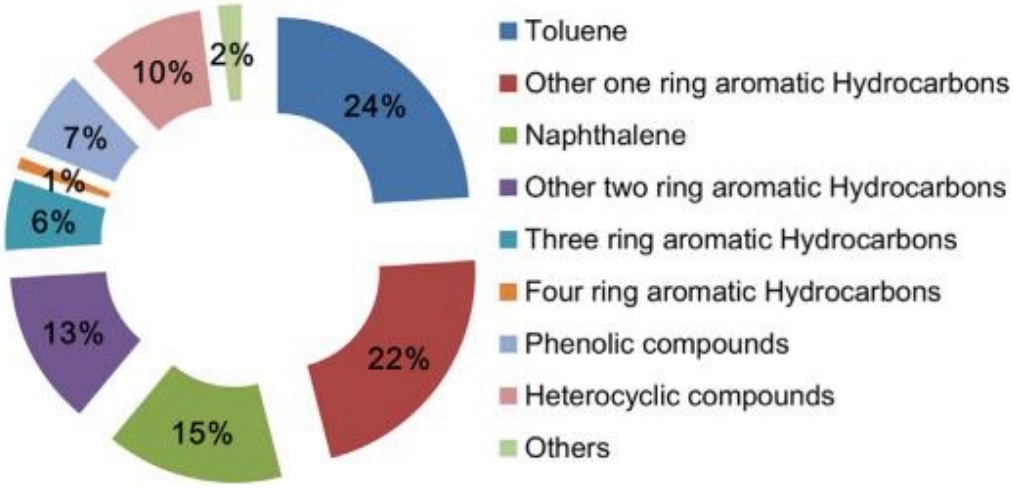

Figure 1-7 : Example of the composition of the tar produced from biomass gasification [5].

Tar formation is summarized in Figure 1-8. The oxygenated tars formed at low temperature are converted into large polycyclic aromatic hydrocarbons (PAH) when the temperature is increased by favoring secondary reactions in the gas phase.

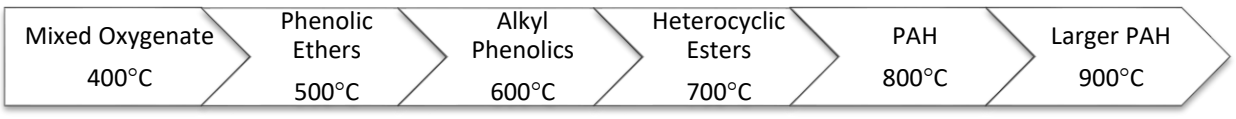

Figure 1-8 : Scheme of tar formation [38]

1.4.2. Tar classification

Tar can be classified according to different characteristics. Table 1-4 presents the classification of tar according to its condensability and solubility. This classification method divides the tar into 5 classes. Another classification divides the tar into 3 groups according to its appearance: primary, secondary and tertiary tars [38]. The specifications of each group are described in Figure 1-9.

Table 1-4 : Tar classification with respect to its molecular weight [4,5,8]

Tar Class	Class Name	Property	Compounds
1	GC-undetectable tar	Very heavy tars compounds that cannot be detected by gas chromatography (GC)	Determined by subtracting the GC-detectable tar fraction from the total gravimetric tar
2	Heterocyclic	Tar containing hetero atoms; very soluble in water	Pyridine, phenol, cresols, quinoline, isoquinoline, dibenzophenol
3	Light aromatic (1 ring)	Light hydrocarbons with single ring, do not pose a problem regarding condensability and solubility	Toluene, ethylbenzene, benzene, xylenes, styrene
4	Light PAHs compounds (2–3 rings)	2 and 3 rings, condense at low temperature at very low concentrations	Indene, naphthalene, methylnaphthalene, biphenyl, acenaphthalene, fluorene, phenanthrene, anthracene
5	Heavy PAHs compounds (4–7 rings)	3 rings and more, condense at high temperatures even at low concentrations	Fluoranthene, pyrene, chrysene, perylene, coronene

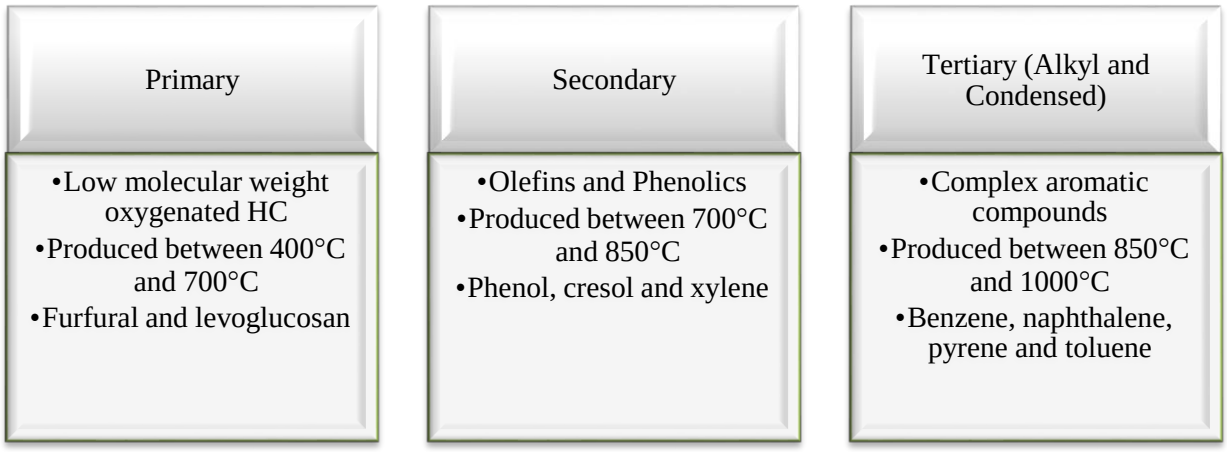

Figure 1-9 : Description of primary, secondary and tertiary tar classification.

1.4.3. Tar content limits

The desired application for the producer gas defines the allowable tar content in the gas phase as seen in Table 1-5. For instance, no restrictions are set for the tar content in direct combustion since the producer gas remains hot by burning it directly. Keeping the producer gas at high temperature eliminates the need of treatment by reducing the risk of condensation. For more advanced applications, limits for the tar content are set to avoid the condensation and therefore the plugging. In particular for CHP applications, the tar content should be lower than 100 $mg.Nm^{-3}$ and 5 $mg.Nm^{-3}$ for internal combustion

engines and for gas turbines respectively. For chemical synthesis applications, stricter limitations are set since the tar problem is not limited to its condensation but also to the catalytic deactivation involved in the synthesis. In methanol synthesis and Fischer Tropsch synthesis, the tar content should be reduced to 1 mg.Nm^{-3}. Note that benzene, toluene and xylene (BTX) are considered in the tar content when dealing with a chemical synthesis application, while they are ignored for CHP.

Table 1-5 : Tar concentration in product gas limits for different applications [3,4].

Application	Tar (mg.Nm^{-3})
Direct combustion	No specified limit
Gas turbine	<5.0
Internal combustion engine	<100
Compressor	50-500
Synthesis of methanol	<0.1
Fischer Tropsch Synthesis	<1.0 µL.L^{-1} (class 2, BTX)
Fuel cells	<1.0

Figure 1-10 indicates the contribution of each class in the tar condensation. Since tar condensation takes place when the vapor pressure of the tar component is higher than its saturation pressure, Bergman et al. [39] linked the dew point of each tar class to its concentration in mg.Nm^{-3} (Figure 1-10). Each individual tar compound in the producer gas affects the condensation behavior due to its contribution in the total vapor pressure. It is expected that tar problems can be solved by reducing the tar dew point to a lower level than lowest temperature in the process. For instance, class 5 components have the highest dew point, even at low concentration. Thus, class 5 dominates the tar dew point and should be totally removed. Reducing the content of class 5 to 0.1 mg.Nm^{-3}, reduces the dew point to around 100°C. The content of classes 2 and 4 should be partially reduced to obtain a tar dew point lower than 25°C. Class 3 has no impact on the condensation behavior due to its very low dew point, even at high concentration. This theory applies only for the applications that do not include catalysts. On the contrary, in chemical synthesis applications, all the classes contribute in the catalytic deactivation at concentration higher than 1 mg.Nm^{-3}. Therefore, BTX components must be included in the analysis.

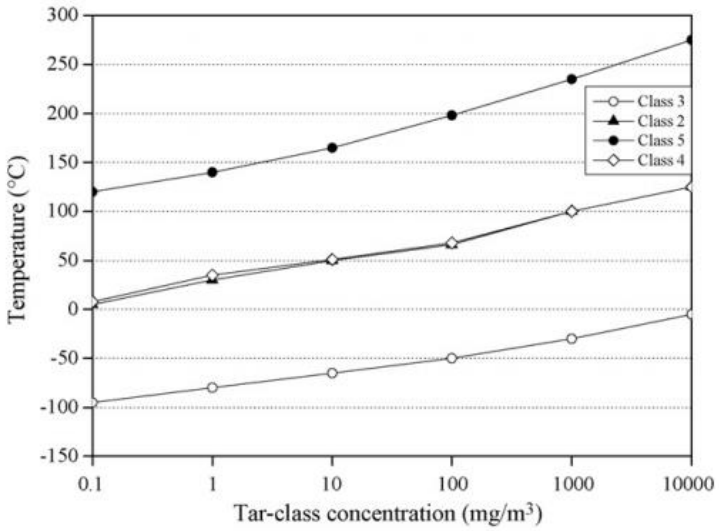

Figure 1-10 : Different tar classes dew point according to their concentration [39,40].

1.5. Tar Treatment

Tar removal can be done through two different methods: primary and secondary. Primary methods are based on reducing the tar formation within the thermo-chemical conversion mainly by varying the operating conditions or changing the configuration design of gasifiers. Secondary methods consist on removing tar after its formation at the end of the conversion process.

1.5.1. Primary methods

'In situ' methods are based on preventing tar formation or converting it within the reactor. This can be done by changing the operating conditions such as temperature, pressure, gasification agent, equivalence ratio (ER) and residence time. An optimal primary method must eliminate the need to add secondary measures for tar removal.

Increasing the gasification temperature reduces tar levels in the producer gas. According to Rapagnà et al. [41], in almond shell gasification, the tar content is reduced from 6.5 to 1.3 $g.Nm^{-3}$, by increasing the temperature from 700 to 820°C. The pressure also affects the tar yield and its composition. Increasing the pressure reduces the tar content and increases the aromatic compounds fraction. Qin Y. et al. [42] showed that increasing the pressure from 0.5 to 2.0 MPa at constant temperature results in reducing the tar content and increasing the aromatic component fraction. It was also shown that the tar content is reduced by increasing the temperature from 700°C to 900°C [42]. In addition, the used gasification agent has an impact on the produced tar. Using steam as a gasification agent results in a higher tar yield than that produced when air is the gasification agent. This can be verified by the observed temperature decrease when steam is injected.

The ratio of biomass to the gasification agent is an important parameter that should also be considered. For air gasification, this parameter is the ER. It is equal to the molar ratio of the actual air fed to biomass ratio, over the stoichiometric air to biomass ratio that is needed for complete combustion. Steam/Biomass ratio (S/B) and Gasifying Ratio (GR) are respectively the parameters for steam and steam/oxygen gasification. ER highly affects the tar content in the producer gas, mainly when operating at high temperature [34]. Increasing the ER leads to increasing the oxygen available to react, in the pyrolysis zone, with the volatile compounds [43]. This reduces the tar content and favors the formation of more polycyclic aromatic hydrocarbons.

The residence time is another operating condition that does not only affect the tar content, but also the tar composition. Increasing the residence time, increases the exposure time of tar with the gasification agent and therefore reduces the tar content [44].
Note that the gasifier type and design have a major impact on the tar yield. The impact of the gasifier type on the gas composition and the tar content has been previously detailed in section 1.3. The most effective design in reducing the tar formation during gasification is a co-current fixed bed gasifier [44].

1.5.2. Secondary methods

Bergman et al. [39] stated that even when primary methods are used to reduce tar formation, the need of a secondary treatment method is necessary in order to reach a complete tar removal. Secondary methods can be splitted into physical (filters and cyclones) and chemical (catalytic and thermal cracking) processes. Note that secondary methods present some disadvantages such as being expensive and producing effluents by shifting the tar problem from the gaseous phase into a liquid phase.

1.5.2.1 Physical/ Mechanical methods

Particulate matters and tars can be removed from the producer gas by physical/mechanical methods. Those methods are separated into dry and wet cleaning methods. Physical/mechanical methods have a lower operating and maintenance cost than that of the chemical methods. Figure 1-11 presents the classification of the physical/mechanical cleaning systems. The main disadvantage of wet cleaning systems is the generation of contaminated water or oil, and thus exchanging the tar problem from the gaseous phase to the liquid phase [38].

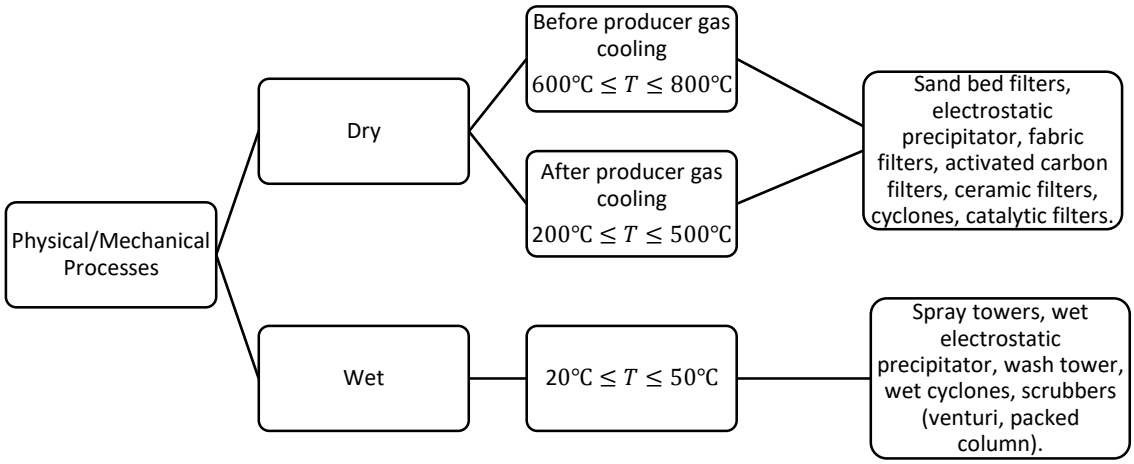

Figure 1-11: Dry and wet tar removal methods.

Physical methods are more effective for particulate removal than tar removal. Mainly tar in the condensed form can be captured. Additional cleaning systems may be required to achieve high tar removal efficiencies. The operating temperatures, tar and particulate removal efficiencies for some cleaning systems are summarized in Table 1-6.

Table 1-6 : Efficiencies of dry and wet tar and particles removal methods [4,8].

Cleaning system	Tar removal efficiency %	Particles removal efficiency %	Temperature ℃
Fixed bed tar adsorber	50-65	-	80
Sand filter bed	50-97	70-99	10-20
Cyclone	30-70	-	100-900
Fabric filter	0-50	70-95	130
Porous catalytic filter disk (1%wt/0.5%wt Ni/CaO)	96-98	-	900
Wash tower	10-25	60-98	50-60
Venturi scrubber	51-91	-	20-100
Wet electrostatic precipitator	40-70	>99	20-30
Diesel scrubber	62	-	20-100

OLGA, a physical treatment for tar removal, was developed at the Energy research Center of the Netherlands (ECN). The objective of OLGA is the selective tar removal while avoiding the generation of a waste stream; without permanent gases or water removal [45]. Figure 1-12 shows the flowsheet of the OLGA process. The gas inlet temperature is kept higher than the tar dew point (320°C-350°C) while the exit gas temperature should be kept higher than the water dew point (60°C-100°C). The gas is being cooled in the first column by means of the scrubbing oil. As a result, heavy tars (class 5 and most

probably class 1) are being condensed in the collector. The collected heavy tars and particulates with a small fraction of the scrubbing liquid are separated and injected in the gasifier. The rest of the liquid stream is recycled back to the collector after being cooled to its initial temperature. In the second column, light tars are absorbed in the scrubbing oil. The latter is regenerated in the stripper using air or steam and recycled to the absorber. The stripping gas charged with light tars is recycled back to the gasifier and acts as the gasification agent [46]. The saturated stripping oil leaving the absorber and the regenerated scrubbing oil leaving the stripper interchange heat and ensure up to 90% of the required cooling and heating. The rest of cooling and heating is added by cooling water and steam, respectively. Operating at optimum conditions of temperatures and scrubbing oil flow rates, reduces the concentration of tar from 7 $g.Nm^{-3}$ to 50 $mg.Nm^{-3}$, while excluding benzene and toluene from the analysis. Heavy tars (class 5) were completely removed, naphthalene and phenol were respectively reduced by 99.5% and 85%. At the outlet of the OLGA process, the tar dew point was reduced to 4°C at those conditions. Another experiment done over 75 hours of operation showed that 98% of tars were removed by OLGA (1223 g out of 1252g). The initial tar content was 10.8 $g.Nm^{-3}$, while the leaving tar content was 250 $mg.Nm^{-3}$ with a dew point of -10°C. Around 570 g of tars were collected in the collector and 650 g were absorbed in the second column. In the stripper, 500 g of tars were removed, while the rest is recycled back with the oil to the absorber.

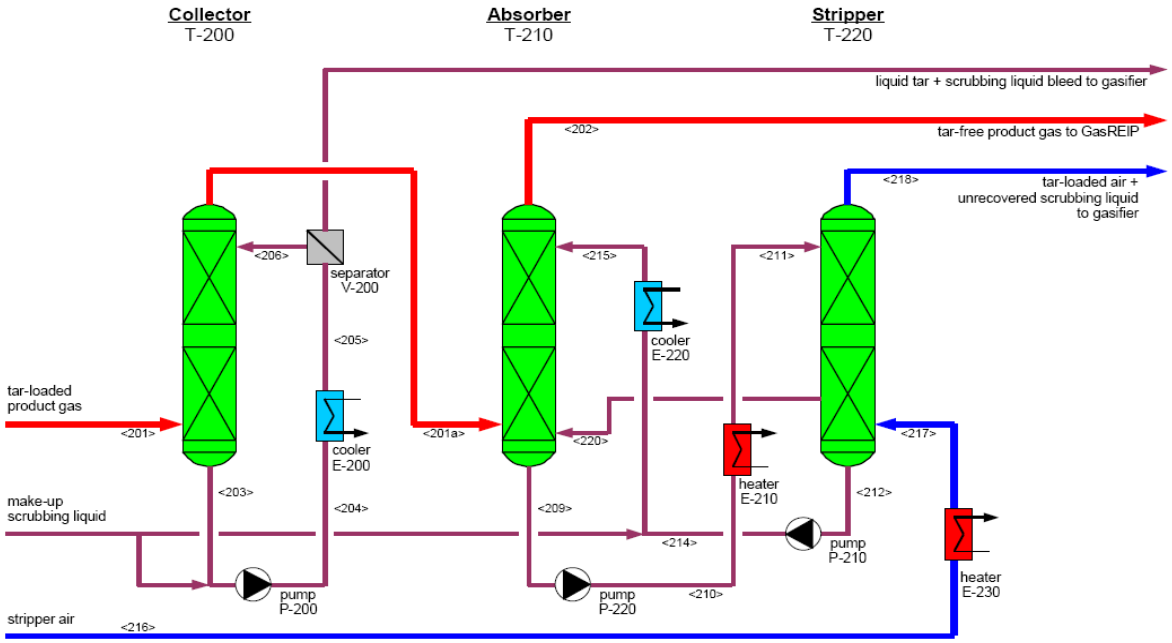

Figure 1-12: Flowsheet of the OLGA process [46].

Many researchers focused on tar removal via physical processes, especially on absorption columns and the effect of the liquid used for reducing tar content. Phuphuakrat et al. [47] evaluate different scrubbing mediums in order to find the one with the highest absorption efficiency: water, biodiesel fuel, diesel fuel, engine oil and vegetable oil. Since no equipment for enhancing the mass transfer are being used, this test only assesses the absorption performance. After the gasification, the producer gas itself is heated again to 800°C in a reformer for a long residence time in order to crack heavy tars into lighter molecules. The contribution of condensation in tar removal will then be reduced. To reduce the cost of tar removal, diesel and biodiesel fuels can be used in boilers and engines after tar absorption. Waste vegetable oil and waste engine oil were used. The initial concentration of gravimetric tar was 13.3 $g.m^{-3}$. The temperature of the gas entering the scrubber varies between 30.8°C and 33.6°C. Using water as

scrubbing medium reduces the tar concentration to 9.1 $g.m^{-3}$. This reduction is mainly caused by condensation rather than by solubility in water. The temperature of water was equal to 28°C. Tars were not dissolved in water; they were condensed forming two separated phase due to the immiscibility of the tar components in the scrubbing liquid. Using engine oil and vegetable oil as scrubbing mediums reduces the tar concentration to 8.7 $g.m^{-3}$ and 5.3 $g.m^{-3}$, respectively. When operating with diesel, the concentration of gravimetric tars was increased to 32.5 $g.m^{-3}$. This is due to the fact that some diesel compounds will easily be evaporated and go into the vapor phase. The use of water as a scrubbing medium results in a high removal efficiency only for class 2 components since they are water soluble, such as phenol for example. When oil is used as a scrubbing medium, oil absorption efficiency increases as the oil viscosity decreases. The absorption efficiency for hydrocarbon scrubbers is much higher than that of water. Even for the hydrophilic compounds, fuels and oils are efficient in phenol absorption, except for diesel. When diesel fuel is used, the concentration of xylene and phenol leaving the scrubber is higher than that entering it. The evaporation of the diesel fuel explains the concentration increment since xylene and phenol that may be present in the diesel fuel as additives, are easily evaporated. Table 1-7 compares the removal efficiency of different tar compounds for different scrubbing mediums. The negative efficiencies in Table 1-7 indicate that phenol and xylene are evaporated from the diesel fuel toward the producer gas.

Table 1-7: Absorption efficiencies of tar components by different absorbents (%) [47].

	Water	Diesel fuel	Biodiesel fuel	Vegetable oil	Engine oil
Benzene	24.1	77.0	86.1	77.6	61.7
Toluene	22.5	63.2	94.7	91.1	82.3
Xylene	22.1	-730.1	97.8	96.4	90.7
Styrene	23.5	57.7	98.1	97.1	91.1
Phenol	92.8	-111.1	99.9	99.7	97.7
Indene	28.2	97.9	97.2	97.6	88.7
Naphthalene	38.9	97.4	90.3	93.5	76.2

In this study, the authors considered that the presence of light aromatic hydrocarbon tars would not cause fouling and clogging problems. The comparison of the absorption efficiency was done for naphthalene, considering that it represents light PAH tars. Water has the lowest absorption efficiency. As for the oils, the efficiency for naphthalene absorption is as follows: diesel fuel > vegetable oil > biodiesel fuel > engine oil.

Paethanom et al. [48] studied the effect of absorption and adsorption, separately and combined, on tar removal. The absorption was tested for two scrubbing mediums: vegetable oil and waste cooking oil. As for the adsorption, tar removal efficiency was tested for a bed height of 100 mm of rice husk and rice husk char. In this study, they use absorption for heavy tar removal and adsorption for the light ones. The inlet tar content of the experiments was 93.7 $g.m^{-3}$. Tar treatment section operates at room temperature and atmospheric pressure. Regarding the absorption, the vegetable oil was able to reduce the tar content to 34.1 $g.m^{-3}$ while the waste cooking oil results in 40.8 $g.m^{-3}$. Further tar reduction can be achieved by adding an agitation. The optimal stirring speed for the vegetable oil was equal to 1000 rpm where tar content is reduced to 9.6 $g.m^{-3}$. While for waste cooking oil, a concentration of 17.4 $g.m^{-3}$ can be achieved for a stirring speed of 750 rpm. Moving to the adsorption, rice husk char has higher tar reduction efficiency than rice husk. This can be justified by its higher specific surface area. However, the bed becomes very soon saturated and requires regeneration. Operating alone, tar removal efficiency decreases dramatically after 24 minutes due to the presence of heavy PAH. Thus, longer operation period is expected after heavy tar fraction removal. Combining absorption and adsorption seems to be an efficient treatment. According to Figure 1-13, using vegetable oil as a scrubbing medium with 1000 rpm

stirring speed followed by a bed of rice husk char leads to the highest tar reduction efficiency (95.4%). The remaining tar content after this treatment was reduced to 4.3 $g.m^{-3}$.

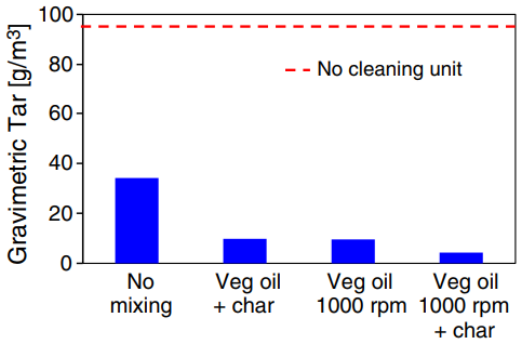

Figure 1-13 : Comparison between the remaining tar concentrations for different treatment absorption – adsorption methods [48].

Phuphuakrat et al. [49] suggest a two-stage process for tar treatment. The process involves a decomposition step followed by a fixed adsorption bed. After the reformer, producer gas flows through a fixed adsorption bed for further tar reduction. The efficiency of three different types of adsorbents was studied: activated carbon, synthetic porous cordierite, and wood chips. Gases are cooled to a temperature between 25°C and 30°C prior to the adsorption step. Wood chips showed the highest adsorption capacity followed by activated carbon and synthetic porous cordierite. However, when calculating the amount of adsorbed tar components, lower values for tar adsorption capacity were obtained for wood chips and synthetic porous cordierite. This reflects that a great amount of steam is being adsorbed on those two beds, and the highest tar adsorption capacity is reserved for activated carbon. The tar content, after the activated carbon filter bed, is reduced to 65 $mg.m^{-3}$, while the gas still contains 1027 mg of $tars.m^{-3}$ for wood chips.

1.5.2.2 Simulations of oil-based scrubbers

In this section, the OLGA process is simulated using Aspen Plus to analyze the parametric impact on the tar removal efficiency. Note that those simulations have been performed in this work rather than extracting the simulation results from the literature. The different columns (collector, absorber, and stripper) are simulated as RadFrac columns based on equilibrium stage model. Rapeseed methyl ester (RME) is one of the most used scrubbing mediums for tar removal through wet scrubbers. Note that RME is a biodiesel type formed of a mixture of saturated and unsaturated C_{16} to C_{22} fatty acids. According to Gateau et al. [50], RME is a mixture of methyl-oleate, methyl-palmitate, methyl-stearate, methyl-linoleate, methyl-linolenate and methyl-myristate. Many previous researches [51, 52] have simulated the RME and the biodiesel as being formed only of methyl-oleate since it forms around 65% of the RME. In this section, two different compositions for the RME are compared. The first composition considers the RME as pure methyl-oleate. The second composition considers the RME as a mixture of methyl-oleate (61%), methyl-linoleate, (22.5%) methyl-linolenate (8%), methyl-palmitate (7.5%) and methyl-stearate (1%).

Figure 1-14 is taken from Aspen Plus simulations and it presents the flowsheet of the scrubbing process for tar removal from the producer gas. The re-cycling streams are not directly connected in the simulations as seen in the flowsheet. The recycling of the scrubbing liquid to the collector and to the absorber is done using VBA.

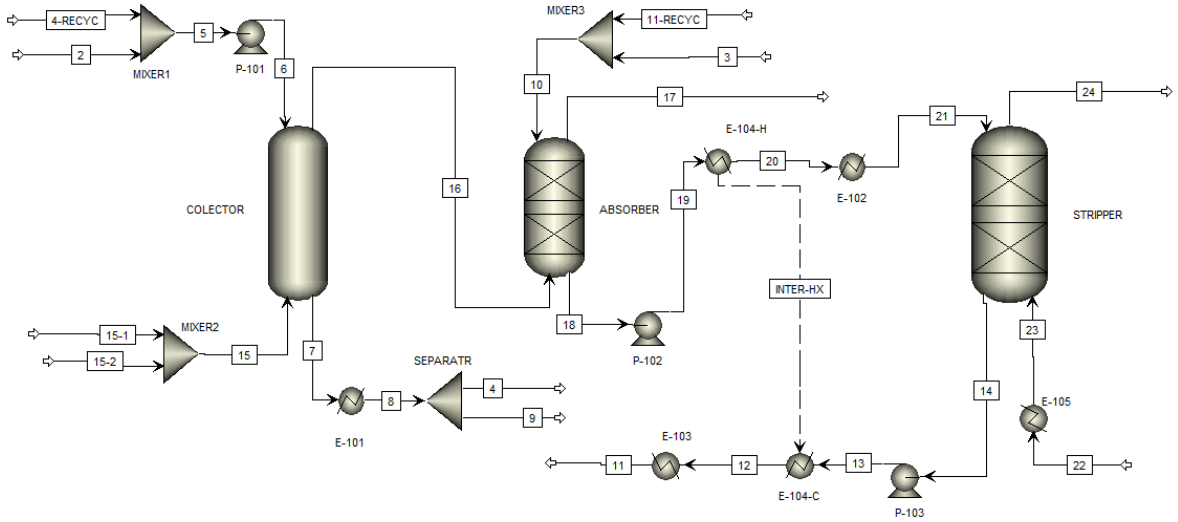

Figure 1-14: Schematic diagram of the scrubbing process for tar removal, using Aspen Plus.

This section aims to validate the simulation and to extract more data on the operating conditions and limitations of the existing OLGA process. The results obtained by our simulation are compared with the ones obtained by Boerrigter et al. [46] and Zwart et al. [53]. The producer gas composition considered in this section is shown in Table 1-8. This composition is retrieved for a Danish straw Circulating Fluidized Bed (CFB) gasifier, operating with air as gasification agent [53]. The initial tar content in the producer gas is presented in the first column of Table 1-10. It is important to mention that several physical property methods including: Peng-Robinson, UNIQUAC, NRTL and SRK have been assessed. However, the selected appropriate physical property method is SR-POLAR since it gives the most appropriate results when comparing them with the ones in the literature. The SR-POLAR method is suitable for mixtures combining light gases and polar compounds. Moreover, vapor-liquid-liquid are set as the valid phases in the simulations, since the condensable components may not form a homogeneous liquid phase. For instance, benzene is slightly soluble in water while toluene is insoluble in water. After the gasifier, the producer gas is first cooled to a temperature of 350°C through an indirect contact heat exchanger, reducing then the required energy of cooling in the first scrubber. At this temperature, the producer gas is then fed to the collector where it comes in contact with the scrubbing liquid, having a temperature of 25°C. Due to the temperature difference, the heavy tar fraction is removed by condensation rather than absorption, since the scrubbing medium is recycled without treatment. Thus, it becomes saturated after a certain time of operation. Contrarily to the collector, the scrubbing liquid is regenerated by means of a hot air stream in the stripper, before recycling it back to the absorber. Note that, in this section, air is used for the regeneration since the gasification takes place with air as gasification agent.

Table 1-8: Producer gas composition considered in the OLGA process simulation [53].

	CO_2	CO	H_2	N_2	CH_4	H_2O	C_2H_y	C_6H_6	C_7H_8
Volume fraction	0.1183	0.1330	0.0286	0.4814	0.0351	0.1840	0.0138	0.005	0.0008
Mass fraction	0.192	0.137	0.002	0.496	0.021	0.122	0.013	0.014	0.003

The main parameters considered in the simulations of oil-based process are summarized in Table 1-9. The stream 4-RECYC is the recycled flow of scrubbing liquid. Therefore, its composition is equal to that of the stream 4 leaving the collector. Streams 2 and 3 are the fresh scrubbing liquid fed into the collector and the absorber, respectively. Stream 11-RECYC presents the recycled flow of scrubbing liquid, which is first regenerated in the stripper. Therefore, its composition is equal to that of stream 11

leaving the stripper. The recycling of both scrubbing liquid streams is calculated through VBA. As a first step, the process is simulated without recycling the scrubbing liquid. Based on those simulations, the composition of the liquid stream leaving the stripper is known. This composition is extracted by linking Aspen to VBA. Then, this composition is used as the inlet composition of the recycled scrubbing liquid to the absorber (11-RECYC). Based on the literature, 90% of the scrubbing liquid is recycled while a fresh flow forming 10% of the scrubbing liquid is required.

Table 1-9: Main operating conditions and stream variables considered in Aspen Plus for simulating OLGA process using two different RME compositions.

Stream ID	15	4	2	16	11	3
Temperature (°C)	350	25	25	71	40-70	40-70
Volumetric flow rate ($m^3.h^{-1}$)	8518	4.8	0.54	4691	7.8	0.78
Mass flow rate ($kg.h^{-1}$)	4501	3150	350	4490	1000-8000	100-800

Two sensitivity studies were conducted in order to assess the impact of the Liquid to Gas (L/G) ratio and the scrubbing liquid temperature, on the tar removal efficiency. Both studies were developed to analyze the impact on the remaining tar content in the gas phase and on the temperature of the gas stream leaving the absorber (stream 17). Note that the gas flow rate is set to 3560 $kg.h^{-1}$. Figure 1-15 illustrates the first study in which the temperature of the scrubbing liquid is set to 60°C while its mass flow rate, and therefore the L/G ratio, are being varied. The second study, illustrated in Figure 1-16, analyzes the impact of the scrubbing liquid temperature while setting the L/G ratio to $1.82x10^{-3}$ $m^3.m^{-3}$, corresponding to a liquid mass flow rate of 5500 $kg.h^{-1}$. Note that the tar content variation is presented over a logarithmic scale for a better illustration in both figures. It can be seen in Figure 1-15 that the removal efficiency of each tar component is increased by increasing the L/G ratio. It is also noticed that the content of the heaviest tar fraction is reduced before the lightest ones, function of the L/G ratio. This validates the order of condensation that was previously discussed. In contrary to the tar content, the variation of the L/G ratio does not have an important impact on the clean gas temperature (*T out*). The temperature variation is limited to 2.5°C. On the other hand, as observed in Figure 1-16, the clean gas temperature is highly affected by the scrubbing liquid temperature. It can be deduced that the scrubbing liquid temperature should be kept above 56°C for a L/G ratio of $1.82x10^{-3}$ $m^3.m^{-3}$, to avoid steam condensation. It can be observed in Figure 1-16 that, by decreasing the scrubbing liquid temperature, the tar removal efficiency increases. Therefore, to reach a high tar removal efficiency while avoiding mixing water with oil, the optimal solution is to operate at a temperature slightly higher than 56°C.

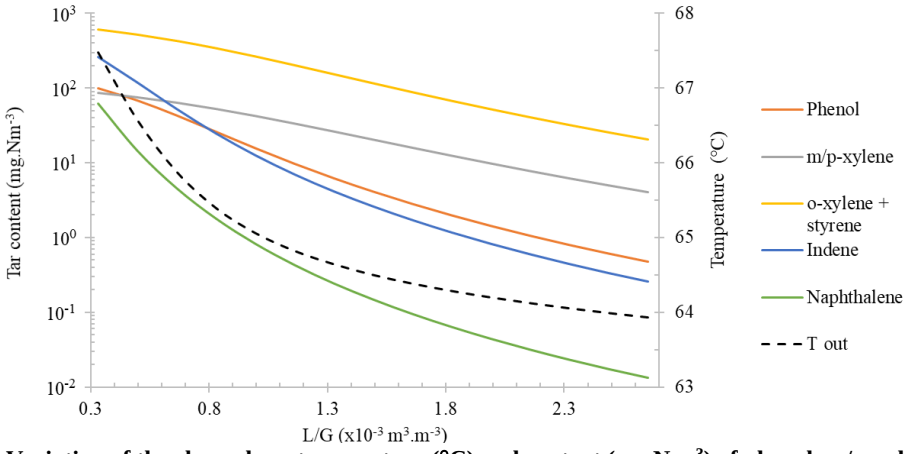

Figure 1-15: Variation of the cleaned gas temperature (°C) and content ($mg.Nm^{-3}$) of phenol, m/p-xylene, o-xylene + styrene, indene and naphthalene, as function of the L/G ratio in the absorber for a scrubbing liquid temperature of 60°C.

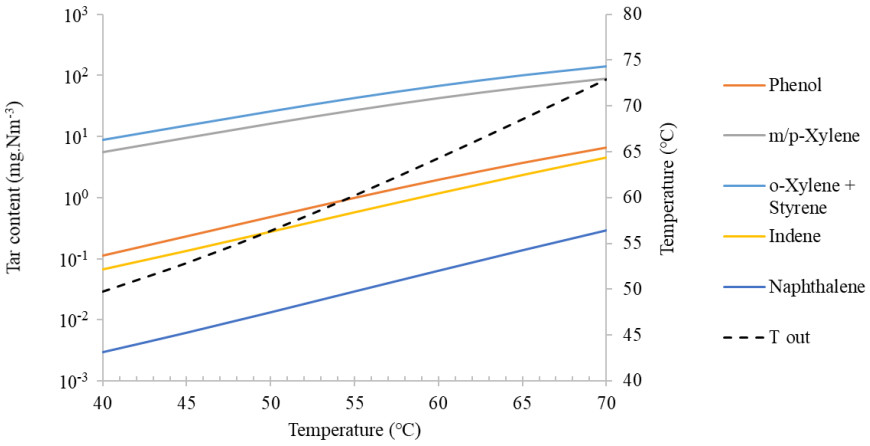

Figure 1-16: Variation of the cleaned gas temperature (°C) and content (mg.Nm^{-3}) of phenol, m/p-xylene, o-xylene + styrene, indene and naphthalene, as function of the scrubbing liquid temperature fed to the absorber, for a L/G ratio of 1.82x10^{-3} m^3.m^{-3}.

While designing the absorber, several constraints must be considered. The first and the most critical one is to keep the producer gas temperature higher than the water due point. For the inlet moisture content of 18.4 vol%, shown in Table 1-8, the water dew point is equal to 61°C. Therefore, the producer gas temperature should be kept higher than 61°C after the absorber. Otherwise, the scrubbing liquid will be mixed with water. The second constraint is the energy consumption of coolers, heaters and pumps. For a gas flow rate of 4000 Nm^3.h^{-1}, the power should be equal to 101 kW for the heater, 8.17 kW for the three pumps and 1.78 m^3.h^{-1} of cooling water for the cooler. The mass flow rate and the temperature of the scrubbing liquid stream were varied until reaching a tar content similar to the experimental one found in the literature [46]. This was achieved for a liquid flow rate of 5500 kg.h^{-1} at a temperature of 60°C. Based on those operating conditions, results showed that the total tar content reduction did not exceed 30% for methyl-oleate and 27% for RME in the first column. The tar content remaining in the producer gas after the collector is detailed in the second and the third columns of Table 1-10, for the methyl-oleate and the RME, respectively. It can be deduced that the heavy tar fraction, mainly class 5, is reduced by 99.97% in the collector, by decreasing the gas temperature from 350°C to 68°C for both scrubbing liquid compositions. The gas is then fed to the second scrubber at this temperature.

A comparison between the obtained results for both scrubbing liquid compositions and the ones extracted from the literature is summarized in Table 1-10. It can be observed that the total tar reduction efficiency is around 98% for all the cases including the experimental results [46]. On the contrary, some of the obtained elementary tar removal efficiencies are different from the experimental ones. The results showed that the clean producer gas is free of tar components that are heavier than naphthalene, for both scrubbing liquid compositions. The producer gas still contains an important amount of light tar compounds, mainly styrene and xylene, in addition to a low content of naphthalene, indene and phenol. In contrast, experiments resulted in a producer gas with a content of quinoline, naphthalene and phenol in addition to some heavier tar compounds such as phenanthrene. This difference between the results is related to the main driving forces that are the scrubbing liquid temperature and the L/G ratio, which were not clearly stated in the literature. Even if all the components of the RME are considered in the simulations, the deviation between the elementary tar content remaining in the gas phase is still the same. It can be seen in Table 1-10 that the results obtained using methyl-oleate are closer to the ones in the literature.

The elementary tar removal is also affected by the solubility of the different tar components, in the scrubbing medium. The solubility affected mainly the removal of the following tar components:

quinoline, naphthalene, styrene, xylene and phenol. The solubility of quinoline, naphthalene and phenol in the scrubbing medium used in the experiment, might be lower than their solubility in methyl-oleate. This led to increase their elementary removal efficiency in the simulations by 2%. On the contrary, the solubility of the lightest components (styrene and xylene) in the scrubbing liquid used in the simulations, is lower than that of the experiment. This results in decreasing their elementary removal efficiency by 8.5%, in the simulations.

Table 1-10: Tar content in the different gas streams for methyl-oleate and RME absorbents at a mass flow rate of 5500 kg.h^{-1} and for an initial scrubbing liquid temperature of 60°C.

Tar Components	Initial tar content [46] (mg.Nm^{-3})	Collector (stream 16)		Absorber (stream 17)		
		Methyl – oleate (mg.Nm^{-3})	RME (mg.Nm^{-3})	Experiment out [46] (mg.Nm^{-3})	Methyl-oleate (mg.Nm^{-3})	RME (mg.Nm^{-3})
Ethylbenzene	7	7	7	0	1	1
m/p-Xylene	110	110	110	0	12	17
o-Xylene + Styrene	784	784	782	3	67	92
Phenol	173	173	172	24	2	3
o-Cresol	3	3	3	0	0	0
Indene	813	813	808	0	1.2	2
m/p-Cresol	6	6	6	0	0	0
Naphthalene	2455	2455	2433	16	0.06	0.13
Quinoline	18	18	18	14	0	0
2-Methylnaphthalene	239	239	235	0	0	0
1-Methylnaphthalene	170	169	167	3	0	0
Diphenyl	88	45	82	0	0	0
Ethylnaphthalene	285	90	250	6	0	0
Acenaphthlalene	416	10	103	0	0	0
Fluorene	198	0.97	0.74	0	0	0
Phenanthrene	552	0.43	0.89	11	0	0
Anthracene	147	0.09	0.19	0	0	0
Fluoranthene	130	0.03	0.07	4	0	0
Pyrene	178	0.01	0.02	5	0	0
Benzo(a)anthracene	64	0	0	0	0	0
Chrysene	81	0	0	0	0	0
Benzo(b)fluoranthene	59	0	0	0	0	0
Benzo(e)pyrene	122	0	0	0	0	0
Total	7098	4923	5178	86	83.26	115.13

The OLGA process is suitable for combining the biomass gasification with a combined heat and power generation unit. However, this process should not be used alone for integrating the producer gas in a biofuel production unit such as methanation, for example. Otherwise, the remaining BTX fraction leads to a catalytic deactivation. In case where benzene and toluene are not accounted for in the calculations of the tar removal efficiency, a value of 98.8% is obtained. However, including benzene and toluene in the calculations leads to a total tar reduction efficiency value of 57.6%. The elementary tar removal efficiency of toluene and benzene is equal to 72.8% and 36.7%, respectively. Their removal efficiency remains low even if the operating conditions change. Therefore, the final composition of the producer gas is not suitable for chemical synthesis process. For a further BTX removal, a supplementary tar treatment unit is required.

1.5.2.3 Thermal treatment

Thermal treatment can be defined as the cracking of tars into lighter hydrocarbons by applying heat for a certain residence time in reactors and at high temperature [4]. Thermal treatment includes thermal cracking and plasma cracking. The suitable temperature range for this treatment varies from 900°C to 1300°C. Bridgwater [54] stated that it is hard to crack the tar derived from biomass by thermal treatment alone. Cracking tar effectively can happen through several ways: (1) increasing the residence time (2) direct contacting an independent heated surface; however, this will increase the energy demand and therefore decrease the overall efficiency (3) adding oxygen or air to promote partial oxidation, thus increasing the CO_2 levels and the operating cost while reducing the overall efficiency. Note that thermal cracking is not ideal for large-scale applications due to its high cost. Brandt and Henriksen [55] showed that a temperature of 1250°C is needed to reach acceptable tar levels with a reasonable residence time. However, the high temperature required for the thermal decomposition has many disadvantages. In fact, to maintain the reactor at the desired temperature, high energy and therefore high cost are required. In addition, thermal decomposition leads to soot agglomeration and the formation of heavier products. Therefore, tar removal by conventional thermal decomposition is not an ideal solution [56].

Phuphuakrat et al. [49] suggest a two-stage process for tar treatment. The process involves a decomposition step followed by a fixed adsorption bed. The decomposition takes place in a reformer placed after the gasifier. A comparison between three decomposition methods was done; thermal cracking, steam reforming and air reforming. Both steam and air should be heated to the reformer temperature (800°C), prior to injection. External electrical heating is required to maintain the temperature of the reformer. Steam and air reformers showed higher tar reduction efficiency than thermal cracking. Thermal cracking, steam reforming (S/B=3) and air reforming (ER=0.4) respectively reduce the tar content from 130 $g.kg^{-1}$ of feedstock, to 29, 16 and 11 $g.kg^{-1}$ of feedstock. During the decomposition, heavy tars (mainly class 5) are cracked into lighter tars and gases, leading to a higher concentration of light tars (classes 2 and 3) and a higher producer gas yield. The use of steam in the reformer increases the yield of H_2, CO, and CH_4, while air reformer enhances the yield of CO_2.

Fassinou et al. [57] analyzed the impact of the biomass flow rate, residence time and temperature on the tar cracking in Pinus pinaster pyrolysis. Increasing the residence time and the temperature promotes tar cracking and simultaneously improves the char quality and the gas production.

Lately, plasma cracking is gaining interest for tar abatement by means of highly excited ions, atoms, molecules, electrons etc. Plasma reforming can be performed through different discharges modes including gliding arc, corona and microwave discharges [4]. Although plasma reforming has high tar removal efficiency, it presents some disadvantages such as its short lifetime, its high cost and its high energetic demand [58].

Nunnally et al. [56] studied the reforming of naphthalene and toluene present in the syngas, by gliding arc plasma reformer. Results showed that the conversion of naphthalene and toluene is over 90% for an initial concentration of 30 $g.m^{-3}$. The conversion of naphthalene and toluene drops to 70% for a higher initial concentration of 75 $g.m^{-3}$.
The comparative study conducted by Tao et al. [59] assessed the performance of thermal decomposition (DD), catalytic steam reforming (CR), plasma-assisted decomposition (PD) and plasma enhanced catalytic steam reforming (PCR) of biomass tar. Toluene was selected as the tar representative compound. The best performance was achieved by the PCR. The introduction of plasma to the catalytic steam reforming method promoted toluene decomposition. Simultaneously, the reforming catalyst (Ni/SiO_2) drove the reactions towards the formation of H_2 and CO. Therefore, the PCR method results

in the highest toluene decomposition and in the highest formation rates of H_2 and CO. Moreover, results showed that the lowest toluene conversion was obtained through DD (5.4%). Toluene conversion through CR and PD is equal to 32.8 and 34%, respectively. Finally, the highest toluene conversion is equal to 57% and it can be achieved through PCR.

1.5.3. Catalytic cracking

Catalytic cracking can be divided into two types. The first one is the case where the catalyst is placed inside the gasifier. This type is known as primary catalyst. It is classified as a primary tar treatment method. In the second type, known as secondary catalyst, the catalyst is placed in a separated reactor downstream the gasifier, to treat the producer gas. Different types of catalysts can be used for tar removal. According to Sutton et al. [60], the catalyst used should be: (1) inexpensive, (2) effective in tar removal, (3) easily regenerated, (4) strong enough, (5) resistant to deactivation in case of carbon sintering and fouling, (6) capable of reducing methane (if the desired product is syngas), and (7) provide an appropriate producer gas ratio. Catalysts can be classified in different categories [3]: (1) Ni-based, (2) Non Ni-based, (3) activated carbon, (4) alkali metal, (5) acid and (6) basic catalysts. Compared to thermal cracking, catalytic cracking requires lower temperatures thus lower energy consumption, at the expense of an additional catalyst cost.

Nickel-based catalysts operate simultaneously on the removal of tar and ammonia in biomass or coal gasification. They are the most widely used catalyst with a tar removal efficiency higher than 90% around 900°C. Nickel-based catalysts promote water gas shift reaction, thus simultaneously reduce tar concentration and increase H_2/CO ratio. However, the deactivation of the catalyst by coke deposition, metal chlorides, sulfides and alkali oxides is a main disadvantage of those catalysts.

A higher tar removal efficiency can be achieved with the transition metal (non-nickel based) catalysts, such as Pd, Pt, Rh and Ru, for example. Those catalysts are also more resistant to sulphides. However, transition metal catalysts are more expensive than nickel-based catalysts. Note that, the performance of the mentioned transition metal catalysts is as follows: $Rh > Pt > Pd > Ni = Ru$ [61].

As for the activated carbon (AC) catalysts and char (derived from coal or biomass), tar reduction depends on the surface area and pore size [62]. AC and char catalysts are relatively inexpensive. However, their activity is rapidly reduced due to pores blockage by the coke deposition.

Alkali metal catalysts are well-known for being effective in tar reforming and for improving the quality of the producer gas. Alkali metal catalysts are directly added to the biomass by wet impregnation or by dry mixing. This makes the recovery of the catalyst difficult, and thus promotes the cost and reduces the ability of recovering the catalyst [60].

Acid catalysts include zeolites and silica-alumina. Zeolites catalysts are renowned for their high surface acidity, surface area and pore structure [63]. Zeolites are relatively inexpensive, easily regenerated and have a high resistance to sulfur and nitrogen components. Nevertheless, they are rapidly deactivated due to coke formation.

Finally, basic catalysts such as olivine and dolomite, are abundant and cheap. They have a considerable tar reduction activity. The use of dolomite as a catalyst increases the content of the permanent gases (H_2 and CO_2) in the gas phase [64]. Natural catalysts (dolomite and olivine) are used after calcination in order to improve their activity [65]. The calcination process requires a great amount of energy to heat up the catalyst to 850°C for 12 to 24 hours. However, they become very fragile after being calcined. Moreover, they are deactivated due to carbon deposition [3,4].

In summary, dolomite and nickel-based catalysts are the most widely used ones. Lately, char is gaining a lot of attention as a catalyst or catalytic support that can be used for reduction of tar. Char's main advantage is its low cost, since it is formed within the process itself through gasification. Several studies on catalytic cracking activity, efficiency, and deactivation are presented in the sequel.

Pallozzi et al. [66] studies the conversion of tar produced via a fluidized bed gasifier containing olivine as a bed material, and operating at 800°C. Tar removal happens by passing the gas through a calcined dolomite bed for conditioning, followed by a vegetable oil scrubber for cleaning. The oil scrubber operates at 50°C and it is heated via a water bath. It was observed that 80% of tars are reduced through the catalytic bed operating at 800°C, for a residence time of 0.2 s. Producer gas continues its way to the scrubber with a residence time between 1 s and 10 s. In the first hour of operation, the reduction of tar in the scrubber was almost 100% for all classes, expect the benzene for which the reduction was 90%. After 90 minutes of operation, the reduction percentage highly decreases due to oil saturation. Note that only 20% of light tars are being removed. This is also verified by the increase of the tar dew point from 0.9°C to 77.3°C, after 90 minutes of operation. The variation of the removal efficiency by class is caused by the difference in the condensation temperature of each class, as shown in Figure 1-17. Thus, the lightest components will remain in the gas phase when the oil is saturated, while the heavier fraction will condense at 50°C. In the dolomite bed, tar was reduced from 6.01 g.Nm^{-3} to 2.46 g.Nm^{-3}, for components heavier than benzene.

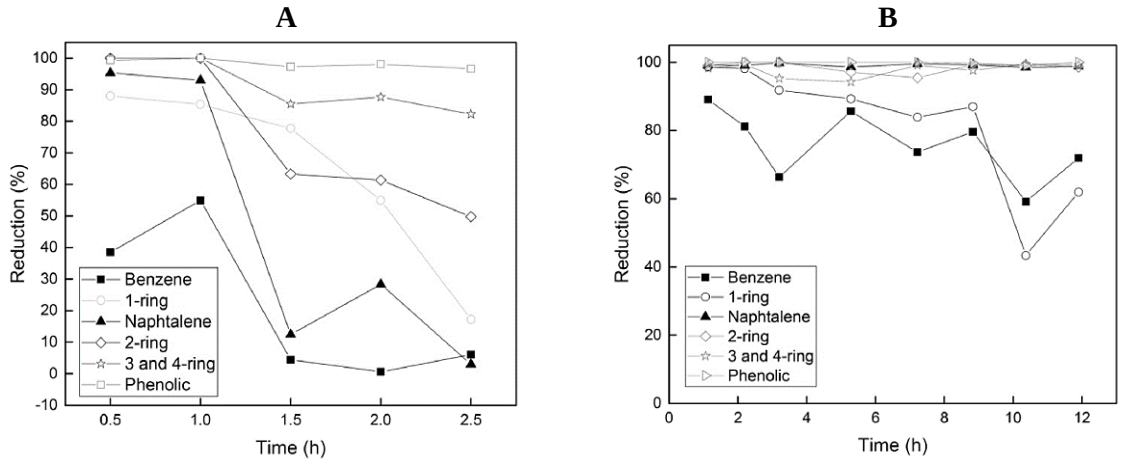

Figure 1-17 : Tar conversion by class in A) oil scrubber B) dolomite bed catalyst [66].

Dou et al. [67] tested the efficiency of different catalysts on tar removal, where 1-methylnaphthalene (1-MN) was considered as a tar representative compound. The initial tar content is equal to 3000 mg.Nm^{-3}. Five different catalysts were tested for 10 hours at 550°C and for a space velocity of 3000 h^{-1}. The studied catalysts are Y-zeolite, NiMo catalyst, silica, alumina and lime. 1-MN conversion efficiency expressed by $(C_{in} - C_{out})/C_{in} \times 100$, highly decreases with time for lime, alumina and silica. In fact, it was reduced from 90-95% to below 80%, after 9 hours of operation. As for the Y-zeolite and NiMo, the conversion efficiency of 1-MN was stable with the time. Regarding temperature effect, conversion efficiency increases with temperature and becomes higher than 90% at 500°C. Another test was conducted for Y-zeolite and NiMo in order to check their resistance to deactivation. At the beginning, tar concentration was equal to 1000 mg.Nm^{-3}. A conversion higher than 95% (50 mg.Nm^{-3} remaining after catalytic cracking) was maintained after 168 hours of operation at 550°C. Even though a high conversion efficiency was maintained for a longer period of time, the tar content reduction was not sufficient for methanation because it is still higher than the acceptable limit for methanation.

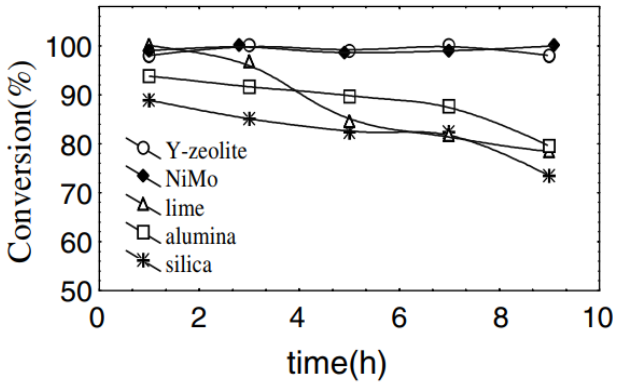

Figure 1-18: 1-MN conversion percentage for different catalyst after 10 hours of operation [67].

D'Orazio et al. [68] studied three types of ceramic filter candles that are implemented in the freeboard of the gasifier, to check and compare their effect on tar reduction. The first one is a non-catalytic candle of Al_2O_3, the second one is a catalytic candle of catalytically activated Al_2O_3 with a catalytic layer of MgO – NiO, and the third one is a catalytic foam candle of catalytically activated Al_2O_3 with MgO – NiO, applied on the filter support and on the integrated catalytic ceramic foam. The catalyst with foam was capable of reducing the tar content to 0.14 $g.Nm^{-3}$, while a concentration of 1 and 8 $g.Nm^{-3}$ was reached for the catalytic and non-catalytic candles, respectively. However, the pressure drop through the candles was linearly increasing: 0.14 cm_{H_2O}/min for the non-catalytic candle, and 0.06 cm_{H_2O}/min for the second two candles. This pressure drop reflects the accumulation of tars and other impurities in the filter, leading to its blockage after a certain operation time.

A study done by El-Rub et al. [69] experimentally compares tar removal efficiency for different catalysts. The comparison was done between commercial nickel catalyst, biomass ash, used fluid catalytic cracking catalyst, calcined dolomite, olivine and biomass char. Phenol and naphthalene are considered as tar representative compounds. Phenol illustrates the behavior of heterocyclic tars, while naphthalene illustrates that of the light PAH and forms one of the major components in tar. In this study, they only considered H_2O and CO_2 in the gas feed, because they are the responsible components for tar reforming. Nitrogen was also introduced as an inert. External heating by electrical furnace is required to maintain the desired catalytic bed temperatures of 700°C and 900°C for phenol and naphthalene conversion, respectively. Catalytic phenol conversion was studied at lower temperature, since at 900°C, most of the phenol will be converted through thermal cracking. Nickel followed by dolomite catalysts have the highest phenol conversion and result in a phenol content of 1 $g.Nm^{-3}$, as seen in Figure 1-19. Different catalytic behaviors were observed during the experiments. Nickel and dolomite catalysts increased notably the hydrogen content in the gas. This indicates that reforming reactions are favored. As for the rest, cracking mechanism was responsible for tar reduction.

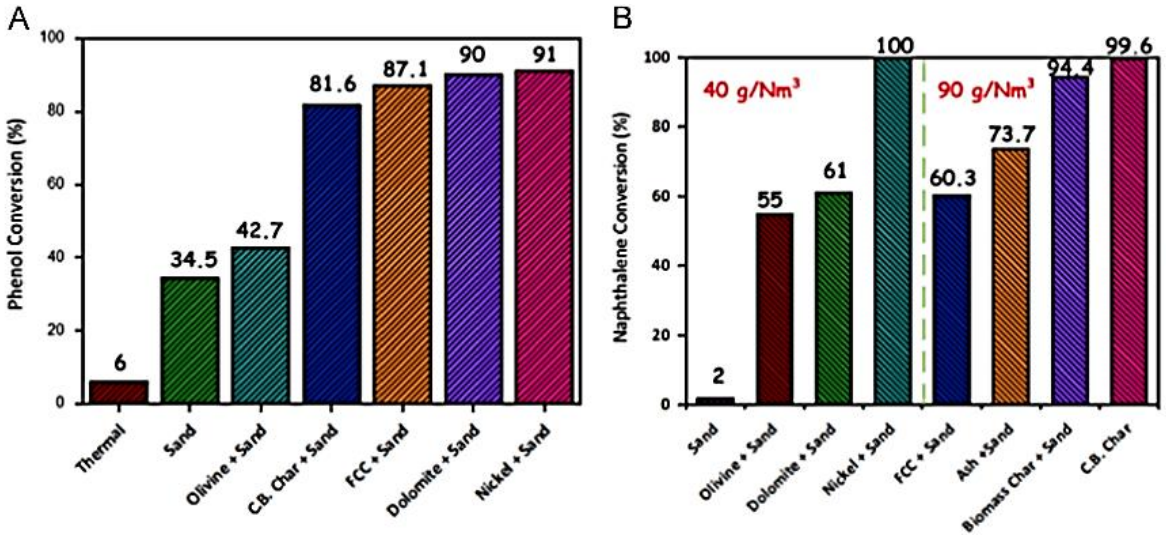

Figure 1-19 : Effect of the catalytic cracking, for a residence time of 0.3 second on A) phenol at 700°C with an initial concentration of 8-12 g.Nm^{-3} B) naphthalene at 900°C with an initial concentration of 40 g.Nm^{-3} and 90 g.Nm^{-3} [69].

It is important to mention that all the catalysts have a limited lifetime due to their deactivation. It was noticed that part of the biomass char is consumed during the catalytic cracking. However, the make-up char can be imported back from the gasifier, where it is continuously formed. Regarding naphthalene conversion, the catalysts performance was studied under a higher initial concentration and a higher temperature. As for the phenol, nickel catalyst gives the best performance with a naphthalene conversion of almost 100%. The high cost of the nickel catalyst and its deactivation, by the presence of H_2S in the producer gas, are the main drawbacks of using this catalyst. Biomass char catalyst also results in a good naphthalene conversion, where the content of naphthalene is reduced from 90 g.Nm^{-3} to 0.36 g.Nm^{-3}, at 900°C.

It can be seen that in many of the described catalytic cracking processes only one representative tar component is considered in the study. For instance, naphthalene is the most considered tar representative component. Table 1-11 summarized the performance of some catalytic cracking studies performed over nickel and transition metal based catalysts that consider naphthalene as a tar representative component [70–73]. Moreover, Myrén et al. [74] analyzed the performance of dolomite and silica catalyst while considering naphthalene as tar representative component. Similarly, Devi et al. [75] analyzed the impact of the calcination time of olivine on the tar removal by considering naphthalene as a representative component. It is deduced that increasing the calcination time from 1h to 10h increases the naphthalene removal efficiency from 30% to 80%. Other researches, such as Simell et al. [76] and Lu et al. [77], considered toluene as a tar representative component. Activated carbon was used by Lu et al. [77] as a support for the following precursors: copper sulfate, copper acetate and copper nitrate. The highest toluene decomposition is reached by the use of copper nitrate (99%), followed by copper acetate (97%) and copper sulfate (80%). Finally, the studies conducted by Dou et al. [67] and El-Rub et al. [69], that were previously described, respectively analyze the catalytic activity based on 1-methylnaphthalene, and on phenol and naphthalene. Therefore, each study considers a different catalyst type, different operating conditions and different tar representative components. Consequently, no clear relation between the catalyst type, the required temperature and the tar removal efficiency can be deduced. This render the catalytic cracking a complicated method for tar removal.

Table 1-11: Performance of nickel and non-nickel metal catalysts.

Catalyst			Tar representative and Operating conditions	Comments	Ref.
Active	Promoter	Support			
Co		MgO	Naphthalene S/C=0.6	Conversion of Co and Ni is equal to 23% and 12%, respectively. Note that tar concentration is 100 times higher than that obtained from gasification.	[70]
Ni		MgO			
Fe	CuO	Al	Naphthalene T=850°C	Fe-Al showed a higher conversion rate ranging between 60% and 90% while that of Fe-Zr ranges from 30% to 80%.	[71]
Fe	CuO	Zr			
Ni		Zeolites SiO_2/Al_2O_3	Naphthalene T=750°C	A conversion of 99.5% in achieved. The catalytic activity is improved by the impregnation of Ni on zeolites. The catalytic activity is affected by coke deposition.	[72]
Pt, Ru, Pd	Mo	γ-Al_2O_3	Naphthalene T=310°C, P=5 MPa	H_2S does not poison the catalyst, it produces an inhibiting effect. The conversion varied between 2% and 23%. It increases in the following order: $PdMo < RuMo < PtMo(2) < PtMo(15) < CoMo$	[73]

Even though catalytic cracking seems to be an effective method for tar removal, its deactivation by coke formation still imposes several restrictions to its high cost. A study that focuses on the catalysts deactivation [78] compared different catalytic beds of biomass char generated from the pyrolysis of food waste, used wood pellets, and coagulation flocculation sludge at 700°C. Ethylbenzene and benzene were considered as tar representative compounds. The conversion of each component was separately studied over different char catalytic beds. Catalytic cracking of ethylbenzene was operated at relatively low temperatures; 400°C (Fischer-Tropsch temperature) and 650°C (producer gas temperature), to avoid the use of external heating. At the beginning, the concentration of ethylbenzene was 40 $g.Nm^{-3}$. Operating at low temperature (400°C) leads to a low catalytic conversion, ranging from 10.9% to 21.6%. In addition, catalysts were totally deactivated within the first 80 minutes of operation. The reason of this deactivation is the coke deposition on the surface of the catalyst, prohibiting tars from reaching active sites. Increasing the catalytic cracking temperature to 650°C increases the average ethylbenzene conversion up to 78% (8.8 $g.Nm^{-3}$ after cracking), after 170 minutes of operation. As for benzene conversion, the cracking takes place at 850°C and 950°C, since it is more stable than ethylbenzene. Benzene was fed at a concentration of 35 $g.Nm^{-3}$. The catalytic activity was low at 850°C for all the char types, with a maximal conversion of 48.4%. Moreover, catalysts were deactivated after 60 minutes of operation. By increasing the operating temperature to 950°C, benzene conversion will increase to 82.4% (6.16 $g.Nm^{-3}$ after cracking) for a certain char type. Char deactivation takes place after 220 minutes for a certain type of char and after 500 minutes for another type.

Another experimental studies [77] show that catalyst deactivation is not only associated with the amount of coke, but also with the nature of coke. The latter can be divided into amorphous and filamentous coke. Formation of one type of coke rather than the other one is mainly affected by the temperature of the catalytic cracking, the concentration of Ni in the catalyst, and steam injection. Toluene was used to represent tar components, with an initial concentration of 15 $g.Nm^{-3}$. Toluene conversion was studied

over a Ni/Al_2O_3 catalyst. Filamentous coke formation was favored for temperatures lower than 700°C, and for a high Ni concentration. Steam injection reduces, not only filamentous coke formation but also the overall coke deposition on the catalyst. Figure 1-20 shows the mechanism of catalytic deactivation. Type I corresponds to amorphous coke where the deactivation takes place into two stages. In stage 1, the catalyst activity dramatically decreases until becoming totally deactivated in stage 2. Filamentous coke is represented by type II, for which an increase in the catalyst activity is encountered in stage 1. Stages 2 and 3 have then the same behavior as stages 1 and 2 for type I. The catalysts deactivation was assessed by the variation of the produced amount of hydrogen function of time, temperature (700°C to 900°C), Ni concentration (Ni-5 to Ni-20), and steam concentration (0 to 2%). Since H_2 is a major catalytic cracking product, it is used as a deactivation indicator as shown in eq. (1-15) in absence of steam, and in eq. (1-16) in presence of steam.

$$C_7H_8 \xrightarrow{catalyst} C + H_2 \tag{1-15}$$

$$C_7H_8 + (7+m)H_2O \xrightarrow{catalyst} (7-m)CO + mCO_2 + (11+m)H_2 \tag{1-16}$$

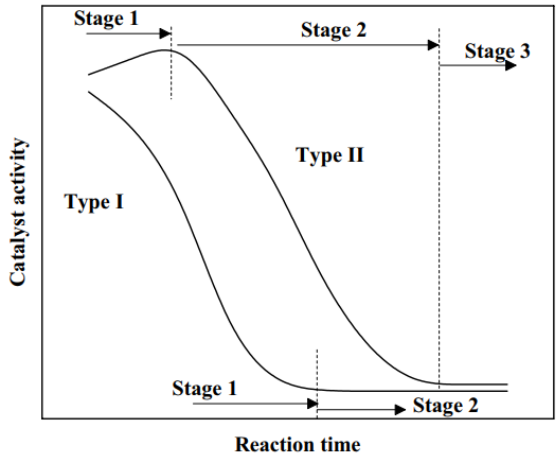

Figure 1-20 : Stages of catalyst deactivation function of the reaction time [77].

For all the cases, the catalysts deactivation was achieved after 20 minutes of operation. It was shown that the produced amount of H_2 highly decreases during the first 20 minutes (stage 1), until reaching a constant value, indicating the deactivation of the catalyst (stage 2). The total amount of coke deposed on the catalyst increases with temperature and with the Ni concentration, while coke deposition was reduced by steam injection. A coke deposition of 0.96 $g/g_{catalyst}$ is reached for a temperature of 900°C, without steam injection over a Ni-10 catalyst. Decreasing the temperature to 700°C while injecting steam (to a concentration of 2%) over a Ni-5 catalyst, decreases the coke deposition to 0.18 $g/g_{catalyst}$.

1.6. Methanation requirements

Based on the literature review, tar removal methods for CHP are well developed. However, an additional work is needed in order to develop tar removal methods that are suitable for methanation and catalytic processes. The main objective of this thesis is the reduction of the tar content to an acceptable level for methanation.

According to GRTgaz [79], many specifications should be met in order to inject the produced (bio)-methane in the grid. Those requirements are summarized in Table 1-12.

Table 1-12: Specifications for the injection of the Synthetic Natural Gas (SNG) in the grid in France [79].

Characteristic	Specification
Higher calorific value (combustion at 0°C and 1.01325 bar)	Gas type H[1]: 10.7 to 12.8 kWh.m^{-3}(n) Gas type B[1]: 9.5 to 10.5 kWh.m^{-3} (n)
Wobbe index (combustion at 0°C and 1.01325 bar)	Gas type H[1]: 13.64 to 15.7 kWh.m^{-3} (n) Gas type B[1]: 12.01 to 13.06 kWh.m^{-3} (n)
Specific gravity	Between 0.555 and 0.7
Water dew point	Lower than -5°C at the maximal pressure of the network downstream the connection
Sulfur content of H_2S (+ COS)	< 5 mgS.m^{-3}(n)
CO_2 content	< 2.5%
Total sulfur content	< 30 mgS.m^{-3}(n)
Mercaptan sulfur content	< 6 mgS.m^{-3}(n)
Hydrocarbons dew point	Lower then -2°C from 1 to 70 bar
Hg content	< 1 µg.m^{-3}(n)
Cl content	< 1 mg.m^{-3}(n)
F content	< 10 mg.m^{-3}(n)
H_2 content	< 6%
CO content	< 2%
NH_3 content	< 3 mg.m^{-3}(n)
Dust content	< 5 mg.m^{-3}(n)

1: Gas type H and B indicate a high and low calorific value gases, respectively.

The dew point of hydrocarbons found in Table 1-12 does not reflect the requirement on tar content for the methanation process. It only indicates the quality of the methane that is required to be injected in the grid. The methanation process imposes stricter restrictions on the tar content. Otherwise, the Water Gas Shift (WGS) reactor catalyst and the methanation catalyst will be deactivated by tar and coke deposition. As seen in eq. (1-17), Fischer-Tropsch (FT) synthesis reaction results in methane formation for n=1. Therefore, the tar content limit for methanation is equal to the limit set for the FT synthesis, which is 1 mg.Nm^{-3}. Although the formation of long chain hydrocarbons is more desired than methane production during FT synthesis, methanation reaction is favored for certain conditions such as catalyst type or temperature.

$$(2n+1)\,H_2 + n\,CO \leftrightarrow C_nH_{2n+2} + n\,H_2O \tag{1-17}$$

H_2/CO and H_2/CO_2 ratios are also important factors to consider for methanation. Stoichiometric requirements of methanation reactions are equal to 3 and 4 for H_2/CO and H_2/CO_2, respectively, as seen in eqs. (1-18) and (1-19). Those ratios are affected by the gasification agent.

$$CO + 3H_2 \leftrightarrow CH_4 + H_2O \qquad \Delta H_r = -206\ kJ.mol^{-1} \tag{1-18}$$

$$CO_2 + 4H_2 \leftrightarrow CH_4 + 2H_2O \qquad \Delta H_r = -166\ kJ.mol^{-1} \tag{1-19}$$

The H_2/CO and H_2/CO_2 ratios for the different used gasification agent has been completed based on the producer gas composition obtained after the gasifier. Accordingly, the impact of the gasification agent on H_2/CO and H_2/CO_2 ratios is illustrated in Figure 1-21. Steam yields the highest ratios where H_2/CO varies from 1 to 2 and H_2/CO_2 varies from 1 to 3, according to the conditions of the gasification. Thus, steam is the most appropriate gasification agent for methanation purposes.

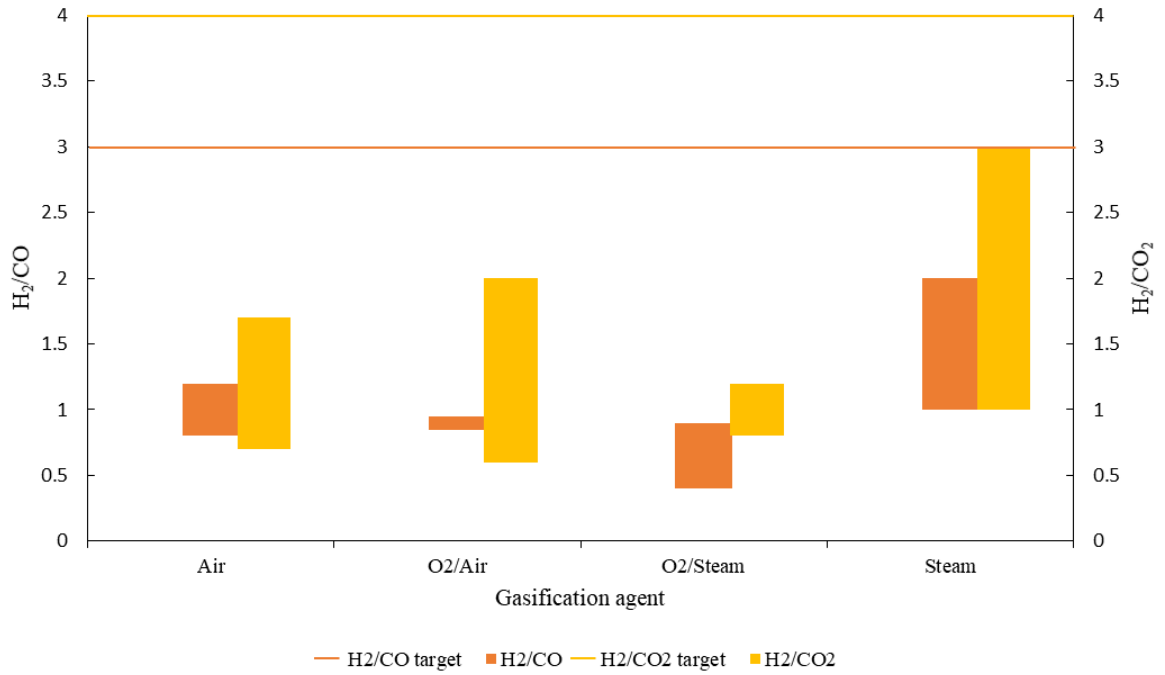

Figure 1-21: Impact of the gasification agent on H_2/CO and H_2/CO_2 ratios.

Several processes for the production of methane from hydrogen and carbon oxides exist. For instance, TREMP, a multi-stages process developed by Haldor Topsøe [80], is one of the most common methanation processes. It is used to convert the gas produced from both biomass and coal gasification to biomethane [81]. Reaching a high methane yield, with low CO and CO_2 content, requires the appropriate composition ratios in the producer gas that is fed to the methanation technology [80]. Even though CO methanation is the predominant methanation reaction, CO_2 content contributes in the overall methanation.

1.7. Biomethane production plants based on biomass gasification

Several projects for the conversion of biomass into biomethane are being developed. Currently, most of the projects are at pilot scale, such as GAYA project, developed by Engie [82]. Only few information related to this project has been published since it is still in progress. In GAYA project, the tar treatment stage consists of gas scrubbers using biodiesel, followed by adsorption over activated carbon beds. BioSNG is another pilot plant that was develop by ECN [83]. Finally, researchers at the Chalmers University of Technology in Sweden [28] were able to build the first of its kind industrial scale biomethane production plant, based on wood gasification. The gasifier handles 150 dry tonnes of biomass per day. It is capable of producing 20 MW of biomethane. This process is known as Gothenburg Biomass Gasification (GoBiGas). The full process for biomethane production is illustrated in Figure 1-22. Methane produced from this process was injected into the natural gas grid in December 2014 in Sweden.

As seen in Figure 1-22, different cleaning equipment are required prior to the methanation step. Note that in this sequel, only the tar treatment section is detailed. Blocks (1) and (2), combined together, represent the dual fluidized bed gasifier. Raw gas leaving the gasifier at a temperature of 815°C was cooled (5), before entering the scrubber, to a temperature of 160°C. Raw gas passes through a filter where dust and condensable particulates were separated (6). In the scrubber (7), RME is used as the scrubbing medium to remove the PAHs. The tar scrubber operates at a temperature of 35°C. The initial tar content prior to the scrubber is 20.5 $g.Nm^{-3}$ (out of which 12.7 $g.Nm^{-3}$ are BTX). The tar content at

the exit of the scrubber is reduced from 7.8 g.Nm^{-3} to 0.7 g.Nm^{-3} if BTX are excluded, and from 20.5 g.Nm^{-3} to 13.3 g.Nm^{-3} if BTX are included in the calculations. This indicates that the scrubber does not significant change the BTX content. The scrubber eliminates all the heavy tars (class 5), 91% of the heavy fraction of class 4, 72% of naphthalene, and 29% of indene. After the scrubber, the gas still contains an important amount of naphthalene and BTX.

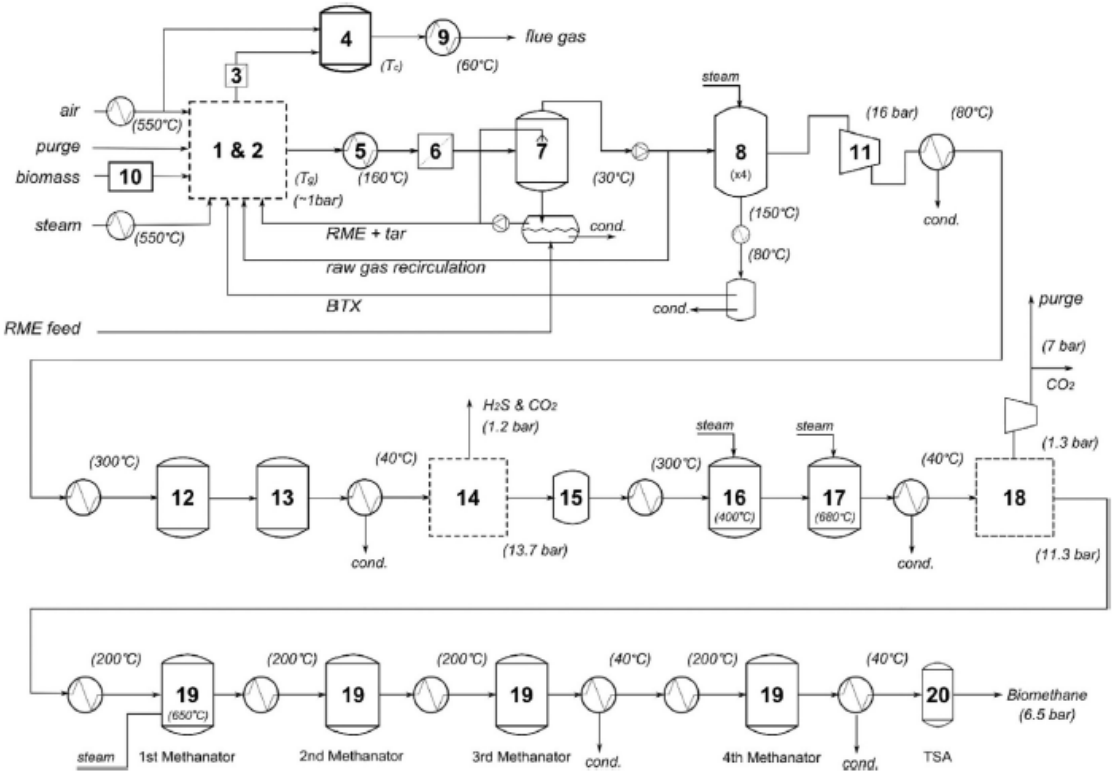

Figure 1-22: Process flow diagram of the full GoBiGas plant. Labels: 1&2) gasification and combustion, 3) cyclone, 4) post-combustion, 5) cooler, 6) filter, 7) scrubber, 8) AC beds, 9) flue gas recovery heat exchanger, 10) biomass feed, 11) compressor, 12) olefins hydrogenation, 13) carbonyl sulfide hydrolyzer, 14) hydrogen sulphides removal, 15) guard bed, 16) water gas shift 17) pre-methanation, 18) carbon dioxide removal, 19) methanation and 20) drying [84].

Note that the methanation section takes place at high pressure. A series of compressors were used to increase the pressure of the producer gas from atmospheric pressure to 16 bars. A producer gas with an extremely high quality should be reached before the compression. Thus, remaining tar components and BTX should be removed with the others impurities present in small quantity, such as H_2S, HCl and ammonia prior to the compressor. The required further cleaning is done through four active carbon (AC) beds, called bridging processes (8). The first bed is considered as a pre-adsorber bed that removes large aromatic compounds (mainly the rest of classes 2 and 4) and impurities. Then, the three adsorber beds operate in series. They are used for the adsorption of BTX compounds (class 3). Each one of the three beds can operate as a regenerator or an adsorber. Steam is used for the regeneration of the beds by progressively increasing their temperature. The gases released from the AC beds were recycled to the combustion chamber. Some restrictions in the process limit the regeneration temperature of the activated carbon beds to 160°C. At this temperature, the beds were not fully regenerated and they will then lose their activity after a certain period of time. To avoid any reduction in the beds activity, the pre-adsorber bed is replaced every 2.5 months. The efficiency of the RME scrubber has a main impact on the beds lifetime. Reducing tar content (especially heavy tars) prior to AC beds, increases their lifetime. At the end of the process, the PAH and BTX content were lower than 0.1 µg.m^{-3} and 100 µg.m^{-3}, respectively. According to an economic assessment for the 20 MW GoBiGas process presented by Thunman et al. [85], the cost of the consumed RME scrubbing liquid and of the activated carbon is equal to 3.01

€.MWh^{-1} and 0.81 €.MWh^{-1}, respectively. It is important to mention that future studies should focus on replacing the RME by a less expensive scrubbing agent since it contributes in 5% to 10% of the operating costs.

Another project, done by ECN in co-operation with HVC Group [86], studied the biomethane production from wood gasification. For this purpose, a pilot plant (BioSNG) was built in the Netherlands. The flowsheet of the adapted process is shown in Figure 1-23. An indirect gasifier (Milena) was adapted for the biomethane production process.
Since the methanation catalyst is easily deactivated by carbon deposition and poisoned by sulfur, a prior extensive cleaning is required. After the gasifier, the producer gas is cooled and it passes then through a cyclone for particles removal. The producer gas continues its way to OLGA unit where heavy tars were totally removed. However, a small content of light tars remains in the gas (around 200 mg.Nm^{-3} excluding BTX). The Hydro-DeSulfurization (HDS) unit converts organic sulfur compounds into H_2S over a ZnO catalyst. The producer gas should be heated, prior to the HDS unit which operates at 300°C. After the removal of impurities in the HDS and adsorbents blocks, BTX compounds requires additional reduction. For this purpose, a catalytic reformer, operating between 550°C and 600°C, is placed prior to the methanation reactor. Thus, another heater was required to reach the temperature of the reformer. In this step, BTX are cracked and part of them is converted into methane. Steam is injected in the reformer to reduce the deposition of coke on the catalyst. An amine scrubber is placed after the reformer in order to absorb the excess CO_2, where 85% of the CO_2 is separated from the gas stream. Amines are regenerated at 130°C and recycled back to the scrubber. The cleaned gas is then compressed and sent to the methanation reactors. Note that a plan for building a demonstration unit of this process, has been discussed.

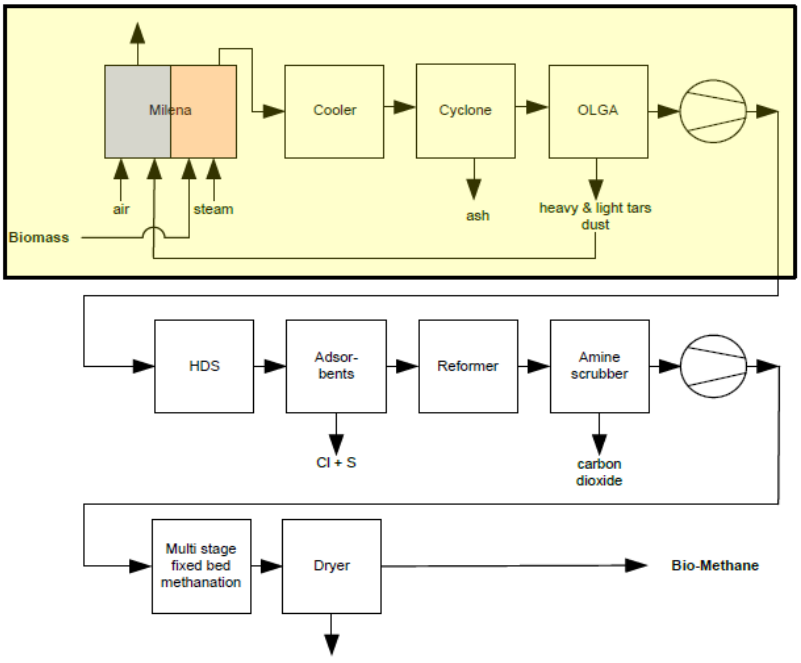

Figure 1-23: Block flow diagram of the biomethane production process from wood gasification using Milena and OLGA [86].

1.8. Conclusion

To sum up, optimizing the gasification process and selecting the optimal operating conditions, including the gasification agent, the temperature, the pressure and the residence time, enhances the producer gas

quality. Moreover, the tar content of the producer gas is not clearly related through a trend to the gasifier type or the gasification operating conditions. For instance, updraft gasifiers yield the highest tar content while the lowest tar content is achieved in downdraft gasifiers. Therefore, additional treatment is required to remove the remaining tar content after the gasifier.

The tar removal by the physical and mechanical processes, including dry and wet methods, efficiently reduce the content of tar classes 2, 4 and 5. This results in a producer gas suitable for combined heat and power production. However, these methods produce a waste stream and potentially decrease the energy conversion efficiency. Tar reduction via thermal cracking could reduce the tar content without generation a waste stream. However, additional energy supply is needed in order to maintain the reactor at high temperature (around 1250°C). Catalytic cracking seems to be a promising method for tar reduction. This method eliminates around 99% of tars (able to reduce the tar content to 0.16 $g.Nm^{-3}$). However, the high tar removal rate is very limited due to the rapid deactivation of the catalyst within few hours of operation due to coke deposition.

Based on the literature review, tar removal methods for CHP are well developed. However, an additional work is needed in order to develop tar removal methods that are suitable for methanation and catalytic processes. Therefore, developing a new method for tar removal that combines several tar treatment steps, which is economically viable and efficient, is necessary.

Very few researchers were able to reduce the tar content to a level suitable for methanation (1 $mg.Nm^{-3}$). Reaching a low tar content is usually achieved by combining two cleaning methods. The first cleaning method targets the removal of the heavy tar fraction, while lighter tars are removed by the second method. For instance, in GoBiGas project, the PAH and BTX contents were respectively lower than 0.1 $\mu g.m^{-3}$ and 100 $\mu g.m^{-3}$, by combining a scrubbing column with 4 activated carbon beds in series. High operating costs are imposed by the treatment section; one of the AC beds should be replaced each 2.5 months and the RME is wasted during scrubbing. Other examples of these techniques include OLGA, oil or water scrubber followed by adsorption bed, thermal cracking followed by a scrubber, and absorption followed by catalytic cracking.

Reaching the acceptable tar limit for bio-methane and bio-fuels production processes has several disadvantages including the high operational cost of the scrubbing liquid, the cost of the activated carbon beds that needs replacement and finally, the deactivation of the catalyst due to coke deposition. Moreover, the main limitations for reaching an extreme clean gas can be summarized by the limited temperature difference, the saturation of the scrubbing medium, the saturation of the adsorbent bed, or the deactivation of the catalyst by coke deposition. Based on the literature review, reducing the tar content of class 3 requires very low temperatures. Consequently, reducing the temperature of the producer gas could be an effective solution for reducing the total tar content to 1 $mg.Nm^{-3}$. For this purpose, psychrometric charts for the different tar representative components are developed in the next chapter in order to assess their dew point and the required energy for their removal. Different methods could be adapted in order to cool the producer gas. The low temperature tar removal process will be divided into two steps: a pre-treatment unit operating at ambient temperature, followed by a low temperature unit. An energy recovery system should be integrated within the tar treatment process in order to reduce the cost of the cold stream.

Chapitre 1 : Etat de l'art des méthodes de gazéification de la biomasse et de traitement de goudron.

1. Introduction

La biomasse est un terme générique utilisé pour désigner une matière organique composée de carbone, d'hydrogène, d'oxygène et d'une petite quantité d'azote et de soufre. Le bois, les résidus agricoles, les déchets alimentaires, industriels ou animaux présentent différentes formes de biomasse [9]. Récemment, la biomasse a été utilisée pour produire de la bioénergie à travers différents processus de conversion. La bioénergie englobe la production d'électricité, de chaleur et des carburants de transport. En 2019, 11% de l'énergie primaire dans le monde était fournie à travers des ressources renouvelables.

L'ADEME, en collaboration avec GRDF et GRTgaz, a réalisé une étude concernant la faisabilité d'une transition complète du réseau gazier vers les gaz renouvelables d'ici 2050, en France. Cette transition énergétique contribue à la réduction des émissions de dioxyde de carbone tout en favorisant la mise en œuvre des énergies renouvelables. Dans cette étude, la partie la plus importante du gaz renouvelable (40%) sera produite à travers la pyro-gazéification. Le reste sera issue de la méthanation par voie biologique (30%) et par le power-to-gas (30%).

La gazéification de la biomasse suivie par la méthanation par voie chimique du gaz produit en biométhane, est une voie prometteuse pour la production de gaz renouvelable. Cependant, la combinaison des deux procédés nécessite des unités d'épuration intensive du gaz produit après la gazéification, afin d'atteindre les exigences du procédé de méthanation chimique et d'assurer son fonctionnement. La réduction de la teneur en goudron contenu dans le gaz produit à un niveau acceptable est la contrainte principale de cette voie. Ce chapitre établit l'état de l'art des procédés de gazéification de la biomasse, des propriétés des goudrons, des multiples procédés de traitement des goudrons et des exigences de la méthanation par voie chimique.

2. Gazéification

2.1. Définition

La conversion thermochimique de la biomasse inclut la combustion, la gazéification, la pyrolyse et la liquéfaction. Parmi ces procédés, la gazéification produit un fuel gazeux qui peut être valorisé. Cette thèse porte sur le procédé de gazéification qui transforme la biomasse en un fuel gazeux, en présence d'un agent oxydant, suite à une série de réactions qui se déroulent à des températures élevées. Il s'agit d'une combustion incomplète qui, en déficit d'oxygène, décompose la biomasse en un mélange gazeux constitué essentiellement d'hydrogène (H_2), et du monoxyde de carbone (CO), aussi bien que de dioxyde de carbone (CO_2), méthane (CH_4), nitrogène (N_2) et de la vapeur d'eau (H_2O). Le mélange gazeux est chargé d'impuretés et de goudron qui doivent être éliminés. La composition du fuel gazeux dépend de la nature de l'agent oxydant utilisé, la composition de la biomasse, le type du réacteur de gazéification et les conditions opératoires. L'agent oxydant peut-être l'air en déficit, la vapeur d'eau, ou bien un mélange de vapeur d'eau et d'oxygène.

La gazéification se déroule selon quatre étapes principales : le séchage, la pyrolyse, l'oxydation et la réduction. En premier lieu, la biomasse subit un séchage afin de réduire sa teneur en humidité. La deuxième étape étant la pyrolyse, est une réaction endothermique qui transforme la biomasse en un mélange de charbon solide, de vapeurs condensables (appelées goudron) et de gaz permanents. Cette réaction se déroule dans un milieu inerte à des températures comprises entre 300°C et 600°C. La quantité

la plus importante de goudron est formée durant la pyrolyse. La chaleur nécessaire à la réaction est assurée soit par la réaction exothermique de l'oxydation partielle qui se produit dans le gazéifieur soit par une source externe. Les produits obtenus subissent alors une série de réactions de réduction, suite à l'introduction de l'agent de gazéification. L'enchainement de ces étapes dépend du type de réacteur de gazéification.

2.2. Différents types de réacteurs

Les différents types de réacteurs sont classés en deux catégories principales : les réacteurs à lit fixe et les réacteurs à lit fluidisé. On peut distinguer les réacteurs à contre-courant et les réacteurs à co-courant pour les réacteurs à lit fixe. D'autre part, les réacteurs à lit fluidisé incluent les réacteurs à lit fluidisé dense ou bouillonnants, les réacteurs à lit fluidisé circulant, les réacteurs à lit fluidisé circulant double et les réacteurs à flux entrainé.
Dans les réacteurs à contre-courant, l'agent oxydant est alimenté en bas de réacteur tandis que la biomasse est alimentée par son sommet. Cela résulte en une zone de basse température au sommet du gazéifieur. Le gaz produit sort du gazéifieur à une température d'environ 250°C avec une forte teneur en goudron (10-150 $g.Nm^{-3}$) [27]. Pour les réacteurs à co-courant, la biomasse et l'agent oxydant sont introduits par la partie supérieure du réacteur. Cela élimine la zone de basse température et réduit la teneur en goudron du gaz produit (0.01-6 $g.Nm^{-3}$) [23]. La température de sortie du gaz produit est d'environ 800°C.
Concernant les réacteurs à lit fluidisé dense et circulant, la biomasse est fluidisée à travers l'agent oxydant injecté au niveau de la partie inférieure du gazéifieur. Une vitesse de gaz entre 0,5 $m.s^{-1}$ et 1 $m.s^{-1}$ est nécessaire pour créer un milieu bouillonnant, tandis qu'une vitesse plus élevée (entre 3,5 $m.s^{-1}$ et 5,5 $m.s^{-1}$) est requise pour un réacteur à lit fluidisé circulant. Un combustible solide est placé dans le gazéifieur fluidisé afin d'améliorer le transfert de chaleur à son intérieur. Le combustible peut être un inerte tel que l'alumine, ou un catalyseur tel que la dolomite. La température de fonctionnement typique du gazéifieur fluidisé ainsi que la température de sortie du gaz varient entre 800°C et 900°C. La teneur en goudron du gaz produit en lit fluidisé varie entre 1 et 30 $g.Nm^{-3}$ [23].
Un nouveau type de gazéifieur, appelé gazéifieur indirect ou bien réacteur à double lit fluidisé circulant, est développé. Les étapes de combustion et de gazéification sont séparées dans deux chambres à lit fluidisé. La biomasse alimente le gazéifieur à lit fluidisé bouillonnant où elle est gazéifiée, en présence de vapeur d'eau (agent oxydant), en gaz produit et en charbon. Le charbon et le combustible solide sont transférés vers la section de combustion à lit fluidisé circulant. Le charbon est brûlé dans la section de combustion par injection d'air, tandis que le matériel du lit chauffé est recyclé vers la chambre de gazéification pour assurer la chaleur de la réaction de gazéification endothermique. Ce type de gazéification est le plus adapté aux applications de synthèse car il donne un gaz produit non dilué par les inertes (azote contenu dans l'air). Le gaz produit sort de la chambre de gazéification à une température proche de 850°C, avec une teneur moyenne en goudron de 30 $g.Nm^{-3}$ [28].
Finalement, les lits fluidisés entrainés nécessitent une vitesse de gaz supérieure à 6 $m.s^{-1}$ et la biomasse doit être sous forme pulvérulente. Ce type produit des faibles quantités de goudron. Toutefois, il ne permet pas une conversion totale de la biomasse. De plus, cette méthode est très couteuse et difficile à mettre en œuvre.

2.3. Composition du gaz produit

Tableau 1.1 présente la composition du gaz produit pour les différents agents oxydants et les différents types de gazéifieur précédemment discutés. Chaque gazéifieur a ses avantages et ses inconvénients en fonction de l'application du gaz produit. Au cas où la méthanation est l'application souhaitée après la gazéification, le gazéifieur à double lit fluidisé circulant (DBF) est le plus approprié.
Le problème principal lié à la gazéification est l'entraînement de goudron vers l'équipement en aval par le gaz produit chaud. Si le goudron n'est pas traité, il se condense suite à son contact avec des surfaces

froides. Cela forme des dépôts collants dans les équipements en aval, encrassant et obstruant les moteurs, les conduites de carburant et les filtres, et limitant les transferts de chaleur dans les échangeurs. De plus, le goudron conduit à une désactivation catalytique dans les applications de synthèse chimique. On peut également constater à partir du Tableau 1.1 que le gazéifieur à double lit fluidisé circulant est le type le plus approprié pour la méthanation, puisqu'il résulte en un gaz produit non diluée avec les inertes et contenant la fraction la plus importante de méthane.

Tableau 1.1: Composition typique du gaz produit pour plusieurs gazéifieurs et agents oxydants [30–35].

Agent Oxydant	Air			Vapeur d'eau (H_2O)		H_2O/O_2
Type du réacteur	Contre-courant	Co-courant	Lit fluidisé circulant	Double lit fluidisé circulant	Lit fluidisé circulant	Co-courant
H_2 ($vol\%_{hum}$)	10-14	17-20	4,5-11,1	18,6-27,8	12,4-27,8	15,9-19
CO ($vol\%_{hum}$)	15-20	18-21	13,5-18,4	16,7-17,5	5,5-15,9	21-23
CO_2 ($vol\%_{hum}$)	8-10	8-12	13,2-14,9	11,1-13,9	4,2-8,5	16,6-19,2
CH_4 ($vol\%_{hum}$)	2-3	1-3	3,5-4,5	6-7,1	2,3-5,9	1,4-2,5
C_2H_n ($vol\%_{hum}$)	n.d.	n.d.	1,2-1,6	1,6-2,7	0.7-1,1	0,16-0,49
N_2 ($vol\%_{hum}$)	45-52	45-50	41,8-50,1	0,05-3,7	0	0
H_2O ($vol\%_{hum}$)	2-6	0,5-2	8,8-16,2	30,3-42,8	52-60	31-61
Goudron ($g.Nm^{-3}$)	10-150	0,01-6	2-30	30-70	37,5-73	2-5,5

3. Propriétés de goudron

Le goudron groupe les hydrocarbures ayant une masse moléculaire supérieure à celle du benzène [37]. Il est difficile de prédire la composition du goudron produit lors de la gazéification car elle dépend de nombreux facteurs tels que le type de biomasse, l'agent oxydant, le type de réacteur, la température et la pression de fonctionnement. Ainsi, pour faciliter la compréhension de la composition du goudron, ce dernier peut être classé selon différentes caractéristiques. La classification la plus adaptée est présentée dans Tableau 1.2 où les composants de goudron sont répartis en cinq classes selon leur condensabilité et leur solubilité.

Tableau 1.2: Classification des composants du goudron en fonction de leur masse moléculaire [4,5,8].

Classe	Nom	Propriété	Composants
1	Non détectable par la chromatographie en phase gazeuse (GC)	Composants très lourds non détectable par GC.	Déterminé en soustrayant la fraction de goudron détectable par GC du goudron gravimétrique total
2	Hétérocyclique	Contenant des hétéroatomes, très soluble dans l'eau	Pyridine, phénol, crésols, quinoléine, etc.
3	Aromatique légère (1 cycle)	Hydrocarbures légers ayant un seul cycle	Toluène, éthylbènzene, benzène, xylènes, styrène, etc.
4	HAP légers (2–3 cycles)	2 et 3 cycles, condense à basses températures pour des faibles concentrations	Indène, naphtalène, méthylnaphtalène, biphényle, etc.
5	HAP lourds (4–7 cycle)	3 cycles et plus, condense à des hautes températures même pour des basses concentrations	Fluoranthene, pyrène, chrysène, périylène, coronène

La teneur en goudron admissible dans la phase gazeuse est définie par l'application souhaitée pour le gaz produit après la gazéification [3,4]. Par exemple, aucune restriction n'est fixée pour la teneur en goudron pour la combustion directe puisque le gaz produit reste chaud en le brûlant directement. Cela élimine le risque de condensation à des températures plus basses et la nécessité d'élimination de goudron. Pour des applications plus avancées, des limites de teneur en goudron sont fixées pour éviter la condensation et donc le colmatage. En particulier, pour les applications de cogénération, la teneur en goudron doit être inférieure à 100 $mg.Nm^{-3}$ et 5 $mg.Nm^{-3}$ pour les moteurs à combustion interne et les turbines à gaz, respectivement. Pour les applications de synthèse chimique, des limitations plus strictes sont fixées puisque le problème du goudron ne se limite pas à sa condensation, mais aussi à la désactivation catalytique impliquée dans la synthèse. Dans la synthèse du méthanol, la méthanation et la synthèse Fischer-Tropsch, la teneur en goudron doit être réduite à 1 $mg.Nm^{-3}$. Il est à noter que le benzène, le toluène et le xylène (BTX) sont pris en compte dans la teneur en goudron lorsqu'il s'agit d'une application de synthèse chimique, alors qu'ils sont ignorés pour la cogénération.

4. Traitement de goudron

Les méthodes existantes pour l'élimination du goudron peuvent être divisées en deux groupes : les méthodes primaires et secondaires [4]. D'une part, les méthodes primaires sont basées sur la réduction de la formation de goudron dans le gazéifieur en variant les conditions opératoires, telles que la température, la pression, l'agent oxydant, le rapport d'équivalence et le temps de séjour, ou en modifiant la conception du gazéifieur. Par exemple, l'augmentation de la température de gazéification réduit la teneur de goudron dans le gaz produit, tout en utilisant un lit d'olivine [87]. La pression affecte également la teneur en goudron et sa composition [42]. L'augmentation de la pression réduit la teneur en goudron et augmente la fraction des composants aromatiques. Cependant, même lorsque des méthodes primaires sont appliquées, le besoin de méthodes secondaires est inévitable pour une élimination complète de goudron en aval du gazéifieur [39].

D'autre part, les méthodes secondaires ciblent l'élimination de goudron après sa formation en aval du gazéifieur. Les méthodes secondaires peuvent être divisées en procédés physiques (filtres et cyclones) et chimiques (craquage catalytique et thermique). Les méthodes secondaires présentent certains inconvénients, comme le fait d'être coûteuses et de produire des effluents résiduaires. Les méthodes physiques/mécaniques ont un coût d'exploitation et de maintenance inférieur à celui des méthodes chimiques. En plus de goudron, les particules peuvent être éliminées du gaz produit par des méthodes physiques/mécaniques, qui sont eux-mêmes divisées en méthodes de nettoyage sèches et humides. Le principal inconvénient des systèmes de nettoyage humides est la génération d'eau ou de flux d'huile contaminés. Ainsi le problème de goudron est transféré de la phase gazeuse à la phase liquide [38].

Parmi les méthodes d'élimination du goudron, les colonnes d'absorption sont les unités les plus appropriées pour les applications à petite échelle [88]. Plusieurs études ont été menées sur les colonnes d'absorption. L'eau, le biodiesel, le diesel, l'huile des moteurs et l'huile végétale ont été évalués expérimentalement comme agents de lavage pour comparer leur efficacité [47]. Les résultats expérimentaux ont montré que l'eau a l'efficacité d'élimination la plus faible, tandis que le carburant biodiesel a l'efficacité la plus élevée. Les expériences menées par Lotfi et al. [88] pour les colonnes d'absorption de gaz, utilisant les huiles de cuisson usagées comme un agent de lavage, ont indiqué que l'élimination du goudron est affectée par le débit de la colonne d'absorption plus que sa température. Unyaphan et al. [89] ont montré que l'huile de canola, utilisée comme liquide de lavage, doit être régénérée par sédimentation centrifuge, toutes les deux heures de fonctionnement. L'huile de canola régénérée peut être réutilisée pour l'élimination du goudron tout en maintenant une efficacité d'élimination supérieure à 90 % après quatre cycles de régénération.

Pour le traitement thermique du goudron, des zones à haute température dans le réacteur sont nécessaires. Ce dernier est défini comme le craquage de goudron en hydrocarbures plus légers tout en chauffant pendant un certain temps de séjour à une certaine température. Le principal inconvénient du craquage thermique est sa forte demande énergétique pour maintenir le réacteur à la température souhaitée. Plus précisément, une température de 1250°C est nécessaire pour atteindre des niveaux de goudron acceptables avec un temps de séjour raisonnable de 0,5 s [55]. Le craquage thermique peut réduire la teneur en goudron jusqu'à 5-7 $g.Nm^{-3}$.

Le craquage catalytique peut être divisé en deux types : le catalyseur primaire (classé comme méthode de traitement primaire) placé à l'intérieur du gazéifieur et le catalyseur secondaire placé dans un réacteur séparé en aval de la gazéification. Différents types de catalyseurs peuvent être utilisés pour l'élimination de goudron. Les catalyseurs à base de nickel sont les plus utilisés. Cependant, ils sont très sensibles aux dépôts de coke [3]. Récemment, le charbon, l'olivine et la dolomite ont suscité beaucoup d'intérêt en raison de leur faible coût et de leur haute disponibilité [90]. Comparé au craquage thermique, le craquage catalytique nécessite des températures plus basses, donc une consommation d'énergie plus faible. Cependant, le catalyseur présente un coût additionnel. Le craquage catalytique semble être une méthode prometteuse pour la réduction de goudron. Cette méthode élimine environ 99% de goudron et elle est capable de réduire la teneur en goudron à 0,16 $g.Nm^{-3}$.

Même si le craquage catalytique est une méthode efficace pour l'élimination de goudron, sa désactivation par la formation de coke impose encore plusieurs restrictions. Une étude portant sur la désactivation des catalyseurs a comparé l'activité de différents lits de charbon catalytique à des températures comprises entre 400°C et 950°C [78]. L'éthylbenzène et le benzène ont été considérés comme des composants représentatifs du goudron. Les résultats ont montré que les lits catalytiques étaient totalement désactivés après 170 minutes de fonctionnement pour l'éthylbenzène à 650°C. L'augmentation de la température à 950°C augmente la durée de vie du catalyseur, avant sa désactivation à une valeur comprise entre 220 et 500 minutes selon le type de catalyseur pour le benzène. La raison de cette désactivation est le dépôt de coke à la surface du catalyseur, empêchant le goudron d'atteindre les sites actifs. Une autre étude expérimentale, portant sur la conversion du toluène sur un catalyseur à base de nickel, a montré que la désactivation du catalyseur n'est pas seulement associée à la quantité de coke, mais aussi à sa nature [77]. La désactivation des catalyseurs a eu lieu après 20 minutes de fonctionnement.

L'atteinte d'une faible teneur en goudron est généralement obtenue en combinant deux méthodes d'élimination du goudron parmi celles décrites précédemment. La première méthode vise à l'élimination de la fraction lourde de goudron, tandis que la seconde élimine la fraction la plus légère. Le concept de combinaison de deux méthodes différentes a été largement utilisé dans plusieurs projets. Par exemple, le projet Gothenburg Biomass Gasification (GoBiGas) [28] combine une colonne d'absorption d'ester méthylique d'huile de colza (RME) avec quatre lits de charbon actif pour l'élimination des BTX. Le procédé OLGA, développé par Energy research Center of the Netherlands (ECN), combine deux colonnes de lavage d'huile avec une troisième colonne pour la régénération d'huile [91]. Ce procédé vise à l'élimination sélective du goudron tout en évitant la condensation d'eau. Cela évite la génération d'un flux de déchets contenant un mélange de goudron et d'eau [92]. À cette fin, la température d'entrée du gaz est maintenue supérieure au point de rosée du goudron (320°C – 350°C), tandis que la température de sortie du gaz doit être maintenue supérieure au point de rosée de l'eau (60°C – 100°C).

5. Production du méthane à partir du gaz produit issue de la gazéification de la biomasse

En se basant sur l'état de l'art, les méthodes d'élimination du goudron pour la cogénération sont bien développées. Cependant, un travail supplémentaire est nécessaire afin de développer des méthodes

d'élimination de goudron adaptées aux procédés de méthanation et de catalyse. L'objectif principal de cette thèse est la réduction de la teneur en goudron à un niveau acceptable pour la méthanation.

Selon GRTgaz [79], de nombreuses normes doivent être respectées afin d'injecter le biométhane produit dans le réseau. Parmi ces normes, la température de rosée des hydrocarbures doit être inférieure à -2°C pour une pression allante de 1 jusqu'à 70 bar. Cependant, cette température ne reflète pas l'exigence de teneur en goudron pour le processus de méthanation. Elle indique uniquement la qualité du méthane qui doit être injecté dans le réseau. Le procédé de méthanation impose des restrictions plus strictes sur la teneur en goudron qui doit atteindre 1 $mg.Nm^{-3}$. Sinon, le catalyseur du réacteur WGS et le catalyseur de méthanation seront désactivés par le dépôt de goudron et de coke.

Plusieurs projets de conversion de biomasse en biométhane sont en cours de développement. Actuellement, la plupart des projets sont à l'échelle pilote, comme le projet GAYA développé par Engie [82], par exemple. Dans ce projet, l'étape de traitement du goudron consiste en des colonnes d'absorption de gaz utilisant du biodiesel, suivis d'une adsorption sur des lits de charbon actif (AC). BioSNG est une autre installation pilote développée par ECN [83]. Finalement, des chercheurs de Chalmers University of Technology en Suède [28] ont pu construire la première usine de production de biométhane à l'échelle industrielle (GoBiGas), basée sur la gazéification du bois. Le gazéifieur traite 150 tonnes sèches de biomasse par jour, afin de produire 20 MW de biométhane.

Dans ce projet, l'élimination du goudron se fait en combinant une colonnes d'absorption qui utilise le RME comme agent de lavage avec quatre lits de charbon actif. Dans la colonne d'absorption, la concentration de goudron est réduite de 7,8 $g.Nm^{-3}$ à 0,7 $g.Nm^{-3}$ si les BTX sont exclus, et de 20,5 $g.Nm^{-3}$ à 13,3 $g.Nm^{-3}$ dans le cas où ils sont pris en considération dans le calcul. Cela indique que la colonne d'absorption n'affecte pas le contenu en BTX. Après la colonne d'absorption, le gaz contient toujours une quantité importante de naphtalène et de BTX. Le nettoyage supplémentaire requis est effectué à travers quatre lits de charbon actif. Le premier lit est un pré-adsorbeur qui élimine les gros composants aromatiques et les impuretés. Ensuite, les trois lits adsorbeurs fonctionnent en série pour l'adsorption des composés BTX. Chacun des trois lits peut fonctionner comme étant régénérateur ou bien adsorbeur. La vapeur d'eau est utilisée pour la régénération des lits en augmentant progressivement leur température. Toutefois, les lits ne peuvent pas être entièrement régénérés sous les conditions opératoires posées, et ils perdront alors leur activité au bout d'un certain temps. Pour éviter toute diminution de l'activité des lits, le lit pré-adsorbeur est remplacé tous les 2,5 mois. En fin de processus, les teneurs en hydrocarbures aromatiques polycycliques (HAP) et BTX sont respectivement inférieures à 0,1 $\mu g.m^{-3}$ et 100 $\mu g.m^{-3}$.

6. Conclusion

Atteindre la limite acceptable de goudron pour les procédés de production de biométhane et de biocarburants présente plusieurs inconvénients comme le coût d'exploitation élevé de l'agent de lavage, le coût des lits de AC à remplacer et la désactivation du catalyseur due au dépôt de coke. Par conséquent, la réduction de la température du gaz produit pourrait être une solution efficace pour réduire la teneur en goudron à 1 $mg.Nm^{-3}$. Différentes méthodes pourraient être adaptées afin de refroidir le gaz produit. Le processus d'élimination du goudron à basse température sera divisé en deux étapes : une unité de prétraitement fonctionnant à température ambiante pour éliminer la fraction lourde de goudron, suivie d'une unité à basse température pour éliminer la fraction légère de goudron. Un système de récupération d'énergie doit être intégré au procédé de traitement de goudron afin de réduire le coût du flux froid.

Chapter 2 : Phase equilibrium for tar-producer gas mixtures and water scrubbing for the removal of the heavy fraction tar.

As seen in the first chapter, the highest tar removal efficiencies are achieved by combining at least two operational units. The objective of the first unit consists of eliminating the heavy fraction of PAH. The second unit ensures a complementary role by reducing the content of light tar fraction including BTX. The first unit is assimilated to a pre-treatment step that increases the lifetime of the second step and reduces its cost. It was also seen that the reduction of tar content, in most cases, was insufficient for combining gasification and methanation. Based on this principle, designing a low temperature process for tar removal was suggested. Adapting low temperature ensures the condensation and the deposition of tars by cooling the producer gas to a temperature lower than the tar dew point, for a concentration of 1 $mg.Nm^{-3}$. In order to do so, this chapter is divided into two main parts. In the first part, solid–vapor and liquid–vapor equilibrium are developed for different tar concentrations, ranging between 0.001 and 100 $g.Nm^{-3}$. To assess tar removal by condensation at low temperatures, psychrometric charts are developed. Since the composition of tar is complex, benzene toluene, phenol, indene, naphthalene and fluoranthene are selected as tar representatives. Each component is studied separately in four different producer gas compositions. Methods for calculating saturation, isenthalpic and constant relative concentration lines are presented. Psychrometric charts of the different tar components are then plotted at atmospheric pressure. The second part evaluates the efficiency of water-based scrubbers as a pre-treatment step on tar removal from the producer gas, based on simulations conducted using Aspen Plus. Two scrubbers are placed in series to increase the tar removal efficiency. Sensitivity studies handling the variation of the liquid to gas ratio and the scrubbing liquid temperature were conducted to study their impact on the tar removal efficiency.

2.1. Process description

A Block Flow Diagram (BFD) of the typical units for combining biomass gasification with methanation is shown in Figure 2-1. Blue blocks represent the different followed steps, from biomass preparation to biomethane grid injection. Note that the interest of this thesis resides in the units inside the red square.

A dual fluidized bed gasifier is the most suitable gasifier type for methanation. The energy content of the flue gas is usually recovered in a heat exchanger after the combustion chamber. The producer gas passes through a cooler and a particle separation unit. The producer gas passes then to the tar treatment unit. After the tar removal, the producer gas is compressed. The compression takes place in multiple stages with intercoolers. Afterwards, removal of other impurities should be performed. For instance, hydrogen sulfide removal can be done in an amine scrubber by means of methyl diethanolamine (MDEA). After H_2S removal, the producer gas flows through a guard bed to protect the catalyst of the water gas shift reactor from contamination. The ratio of H_2/CO was approximately increased to 3, in the WGS reactor operating at 300°C. This ratio can be adjusted to the desired value by changing the flow of the by-pass stream around the WGS reactor. Details about the WGS reaction and the equilibrium constant can be found in Appendix B. CO_2 separation is then performed to remove the excess of CO_2. The same type of scrubbing medium used for H_2S removal can be used for CO_2 separation with the addition of piperazine. Since methanation reaction from CO is more favored than that from CO_2, almost all the CO_2 can be removed or adjusted in a way to have a ratio of $(H_2 - CO_2)/(CO + CO_2) \approx 3$. After cleaning the producer gas, a methanation step was performed in multiple stage reactors, followed by a

drying step. The end product should have an H_2, CO_2 and CO content lower than 6%, 2.5% and 2%, respectively. Finally, the product should be pressurized prior to its injection in the grid.

Several tar treatment units and integrations are possible. Those treatment units are illustrated by pink blocks in Figure 2-1. Intel and outlet conditions for the tar treatment sections are also shown in Figure 2-1. The producer gas enters the first unit at a temperature near 350°C with a tar content of 100 $g.Nm^{-3}$. The first unit can be assimilated to a pre-treatment step where the producer gas is cooled to room temperature and the tar content is reduced to a value between 10 $g.Nm^{-3}$ and 30 $g.Nm^{-3}$, according to the selected treatment unit. The producer gas is then subject to additional cooling in the second treatment unit. This latter is denoted by the low temperature unit, since temperatures below ambient should be achieved in order to reach a tar content lower than 1 $mg.Nm^{-3}$, at the end of the process.

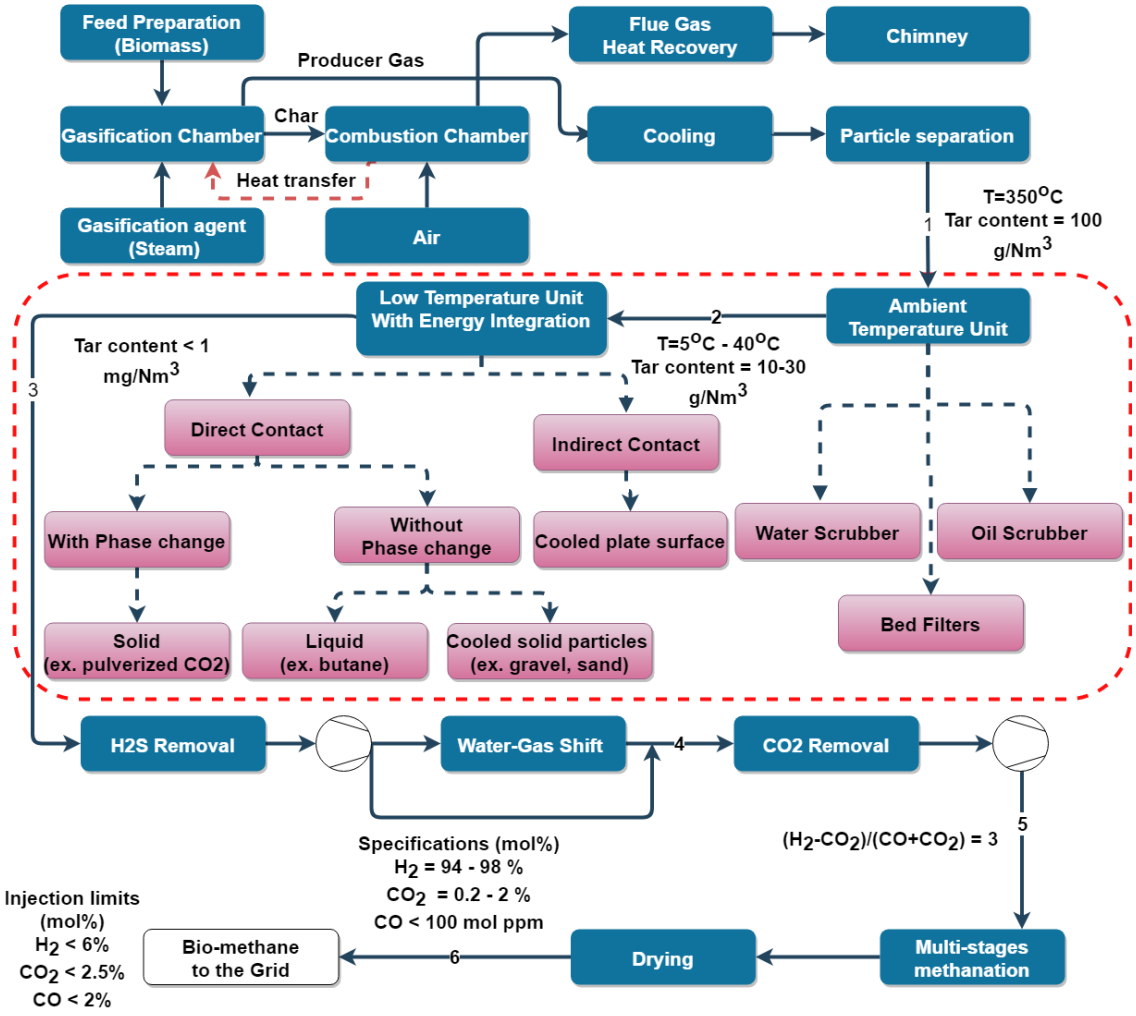

Figure 2-1: BFD showing one possible configuration for producing biomethane, based on biomass gasification.

The first unit of the suggested tar treatment process could be a conventional scrubber or a bed filter. The main function of the first scrubber is the removal of the heavy tar fraction, mainly class 5 and part of classes 2 and 4. This unit operates at room temperature and atmospheric pressure. The first tar treatment unit could be done by one of the following methods:

- Water scrubbing: Producer gas is cooled by means of water. Part of the tar is condensed or absorbed (mainly phenolic compounds) in the water. Since most tar components are not soluble in water, tar will float on the surface of the water that could be separated by decantation. Water

with the remaining impurities after decantation could be sent to the gasification chamber, and acts as the gasification agent.

- Oil scrubbing: Producer gas is cooled by means of an oil. Tar components will be absorbed in the oil or condensed due to the temperature difference. Oil could be regenerated in a stripper by steam or hot air. The stream used for the regeneration is injected into the gasifier (or combustion chamber).
- Bed filter: An alternative method for removing the heavy tar fraction consists in passing the producer gas through a bed filter (sand, gravel, or sawdust). Tar components will stick to the surface of solid particles by flowing through the length of the column. In order to enhance the heat transfer, a moving bed filter could be adapted where solid particles are injected from the top of the column while the producer gas in injected from the bottom.

The second step operates at a temperature much lower than the first one. The objective of this unit is to remove the rest of the heavy PAH fraction that escaped from the first scrubber, with the light tars and BTX. The gas leaving the second scrubber should have a tar content lower than 1 $mg.Nm^{-3}$. Different methods for the low temperature unit are suggested. Tar removal by low temperature could be done through direct or indirect contact heat transfer. Different behaviors are encountered when the producer gas is cooled by directly contacting another stream. In some cases, the cold stream used to cool the producer gas could be subject to phase change. For instance, the producer gas could be in direct contact with a solid stream such as carbon dioxide (dry ice), for example. The CO_2 is pulverized into the scrubber. When in contact with the producer gas charged in tar, solid particles will start to sublimate and escape with the gas stream, while tars will condense and form a solid residue at the bottom of the scrubber that should be removed.

In other cases of direct contact, no phase change is encountered. For instance, the stream contacting the producer gas could be a cold liquid (such as a hydrocarbon) where heat is exchanged between the two phases, leading to the condensation/deposition of tars that leave the scrubber with the liquid stream. An alternative way consists in cooling the producer gas by direct contacting particles such as gravel, for example. The temperature of the gravel should be reduced to drive tar condensation/deposition on its surface. This application is quite limited since very low temperatures are required to reach a tar content lower than 1 $mg.Nm^{-3}$, in the gas phase.

As for the indirect contact heat transfer, tar could be condensed on a cooled solid surface. This method should be developed at a first place in order to study the frosting and the condensation behavior of tar compounds. The steps considered for assessing the proposed process consist in studying phase equilibria, focusing on the heat and mass transfer phenomena for tar removal and finally estimating energy intensity and cold recovery to quantify the potential of low temperature tar removal.

The high-energy demand required to ensure the cold stream is the main restriction of the low temperature process for tar removal. To overcome this restriction, an energy recovery system should be added.

2.2. Phase equilibrium development for tar components – producer gas mixtures

In order to analyze the condensation behavior of the tar components at low temperature and assess the energy required to condense tar compounds, psychrometric charts for tar components in the producer gas are plotted. Aspen Properties V10 was used to find the phase equilibrium composition at saturation, as well as assessing the impact of producer gas composition at different temperatures. Equations are developed for calculating the enthalpy of mixtures and the constant relative concentration lines. The

psychrometric charts are used to illustrate the tar content in the producer gas at different temperatures and the energy required for condensing tars at different concentrations.

As a part of the state of the art, an open source tool developed by the Energy research Center of the Netherlands (ECN) is available online [93]. This tool enables the calculations of the dew point for a single tar component or a mixture of tar components. It was developed to calculate the temperature at which the tar condensation starts for a given tar content, expressed in $g.Nm^{-3}$ on wet basis [94]. Tar vapors are assumed as ideal gas and have an ideal mixing behavior. The main drawback of this tool is that the composition of the producer gas is not clearly defined and cannot be modified. Moreover, the calculation of the dew point is limited between -20°C and 200°C. Thus, dew point calculations are limited.

In order to study the impact of the producer gas composition on the condensation behavior of the tar components, their dew point is studied for four different producer gas compositions. Those compositions are selected in a way to cover the producer gas compositions obtained from several types of gasifiers and gasification agents. This allows the comparison of the simulated results with those obtained from the ECN online tool. A special attention will then be given to the energy required for the tar condensation by finding the enthalpy of mixtures at several points. The Non-Random Two-Liquid model (NRTL) is the physical property method used in Aspen simulations and calculations since it can handle any mixture of polar and non-polar components. This method is widely used for phase equilibria calculations (vapor-liquid and liquid-liquid equilibrium) [95]. Moreover, according to a study completed by Bassil [27], three different property methods (NRTL, WILSON and UNIQUAC) were compared in order to select the most suitable one for the tar removal. Among the three models briefly exposed, the NRTL and UNIQUAC models are able to represent liquid-liquid equilibria. The NRTL model, comprising a greater number of adjustable parameters (three or six parameters per binary if the effect of temperature is taken into account) in principle allows a better representation of the deviations from ideality than the UNIQUAC model (two parameters adjustable by binary, four parameters if the effect of temperature is taken into account). The different coefficients were available in the Aspen libraries for the water-benzene, water-toluene interactions, in addition to the other compounds.

2.2.1. Assumptions and methodology

Four producer gas compositions are considered to study their impact on the tar dew point. One tar component will be considered at each time. Note that the selection criteria of the tar components and the producer gas composition will be explained in the sequel.

2.2.1.1 Tar representative components

Some physical properties with the class and the mass percentage of the most common components forming the tar are summarized in Table 2-1.

Since tar is a complex mixture, some tar compounds are selected as tar representative components for which psychrometric charts are separately plotted. The selection criteria of the tar representative components are:

- the lightest component in each class should be selected, thus the rest of the components in the same class will condense eventually at higher temperatures.
- the fraction of the component should not be negligible.

Based on the selection criteria, it can be deduced from Table 2-1 that the tar representative components are phenol for class 2, benzene and toluene for class 3, indene and naphthalene for class 4 and fluoranthene for class 5. Benzene and toluene are considered from class 3 since they both are major components. From class 4, indene and naphthalene are considered. This is due to the fact that indene is the lightest component in this class, while naphthalene is present in an important amount and it was considered as tar representative component in several studies [30,96,97].

Table 2-1: Physical properties of common tar components.

Component	Boiling point °C	Freezing point °C	Molecular weight kg.kmol^{-1}	Class	Mass percentage [36,44,74]
Benzene	80.09	5.53	78.11	3	15-50%
o-cresol	191.004	31.04	108.10	2	0.4-8%
2,6-xylenol	201.07	45.61	122.10	2	0.1-2.5%
Toluene	110.63	-94.97	92.13	3	8-22%
o-xylene	138.36	13.26	106.10	3	1-10%
Indene	182.62	-1.45	116.16	4	1-11%
Phenol	181.84	40.91	94.11	2	3-11%
Naphthalene	217.99	80.28	128.17	4	10-30%
2-mehtylnaphthalene	241.11	34.58	142.19	4	0-4%
Biphenyl	255.00	89.50	154.20	4	0-2%
Acenaphthalene	270.00	69.20	152.19	4	0.2-4%
Acenaphthene	277.39	93.41	154.20	4	0-0.5%
Fluorene	297.29	114.79	166.21	4	0-2%
Phenanthrene	336.88	99.23	178.22	4	0.2-3%
Anthracene	342.03	215.78	178.22	4	0.1-2%
Fluoranthene	382.80	110.18	202.25	5	1-2.5%
Pyrene	394.80	150.66	202.25	5	0-1%

2.2.1.2 Producer gas composition

Different producer gas compositions are studied in order to check their impact on the dew point of the tar components. The main variation in the composition is the mole fraction of steam (H_2O) and nitrogen (N_2). Steam gasification, for direct and indirect gasifier, yields a producer gas with a high moisture content (30 to 60 mol% on wet basis), while air gasification yields a producer gas with a high nitrogen content (40 to 60 mol% on dry basis). The molar fraction of the remaining components is also affected by the gasification agent. However, this variation is negligible compared to the steam and nitrogen content variation. Table 2-2 illustrates the different producer gas compositions used in the calculations of the psychrometric charts parameters. The first case in Table 2-2 corresponds to a Dual Fluidized Bed (DFB) gasifier or indirect gasifier [98]. The latter is selected as the appropriate gasifier type used for methanation since it yields a suitable producer gas composition for this application, which is inert free with high hydrogen to carbon ratios [30,86]. The second and the third cases correspond to a bubbling fluidized bed gasifier operating with air as gasification agent. Case 2 [34] corresponds to the gasification of pine wood at 800°C with an equivalence ratio (*ER*) of 0.25. As for case 3 [99], refused-derived fuel (RDF) is gasified at 820°C with an *ER* equal to 0.21. The last case (case 4) represents a downdraft gasifier that uses air as gasification agent yielding a producer gas with a low water content [100]. The dew point of each tar representative compound is calculated in each case for different concentrations. This reflects the impact of the producer gas composition on the tar condensation. The calculated dew

points of tar compounds are compared with those obtained from the online tool provided by ECN for the same tar concentration. The producer gas composition, used by ECN for the calculations of the tar dew point based on tar concentration, is not given. Their calculations were based on an atmospheric bubbling fluidized bed gasifier operating at 850°C. The tar dew point calculation, forming the saturation line, is explained in the sequel.

Table 2-2: Different raw gas compositions in wet basis used for the tar dew point calculation.

	Case 1 [98]	**Case 2** [34]	**Case 3** [99]	**Case 4** [100]
H_2, mol%	27.8	9.6	6.0	11.0
CO, mol%	16.7	14.4	10.9	20.0
CO_2, mol%	13.8	11.2	12.3	10.0
CH_4, mol%	6.0	4.0	5.7	3.0
C_2H_n, mol%	1.6	2.0	4.6	-
N_2, mol%	3.7	38.8	48.0	50.0
H_2O, mol%	30.4	20.0	12.5	6

The presence of large amounts of water in the producer gas affects the tar dew point and the enthalpy, mainly for temperatures lower than the water dew point. The initial tar content was set to 100 g.Nm^{-3}. The presence of water in the mixture imposes the use of a suitable property method for polar mixtures. Note that NRTL is used in this section.

2.2.1.3 Saturation and constant relative concentration lines

Calculations are based on an initial concentration of 100 g of tar per 1 Nm^3 of raw gas, for each tar component. This concentration was selected since it is equal to the highest tar level that could be obtained from the gasification. In this section, "raw gas" corresponds to the mixture of components forming the producer gas, excluding the tar compounds. The same calculations are repeated for every selected tar component (phenol, benzene, toluene, indene, naphthalene and fluoranthene).

The saturation line points were first calculated for each case. The saturation line, which corresponds to the liquid-vapor above the triple point and the solid-vapor below it, represents the limit at which tar condensation in the producer gas starts. To do so, the vapor fraction (*VF*) was calculated at different temperatures (T_i) in order to detect the temperature at which condensation begins ($VF \neq 1$). At this temperature, the gas phase molar fraction (y_j) was calculated to compute the amount of the condensed tar, using a defined property method in Aspen Properties, where j represents the different components of the producer gas. The amount of tar remaining in the gas phase is calculated according to eq. (2-1) and eq. (2-2) where w_{tar} is the tar content, in kg.kg^{-1} raw gas, which is equal to the ratio of tar weight (m_{tar}) to the raw gas weight ($m_{raw\ gas}$). The tar concentration (C_{tar}) is deduced from eq. (2-3) in mg of tar.Nm^{-3} of raw gas. Same calculations are repeated for different temperatures. The temperature decreases with an interval of 10°C until reaching a tar concentration of 1 mg of tar.Nm^{-3} of raw gas. Plotting the tar content in function of temperature yields the saturation line.

$$P_{sat}(T_i) = y_{tar}(T_i).P_{total} \quad (2\text{-}1)$$

$$w_{tar} = \frac{m_{tar}}{m_{raw\ gas}} = \frac{P_{sat}(T_i)}{P_{total} - P_{sat}(T_i)}.\frac{M_{tar}}{M_{raw\ gas}} \quad (2\text{-}2)$$

$$C_{tar} = w_{tar}.\rho_{raw\ gas}.10^6 \quad (2\text{-}3)$$

where M_{tar} and $M_{raw\ gas}$ are respectively tar and raw gas molecular masses in g.mol^{-1}, P_{sat} is the saturated tar partial pressure in the raw gas in Pa, P_{total} is the total mixture pressure that is equal to the atmospheric pressure in Pa, and $\rho_{raw\ gas}$ is the density of the raw gas in kg.m^{-3}.

Constant tar relative concentration (ϕ) curves are then plotted. Constant tar relative concentration (ϕ) curves are then plotted. ϕ is equal to the ratio of the tar partial pressure in the raw gas to the saturated tar partial pressure at the same temperature (T_i), as expressed in eq. (2-4). To plot those curves, tar partial pressure was calculated at each T_i for a fixed value of ϕ, according to eq. (2-5). Tar vapors are assumed to behave as ideal gases. For each value of ϕ, ranging between 10% and 90%, and for a total pressure of one atmosphere, the tar content was calculated for different temperatures according to eq. (2-6). Finally, tar content is plotted with respect to the temperature for each value of ϕ.

$$\phi = \frac{P_{tar}(T_i)}{P_{sat}(T_i)} \tag{2-4}$$

$$P_{tar}(T_i) = \phi . P_{sat}(T_i) = \phi . y_{tar} . P_{total} \tag{2-5}$$

$$w_{tar} = \frac{\phi . y_{tar}(T_i)}{1 - \phi . y_{tar}(T_i)} . \frac{M_{tar}}{M_{raw\ gas}} \tag{2-6}$$

2.2.1.4 Saturation enthalpy and isenthalpic lines

Isenthalpic lines help in finding, at any condition, the enthalpy of the mixture. They join several points having an equal enthalpy. The enthalpy of the gas mixture is calculated per kilogram of raw gas. Calculations begin by finding the enthalpy at saturation. Plotting enthalpies at saturation function of the temperature yields the saturation enthalpy line. Constant enthalpy lines, also referred to as isenthalpic lines, are then plotted. Figure 2-2 illustrates the constant enthalpy line calculations. In this figure, points 1 and 2 of the saturation line are considered in our calculation. The tar contents, the dew points and the enthalpies of those points are known. Note that point 1 has the highest dew point. A constant tar content line, drawn as a horizontal line starting from point 2, intersects with the constant enthalpy line of point 1. The intersection point is denoted as point 3. Consequently, it can be deduce that: $h_1=h_3$, $w_{tar,2}=w_{tar,3}$ and $w_{wat,2}=w_{wat,3}$. The enthalpy of the raw gas at any point, expressed in kJ.kg^{-1}, is given in eq. (2-7). This equation describes the conventional enthalpy calculation at dry bulb conditions, while considering gas, liquid and solid phases. As operating temperatures considered for tar removal are below 25°C, the risk of ice and tar deposit formation exists. Although preliminary calculations show limited discrepancies between calculated and existing data on psychrometric charts for water, an assessment for the impact of considering L-V or S-L-V phases on enthalpy calculations including water and tars, is needed.

$$\begin{aligned} h = C_{p,raw\ gas} . (T_{DB} - T_{ref}) + w_{tar}\left[h_{fg,tar\ (25°C)} + C_{p,tar,vap} . (T_{DP,tar} - T_{ref})\right] \\ + \ w_{wat}\left[h_{fg,wat\ (25°C)} + C_{p,wat,vap} . (T_{DP,wat} - T_{ref})\right] \end{aligned} \tag{2-7}$$

where $C_{p,raw\ gas}$ is the heat capacity of the mixture excluding water and tar component, $C_{p,tar,vap}$ and $C_{p,wat,vap}$ are respectively the heat capacity of the tar component and water in the vapor phase expressed in kJ.kg^{-1}.K^{-1}, T_{DB} is the dry bulb temperature expressed in K, T_{ref} is the reference temperature expressed in K, $h_{fg,tar}$ is the latent heat of vaporization or the latent heat of sublimation of tar component depending on its triple point expressed in kJ.kg^{-1}, $h_{fg,wat}$ is the latent heat of vaporization of water expressed in kJ.kg^{-1} and T_{DP} is the dew point temperature expressed in K.

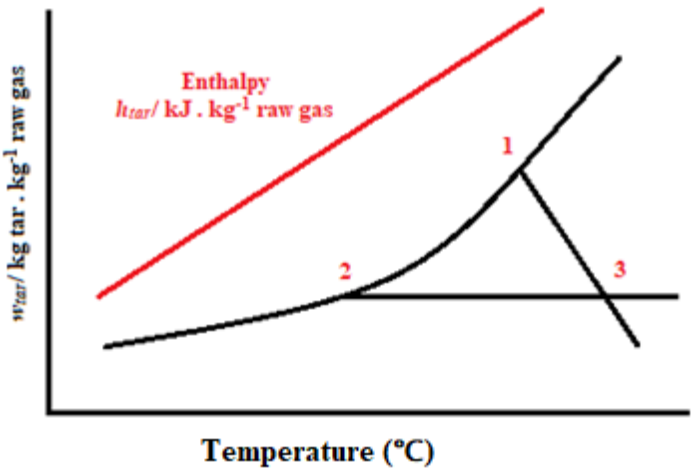

Figure 2-2: Illustration of the constant enthalpy line calculations.

By solving eq. (2-7) for points 1, 2 and 3, eq. (2-8) can be deduced. The latter is solved for $T_{DB,3}$, thus the coordinates of a new point on the constant enthalpy line are found. To reach a better accuracy, three-to-four points are considered in the plot of the constant enthalpy line.

$$h_3 - h_2 = C_{p,raw\ gas,3}.\left(T_{DB,3} - T_{ref}\right) - C_{p,raw\ gas,2}.\left(T_{DB,2} - T_{ref}\right) \quad (2\text{-}8)$$

When the condensation takes place at a temperature lower than the triple point, in solid phase, the built-in correlations in Aspen Properties do not consider the solid phase condensation and may yield non-accurate results. Studying the solid condensation behavior for each tar compound separately is very time consuming, because the tar composition is complicated and encloses too many compounds. In addition, developing a solid phase characteristic curve for all the compounds is not necessary. Therefore, an investigation in a general way is completed to develop a solid condensation characteristic curve by expanding the liquid condensation laws into the solid phase. To justify the decision of expanding the laws into the solid phase, a comparison between the vapor pressure obtained in our simulations and that found in the literature for multiple compounds, is done for a defined temperature interval below the triple point. The comparison was done for fluoranthene, naphthalene, phenol and benzene. Note that this comparison could not be completed for the solid vapor pressure of indene because the latter was not found in the literature. Similarly for toluene, which triple point is too low. It is important to mention that the comparison was done based on dry basis raw gas composition. Otherwise, the curves could not be compared since the condensation of water affects the tar condensation.

2.2.2. Results and discussion

2.2.2.1 Solid – gas equilibrium

A comparison between the experimental vapor pressures (VP) and calculated ones using built-in correlations for solid – gas equilibrium is illustrated in Figure 2-3.

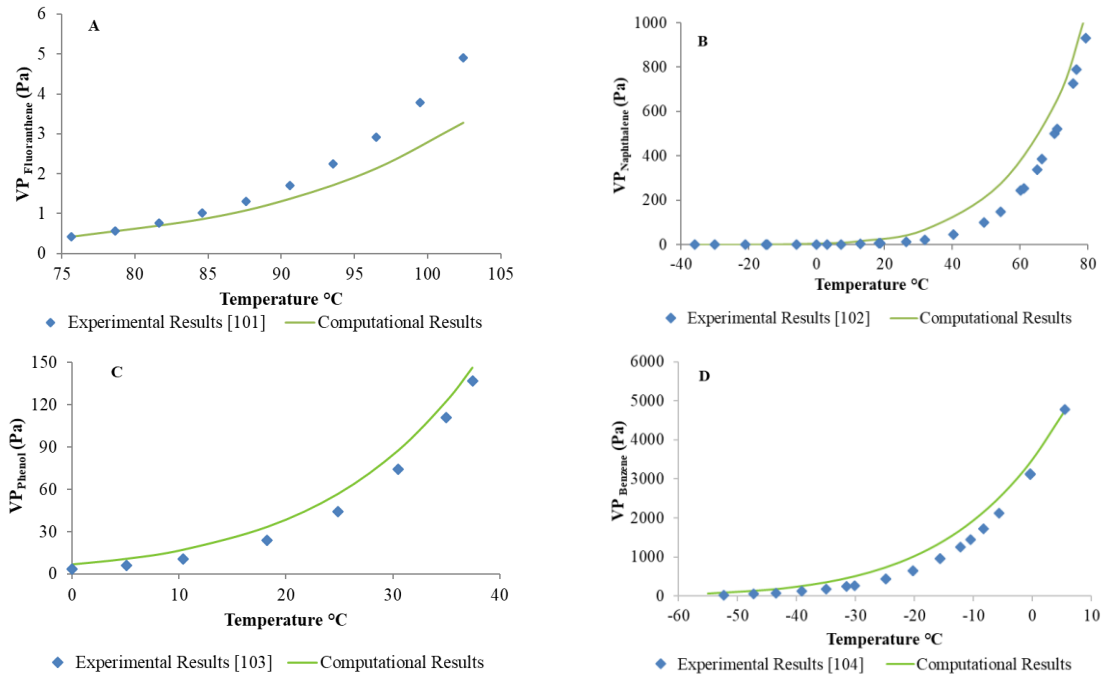

Figure 2-3: Comparison between the experimental VP and the calculated ones based on Aspen for A) fluoranthene [101], B) naphthalene [102], C) phenol [103] and D) benzene [104] at temperatures lower than their triple point.

The experimental values of vapor pressures for temperatures lower than the triple point for fluoranthene [101], naphthalene [102], phenol [103] and benzene [104] were taken from literature studies. The agreement between the experimental values and the calculated ones, shown in Figure 2-3, indicates the possibility of extending the correlations used for gas and liquid phases to cover the solid phase. Note that the vapor pressure taken from the literature review are for mixtures of fluoranthene, naphthalene, phenol and benzene in air and not in producer gas. This might lead to a certain deviation between the calculated and the experimental vapor pressure values.

2.2.2.2 Tar dew point

After validating that the correlations could be extended to cover also the solid - gas equilibrium, the dew point of the tar representative components can be calculated. A comparison between the calculated dew point of those components and the ones retrieved from the ECN tool is performed. The different cases, summarized in Table 2-2, are considered to check the impact of the producer gas composition on tar condensation. The calculations are carried out for a single tar component at a time. Figure 2-4 groups all the results that are obtained for the different producer gas compositions, and compare them to the dew point obtained from the ECN online tool for the same tar concentration. It can be seen in Figure 2-4 that, except for fluoranthene, the dew point of the tar components varies according to the producer gas composition. Note that, by decreasing the temperature, tar and water that are initially in the producer gas are condensed.

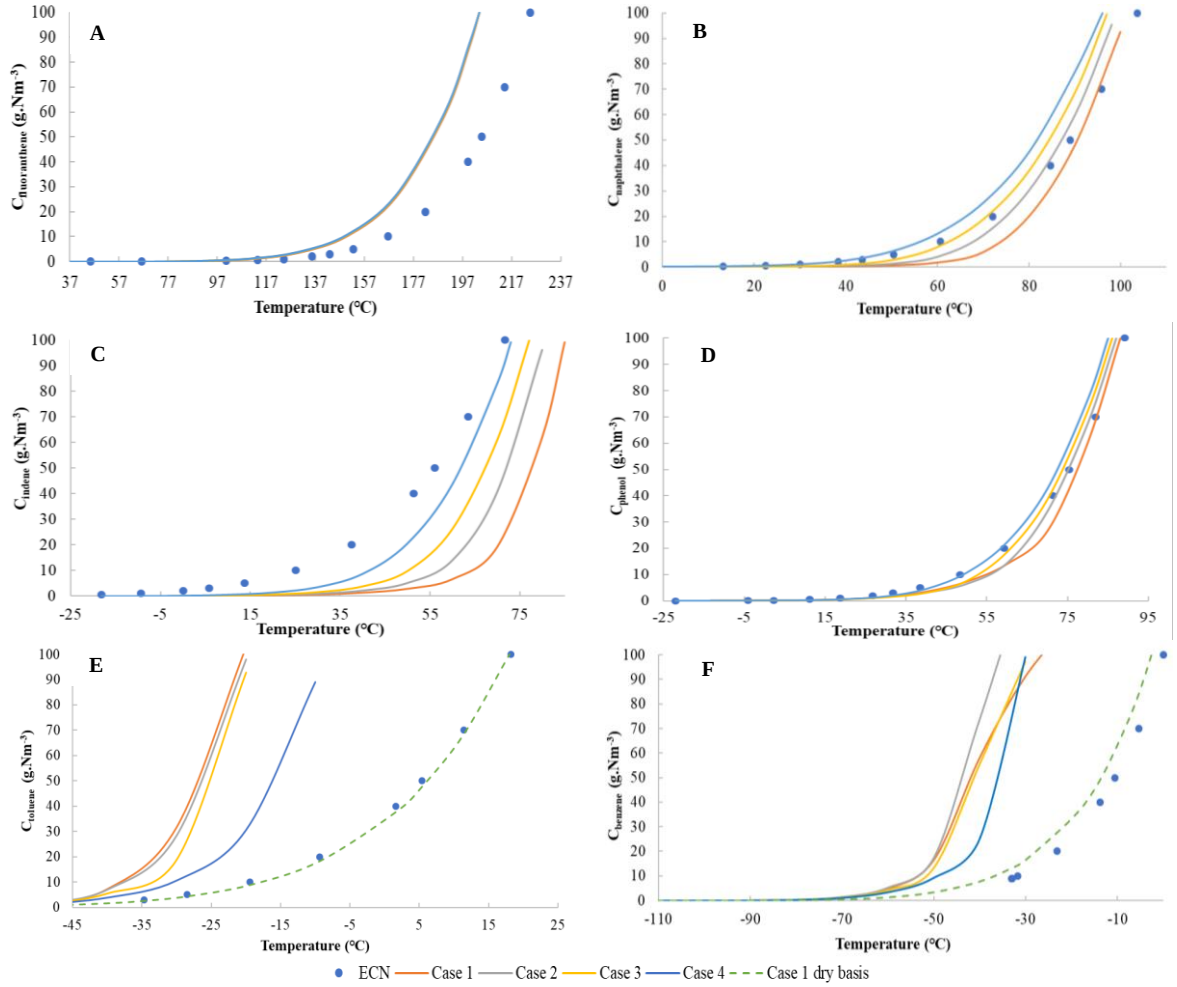

Figure 2-4: Dew point of A) fluoranthene, B) naphthalene, C) indene, D) phenol, E) toluene and F) benzene in producer gas mixtures for different compositions.

The dew point of fluoranthene is expected to be the highest one since this latter is the heaviest component. ECN stated that their online tool overestimates the dew point of tar by 7°C to 14°C at temperature higher than 167°C. This explains the large deviation between the calculated dew points and those obtained from their online tool, at high temperatures. The major part of fluoranthene is removed by condensation before reaching the water dew point. The latter depends on the initial moisture content (shown in Table 2-2) ranging between 30°C and 70°C. It can be concluded that the dew point of the tar components is mainly affected by the moisture content and the condensation of steam in the producer gas, rather than the composition of the non-condensable gases.

The dew point of naphthalene (Figure 2-4 (B)), indene (Figure 2-4 (C)) and phenol (Figure 2-4 (D)) decreases with the initial moisture content, while the dew point of toluene (Figure 2-4 (E)) and benzene (Figure 2-4 (F)) decreases for a higher initial moisture content. In contrast to other tar representative components, toluene and benzene form with water azeotropic mixtures. This explains the difference in the behavior from the rest of the tar components, regarding the variation of the initial moisture content present in the producer gas. In order to verify justify this statement, toluene and benzene dew points are computed for case 1 on dry basis. This eliminates toluene-water and benzene-water interactions. It can be seen that, operating on dry basis reduces the deviation between computed and literature results.
The best agreement between the calculated dew points and the ones available online is encountered for phenol and naphthalene. Indene shows a high deviation for high moisture content. The deviation decreases for a low moisture content in the producer gas (6 mol $\%_{wet}$). The same analogy applies for the

toluene and benzene. The highest deviation occurs in case 1, which corresponds to the highest moisture content (30.4 mol $\%_{wet}$). The lowest deviation occurs in case 4 having the lowest initial moisture content. Although the deviation decreases with the initial moisture content for toluene and benzene, the difference is still high since those components form azeotropic mixtures with water. In addition, ice formation at temperatures lower than 0°C could have an impact on the dew point.
It can be deduced that, the tar dew point depends on the composition of the producer gas. However, this composition is not defined for the online tool calculator. All these factors increase the deviation between the calculated tar dew points and those obtained by the online dew point calculator.

2.2.2.3 Psychrometric charts

By completing the calculations for all the mixtures of tar representative components in the raw gas, psychrometric charts for tar representatiive components -raw gas mixtures were plotted. Calculations in this section are based on Case 1 in Table 2-2 referring to a DFB gasifier. The latter is selected since it yields a suitable producer gas composition for methanation. The six psychrometric charts of fluoranthene, naphthalene, indene, phenol, toluene and benzene – raw gas mixtures are illustrated in Figure 2-5, Figure 2-6, Figure 2-7, Figure 2-8, Figure 2-9 and Figure 2-10, respectively. The aim is to obtain producer gas having a tar content lower than 1 $mg.Nm^{-3}$. It can be deduced that a temperature around -110°C is then required. Note that the enthalpy difference, calculated between two points, is more significant than the one calculated at each point, since it reflects the required energy for condensing a certain mass of tars. To find the enthalpy of a point that is not at saturation, the isenthalpic lines on the charts are projected until they reach the enthalpy line at saturation. The intersection between the projection and the enthalpy at the saturation line is then read on the right axis. This value corresponds to the enthalpy in $kJ.kg^{-1}$. In the psychrometric charts, the light grey lines represent the projection of the isenthalpic lines for better understanding.

At a tar content of 100 $g.Nm^{-3}$, the condensation of water and the tar representative component take place simultaneously, except for the heaviest one (fluoranthene) and the lightest ones (toluene and benzene). The condensation of fluoranthene, toluene, benzene and water starts at a temperature of 203°C, -20°C, -30°C and 70°C, respectively. In other words, fluoranthene condenses prior to water while toluene and benzene condense after it. It can be deduced from the figures below that the condensation of water has the highest impact on the enthalpy change. This is justified by the enthalpy slope increase for temperatures lower than that of the water dew point. It can be observed in Figure 2-5 that the enthalpy varies linearly, function of temperatures greater than 70°C. This section only presents the condensation of fluoranthene. Below this temperature, water condensation starts, leading to a higher enthalpy variation thus a steeper enthalpy slope. In addition, the water fraction is higher than the tar fraction in the producer gas, thus the impact of water condensation on the enthalpy is higher. As for indene, naphthalene and phenol, the slope of the enthalpy is notably higher than that of fluoranthene. According to Figure 2-5 and Figure 2-7, to reduce the tar content (w) from 0.06 $kg.kg^{-1}$ to 0.02 $kg.kg^{-1}$, the required energy is 98.7 $kJ.kg^{-1}$ for fluoranthene and 217.4 $kJ.kg^{-1}$ for indene. The condensation of toluene and benzene begins after the removal of a high fraction of water. As a result, the energy required for toluene (28.5 $kJ.kg^{-1}$) and benzene (34.6 $kJ.kg^{-1}$) condensation to reduce the content from 0.06 to 0.02 $kg.kg^{-1}$ are the lowest ones, as seen in Figure 2-9 and Figure 2-10.

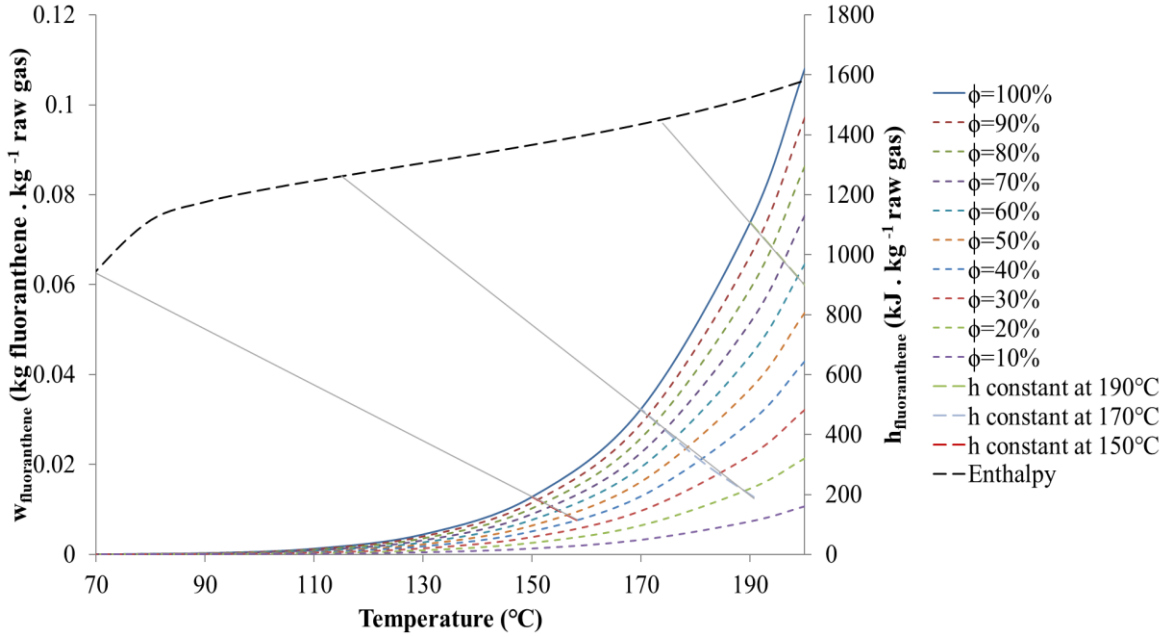

Figure 2-5: Psychrometric charts of fluoranthene-raw gas mixture.

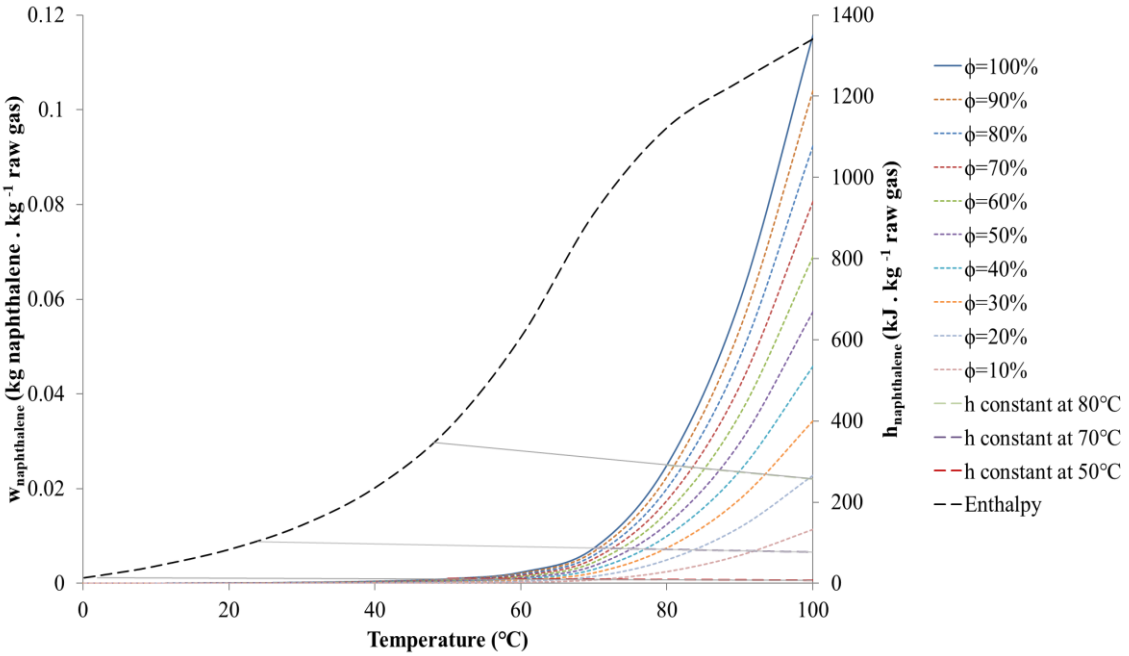

Figure 2-6: Psychrometric charts of naphthalene-raw gas mixture.

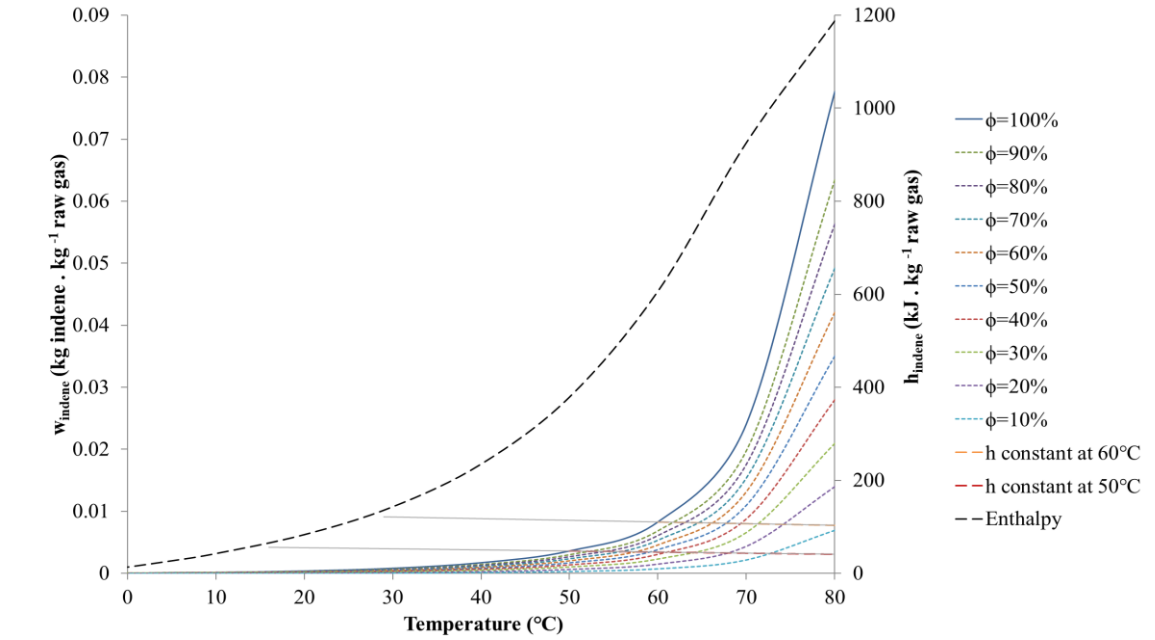

Figure 2-7: Psychrometric charts of indene-raw gas mixture.

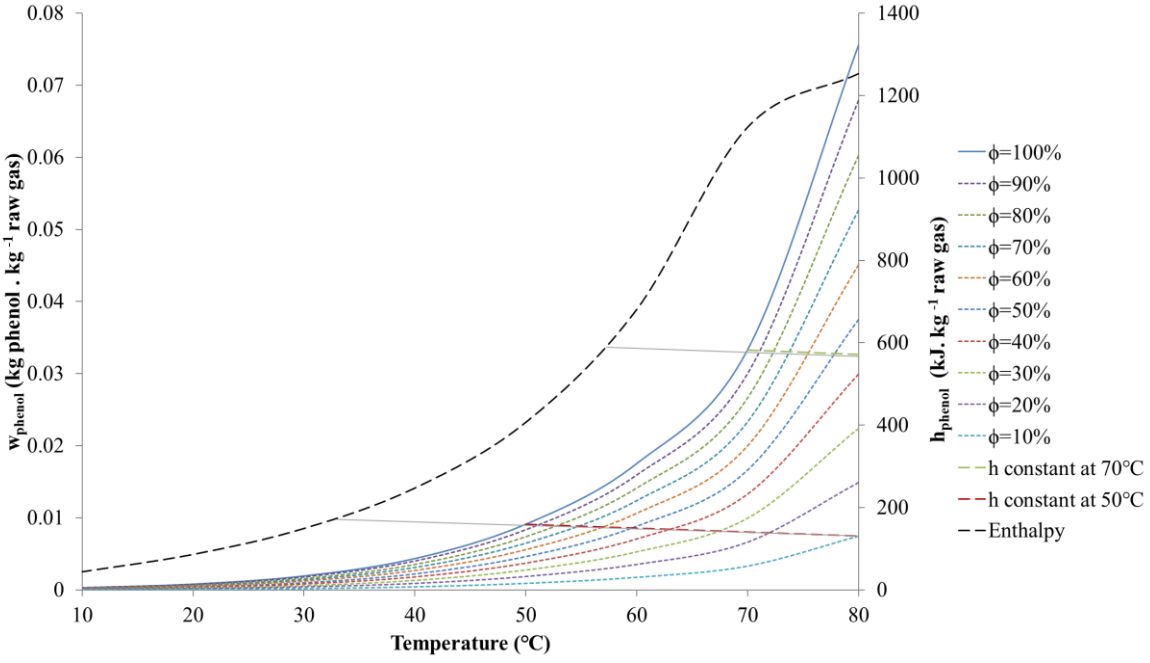

Figure 2-8: Psychrometric charts of phenol-raw gas mixture.

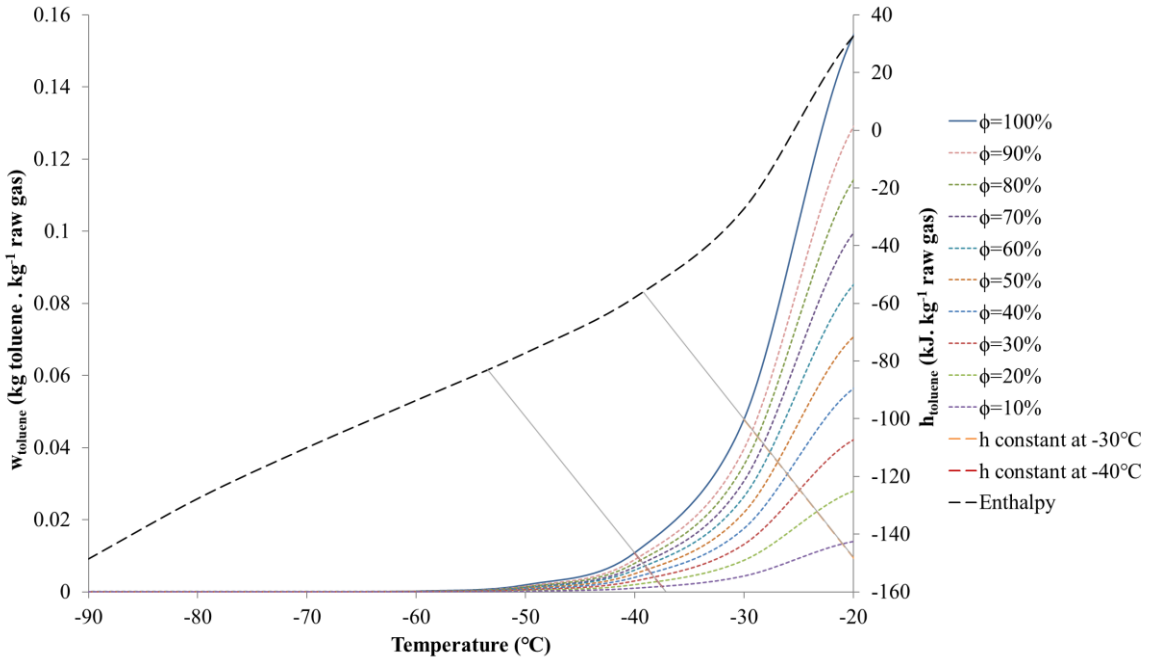

Figure 2-9: Psychrometric charts of toluene-raw gas mixture.

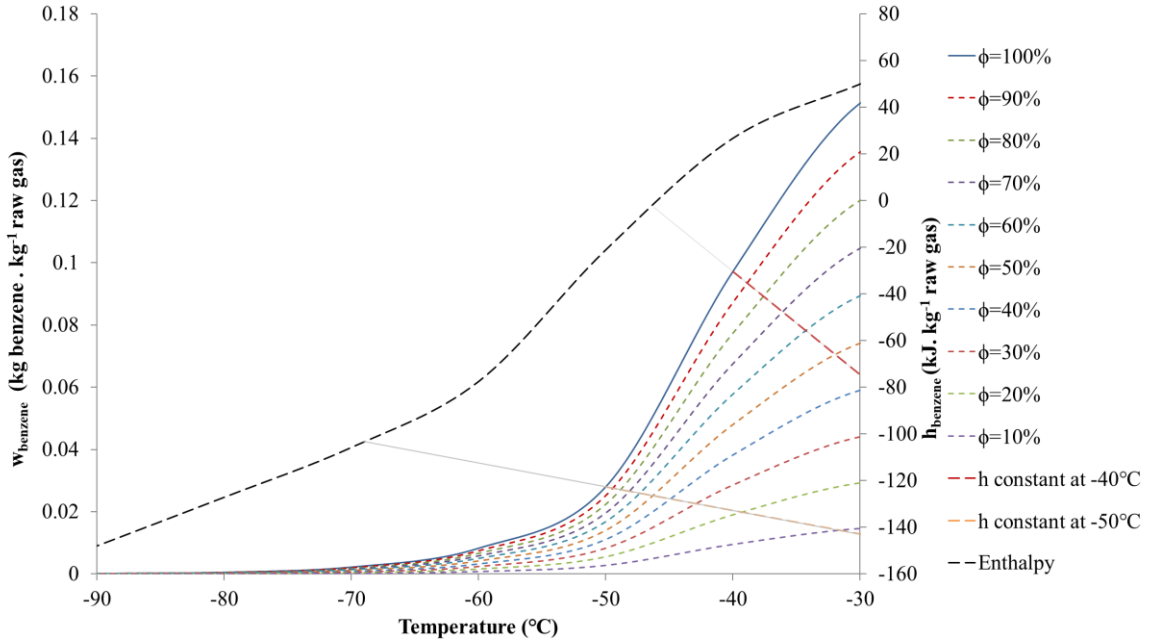

Figure 2-10: Psychrometric charts of benzene-raw gas mixture.

It can be observed in the figures above that, at low temperatures, the charts have very small values. Therefore, the tar content is not readable. Table A.1, Table A.2, Table A.3, Table A.4, Table A.5 and Table A. 6 present the tar content of fluoranthene, indene, naphthalene, phenol, toluene and benzene, respectively. The more accurate values may be of a great benefit for the researchers working on gasification and tar removal by physical methods. In addition, those tables reflect the required temperature for reaching the limit for any application, not only for biomethane production. Note that the values presented in these tables correspond to the saturation line where ϕ=100%.

2.3. Removal of the heavy tar fraction by two water scrubbers placed in series.

Existing methods for the removal of the heavy fraction of tars are efficient, while more attention should be given to the removal of the lightest tar fraction (benzene, toluene, and xylene) [3,4,7]. Since the latter has market value, it is important to keep their content unaffected in the first stage of tar removal while reducing the producer gas temperature and the heavy tar fraction. Thus, to obtain a producer gas having those specifications after the first tar removal stage, a configuration consisting of two water scrubbers is proposed.

In addition, since the targeted end use application of the producer gas is biomethane production, a dual fluidized bed gasifier operating with steam is favored over an air blow gasifier. This results in a producer gas having a high content of water vapor, that varies between 30 vol % and 42 vol %. This composition increases the water dew point to around 70°C. Consequently, the efficiency of the oil-based scrubbers decreases by limiting the absorber temperature to 70°C. Therefore, water is tested as scrubbing medium to avoid mixing the condensing water from the producer gas with the scrubbing oil. This eliminates the need of an additional treatment step and avoids the restrictions imposed on the scrubber temperature. Moreover, water is the cheapest and most available scrubbing medium. Furthermore, part of the water used for scrubbing can be heated and then reused as a gasification agent. This enriches the hydrogen content of the producer gas and fosters the methanation reaction. Finally, the condensation of the lightest tar compounds, that can be valorized if condensed at low temperature, is minimized. Besides reducing the tar content, water scrubbers also reduce the temperature, the moisture and then the required energy in the cold stages.

Although the target of this thesis is to study the removal of remaining tars after the two scrubbers, the assessment of the scrubbing process is also essential. This helps understanding the producer gas composition and the tar components left after scrubbing. The outlet composition of the scrubbers will be the inlet for the low temperature process of tar removal.

The removal of the heavy fraction of tar by means of water scrubbers, based on different operating conditions, is studied using Aspen Plus. The different columns (collector, absorber and stripper) are simulated as RadFrac columns based on equilibrium stage model. Moreover, vapor-liquid-liquid are set as the valid phases in the simulations, since the condensable components may not form a homogeneous liquid phase. For instance, benzene is slightly soluble in water while toluene is insoluble in water. The inlet gas composition retrieved from GoBiGas plant [98] and used in the sequel, is shown in Table 2-3. It corresponds to a DFB gasifier or indirect gasifier where wood-based biomass is gasified using steam as the gasification agent. The inlet tar composition is restricted to the tar representative components that were selected in section 2.2.1.1, based on their fraction and classes. The inlet tar content was set to 100 $g.Nm^{-3}$ in order to consider the worst-case scenario, which corresponds to the highest tar content after a gasifier. Figure 2-11 presents the process flow diagram of the two water scrubbers. Note that the separator placed after the collector is a tar settling tank. An alternative method consists in directly using the water stream leaving the absorber as the gasification agent instead of regenerating it or by decantation.

In order to select the optimal operating conditions and assess their impact on the tar removal efficiency, three sensitivity studies were developed. The first and second ones evaluate the impact of the water flow rate, and therefore the L/G ratio, on the tar removal efficiency, while fixing the scrubbing liquid temperature for the collector and the absorber, respectively. The third one assesses the impact of the water temperature on the tar removal efficiency, while fixing the L/G ratio in the absorber.

Table 2-3: Producer gas mass composition obtained from a wood-based biomass dual fluidized bed gasifier, operating with steam as gasifying agent (Thunman et al. 2018b).

Component	Mass fraction
Hydrogen (H_2)	0.0260
Carbon Monoxide (CO)	0.2167
Carbone Dioxide (CO_2)	0.2831
Methane (CH_4)	0.0449
Ethylene (C_2H_4)	0.0209
Nitrogen (N_2)	0.0483
Water (H_2O)	0.2800
Benzene (C_6H_6)	0.0462
Toluene (C_7H_8)	0.0073
Indene (C_9H_8)	0.0033
Phenol (C_6H_6O)	0.0013
Naphthalene ($C_{10}H_8$)	0.0176
Fluoranthene ($C_{16}H_{10}$)	0.0044
Total	1

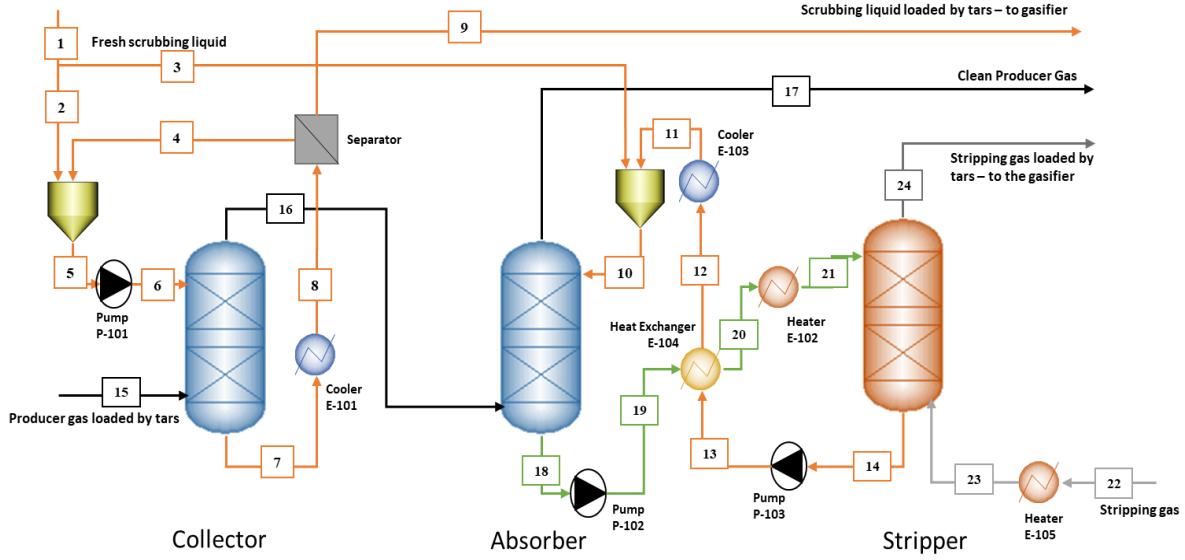

Figure 2-11: Process Flow Diagram (PFD) for tar removal from producer gas.

Table 2-4 summarizes the main parameters and ranges of operation that are considered for the sensitivity studies, in water scrubbers' simulations.

Table 2-4: Main operating conditions and stream variables considered in water scrubbers.

Stream ID	15	4	2	16	11	3
Temperature (°C)	350	25	25	71	5-65	25
Volumetric flow rate ($m^3.h^{-1}$)	11316	4.5-16.65	0.5-1.85	6218.16	5.4-18	6-20
Flow rate ($kg.h^{-1}$)	4480	4500-16650	500-1850	4440	5400-18000	600-2000

2.3.1. Liquid to gas ratio

2.3.1.1 First scrubber: collector

In the first sensitivity study, the impact of the variation of the L/G ratio on the remaining tar content is studied in the collector. The gas flow rate is fixed while the liquid flow rate is varied. The temperature of the water entering the first scrubber is set to 25°C.

Figure 2-12 illustrates the temperature variation of the producer gas leaving the collector (stream 16) and the remaining content of phenol, naphthalene, indene and fluoranthene in this stream, function of the L/G for a scrubbing liquid temperature of 25°C. The tar content variation is presented on a logarithmic scale. It can be observed from Figure 2-12 that, in general, the elementary tar removal efficiency increases by increasing the L/G ratio. In particular, the phenol content is reduced from 1650 $mg.Nm^{-3}$ to 135 $mg.Nm^{-3}$ for a L/G ratio of $0.44x10^{-3}$ $m^3.m^{-3}$. By increasing the L/G ratio to $1.65x10^{-3}$ $m^3.m^{-3}$, the phenol content is reduced to 21.5 $mg.Nm^{-3}$. This high reduction in the phenol content is justified by the addition of a fresh water flow rate. Therefore, the solubility of phenol in the fresh water stream (0.0828 kg_{phenol}/L_{water}) was enough to reduce importantly its content. For a L/G ratio lower than $1.4x10^{-3}$ $m^3.m^{-3}$, the naphthalene content is not affected. For higher flow rates, the naphthalene content sharply decreases. The indene content is not highly affected by the L/G ratio and remains almost constant (around 4000 $mg.Nm^{-3}$). The fluoranthene content is reduced from 5520 $mg.Nm^{-3}$ to around 140 $mg.Nm^{-3}$ for a L/G ratio of $0.44x10^{-3}$ $m^3.m^{-3}$. By increasing the L/G ratio to $1.65x10^{-3}$ $m^3.m^{-3}$, the fluoranthene content becomes negligible. The temperature of the producer gas leaving the collector is also affected by the L/G ratio. The temperature of the producer gas is reduced from 350°C at the collector inlet to 75°C at the collector exit, for a L/G ratio of $4.45x10^{-4}$ $m^3.m^{-3}$. By increasing the L/G ratio to $1.65x10^{-3}$ $m^3.m^{-3}$, the temperature of the producer gas leaving the collector is reduced to 53°C.

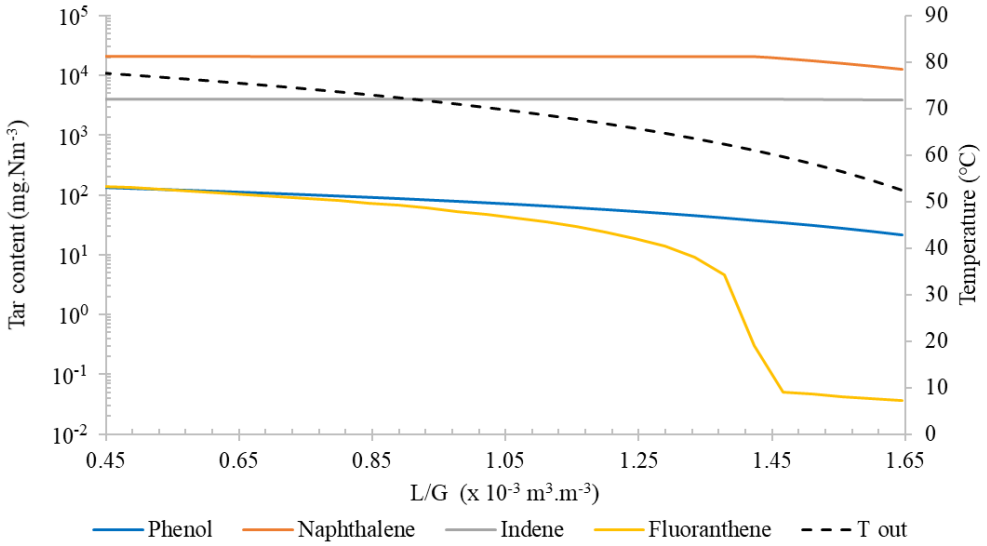

Figure 2-12: Variation of the remaining content of phenol, naphthalene, indene and fluoranthene, and variation of the temperature of the gas stream leaving the first scrubber (stream 16), function of the L/G ratio in the collector, for a water temperature of 25°C.

In general, increasing the L/G ratio leads to a higher density of scrubbing medium droplets across a defined cross section, leading to a higher tar removal efficiency. Note that the efficiency increases by increasing the L/G ratio at the expense of an operational cost increase, due to the higher scrubbing liquid flow rate and the pump usage. For this reason, the L/G is limited to $1.65x10^{-3}$ $m^3.m^{-3}$.

2.3.1.2 Second scrubber: absorber

In the second sensitivity study, the impact of the variation of the L/G ratio on the remaining tar content is studied in the absorber. The gas flow rate is fixed while the liquid flow rate is varied. The temperature of the water entering the second scrubber is set to 20°C. The L/G ratio and the temperature in the collector are fixed to $0.89x10^{-3}$ $m^3.m^{-3}$ and 25°C, respectively. After setting those conditions in the collector, the producer gas temperature and the tar content remaining in the producer gas fed to the absorber, are deduced from Figure 2-12. Note that, in this sensitivity study, a higher L/G ratio is considered since it is noticed from the first sensitivity study that for an efficient tar removal, a higher L/G ratio is required.

Figure 2-13 illustrates the temperature variation of the producer gas leaving the absorber (stream 17) and the remaining content of phenol, naphthalene, indene and fluoranthene in this stream function of the L/G ratio, for a scrubbing liquid temperature of 20°C. The tar content variation is presented on a logarithmic scale. It can be observed from Figure 2-13 that the same elementary tar removal efficiency behavior is encountered in the absorber. In general, the elementary tar removal efficiency increases by increasing the L/G ratio. In particular, the phenol content is reduced from 88 $mg.Nm^{-3}$ to almost zero, even for the lowest L/G ratio. The naphthalene content is constant for a L/G ratio lower than $1.05x10^{-3}$ $m^3.m^{-3}$. As the L/G ratio becomes higher than $1.05x10^{-3}$ $m^3.m^{-3}$, the naphthalene content sharply decreases from 20746 $mg.Nm^{-3}$ to 793 $mg.Nm^{-3}$, for a L/G ratio of $2.58x10^{-3}$ $m^3.m^{-3}$. For higher L/G ratios, the naphthalene tar content becomes almost constant and it reaches 615 $mg.Nm^{-3}$ for a L/G ratio of $3.22x10^{-3}$ $m^3.m^{-3}$. Therefore, the naphthalene removal efficiency increases from 96.17% to 97.03% by increasing the L/G ratio by 29% (from $2.58x10^{-3}$ $m^3.m^{-3}$ to $3.22x10^{-3}$ $m^3.m^{-3}$). As seen in the previous section, indene was the least affected component by the L/G ratio, in the collector. Similarly in the absorber, the indene content is only reduced by 0.25% (from 4003 $mg.Nm^{-3}$ at the absorber inlet to 3993 $mg.Nm^{-3}$ at the absorber outlet) for a L/G ratio of 0.97 $x10^{-3}$ $m^3.m^{-3}$. By increasing the L/G ratio, the indene removal efficiency highly increases and becomes 53% for a L/G ratio of $3.22x10^{-3}$ $m^3.m^{-3}$. Fluoranthene content drops from 66.6 $mg.Nm^{-3}$ to 4.78 $mg.Nm^{-3}$ for the lowest L/G ratio, and becomes negligible for L/G ratios higher than $1.13x10^{-3}$ $m^3.m^{-3}$. The temperature of the producer gas leaving the absorber is also affected by the L/G ratio. The temperature of the producer gas is reduced from 72°C at the absorber inlet to 61.5°C at the absorber exit, for a L/G ratio of $9.67x10^{-4}$ $m^3.m^{-3}$. By increasing the L/G ratio to $3.22x10^{-3}$ $m^3.m^{-3}$, the temperature of the producer gas leaving the collector is reduced to 20.85°C.

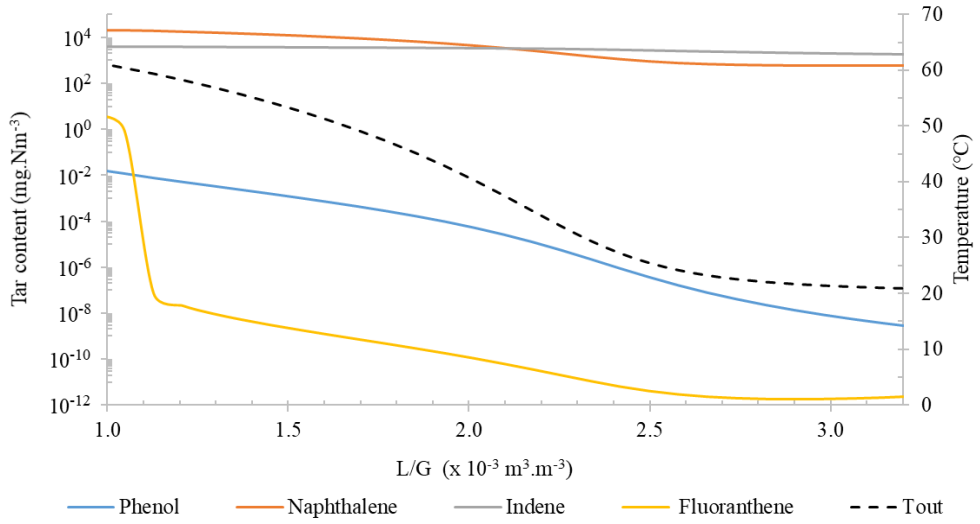

Figure 2-13: Variation of the remaining contents of phenol, naphthalene, indene and fluoranthene, and variation of the temperature of the gas stream leaving the second scrubber (stream 17), function of the L/G ratio in the absorber, for a water temperature of 20°C.

Figure 2-14 illustrates the variation of the remaining benzene and toluene content in the producer gas leaving both the collector and the absorber, function of the L/G ratio, while fixing the scrubbing liquid temperature to 25°C and 20°C in the collector and in the absorber, respectively. It can be observed that the benzene and toluene contents are slightly affected by the L/G ratio. Benzene and toluene contents are respectively reduced in the collector by 0.43% and 0.66%, for a L/G ratio of $1.65x10^{-3}$ $m^3.m^{-3}$. In the absorber, benzene and toluene contents are respectively reduced by 1.58% and 2.95%, for a L/G ratio of $3.22x10^{-3}$ $m^3.m^{-3}$.

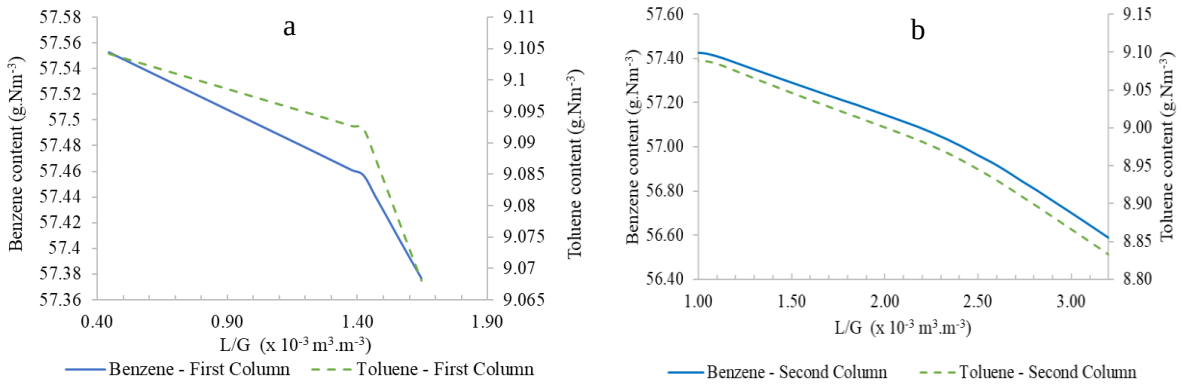

Figure 2-14: Variation of the benzene and toluene contents remaining in the gas phase, function of the L/G ratio in the collector for a temperature of 25°C (a) and in the absorber for a temperature of 20°C (b).

2.3.2. Water temperature

In the third sensitivity study, the impact of the scrubbing liquid temperature variation on the remaining tar content is studied in the absorber. The L/G ratios in the collector and in the absorber are set to 0.89 $x10^{-3}$ $m^3.m^{-3}$ and $2.57x10^{-3}$ $m^3.m^{-3}$, respectively. The temperature of the water fed to the collector is set to 25°C.

Figure 2-15 illustrates the temperature variation of the producer gas leaving the absorber (stream 17) and the remaining content of phenol, naphthalene, indene and fluoranthene in this stream, function of the scrubbing liquid temperature entering the absorber, for a L/G ratio of $2.57x10^{-3}$ $m^3.m^{-3}$. The tar content variation is presented on a logarithmic scale.

It can be observed in Figure 2-15 that, by reducing the scrubbing liquid temperature, the remaining tar content in the producer gas decreases, and therefore the tar removal efficiency increases. In particular, the majority of phenol is removed in the first scrubber. Therefore, its content is low even at high scrubbing liquid temperatures. The naphthalene content is constant for scrubbing liquid temperatures higher than 50°C. As the scrubbing liquid temperature decreases and becomes lower than 50°C, the naphthalene content sharply decreases from 20746 $mg.Nm^{-3}$ to 43 $mg.Nm^{-3}$ for a scrubbing liquid temperature of 5°C. Therefore, the naphthalene content is reduced by 99.79%. It can be seen that the variation of the scrubbing liquid temperature has a higher impact than the variation of the L/G ratio, on the indene content. In other words, indene content is reduced by 88.84% for a water temperature of 5°C. For water temperatures higher than 25°C, indene content is slightly affected. More precisely, it is reduced from 4003 $mg.Nm^{-3}$ to 3053 $mg.Nm^{-3}$ for a temperature of 25°C. Below this temperature, the indene content starts to highly decrease until reaching 450 $mg.Nm^{-3}$ for a temperature of 5°C. The fluoranthene content decreases with the scrubbing liquid temperature and reaches zero for temperatures lower than 50°C. The temperature of the producer gas leaving the collector is also affected by the

scrubbing liquid temperature. The temperature of the producer gas is reduced from 72°C at the absorber inlet to 68°C at the absorber exit, for a scrubbing liquid temperature of 64°C. By reducing the scrubbing liquid temperature to 5°C, the temperature of the producer gas leaving the collector is reduced to 5.8°C.

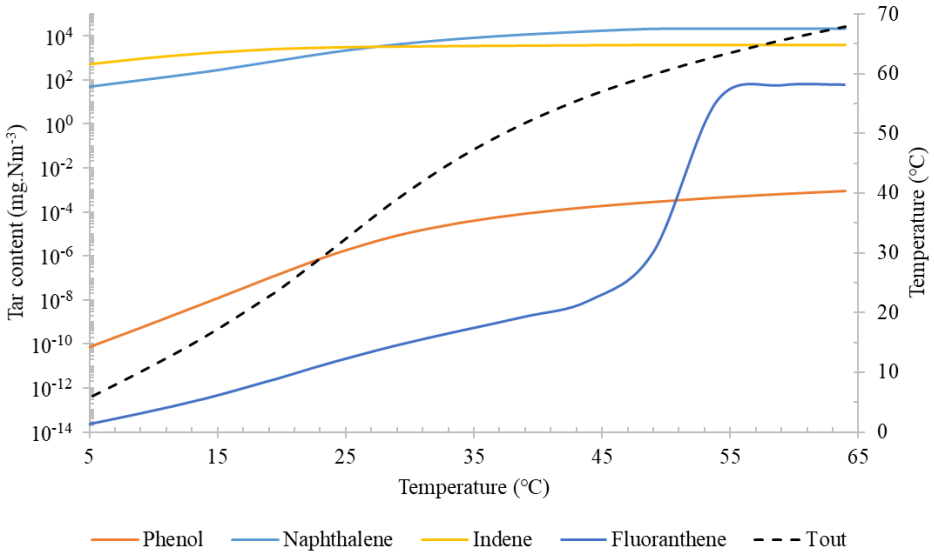

Figure 2-15: Variation of the remaining content of phenol, naphthalene, indene and fluoranthene, and variation of the temperature of the gas stream leaving the second scrubber (stream 17), function of the water temperature, for a L/G ratio of 2.57x10^{-3} m^3.m^{-3}.

Figure 2-16 illustrates the variation of the remaining contents of benzene and toluene in the producer gas after the absorber, function of the scrubbing liquid temperature, for a L/G ratio of 2.57x10^{-3} m^3.m^{-3}. Similar to the L/G ratio, it can be observed in Figure 2-16 that the benzene and toluene contents are slightly affected by the water temperature. The benzene and toluene contents are respectively reduced by 0.35% and 0.26%, for a scrubbing liquid temperature of 64°C. By reducing the scrubbing liquid temperature to 5°C, the removal efficiencies of benzene and toluene increase to 1.85% and 3.88%, respectively.

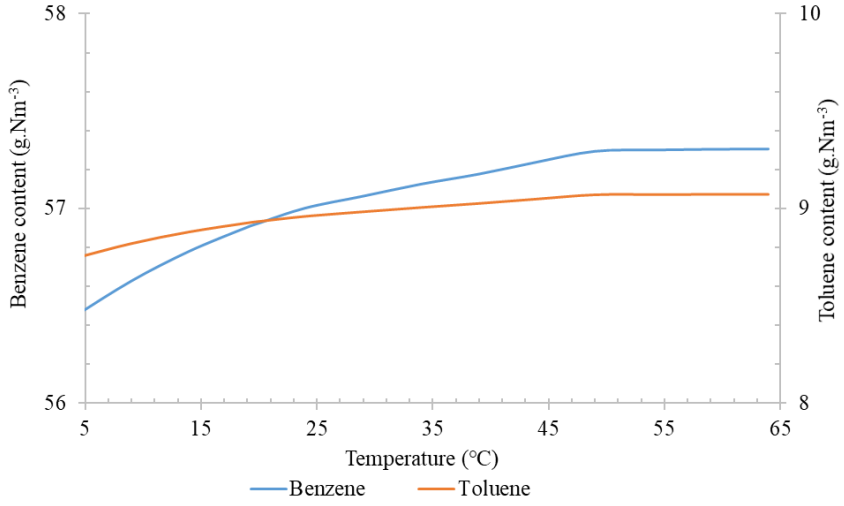

Figure 2-16: Variation of the benzene and toluene contents remaining in the gas phase, function of the scrubbing liquid temperature after the absorber, for a L/G ratio of 2.57x10^{-3} m^3.m^{-3}.

2.3.3. Results analysis

The optimal operating conditions for water scrubbers can be then selected based on the developed sensitivity studies. For the first scrubber (collector), a L/G ratio of $1.60x10^{-3}$ $m^3.m^{-3}$ and a temperature of 30°C, are selected. The selected temperature is almost equal to the ambient temperature. This eliminates the need of additional refrigeration used to reduce the water temperature to below the ambient temperature, and thus reduces the cost. In addition, it was previously deduced that, for an efficient tar removal, the L/G ratio should be higher than $1.45x10^{-3}$ $m^3.m^{-3}$. However, the operational cost increases with the increase of the L/G ratio. Therefore, the best compromise is to select a slightly higher L/G ratio. Moving to the second scrubber (absorber), the L/G ratio is set to $3.06x10^{-3}$ $m^3.m^{-3}$, while the water temperature is set to 5°C. A temperature of 5°C is selected to avoid any potential formation of solid benzene in the absorber. Note that this low temperature was selected since it can be noticed from Figure 2-15 that the tar removal efficiency highly increases for scrubbing liquid temperatures lower than 15°C. Therefore, the scrubbing liquid cooling and refrigeration requirements are compensated by the higher tar removal efficiency. Moreover, a critical point to consider is the removal of the excess of steam present in the producer gas within the absorber. This highly reduces the energy required in the low temperature process for the remaining tar condensation. Finally, it was deduced that, for an efficient tar removal, a L/G ratio higher than $2.58x10^{-3}$ $m^3.m^{-3}$ is required. Consequently, a ratio of 3.06 $x10^{-3}$ $m^3.m^{-3}$ is selected to compromise between the operational cost and the tar removal efficiency. Table 2-5 summarizes the optimal operating conditions selected for each scrubbing liquid. The operational cost analysis will be detailed in Chapter 4.

Table 2-5: The selected optimal operating conditions for methyl-oleate and water scrubbers.

	Methyl-oleate		Water	
	Collector	Absorber	Collector	Absorber
L/G $(\times 10^{-3}\ m^3/m^{-3})$	0.56	1.82	1.60	3.06
$T_{scrubbing\ liquid}$ (°C)	25	60	30	5

A comparison between the elementary tar removal efficiencies obtained using methyl-oleate (studied in section 1.5.2.2) and water as scrubbing liquids, is illustrated in Figure 2-17.

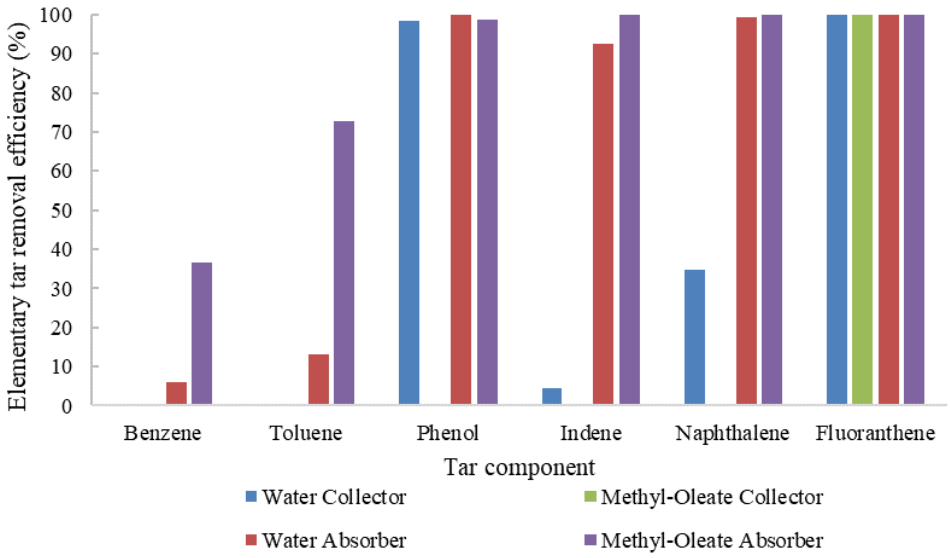

Figure 2-17: Comparison between the elementary tar removal efficiencies obtained by using methyl-oleate and water as scrubbing mediums, in the collector and the absorber.

This comparison, based on the obtained simulation results, includes the elementary tar removal efficiency in the collector and the absorber. Starting with the collector, benzene and toluene contents are slightly affected by both methyl-oleate and water. Due to its solubility in water, phenol content is highly reduced in the collector operating with water as a scrubbing medium. In contrary, the phenol content is not affected when methyl-oleate is used as a scrubbing liquid in the collector. Indene is slightly affected for both scrubbing liquids. However, its removal efficiency is higher when operating with water as a scrubbing liquid. The naphthalene content is reduced by 35% when operating at the selected optimal conditions in the water-based collector. On the contrary, the naphthalene content remains intact when operating with methyl-oleate. Finally, the fluoranthene content is almost totally removed for both scrubbing liquids.

Operating with water as a scrubbing liquid results in a higher tar removal efficiency in the collector. The main reason is that, when operating with water, no limitations are imposed on the water temperature. Therefore, the temperature difference, which is the main driving force in the collector, is higher when water is used as a scrubbing liquid. The total tar removal efficiency in the collector is equal to 9.8% and 15.24% for methyl-oleate and water, respectively.

Moving to the absorber, benzene and toluene removal efficiencies are higher when methyl-oleate is used as a scrubbing liquid. Since phenol is water soluble, its removal efficiency is slightly higher if water is used in the absorber instead of methyl-oleate. On the contrary, operating with methyl-oleate yields an indene removal efficiency higher by 7% than that obtained in the case of water. The naphthalene removal efficiency is almost similar for both scrubbing liquids. Finally, the remaining fraction of fluoranthene is totally removed for both scrubbing liquids. The total tar removal efficiency in the absorber is equal to 55.07% and 26.60% for methyl-oleate and water, respectively. In summary, the overall tar removal efficiency for both scrubbers, at the optimal operating conditions, is equal to 66% and 44.6% for methyl-oleate and water, respectively. Benzene and toluene are the main two components that remain in the producer gas after the scrubbers. Although methyl-oleate results in a higher tar removal efficiency, the use of water is more advantageous for the low temperature tar removal where benzene and toluene can be valorized.

Table 2-6 presents the producer gas temperatures and compositions at the exit of the water-based collector (stream 16) and at the exit of the water-based absorber (stream 17), for the selected optimal operating conditions. It can be seen that the moisture content is reduced by 48.5%, in the collector. However, the moisture content in the producer gas remains high and requires additional reduction. Reducing the producer gas temperature to 5.2°C, in the absorber, results in an overall moisture reduction of 98.12%.

Table 2-7 presents the tar content on a dry basis at the inlet of the collector, at the exit of the collector and at the exit of the absorber, that are characterized by streams 15, 16 and 17, respectively. It can be observed that, at optimal operating conditions, class 2 and class 5, that are respectively represented by phenol and fluoranthene, are totally removed in the water scrubbers. In addition, 98.6% of the tar components of class 4 (indene and naphthalene) is removed within the water scrubbers. The remaining content of indene and naphthalene only forms 0.6% of the total remaining tar content in the producer gas. Benzene and toluene, that represent class 3, are the major components remaining in the producer gas. Therefore, the low temperature process targets the removal of the class 3 components, by simultaneous deposition and condensation.

Table 2-6: Producer gas mass composition after the water-based collector and absorber, at the selected optimal operating conditions.

	Stream 16	Stream 17
Temperature (°C)	59	5.2
Component	Mass fraction	
Hydrogen (H_2)	0.0304	0.0376
Carbon Monoxide (CO)	0.2527	0.3106
Carbone Dioxide (CO_2)	0.3306	0.4074
Methane (CH_4)	0.0524	0.0648
Ethylene (C_2H_4)	0.0244	0.0301
Nitrogen (N_2)	0.0563	0.0694
Water (H_2O)	0.1686	0.0076
Benzene (C_6H_6)	0.0538	0.0629
Toluene (C_7H_8)	0.0086	0.0092
Indene (C_9H_8)	0.0037	0.0003
Phenol (C_6H_6O)	$3.3x10^{-5}$	$1.7x10^{-19}$
Naphthalene ($C_{10}H_8$)	0.0185	0.0001
Fluoranthene ($C_{16}H_{10}$)	$5.5x10^{-8}$	$1.0x10^{-20}$
Total	1	1

Table 2-7: Content of the tar representative components in the different producer gas streams.

Tar Component	Tar content $mg.Nm^{-3}$		
	Stream 15	Stream 16	Stream 17
Benzene (C_6H_6)	57223	57074	53823
Toluene (C_7H_8)	9193	9031	7881
Indene (C_9H_8)	4192	3954	277
Phenol (C_6H_6O)	1795	35	0
Naphthalene ($C_{10}H_8$)	21968	19672	78
Fluoranthene ($C_{16}H_{10}$)	5628	0	0
Total	100000	89765	62058

2.3.4. Regeneration of the scrubbing liquid

The scrubbing liquid leaving the absorber is charged with tar components. This stream must be regenerated in the last column. In order to do so, a counter-current steam flows in the last column at a high temperature. Several values for the steam mass flow rate and the steam temperature are considered. For the selected optimal operating conditions in the water scrubbers, the best results in the regenerator were obtained for a steam mass flow rate of 10000 $kg.h^{-1}$ and at a temperature of 200°C (stream 23). At those operating conditions, most of the tar components were recuperated in the steam flow leaving the regenerator (stream 24), and the clean water stream leaving the regenerator (stream 14) can be reinjected into the second absorption column. Table 2-8 summarizes the composition of the different streams entering and leaving the regeneration column.

Table 2-8: Temperature and composition of the streams entering and leaving the regeneration column.

	Flux 21	Flux 24	Flux 14
Temperature (°C)	80	99.60	99.65
Component	$\boldsymbol{Mass\ flow\ rate\ (kg.h^{-1})}$		
Water (H_2O)	20229.83	10063.00	20167.39
Hydrogen (H_2)	0.069	0.069	$9.75x10^{-21}$
Carbon monoxide (CO)	4.90	4.90	$3.30x10^{-15}$
Carbon dioxide (CO_2)	3.17	3.17	$2.25x10^{-17}$
Methane (CH_4)	0.19	0.19	$5.76x10^{-20}$
Ethylene (C_2H_4)	0.19	0.19	$1.31x10^{-18}$
Nitrogen (N_2)	0.90	0.89	$3.24x10^{-16}$
Benzene (C_6H_6)	5.37	5.37	$2.73x10^{-15}$
Toluene (C_7H_8)	1.80	1.80	$1.79x10^{-16}$
Indene (C_9H_8)	12.9	12.9	$7.66x10^{-15}$
Phenol (C_6H_6O)	0.60	0.38	0.22
Naphthalene ($C_{10}H_8$)	74.8	74.8	$6.31x10^{-13}$
Fluoranthene ($C_{16}H_{10}$)	0.24	0.24	$4.46x10^{-15}$
Total	20335.00	10167.96	20167.61

2.4. Phase distribution function of temperature

In order to study the condensation behavior of the tar components, it is necessary to study the phase distribution between liquid and solid, in the condensate phase. The phase distribution of the condensate is studied function of the temperature.

Figure 2-18 shows the component distribution plotted using the previously drawn saturation curves, function of the gas temperature. The condensed mass of each component is calculated, according to eq. (2-9), by subtracting the remaining mass of the tar component in the gas phase at temperature T_1 ($m_{sat,T1}$) from its remaining mass at a lower temperature T_2 ($m_{sat,T2}$), based on the saturation curves. The difference between those two temperatures is set to 1°C.

$$m_{condensed} = m_{sat,T1} - m_{sat,T2} \quad (2\text{-}9)$$

It can be seen from Figure 2-18 that the remaining content of phenol, indene, naphthalene and fluoranthene, is too low and does not have an impact on the condensable phase formation. The main components to be studied in the next section are then benzene, toluene and water.

Figure 2-19 illustrates the different tar representative components that undergo a solid deposition depending on the gas temperature. For instance, at temperatures lower than -1.45°C and higher than -94.97°C, toluene is the only component that condenses in a liquid form. All the remaining components condensate in the solid state.

Figure 2-20 shows the phase distribution function of the gas temperature rather than the cold surface temperature. The gas temperature will be equal to the cold surface temperature after a certain time of operation or for high heat transfer areas, thus the distribution of the phases is a theoretical representation. Therefore, Figure 2-20 reflects an idea on the percentage of the phase distribution while taking into consideration the ice formation. The latter is based on the normal boiling and

freezing points presented in Table 2-1. The solid phase is formed from the components having a freezing point higher than the gas temperature. The opposite case occurs for the liquid phase.

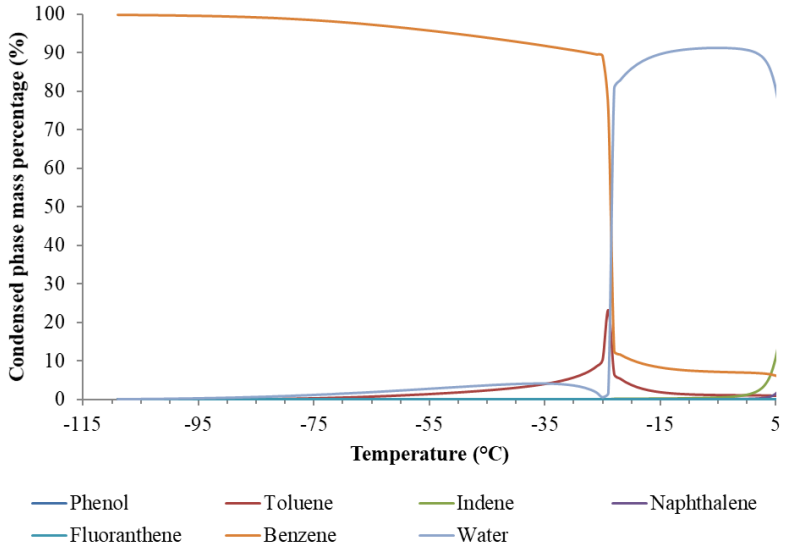

Figure 2-18: Variation of the mass percentage of the condensable components (tars and water) in the condensate, function of the gas temperature.

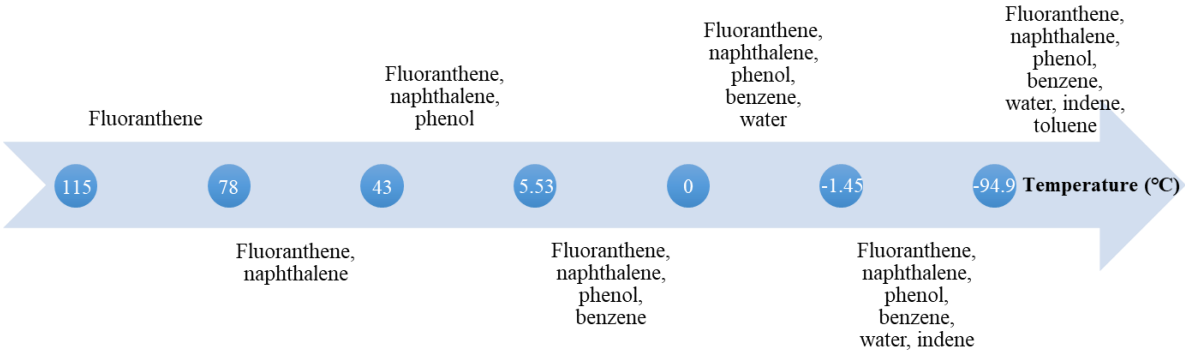

Figure 2-19: Freezing temperature for each tar component.

As a result, the solid phase will always be the dominant one. The liquid phase is only dominant above 0°C while the cold surface temperature will always be lower. This means that the water vapor will form a frost layer and not a liquid film. The liquid high fraction encountered at a temperature of -23°C in Figure 2-20, represents the beginning of toluene condensation for the inlet content. The co-existence of solid and liquid phases in the condensate starts with the condensation of toluene, and becomes negligible for temperatures lower than -55°C. To reach a final tar content of 1 mg.Nm^{-3}, the gas temperature should be reduced to -110°C.

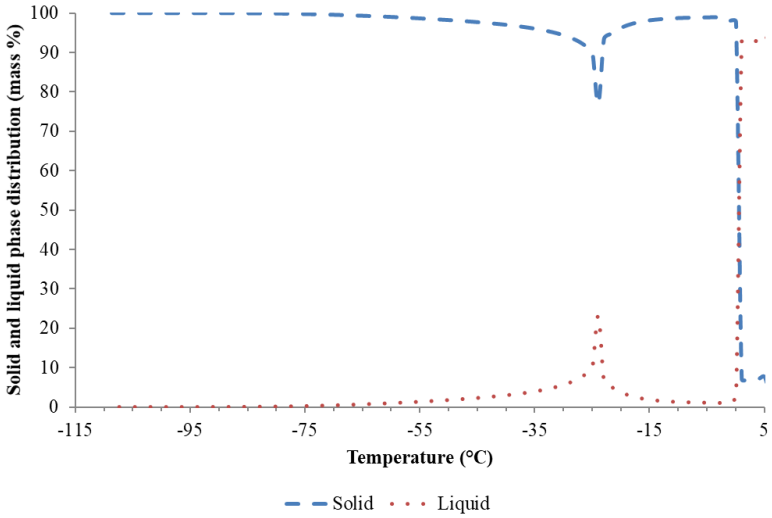

Figure 2-20: Variation of the phase distribution in the condensed phase, function of the gas temperature.

2.5. Conclusion

In this chapter, four different producer gas compositions are studied to check their impact on tar deposition. Besides water, this study involves the calculation of the dew point of several other components, that are fluoranthene, naphthalene, indene, phenol, toluene and benzene. Each component is separately studied in the producer gas. The dew point is calculated for tar concentrations ranging between 0.001 and 100 $g.Nm^{-3}$. Psychrometric charts are plotted for the gas composition of the dual fluidized bed gasifier to represent gas stream thermodynamic properties variations during tar capture, by applying low temperatures. It can be noticed that the presence of moisture in the producer gas highly increases the required energy for tar removal, at temperatures lower than the water dew point. Therefore, the removal of water vapor present in the producer gas is a key factor in reducing the energetic demand, in the low temperature process. For this reason, water scrubbers are suggested for the simultaneous removal of water vapor and tar. If benzene and toluene are excluded from the calculation, the tar content is reduced by 45.02% in the first scrubber and then by 98.01% in the second one, for a L/G ratio of $3.06x10^{-3}$ $m^3.m^{-3}$ and a temperature of 5°C. Phenol and fluoranthene are mainly removed in the first scrubber, since phenol is water-soluble and fluoranthene is the heaviest tar component. Naphthalene content is partially reduced in the first scrubber. The remaining naphthalene content is then reduced in the second one. Indene content is mainly reduced in the second scrubber. The benzene and toluene contents are slightly affected. As for the water vapor content, a reduction of 98.12% is achieved for a producer gas temperature of 5.2°C. Moreover, it can be seen from the psychrometric charts that the removal of benzene and toluene requires very low temperatures. Therefore, a novel method for tar removal based on the simultaneous condensation/deposition of the remaining tar content is proposed. The composition of tars that will be treated in the next chapter by the low temperature process, is known and it is formed of benzene and toluene. In addition to those two components, water vapor remaining in the gas phase after the scrubber will also condense, leading to the formation of an additional frost layer. Many studies have handled the mechanism of frost formation and of condensation but separately. Most of these studies cover the deposition of water vapor present in the moist air for domestic or industrial applications, while none of them covers organic compounds, such as tar components. Simultaneous heat and mass transfer takes place during frost deposition and condensation. The formation of frost layers limits the heat transfer due to its high thermal resistivity. The multi-phase deposition process is explained and the equations governing the heat and mass transfer are applied for each sub-domain.

Chapitre 2 : Equilibre entre phases pour les mélanges de goudron-gaz produit et colonnes d'absorption à base d'eau pour l'élimination de la fraction lourde de goudron.

1. Introduction

On peut déduire du premier chapitre que les plus grandes efficacités d'élimination du goudron sont obtenues en combinant au moins deux unités opérationnelles. L'objectif de la première unité consiste à éliminer la fraction lourde des HAP. La seconde unité assure un rôle complémentaire en réduisant la teneur de la fraction légère de goudron qui inclut les composants BTX. La première unité est assimilée à une étape de prétraitement qui augmente la durée de vie de la deuxième étape et réduit son coût. On peut également constater que la réduction de la teneur en goudron, dans la plupart des cas, est insuffisante pour combiner la gazéification et la méthanation. En se basant sur ce principe, la conception d'un procédé à basse température pour l'élimination du goudron a été suggérée. Opérer à basse température, assure la condensation et le dépôt de goudron en refroidissant le gaz produit à une température inférieure au point de rosée de goudron pour une concentration de 1 $mg.Nm^{-3}$.

Plusieurs unités de traitement de goudron et plusieurs configurations sont possibles. Le gaz produit est introduit dans la première unité à une température proche de 350°C, avec une teneur initiale en goudron de 100 $g.Nm^{-3}$. La première unité sert à refroidir le gaz produit à une température proche de l'ambiante, et à réduire sa teneur en goudron. La première unité du processus de traitement du goudron suggéré peut être une colonne d'absorption conventionnelle ou un lit à filtration classique. L'efficacité d'élimination de goudron est étudiée pour des colonnes d'absorption utilisant l'huile et l'eau comme agent de lavage. Le gaz produit est ensuite soumis à un refroidissement complémentaire dans la deuxième unité de traitement. On désigne cette dernière par l'unité à basse température, puisqu'elle exige des températures plus basses que l'ambiante pour atteindre une teneur en goudron inférieure à 1 $mg.Nm^{-3}$, en fin de processus. L'élimination du goudron dans la deuxième unité se fait par transfert de chaleur par contact indirect où la condensation et le dépôt simultanés ont lieu sur des surfaces froides.

2. Equilibre entre phases pour les mélanges de composants de goudron - gaz produit

Afin d'analyser le comportement de condensation des composants de goudron à basse température et d'évaluer l'énergie nécessaire pour condenser les composants de goudron, des diagrammes psychrométriques pour ces derniers dans le gaz produit sont construits. Aspen Properties V10 a été utilisé pour trouver la composition d'équilibre entre phases à saturation, ainsi que pour évaluer l'impact des compositions de mélanges gazeux à différentes températures sur l'équilibre entre phases. Des équations sont développées pour calculer l'enthalpie des mélanges et les courbes de concentration relative constante. Les diagrammes psychrométriques sont utilisés pour illustrer la teneur de goudron dans le gaz produit à différentes températures et l'énergie requise pour condenser le goudron à différentes concentrations.

2.1. Hypothèses et méthodologie

2.1.1. Composants représentatifs du goudron

Le goudron étant un mélange complexe, certains composants de goudron sont sélectionnés comme composants représentatifs pour lesquels des diagrammes psychrométriques sont tracés séparément. Les critères de sélection des composants représentatifs du goudron sont :

- le composant le plus léger de chaque classe doit être sélectionné, le reste des composants de la même classe est supposé se condenser à des températures plus élevées.
- la fraction du composant ne doit pas être négligeable.

En se basant sur les critères de sélection, on peut déduire à partir des propriétés physiques des composants du goudron que les composants représentatifs sont le phénol pour la classe 2, le benzène et le toluène pour la classe 3, l'indène et le naphtalène pour la classe 4 et le fluoranthene pour la classe 5. Le benzène et le toluène sont considérés car ils sont des composants majeurs. La sélection de l'indène et le naphtalène de la classe 4 relève du fait que l'indène est le composant le plus léger de cette classe, tandis que le naphtalène est présent en quantité importante et il est considéré comme un composant représentatif du goudron dans plusieurs études [30,47,69].

2.1.2. Courbes de saturation et de concentration relative

Les points de la courbe de saturation sont d'abord calculés pour chaque composant représentatif du goudron. La courbe de saturation, qui correspond à la courbe liquide-vapeur au-dessus du point triple et à la courbe solide-vapeur au-dessous de ce point, représente la limite à laquelle commence la condensation ou la déposition du goudron contenu dans le gaz produit. La fraction molaire en phase gazeuse (y_j) à une température T_i, est calculée afin de déterminer la quantité de goudron condensée, en utilisant une méthode de propriété définie dans Aspen Properties, où j représente les différents composants représentatifs de goudron. La quantité de goudron qui reste dans la phase gazeuse est calculée selon Eq. 2.1 pour ϕ=1, où w_j est la teneur en goudron en kg.kg^{-1} de gaz, qui est égal au rapport entre le poids de goudron (m_j) et le poids de gaz (m_{gaz}).

Les courbes de concentration relative constante de goudron (ϕ) sont ensuite tracées. ϕ est égal au rapport de la pression partielle de goudron dans le gaz (P_j) sur la pression partielle de goudron saturé à la même température (T_i). Afin de tracer ces courbes la quantité résiduelle de goudron dans la phase gazeuse est calculée selon Eq. 2.1 pour une ϕ allante de 0.1 à 0.9.

$$w_j = \frac{m_j}{m_{gaz}} = \frac{P_j(T_i)}{P_{total} - P_j(T_i)} \cdot \frac{M_j}{M_{gaz}} = \frac{\phi . y_j(T_i)}{1 - \phi . y_j(T_i)} \cdot \frac{M_j}{M_{gaz}} \qquad \textit{Eq. 2.1}$$

2.1.3. L'enthalpie spécifique de saturation et les lignes isenthalpiques

Premièrement, l'enthalpie de saturation est calculée selon Eq. 2.2. L'enthalpie du mélange gazeux est calculée par kilogramme de gaz. Le tracé des enthalpies de saturation en fonction de la température donne la ligne d'enthalpie de saturation.

$$\begin{aligned} h = C_{p,gaz} . \left(T_{DB} - T_{ref}\right) + w_j \left[h_{fg,j\ (25°C)} + C_{p,j,vap} . \left(T_{DP,j} - T_{ref}\right)\right] \\ + \ w_{wat} \left[h_{fg,wat\ (25°C)} + C_{p,wat,vap} . \left(T_{DP,wat} - T_{ref}\right)\right] \end{aligned} \qquad \textit{Eq. 2.2}$$

Ensuite, les lignes d'enthalpie constante, également appelées lignes isenthalpiques, sont tracées. Ces lignes sont utilisées afin de trouver l'enthalpie du mélange sous n'importe quelles conditions. Ils rejoignent plusieurs points ayant une enthalpie égale. Afin de trouver ces points, deux points sur la lignes d'enthalpie constante sont considérés. L'intersection entre la ligne horizontale de la teneur en goudron constante partante du premier point (dénotée point 2) et la ligne d'enthalpie constante partante du deuxième point (dénotée point 2), est dénotée point 3. On peut en déduire que h_1=h_3, $w_{j,2}$=$w_{j,3}$ et $w_{wat,2}$=$w_{wat,3}$. Résoudre Eq. 2.2 pour les 3 points résulte en Eq. 2.3. Cette dernière est résolue afin de trouver la température sèche du point 3 $(T_{DB,3})$.

$$h_3 - h_2 = C_{p,raw\ gas,3}.\left(T_{DB,3} - T_{ref}\right) - C_{p,raw\ gas,2}.\left(T_{DB,2} - T_{ref}\right) \qquad Eq.\ 2.3$$

2.2. Résultats et discussion

2.2.1. Equilibre solide-gaz

Les corrélations intégrées dans Aspen Properties ne tiennent pas compte de la condensation en phase solide et peuvent donner des résultats imprécis. Pour cette raison, les résultats obtenus par les simulations sont comparés à des données expérimentales publiées pour les composants suivants : fluoranthene [101], naphtalène [102], phénol [103] et benzène [104]. La comparaison montre un accord entre les résultats obtenus et les résultats tirés de la littérature. Par conséquent, les librairies intégrées dans Aspen Properties peuvent être utilisées afin de prédire la fraction du composant représentatif de goudron à des températures inférieures au point triple.

2.2.2. Point de rosée pour les composants représentatifs de goudron

Quatre compositions différentes de gaz produit sont étudiées afin d'analyser leur impact sur le point de rosée des composants du goudron. La variation principale dans la composition est la fraction molaire de la vapeur d'eau (H_2O) et d'azote (N_2). La gazéification à la vapeur d'eau, pour gazéifieur direct et indirect, donne un gaz produit à forte teneur en humidité (30 à 60 % mol à base humide), tandis que la gazéification à l'air donne un gaz produit à forte teneur en azote (40 à 60 % mol à base sèche).
Une comparaison entre le point de rosée calculé de ces composants pour les quatre différentes compositions considérées et ceux extraits de l'outil ECN [93] est effectuée. Cet outil permet de calculer le point de rosée d'un seul composant de goudron ou d'un mélange de composants de goudron. Il a été développé pour calculer la température à laquelle débute la condensation de goudron pour une teneur bien définie, exprimée en $g.Nm^{-3}$ sur base humide [94]. Les calculs sont effectués pour un seul composant de goudron à la fois. Les résultats ont montré qu'à l'exception du fluoranthene, le point de rosée des composants du goudron varie en fonction de la composition du gaz produit. La température de rosée du fluoranthene est la plus élevée, puisqu'il est le composant le plus lourd. La partie la plus importante du fluoranthene est éliminée par condensation avant d'atteindre le point de rosée de l'eau. Ce dernier dépend du taux d'humidité initial et il est compris entre 30°C et 70°C. Pour cela, la température de rosée du fluoranthene n'est pas affectée par la composition initiale du gaz produit.
Le point de rosée du naphtalène, de l'indène et du phénol diminue avec la teneur en humidité initiale, tandis que celui du toluène et du benzène diminue pour une teneur en humidité initiale plus élevée. Contrairement aux autres composants représentatifs du goudron, le toluène et le benzène forment des mélanges azéotropiques avec l'eau. Ceci explique leur comportement différent par rapport au reste des composants du goudron, concernant la variation de la teneur en humidité initiale présente dans le gaz produit.

On peut conclure que le point de rosée des composants représentatifs de goudron est plutôt affecté par la teneur en humidité initiale et par la condensation du vapeur présente dans le gaz produit, que par la composition des gaz non-condensables. Cependant, cette composition n'est pas définie pour l'outil en ligne. Dans la littérature, il est seulement mentionné que l'outil est basé sur un lit fluidisé bouillonnant atmosphérique, fonctionnant à 850°C et utilisant l'air comme agent oxydant. Tous ces facteurs augmentent l'écart entre les points de rosée calculés et ceux obtenus par l'outil de calcul du point de rosée en ligne.

2.2.3. Diagramme psychrométrique

Six diagrammes psychrométriques pour des mélanges de fluoranthene, naphtalène, indène, phénol, toluène et benzène – gaz produit sont tracés. Un des diagrammes psychrométrique pour le mélange toluène-gaz est illustré dans Fig. 2.1. Les calculs de cette section sont basés sur une composition de gaz

produit issue d'un gazéifieur DFB [98]. Une température autour de -110°C est alors requise afin d'obtenir un gaz ayant une teneur en goudron inférieure à 1 mg.Nm^{-3}. Il est à noter que la différence d'enthalpie, calculée entre deux points, est plus importante que celle calculée pour chaque point, puisqu'elle reflète l'énergie nécessaire pour condenser une certaine masse de goudron.
Pour une teneur de goudron initiale égale à 100 g.Nm^{-3}, la condensation d'eau et des composants représentatifs de goudron a lieu simultanément, à l'exception du composant le plus lourd (fluoranthene) et des composants les plus légers (toluène et benzène). La condensation du fluoranthene, du toluène, du benzène et de l'eau commence à une température de 203°C, -20°C, -30°C et 70°C, respectivement. En d'autres termes, le fluoranthene se condense avant l'eau, tandis que le toluène et le benzène se condensent après.

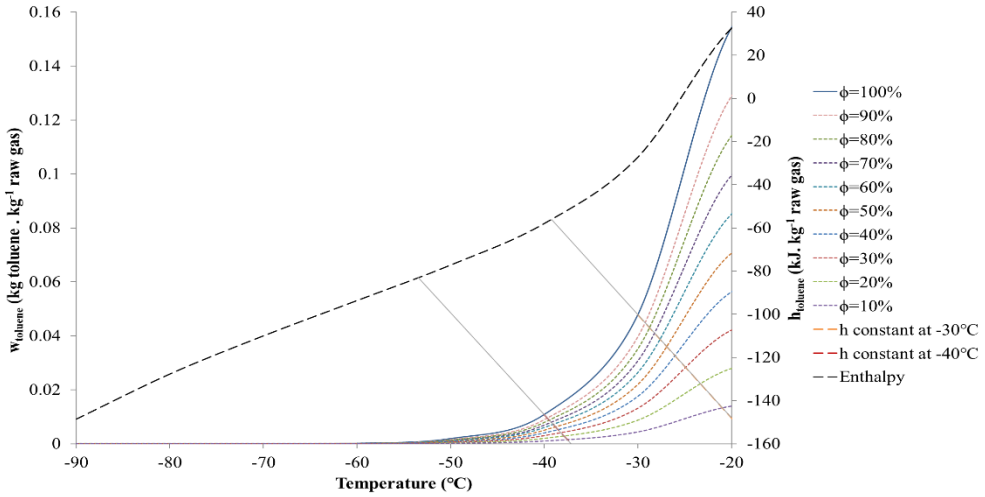

Fig. 2.1: Diagramme psychrométrique pour le mélange toluène-gaz produit.

3. Elimination de la fraction lourde de goudron par deux colonnes d'absorption à eau placés en série

Les méthodes existantes pour l'élimination de la fraction lourde de goudron sont efficaces, alors que plus d'attention devrait être accordée à l'élimination de la fraction la plus légère de goudron (benzène, toluène et xylène) [3,4,7]. Puisque ces derniers peuvent être valorisés, il est important de conserver leur teneur inchangée dans la première étape d'élimination de goudron tout en réduisant la température du gaz produit et la fraction lourde de goudron. A cette fin, une configuration constituée de deux colonnes d'absorption à eau est proposée.

De plus, les gazéifieurs DFB conduisent à un gaz produit ayant une teneur élevée en vapeur d'eau. Cela augmente le point de rosée de l'eau à environ 70°C. Ensuite, l'efficacité des colonnes d'absorption à l'huile diminue puisque la température d'opération sera limitée à 70°C. Par conséquent, l'eau est utilisée en tant qu'agent de lavage pour éviter de mélanger l'eau qui se condense du gaz produit avec l'huile de lavage. Ceci évite les restrictions imposées sur la température de la colonne d'absorption. De plus, l'eau est l'agent de lavage le moins cher et le plus disponible. De plus, une partie de l'eau utilisée pour le lavage peut être chauffée puis réutilisée comme agent de gazéification. Ceci enrichit la teneur en hydrogène du gaz produit et favorise la méthanation. Enfin, la condensation des composants de goudron les plus légers, valorisables dans le cas où ils sont condensés à basse température, est minimisée. En outre, les colonnes d'absorption à eau réduisent également la température, la concentration de vapeur d'eau et donc l'énergie requise dans les étapes froides.

Le procédé étudié est composé de deux colonnes d'absorption et d'une colonne de régénération. Le diagramme des opérations est illustré dans Fig. 2.2. Le gaz produit est introduit à la première colonne

d'absorption (collecteur) à une température égale à 350°C. Suite à son contact avec l'agent de lavage, la température du gaz produit diminue et la condensation des composants lourds de goudron se déroule. Une partie de l'agent de lavage est recyclée et réinjectée dans le gazéifieur, alors que la deuxième partie est re-refroidie à sa température initiale et recyclée vers la partie supérieure du collecteur. Ainsi, après un certain temps de fonctionnement, l'agent de lavage au niveau de la première colonne d'absorption se sature et agit sur l'élimination de goudron par condensation et non par absorption. Le gaz produit alimente ensuite la deuxième colonne, appelée absorbeur, dans laquelle la fraction légère de goudron est absorbée à travers l'agent de lavage, en appliquant différentes conditions opératoires. Le liquide de lavage utilisé dans la deuxième colonne est régénéré dans la troisième colonne, à l'aide d'air ou de vapeur d'eau. Après régénération, le liquide de lavage est recyclé vers la deuxième colonne d'absorption.

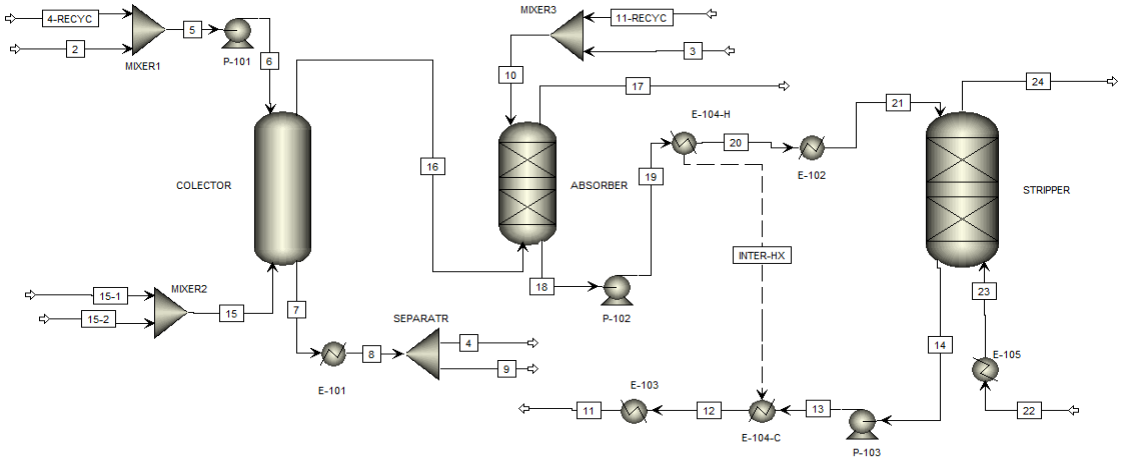

Fig. 2.2: Diagramme schématique du processus des colonnes d'absorption en série pour l'élimination de goudron, extrait d'Aspen Plus.

Afin de sélectionner les conditions opératoires optimales et d'évaluer leur impact sur l'efficacité d'élimination du goudron, trois études de sensibilité ont été développées.
La première étude évalue l'impact du débit d'eau, et donc du rapport L/G qui varie entre 0,45 $x10^{-3}$ $m^3.m^{-3}$ et 1,65$x10^{-3}$ $m^3.m^{-3}$, sur l'efficacité d'élimination de goudron, tout en fixant la température d'agent de lavage dans le collecteur à 25°C. En général, l'efficacité élémentaire d'élimination de goudron augmente en augmentant le ratio L/G. La concentration de phénol est considérément réduite même pour des faibles L/G. La concentration de naphtalène n'est pas affectée pour un L/G inférieur à 1,4$x10^{-3}$ $m^3.m^{-3}$. La concentration d'indène reste quasiment constante dans le collecteur. Alors que la concentration de fluoranthene devient pratiquement nulle pour des valeurs élevées de L/G. De plus, la concentration de benzène et celle de toluène restent inchangées. Finalement, la température du gaz produit diminue jusqu'à 53°C en augmentant L/G.

La deuxième étude évalue l'impact du débit d'eau, et donc du rapport L/G qui varie entre $1x10^{-3}$ $m^3.m^{-3}$ et 3,2$x10^{-3}$ $m^3.m^{-3}$, sur l'efficacité d'élimination de goudron, tout en fixant la température d'agent de lavage dans l'absorbeur à 20°C. Les concentrations de phénol et du fluoranthene sont totalement réduites. La concentration du naphtalène décroit notamment pour un L/G plus grand que 2,58$x10^{-3}$ $m^3.m^{-3}$. La concentration d'indène est réduite de 50% pour le plus important L/G. De plus, les concentrations du benzène et du toluène sont légèrement réduites dans l'absorbeur. Finalement, la température du gaz produit diminue jusqu'à 21°C en augmentant L/G.

La troisième étude évalue l'impact de la température d'eau, qui varie entre 5°C et 65°C, sur l'efficacité d'élimination de goudron, tout en fixant le ratio L/G dans l'absorbeur. En général, l'efficacité élémentaire d'élimination de goudron augmente en diminuant la température. La majorité de la concentration du

phénol est déjà réduite dans le collecteur. La concentration de naphtalène décroit notamment pour des températures inférieures à 50°C. La concentration du naphtalène est réduite de 99,78% à une température de 5°C. Pour cette même température, la concentration d'indène est réduite de 88,84%. La concentration du fluoranthene devient négligeable pour des température inférieures à 50°C. De plus, les concentrations de benzène et de toluène sont respectivement réduites de 1,85% et 3,88% pour une température d'eau égale à 5°C. Pour cette température, la température du gaz produit diminue à 6°C.
Des études paramétriques similaires sont complétées pour des colonnes d'absorption à l'huile assimilée à l'oléate de méthyle. Par la suite, les conditions opératoires sont choisies en se basant sur les études de sensibilités. Fig. 2.3 illustre une comparaison entre les efficacités élémentaires d'élimination de goudron obtenues en utilisant l'oléate de méthyle et l'eau comme agents de lavage, dans le collecteur et l'absorbeur.

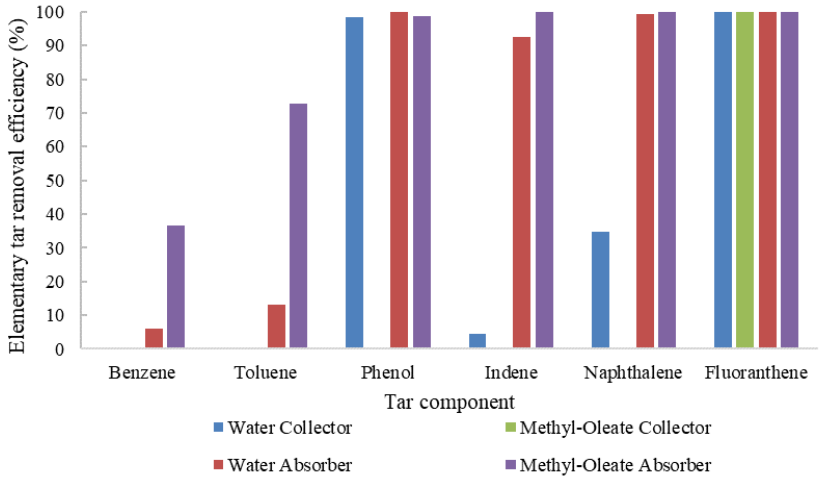

Fig. 2.3: Comparaison entre les efficacités élémentaires d'élimination de goudron obtenues en utilisant l'oléate de méthyle et l'eau comme agents de lavage, dans le collecteur et l'absorbeur.

En résumé, l'efficacité globale d'élimination du goudron pour les deux colonnes d'absorption, aux conditions d'opération optimales, est égale à 66 % et 44,6 % pour l'oléate de méthyle et l'eau, respectivement. Le benzène et le toluène sont les deux principaux composants qui restent dans le gaz produit après les colonnes d'absorption. Bien que l'oléate de méthyle a une efficacité d'élimination du goudron plus élevée, l'utilisation de l'eau est plus avantageuse pour l'élimination du goudron à basse température où le benzène et le toluène peuvent être valorisés. De plus, l'utilisation de l'eau mène à des températures de gaz et à des concentrations de vapeur d'eau restant dans le gaz, plus basses.

4. Distribution des phases en fonction de la température

Afin d'étudier le comportement de condensation et de déposition des composants représentatifs de goudron, la distribution des phases du condensat entre les phases liquide et solide, en fonction de la température est complétée. Fig. 2.4 présente les composants qui subissent une déposition solide en fonction des température de sublimation de chaque composant.

On peut déduire de la composition du gaz produit après les deux colonnes d'absorption que la teneur restante de phénol, indène, naphtalène et fluoranthene, est trop faible et n'affecte pas les propriétés de la phase condensable. Les principaux composants à étudier dans la section suivante sont alors le benzène, le toluène et l'eau.

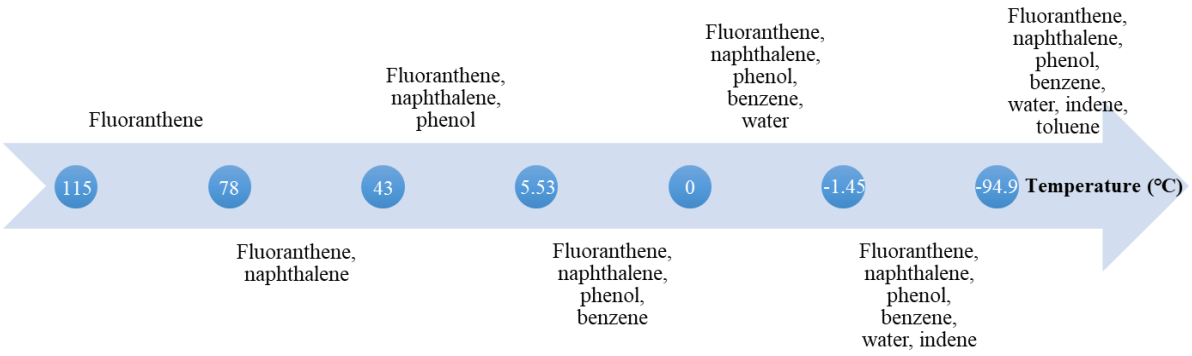

Fig. 2.4: Composants subissant un dépôt solide en fonction de la température.

La phase solide sera toujours dominante pour des températures inférieures à 0°C, alors que la température de surface froide sera toujours plus basse. Cela signifie que la vapeur d'eau forme une couche de givre et non pas un film liquide. Une fraction liquide élevée est rencontrée à une température de -23°C. Cette température représente le début de la condensation du toluène. La coexistence des phases solide et liquide dans le condensat débute avec la condensation du toluène, et devient négligeable pour des températures inférieures à -55°C. Pour atteindre une teneur finale en goudron de 1 mg.Nm^{-3}, la température du gaz doit être réduite à -110°C.

5. Conclusion

Des diagrammes psychrométriques ont été tracés pour la composition du gaz obtenue d'un gazéifieur à double lit fluidisé circulant, afin de représenter les variations des propriétés thermodynamiques du flux de gaz pendant la capture du goudron, en appliquant des basses températures. On peut remarquer que la présence d'humidité dans le gaz produit augmente fortement l'énergie requise pour l'élimination du goudron, à des températures inférieures au point de rosée de l'eau. Par conséquent, l'élimination de la vapeur d'eau présente dans le gaz produit, est un facteur clé dans la réduction de la demande énergétique, dans le procédé d'élimination de goudron à basses températures. Pour cette raison, des colonnes d'absorption à l'eau sont suggérés pour l'élimination simultanée de la vapeur d'eau et du goudron. De plus, les colonnes d'absorption diminuent la température du gaz produit.

Chapter 3 : Condensation of tars at low temperature over cold plates

Low temperatures are required to reduce the tar content to 1 mg.Nm^{-3}, as previously mentioned. This concentration is needed to ensure a proper operation of the SNG synthesis process. Based on the literature review (cf. Chapter 1), it can be deduced that several tar removal technologies exist. Each existing approach has its own advantages and disadvantages. However, at least two separate steps are required for an effective tar removal. Rabou and Van der Drift [105] mentioned that developing a cryogenic treatment for the removal of the remaining light fraction is important for certain gasification processes. This method allows the separation of BTX components from the producer gas and integrating them in the gasification process. The condensed phase can then be used as an additional heat source for the gasifier, or in a separate boiler as fuel. For this purpose, the producer gas is cooled by passing it over a cold surface, whose temperature is lower than that of the producer gas. This leads to a simultaneous multi-component frosting and condensation phenomenon. The multi-phase deposition process is explained in the first part. Then the equations governing the heat and mass transfer in the different sub-domains are presented. The proposed model is then validated by comparing it to published experimental studies. A parametric study is then completed in order to analyse the impact of the gas flow rate, the wall temperature and the surface dimensions on the frosting parameters including the gas temperature, the frost thickness and the frost density. Finally, several plates are placed in series, while selecting the optimal operating conditions, in order to reach the targeted limit of the tar content.

3.1. Model approach for tar and water condensation

Several surfaces are involved to condense the remaining fraction of tars and water until reaching a tar content of 1 mg.Nm^{-3} (mainly BTX components). The operating temperature of the cold surface is distributed according to the condensation stages and the condensate phases, described in the previous chapter. Note that it is important to define a geometry, at this stage. Different geometries can be considered, such as tubes or plates, for example. Since most of the previous studies were developed based on plate geometry, flat plates are considered in this thesis. This allows validating the proposed model for the tar removal by comparing it with previous experimental and simulated results.

To deal with the multi-component condensation issue and the required high energy, the cooling process is divided into several stages. This configuration reduces the number of components that are simultaneously treated, by dividing the problem into several steps. It also reduces the exergy destruction by reducing the temperature difference between the cold plate and the gas stream. As it can be seen from Figure 2-20, the optimal configuration consists in dividing the cooling process into four stages, at least. Figure 3-1 describes the configuration of tar and water vapor condensation/deposition.

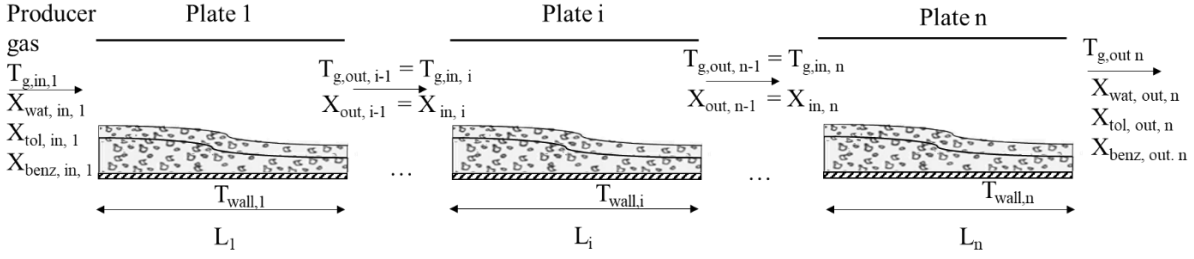

Figure 3-1: Cold plates placed in series, targeting the tar condensation.

In the first cooling stage, between 5°C and -23°C, simultaneous water vapor and benzene condensation takes place and it assumed that this leads to the formation of two separate frost layers. The second cooling stage, between -23°C and -60°C, is the most complex stage where simultaneous solid and liquid condensation takes place. The condensate is a mixture of ice, solid benzene and liquid toluene. Ice and solid benzene, which are assumed to form two separate frost layers, are treated as porous mediums, while the liquid toluene is assumed to fill a part of the frost layers' pores. In the third cooling stage, ranging between -60°C and -94.97°C, the fraction of liquid toluene in the condensate phase becomes negligible. In the last cooling stage, which corresponds to temperatures lower than -94.97°C, all the three components undergo a solid deposition. However, benzene is the dominant component. All the described phenomena will be detailed in the next section.

3.2. Tar deposition modelling

As mentioned in the previous section, the objective of cooling the producer gas to reach -110°C, is to condense tars that remain in the gas phase. More precisely, the benzene, the toluene, and a small amount of water. In order to assess the condensation behavior of those components, an exhaustive frosting study was conducted.

Several studies tackled the mechanism of frost formation. However, most of these studies cover the deposition of water vapor present in the moist air, for many domestic or industrial applications. Frost deposition is mainly encountered in refrigeration, cryogenics and aerospace applications. Gas purification by freezing, refrigerators, gas coolers and cryogenic liquid storage, are the main processes were simultaneous frost formation and heat transfer take place [106]. Although numerous studies tackled the frost formation, few of them covers the organic compounds, such as tar components, for example.

Some previous studies analyze the frosting of benzene over cold surfaces. For instance, Ueda and Takashima [107] have studied the frosting of benzene from C_6H_6-N_2 and C_6H_6-He mixtures on the external surface of a cylindrical tube. However, their study was based on high values of initial condensable content and on low total pressure. The initial benzene mass fraction varies between 0.86 and 0.93. In addition, the total pressure varies between 3.51 and 9.71 mmHg. This is not case of this thesis, where the initial benzene mass fraction is equal to 0.0462.

Another study completed by Hendry [108] analyses the nucleation of benzene during its abatement by cryogenic condensation. According to his model, developed on CFD, he deduced that 97% of benzene is captured by cryogenic condensation, with around 1% escaping as particulates. Therefore, we can deduce that the nucleation phenomenon does not have an important impact of the benzene removal by cryogenic condensation and thus the nucleation phenomenon is not included in the mathematical model.

The formation of a frost layer limits the heat transfer due to its high thermal resistivity. Therefore, in order to study the purification of the producer gas by freezing out the remaining tar components, it is important to understand the simultaneous heat and mass transfer during the frost growth.

Hayashi et al. [109] were among the first to study the frost growth process while dividing it into three different periods; the "crystal growth", the "frost layer growth" and the "frost layer full growth" periods.

The crystal growth period is relatively short in time with respect to the whole frost formation process. During the first moments, the frost layer is considered as frost columns rather than a porous medium. There will be no significant increase in the frost thickness. Thus, in this stage, the convective heat and mass transfer are more important than the diffusion through the frost layer. Due to its short duration and its complexity, this early stage is not usually modeled when assessing the frost growth process. In order

to consider the impact of this period on the frost growth, appropriate initial conditions, for the frost thickness and frost density, should be considered [110].

In the frost layer growth period, the frost growth takes place in the form of a porous structure. The latter consists of ice or solid benzene containing gaps filled by the producer gas, as in the case of our system. During this period, the producer gas that comes in contact with the cold surface, is cooled by convection. When the dew point of the condensable components is reached, the deposition begins and simultaneously increases the thickness and the density of the frost. Note that, the most studied period is that of the frost layer growth.

Finally, the fully developed or the frost layer full growth period starts when the surface temperature of the frost layer reaches the melting point of the condensable components. At this point, the condensed vapor starts to melt and soak into the porous frost layer, where it gradually freezes due to the temperature gradient. This generates a cyclic process that stops with the frost densification, and when reaching the thermal equilibrium.

Existing frost growth models can be generally divided into different groups, according to several criteria [110,111]. The first group includes the models that are based on empirical correlations [109,112,113]. These models are limited to simple defined geometries and they can only be used in the range of the operating conditions (i.e. validity of correlations) [111]. Empirical models yield reasonable results unless used outside the range of the operating conditions or for geometries other than the defined ones. Frost thickness and frost density are the two main properties that are predicted using empirical correlations. Hermes et al. [112] and Hayashi et al. [109] respectively developed semi-empirical and empirical correlations, for the prediction of the frost density.

The second group [110,114–116] consists in the analytical models that avoid the use of empirical correlations, and develop mathematical models based on heat and mass transfer in air and frost domains. This group treats the frost as a porous solid, while taking into consideration the diffusion of the gas through the pores. Most of this group approaches consider a one-dimensional frost growth. They can also be applied for wider ranges of operating conditions and geometries other than those of the first group.

The third group [117–120] is based on Computational Fluid Dynamic (CFD) models. CFD-based models allow the development of two-dimensional frost growth solutions, leading to a better agreement between experimental and simulated results.

In all the frost growth models, several parameters are similarly treated, such as the water vapor content calculation, for example. Most of the literature review methods [106,114,119,121] that tackle the water vapor frosting in humid air, consider that the water vapor is saturated at the solid-vapor interface and inside the frost. In contrast, Na and Webb [115,122] considered that the water vapor is supersaturated at the frost surface, which increases the accuracy of the model.

Besides the saturation condition, several researches focused on assessing the impact of the different coefficients, used in the heat and mass transfer equations, on the results [111,123]. The main coefficients that affect the results are the effective thermal conductivity, the effective diffusion coefficient and the heat and mass transfer coefficients. These coefficients will be detailed in the sequel.

In addition to the two frost layers, the tackled tar condensation needs to take into account the simultaneous toluene liquid condensation, rather than a solid-gas phase, as in other cases. Previous studies on the vapor condensation, in presence of non-condensable gases, have divided the liquid

condensation into filmwise and dropwise condensations [124,125]. Several studies on the condensation over a porous media were also developed [126,127]. For instance, the filmwise condensation (FWC), which forms a continuous liquid film on the cold surface, is the most known and industrially used condensation mode. The dropwise condensation (DWC) results in a higher heat transfer coefficient than FWC. DWC is hard to maintain for a long duration in heat exchangers [128]. In several previous studies, the condensation film resistance was neglected since its contribution in the total film resistance is limited to 1-3% [129,130]. In this thesis, the condensation of toluene takes place over the frost, which is a porous media. Therefore, the impact of the liquid formation is integrated in the effective thermal conductivity. The volume of the condensed toluene is calculated. If the liquid volume is smaller than the volume of the frost layers pores, the liquid toluene is assumed to fill a part of those pores. Otherwise, an additional liquid layer will be formed at the surface.

The well-known Chilton–Colburn analogy [131] is the most widely used analogy for heat, mass and momentum transfer. Therefore, it is also used in this thesis to study the liquid condensation of toluene, and thus to predict the mass transfer coefficient [129,130]. This allows the computation of the latent heat of toluene condensation and its integration in the model.

All the mentioned frost growth models of the literature target water vapor frosting and liquid condensation. However, models that simultaneously deal with water vapor frosting, organic component frosting and liquid condensation, do not exist. This thesis aims the development of a two-dimensional novel physical tar treatment method, at low temperatures, while simultaneously tackling water vapor frosting, organic component frosting and liquid condensation. The proposed model corresponds to the second group of models that is based on analytical solutions, and considers the frost as a porous media. It allows a deep understanding of the behavior of the multi-component condensation/deposition on cold surfaces.

3.2.1. Model presentation

The model development includes studying the frost thickness, the frost density, the gas temperature, the gas composition, the required energy and the plate dimensions that yield a suitable tar content for methanation.

The producer gas is cooled by flowing over a cold plate whose temperature is lower than the dew point of the condensable components. Frost will appear if the surface temperature is lower than the freezing point. This is the case for benzene and for water vapor. At the inlet composition, shown in the last column of Table 2-6, water vapor is the first one that forms the frost layer, followed by a frost layer of benzene, and then a liquid toluene condensation. Since studies tackling this simultaneous deposition-condensation do not exist, each phase is separately treated. Moreover, no correlations for the properties of a multi-component frost layer are found in the literature. It is therefore assumed that each component forms a pure frost layer separately. In other words, two separate frost layers are considered. The first one is for benzene and the second one is for ice, in addition to a liquid toluene film that fills a certain volume from the pores. This is considered since as the gas temperature is reduced along the plate length, the remaining amount of water in the gas phase decreases and becomes much lower than that of the benzene. Note that in the proposed model, the producer gas flows through a duct where the upper plate is insulated, in order to avoid heat transfer between the gas and the environment. The frosting and condensation processes only take place on the lower plate of the duct, which is maintained at a constant low temperature. As the temperature of the producer gas decreases, part of the toluene, benzene and water vapor condenses depending on the plate temperature. As for the frost growth, the mass transferred from the gas phase to the cold surface is divided into two parts. The first one deposits on the surface of

the frost and tends to increase the frost density, while the second one diffuses through the frost layer and contributes in increasing the frost thickness [118,132].

Figure 3-2 describes the physical model of heat and mass transfer between the gas and the condensable components. The process is divided into 6 subdomains; the gas, the interface between the ice frost layer and the gas, the ice frost layer, the interface between the ice and the benzene frost layers, the benzene frost layer and the toluene liquid volume. The temperature difference between the cold surface and the gas temperature, in addition to the concentration difference between the condensed and the gas phases, lead to the simultaneous heat and mass transfer phenomena. The proposed model is conducted on Dymola according to a two-dimensional frost growth analysis, based on the finite volume method.

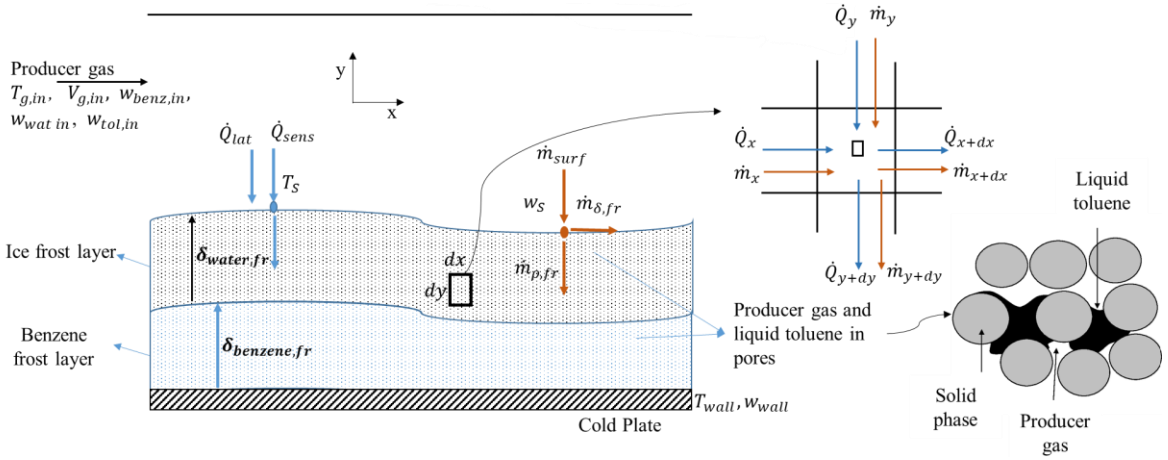

Figure 3-2: Frosting and condensation process diagram.

3.2.2. Main assumptions

Several assumptions were considered in each of the subdomains in order to simplify the mathematical model:

- The processes of heat and mass transfer inside the frost layer are handled in two dimensions. The frost layer grows in both directions; parallel and perpendicular to the cold plate.
- The frost density and thickness are considered constant along the plate width.
- Since no previous studies exist on the simultaneous condensation of several components, separate benzene and water layers are assumed to be formed one on the top of the other. The benzene frost layer is considered at the bottom, while the ice frost layer is built on the top of the benzene frost layer, since the freezing point of benzene is slightly higher than that of water. As for the toluene, the liquid is assumed to condense first on the surface of the frost, and then penetrates to fill the frost pores.
- The producer gas is considered as an incompressible Newtonian fluid.
- The producer gas is considered at saturation within the frost layer and at the gas-frost interface.
- Constant atmospheric pressure is considered in the gas phase and inside the frost layer.
- The gas velocity is constant along the y-axis while it varies along the x-axis. The gas velocity depends on the effective hydraulic diameter that changes along the plate length due to frost growth.
- Gas is not dissolved in the liquid toluene
- No gravitational effect is considered.
- No heat transfer by radiation is considered.

3.2.3. Governing equations

The mathematical model is formulated using 1D and 2D Cartesian coordinate systems for the gas side and for the condensate, respectively. Note that the main differences between benzene and water vapor are the physical properties, the thermodynamic properties and the boundary conditions. However, several heat and mass transfer equations are the same for both frost layers. Therefore, in the sequel, subscript 'i' ($i \in \{benzene, water\ vapor\}$) is used in the equations, to avoid repetition.

The frost layer is considered as a porous medium. The porosity (ε) of the frost subdomain can be calculated as follows:

$$\varepsilon_i = \frac{\rho_{fr,i} - \rho_{solid,i}}{\rho_g - \rho_{solid,i}} \tag{3-1}$$

where ρ_{fr}, ρ_{solid} and ρ_g respectively represent the density of the frost layer, the bulk solid and the gas density inside the frost pores, in kg.m^{-3}.

Note that the densities of the solids used in this thesis are; $\rho_{solid,benz} = 1012\ kg.m^{-3}$, $\rho_{solid,wat} = 917\ kg.m^{-3}$, while the gas density is calculated using eq. (3-52).

3.2.3.1 Producer gas stream

The sensible heat transferred from the producer gas to the frost surface ($\dot{Q}_{sens}$) is calculated as follows:

$$\dot{Q}_{sens} = h_{c,g}.S.\left(T_g - T_{fr,s}\right) \tag{3-2}$$

where $h_{c,g}$ represents the convective heat transfer coefficient in W.m^{-2}.K^{-1}, S is the gas side heat transfer area in m^2, T_g, and $T_{fr,s}$ represent the gas and the frost surface temperatures in K, respectively.

The total mass flow rates of benzene ($\dot{m}_{s,benz}$), water vapor ($\dot{m}_{s,wat}$) and toluene ($\dot{m}_{s,tol}$), transferred from the producer gas to the frost surface, are calculated according to the heat and mass transfer analogy as in eqs. (3-3), (3-4) and (3-5), respectively. Those mass flow rates will undergo a phase change. Benzene and water vapor are subject to frosting while toluene is subject to condensation.

$$\dot{m}_{s,benz} = k_{m,benz}.S.\rho_g.\left(w_{g,benz} - w_{s,benz}\right) \tag{3-3}$$
$$\dot{m}_{s,wat} = k_{m,wat}.S.\rho_g.\left(w_{g,wat} - w_{s,wat}\right) \tag{3-4}$$
$$\dot{m}_{s,tol} = k_{m,tol}.S.\rho_g.\left(w_{g,tol} - w_{s,tol}\right) \tag{3-5}$$

where $k_{m,benz}$, $k_{m,wat}$ and $k_{m,tol}$ respectively represent the mass transfer coefficients of benzene, water vapor and toluene in m.s^{-1}, $w_{g,benz}$ and $w_{s,benz}$ are respectively the mass fraction of the benzene in the gas and at the frost surface, $w_{g,wat}$ and $w_{s,wat}$ are respectively the mass fraction of the water vapor in the gas and at the frost surface, $w_{g,tol}$ and $w_{s,tol}$ are respectively the mass fraction of toluene in the gas and at the frost surface.

Note that the frost surface is considered at thermodynamic equilibrium. Thus, the mass fraction at the frost surface ($w_{s,i}$) can be linked to the saturation curves, previously developed in section 2.2.2.3, for each component at the surface temperate ($T_{fr,s,i}$):

$$w_{s,i} = f(T_{fr,s,i}) \tag{3-6}$$

More details on the mass fraction of the different condensable components are provided in section 3.2.9.

Moreover, an energy balance around each control volume in the gas side is developed:

$$\dot{Q}_{total} = \dot{Q}_{sens} + \sum \dot{Q}_{lat} \quad \text{(3-7)}$$

such that:

$$\dot{Q}_{total} = \dot{m}_{g,in,}.h_{g,in} - \dot{m}_{g,out}.h_{g,out} \quad \text{(3-8)}$$

$$\dot{m}_{g,out} = \dot{m}_{g,in,} - \left(\dot{m}_{s,benz} + \dot{m}_{s,wat} + \dot{m}_{s,tol}\right) \quad \text{(3-9)}$$

$$\begin{aligned} h_g = C_{p,g}.T_g &+ w_{benz}\left[L_{sv,benz} + C_{p,benz}.\left(T_g - T_{ref}\right)\right] \\ &+ w_{wat}\left[L_{sv,wat} + C_{p,wat}.\left(T_g - T_{ref}\right)\right] \\ &+ w_{tol}\left[L_{vap,tol} + C_{p,tol}.\left(T_g - T_{ref}\right)\right] \end{aligned} \quad \text{(3-10)}$$

$$\sum \dot{Q}_{lat} = \dot{m}_{s,benz}.L_{sv,benz} + \dot{m}_{s,wat}.L_{sv,wat} + \dot{m}_{s,tol}.L_{vap,tol} \quad \text{(3-11)}$$

where $\dot{Q}_{total}$ is the total heat flow rate transferred from the gas phase to the frost in J.s^{-1}, $\dot{Q}_{lat}$ is the latent heat flow rate in J.s^{-1}, $\dot{m}_g$ is the mass flow of the producer gas in kg.s^{-1}, $C_{p,g}$ is the specific heat capacity of the producer gas in J.kg^{-1}.K^{-1}, $L_{sv,benz}$ and $L_{sv,wat}$ respectively represent the latent heat of sublimation of benzene and water vapor in J.kg^{-1}, and $L_{vap,tol}$ is the latent heat of toluene condensation in J.kg^{-1}.

Note that the different latent heat values are; $L_{vap,tol} = 351 \times 10^3\, J.kg^{-1}$, $L_{sv,benz} = 534 \times 10^3\, J.kg^{-1}$, and $L_{sv,wat} = -1.083 \times 10^2[(1.8 \times (T - 273) + 32)] + 2.833 \times 10^6$.

3.2.3.2 Frost Surface

As mentioned earlier, the total mass flow rate transfered from the gas to the frost surface ($\dot{m}_{s,i}$) is splitted into two terms. The first term corresponds to the mass flow rate that increases the frost thickness by deposition on the surface ($\dot{m}_{\delta}$), while the second term is the mass flow rate that increases the frost density by diffusion inside the frost ($\dot{m}_{\rho}$). Eq. (3-12) applies for the benzene and the ice frost layers.

$$\dot{m}_{s,i} = \dot{m}_{\delta,i} + \dot{m}_{\rho,i} \quad \text{(3-12)}$$

The mass flow rate that increases the frost density by diffusion inside the frost ($\dot{m}_{\rho,wat}$) can be calculated as follows:

$$\dot{m}_{\rho,wat} = -D_{eff,wat}.S.\rho_g.\left(\frac{dw_{wat}}{dy}\right)_s \quad \text{(3-13)}$$

where $(dw_{wat}/dy)_s$ is the water vapor mass fraction variation inside the frost pores when *y* tends to the frost thickness ($\delta_{fr,wat}$), and $D_{eff,wat}$ represents the effective diffusion coefficient of the water vapor in the gas of the frost pores.

Once the diffusing mass flow rate is calculated, the increasing thickness mass flow rate can be deduced from eq. (3-12). The variation of the frost layer thickness ($d\delta_i/dt$) can then be calculated:

$$\dot{m}_{\delta,i} = \rho_{fr,i}.S.\frac{d\delta_i}{dt} \quad \text{(3-14)}$$

The heat transfer at the frost surface can be expressed by eq. (3-15). The conductive heat transfer flow rate at the surface ($\dot{Q}_{cond,wat,s}$) is calculated function of the temperature variation in the water frost $\left(dT_{fr,wat}/dy\right)_s$ when y tends to $\delta_{fr,wat}$ and the effective thermal conductivity of the water frost ($k_{eff,wat}$) as in eq. (3-16).

$$\dot{Q}_{cond,wat,s} = \dot{Q}_{sens} + \dot{m}_{\delta,wat} L_{sv,wat} + \dot{m}_{tol} L_{vap,tol} \tag{3-15}$$

$$\dot{Q}_{cond,wat,s} = -k_{eff,wat}.S.\left(\frac{dT_{fr,wat}}{dy}\right)_s \tag{3-16}$$

3.2.3.3 Interface between the benzene and the ice frost layers

The same equations for the mass fluxes apply for the benzene-ice interface. The difference between them is that the mass flux leading to the benzene frost densification is calculated function of the benzene mass fraction variation at the interface. The total mass flow rate of the benzene, transferred from the gas to the benzene frost surface, is calculated as in eq. (3-12).

The benzene mass flow rate that increases the frost density by diffusion inside the frost ($\dot{m}_{\rho,benz}$) is calculated as:

$$\dot{m}_{\rho,benz} = -D_{eff,benz}.S.\rho_g.\left(\frac{dw_{benz}}{dy}\right)_{int} \tag{3-17}$$

where $(dw_{benz}/dx)_{int}$ is the benzene mass fraction variation inside the frost pores when y tends to the frost thickness ($\delta_{fr,benz}$), and $D_{eff,benz}$ represents the effective diffusion coefficient of benzene in the gas of the frost pores.

Once the diffusing mass flow rate is calculated, the increasing thickness mass flow rate can be deduced from eq. (3-12). The variation of the benzene frost layer thickness ($d\delta_{benz}/dt$) can then be calculated as in eq. (3-14).

The heat balance, at the interface between the two frost layers of benzene and ice, is expressed as:

$$\left(-k_{eff,wat}.S.\left(\frac{dT_{fr,wat}}{dy}\right)_{int}\right) = \left(-k_{eff,benz}.S.\left(\frac{dT_{fr,benz}}{dy}\right)_{int}\right) + \dot{m}_{\delta,benz} L_{sv,benz} \tag{3-18}$$

where $\left(dT_{benz,fr}/dy\right)_{int}$ is the temperature variation in the benzene frost when y tends to the interface, and $k_{eff,benz}$ represents the effective thermal conductivity of the benzene frost.

3.2.3.4 Frost layer

The mass balance of benzene or water vapor inside the frost layers is predicted according to Fick's law, and it is given by:

$$\frac{\partial}{\partial x}\left(-D_{eff,i}.\rho_g.\frac{\partial w_i}{\partial x}\right) + \frac{\partial}{\partial y}\left(-D_{eff,i}.\rho_g.\frac{\partial w_i}{\partial y}\right) = -\alpha_i \tag{3-19}$$

where α_i represents the mass absorption rate per unit volume of the frost, expressed in $kg.s^{-1}.m^{-3}$ and w_i is the mass fraction.

Note that the saturation condition is also considered inside the frost layer. Thus, the same analogy discussed in the previous section also applies for the mass fraction gradient inside the frost layer.

The densification of the frost layers can then be calculated:

$$\frac{d\rho_{fr,i}}{dt} = \alpha_i \tag{3-20}$$

The energy balance inside the frost layer can then be applied:

$$\frac{\partial}{\partial x}\left(-k_{eff,i}.\frac{\partial T_{fr,i}}{\partial x}\right) + \frac{\partial}{\partial y}\left(-k_{eff,i}.\frac{\partial T_{fr,i}}{\partial y}\right) = \alpha_i.L_{sv,i} \tag{3-21}$$

The latter links between the heat transfer based on Fourier's law and the latent heat related to the mass densification.

3.2.3.5 Liquid toluene film

As for the condensation of the liquid toluene, the volume of the condensed toluene (V_{tol}) is calculated function of the total mass of toluene transferred from the gas phase to the cold surface:

$$V_{tol} = \frac{\dot{m}_{s,tol}}{\rho_{tol}}.t \tag{3-22}$$

$$\rho_{tol} = -0.8394 \times T + 1115.9 \tag{3-23}$$

where t is the time in s, and ρ_{tol} represents the liquid density of toluene in kg.m^{-3} function of the temperature in K.

Afterwards, the volume fraction of the pores that will be filled by the liquid toluene (v_{tol}), instead of the producer gas, is computed as:

$$v_{tol} = \frac{V_{tol}}{V_{pores}} \tag{3-24}$$

where V_{pores} represents the total volume of the pores of the two frost layers in m^3, calculated as:

$$V_{pores} = \left(\delta_{fr,benz} + \delta_{fr,wat}\right).w_p.L_p.\varepsilon \tag{3-25}$$

where w_p and L_p are respectively the plate width and length in m.

3.2.3.6 Refrigerant side

As a first step, the model was completed based on a constant wall temperature. It was then modified to cover the flow of a counter current refrigerant, which is used to cool the producer gas. Modeling the refrigerant flow is of a great importance in analyzing the exergy efficiency of the system and completing the economic analysis. Figure 3-3 illustrates the physical model of the process with a counter-current flow of refrigerant, in addition to the thermal resistances of the different mediums.

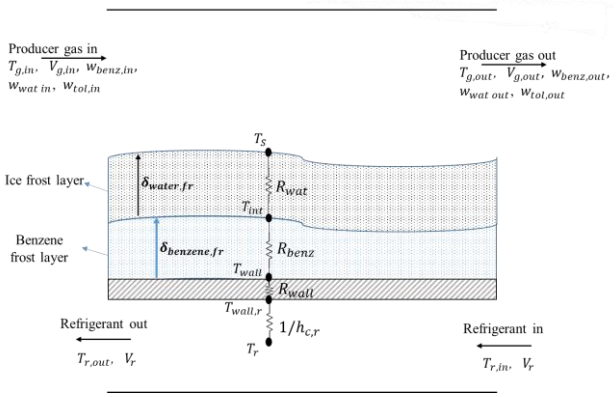

Figure 3-3: Physical representation of the system with a counter-current refrigerant flow (not to scale).

An additional overall heat balance should also be considered in the model, in order to account for the refrigerant flow. Note that the thermal capacitance of a frost layer is negligible and the frost layer is assumed to be in quasi-steady state [111,114]. The total heat transferred from the producer gas to the refrigerant is equal to the sum of the sensible heat and the latent heats of benzene, water and toluene:

$$h_{c,g}.S.\left(T_g - T_{fr,s}\right) + \dot{m}_{s,benz}L_{sv,benz} + \dot{m}_{s,wat}L_{sv,wat} + \dot{m}_{s,tol}L_{vap,tol} = U.S.\left(T_S - T_r\right) \quad (3\text{-}26)$$

where U is the overall heat transfer coefficient in $W.m^{-2}.K^{-1}$ and T_r is the refrigerant temperature in K.

The overall heat transfer coefficient is calculated function of the refrigerant convective heat transfer coefficient ($h_{c,r}$), the frost layer thermal resistivity, and the wall thermal resistivity:

$$\frac{1}{U} = \frac{1}{h_{c,r}} + \frac{\delta_{fr,benz}}{k_{eff,benz}} + \frac{\delta_{fr,wat}}{k_{eff,wat}} + \frac{\delta_{wall}}{k_{wall}} \quad (3\text{-}27)$$

where δ_{wall} is the wall thickness in m and k_{wall} is the wall thermal conductivity in $W.m^{-1}.K^{-1}$.

The refrigerant heat flow ($\dot{Q}_r$) is calculated as:

$$\dot{Q}_r = h_{c,r}S\left(T_{wall,r} - T_{r,avg}\right) \quad (3\text{-}28)$$

where $T_{wall,r}$ is the wall temperature on the refrigerant side and $T_{r,avg}$ is the average refrigerant temperature equal to $\left(T_{r,in} + T_{r,out}\right)/2$.

The variation of the refrigerant temperature can be calculated from:

$$\dot{Q}_r = \dot{m}_r C_{p,r}\left(T_{r,out} - T_{r,in}\right) \quad (3\text{-}29)$$

where $\dot{m}_r$ is the mass flow rate of the refrigerant stream in $kg.s^{-1}$, $C_{p,r}$ is the refrigerant specific heat capacity in $J.kg^{-1}.K^{-1}$, $T_{r,in}$ and $T_{r,out}$ are respectively the inlet and the outlet temperature of the refrigerant.

3.2.4. The modelling approach: Finite volume method

The heat and mass transfer equations, presented in the previous sections, are implemented in Dymola. The latter is based on the Modelica language and is an object-oriented modeling environment. Modelica is an acausal language, and thus the heat and mass transfer equations should not be re-arranged [133].

The equations can be implemented without taking into consideration the computational order. Therefore, no additional coding for solving the equations is required. This allows an extensive model reuse for several applications and makes the model extremely versatile. In this study, the relative tolerance is set to 0.0001. When the computed local error becomes lower that the user defined tolerance, the convergence criterion is satisfied. In addition, DASSL method is used to solve to mathematical model which is a system of ordinary differential equations. This method has a multi-step solver with a step-size control. This allows to have stable results for a wide range of applications.

Figure 3-4 is a representation of a typical orthogonal cell arrangement in a two-dimensional Cartesian coordinate system. The Finite Volume Method (FVM) is used to model the frost growth in 2D, where the total frost volume is discretized into smaller control volumes called cells. In the FVM, the governing differential equations, previously presented, are applied for each control volume. Moreover, the properties of each cell are stored in the center of the cells O, W, E, N, and S, as shown in Figure 3-4. The lower case letters w, n, e and s denote the faces, which represent the surfaces between the cells [134]. The number of meshes considered in the model depends on several factors and it will be indicated for each case separately, based on a sensitivity analysis.

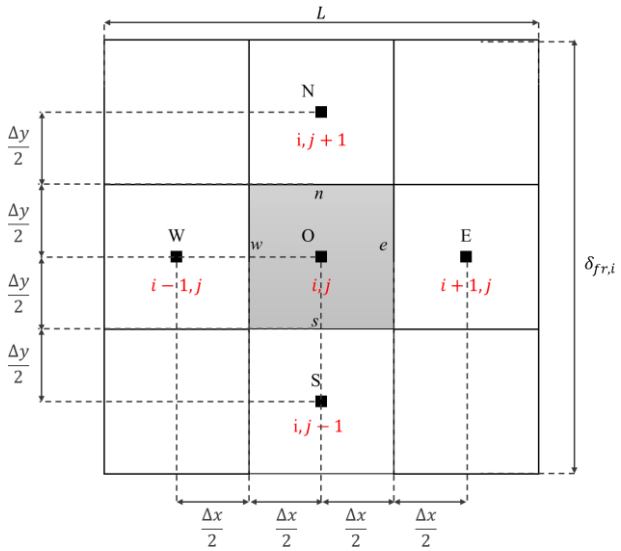

Figure 3-4: Schematic illustration of the cell arrangement in a two-dimensional Cartesian coordinate system.

For instance, eq. (3-21), should be integrated over the control volume O in order to be solved, as follows:

$$\int_s^n \int_w^e \frac{\partial}{\partial x}\left(-k_{eff}.\frac{\partial T_{fr}}{\partial x}\right)dxdy + \int_s^n \int_w^e \frac{\partial}{\partial y}\left(-k_{eff}.\frac{\partial T_{fr}}{\partial y}\right)dxdy = \int_s^n \int_w^e \alpha.L_{sv}dxdy \qquad (3\text{-}30)$$

By integrating once the left side of eq. (3-30), it can be written as:

$$\int_s^n \left[-k_{eff}.\frac{\partial T_{fr}}{\partial x}\right]_w^e dy + \int_w^e \left[-k_{eff}.\frac{\partial T_{fr}}{\partial y}\right]_s^n dx = \int_s^n \int_w^e \alpha.L_{sv}dxdy \qquad (3\text{-}31)$$

Considering the average value of the fluxes and integrating eq. (3-31), yields the following:

$$\left(\left[-k_{eff}.\frac{\partial T_{fr}}{\partial x}\right]_e - \left[-k_{eff}.\frac{\partial T_{fr}}{\partial x}\right]_w\right)\Delta y + \left(\left[-k_{eff}.\frac{\partial T_{fr}}{\partial y}\right]_n - \left[-k_{eff}.\frac{\partial T_{fr}}{\partial y}\right]_s\right)\Delta x = \alpha_O.L_{sv,O}.\Delta x.\Delta y \qquad (3\text{-}32)$$

A uniform meshing $\Delta x = L_p/M_c$ and $\Delta y = \delta_{fr}/N_c$ is considered, where M_c and N_c present the number of meshes along the x-axis and the y-axis, respectively.

3.2.4.1 Middle cells

The derivatives in eq. (3-32) can be approximated by applying the Taylor series expansion. The derivatives are presented in eqs. (3-33) and (3-34) for the middle cells.

$$\left[\frac{\partial T_{fr}}{\partial x}\right]_e = \frac{T_{fr_E} - T_{fr_O}}{\Delta x} \quad \text{and} \quad \left[\frac{\partial T_{fr}}{\partial x}\right]_w = \frac{T_{fr_O} - T_{fr_W}}{\Delta x} \tag{3-33}$$

$$\left[\frac{\partial T_{fr}}{\partial y}\right]_n = \frac{T_{fr_N} - T_{fr_O}}{\Delta y} \quad \text{and} \quad \left[\frac{\partial T_{fr}}{\partial x}\right]_s = \frac{T_{fr_O} - T_{fr_S}}{\Delta y} \tag{3-34}$$

The last step consists in determining the effective thermal conductivities in eq. (3-32) at the cell faces. Those parameters are computed by interpolation. Since a uniform meshing is considered, the effective thermal conductivities at the cell faces can be expressed as in eqs. (3-35) and (3-36), for the middle cells.

$$k_{eff_e} = \frac{k_{eff_O} + k_{eff_E}}{2} \quad \text{and} \quad k_{eff_w} = \frac{k_{eff_O} + k_{eff_W}}{2} \tag{3-35}$$

$$k_{eff_n} = \frac{k_{eff_O} + k_{eff_N}}{2} \quad \text{and} \quad k_{eff_s} = \frac{k_{eff_O} + k_{eff_S}}{2} \tag{3-36}$$

3.2.4.2 Boundary cells

A notable feature of the Finite Volume Method is that the boundary cells must be differently treated. Figure 3-5 is a schematic representation of the top boundary cell of the ice frost layer, in which the temperature at the northern face is equal to the frost surface temperature, while the temperature of the western face is equal to the inlet temperature of the gas stream.

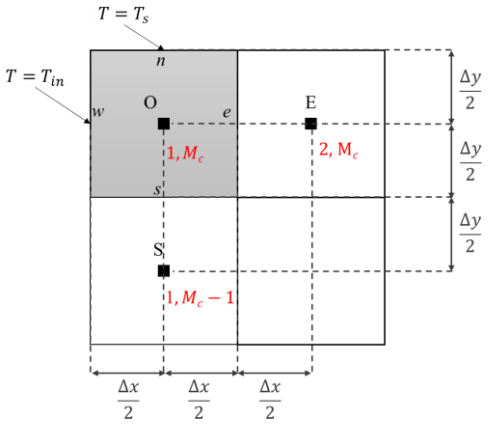

Figure 3-5: Schematic illustration of the top boundary cell of the ice frost layer.

In order to get the approximation of the derivatives at the boundaries, two Taylor series expansions are performed for each cell face. For instance, for the northern face, the following two equations are developed:

$$T_{fr_O} = T_{fr_n} - \frac{\Delta y}{2}\frac{\partial T_{fr}}{\partial y}\bigg|_n + \frac{1}{2}\left(\frac{\Delta y}{2}\right)^2 \frac{\partial^2 T_{fr}}{\partial y^2}\bigg|_n - \frac{1}{6}\left(\frac{\Delta y}{2}\right)^3 \frac{\partial^3 T_{fr}}{\partial y^3}\bigg|_n + \cdots \tag{3-37}$$

$$T_{fr_S} = T_{fr_n} - \frac{3\Delta y}{2}\frac{\partial T_{fr}}{\partial y}\bigg|_n + \frac{1}{2}\left(\frac{3\Delta y}{2}\right)^2 \frac{\partial^2 T_{fr}}{\partial y^2}\bigg|_n - \frac{1}{6}\left(\frac{3\Delta y}{2}\right)^3 \frac{\partial^3 T_{fr}}{\partial y^3}\bigg|_n + \cdots \tag{3-38}$$

Several modifications can be then made in order to compute the derivative at the northern face. First, the denoted boundary condition $\left(T_{fr_n} = T_S\right)$ in Figure 3-5, is substituted in the equations. Eq. (3-37) is then multiplied by 9, and eq. (3-38) is subtracted from it. After arrangement, this leads to the following northern face derivative:

$$\left.\frac{\partial T_{fr}}{\partial y}\right|_n \approx \frac{8T_S + T_{fr_S} - 9T_{fr_O}}{3\Delta y} \tag{3-39}$$

As for the effective thermal conductivity, two Taylor series expansions are performed for each cell face. However, the effective thermal conductivity does not have a boundary condition. For instance, for the northern face, the following two equations are developed:

$$k_{eff_O} = k_{eff_n} - \frac{\Delta y}{2}\left.\frac{\partial k_{eff}}{\partial y}\right|_n + \cdots \tag{3-40}$$

$$k_{eff_S} = k_{eff_n} - \frac{3\Delta y}{2}\left.\frac{\partial k_{eff}}{\partial y}\right|_n + \cdots \tag{3-41}$$

Multiplying eq. (3-40) by 3 and subtracting eq. (3-41) from it, yields after rearrangement the following approximation of first-order:

$$k_{eff_n} \approx \frac{3k_{eff_O} - k_{eff_S}}{2} \tag{3-42}$$

The same analogy applies for the rest of the boundary cells. However, only the northern face of the top boundary cell is detailed, while the effective thermal conductivities and the derivatives for the rest of the faces, are directly summarized in Table 3-1.

Table 3-1: Summary of the approximated effective thermal conductivities and derivatives at the boundary cell faces of the ice frost layer.

Boundary	Effective thermal conductivity		Derivatives	
Left	$k_{eff,w} \approx \frac{3k_{eff,O} - k_{eff,E}}{2}$	(3-43)	$\left[\frac{\partial T_{fr}}{\partial x}\right]_w \approx \frac{9T_{fr_O} - T_{fr_E} - 8T_{in}}{3\Delta x}$	(3-44)
Right	$k_{eff,e} \approx \frac{3k_{eff,O} - k_{eff,W}}{2}$	(3-45)	$\left[\frac{\partial T_{fr}}{\partial x}\right]_e \approx \frac{8T_{out} + T_{fr_W} - 9T_{fr_O}}{3\Delta x}$	(3-46)
Top	$k_{eff,n} \approx \frac{3k_{eff,O} - k_{eff,S}}{2}$	(3-47)	$\left[\frac{\partial T_{fr}}{\partial y}\right]_n \approx \frac{8T_S + T_{fr_S} - 9T_{fr_O}}{3\Delta y}$	(3-48)
Bottom	$k_{eff,s} \approx \frac{3k_{eff,O} - k_{eff,N}}{2}$	(3-49)	$\left[\frac{\partial T_{fr}}{\partial y}\right]_s \approx \frac{9T_{fr_O} - T_{fr_N} - 8T_{int}}{3\Delta y}$	(3-50)

Note that the same steps are repeated in order to derive the equations to be implemented in Dymola, for the different differential governing equations in 1D and 2D analyses.

3.2.5. Boundary and initial conditions

Initial conditions, t=0

An initial frost density and frost thickness should be considered in order to take into account the first period of frost growth, also known as "crystal growth period". Based on previous studies, the considered

optimal values for the frost thickness and density are; $\delta_{fr,int} = 2 \times 10^{-5}\ m$, $\rho_{fr,int} = 25\ kg.m^{-3}$ and $T_{fr,int} = T_{wall}$ [90, 91, 99, 112, 115].

Boundary conditions, t>0

The boundary conditions for the computational domain are:

- Plate ($0 \leq x \leq L_p$):
  $\frac{\partial w}{\partial y} = 0; T = T_{wall}$
- Left boundary, inlet gas subdomain ($x = 0,\ \left(\delta_{benz,fr} + \delta_{wat,fr}\right) \leq y \leq h_p$):
  $u = u_{in}; T = T_{in}; w = w_{in}$
- Right boundary, outlet gas subdomain ($x = L_p,\ \left(\delta_{benz,fr} + \delta_{wat,fr}\right) \leq y \leq h_p$):
  $\frac{\partial u}{\partial x} = \frac{\partial T}{\partial x} = \frac{\partial w}{\partial x} = 0$
- Left and right boundaries, frost subdomain $\left(x = 0,\ x = L_p,\ 0 \leq y \leq \left(\delta_{benz,fr} + \delta_{wat,fr}\right)\right)$:
  $\frac{\partial T}{\partial x} = \frac{\partial w}{\partial x} = 0$
- Top boundary $\left(0 \leq x \leq L_p,\ y = h_p\right)$:
  $\frac{\partial u}{\partial y} = \frac{\partial T}{\partial y} = \frac{\partial w}{\partial y} = 0$

3.2.6. Gas Thermophysical properties

The thermal conductivity (k_g), density (ρ_g), molar heat capacity ($C_{pm,g}$), and viscosity (μ_g) should be known for the producer gas to model the heat and mass transfer equations. Those thermophysical properties are calculated using Aspen Properties in the range of the operating conditions. Figure 3-6 illustrates the variation of each property, function of the temperature. Based on Figure 3-6, a correlation is developed, for each property, to be integrated later in the Dymola model. Eqs. (3-51) to (3-54) present the developed correlations for the thermal conductivity, density, molar heat capacity and viscosity.

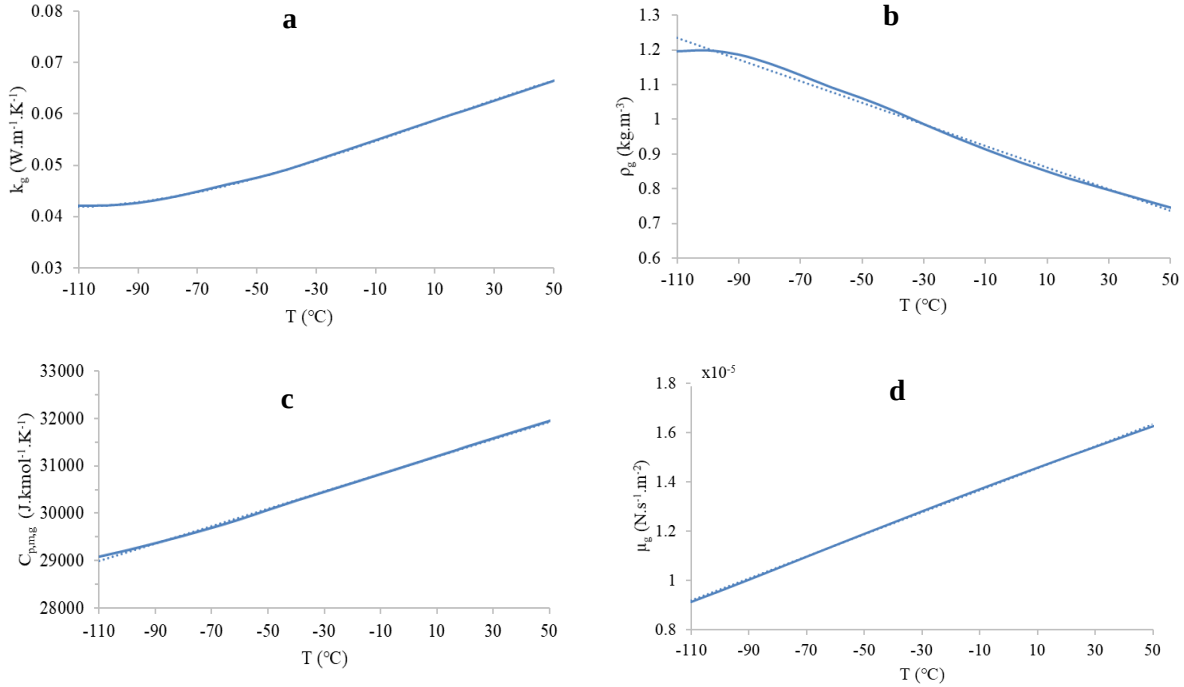

Figure 3-6: Variation of the gas a) thermal conductivity in W.m^{-1}.K^{-1}, b) density in kg.m^{-3}, c) molar heat capacity in J.kmol^{-1}.K^{-1}, and d) viscosity in N.s.m^{-2}, function of the temperature in °C.

$$k_g = -4.42 \times 10^{-9} \times \mathrm{T}^3 + 3.74 \times 10^{-6} \times \mathrm{T}^2 - 8.50 \times 10^{-4} \times \mathrm{T} + 0.1 \quad (3\text{-}51)$$

$$\rho_g = -3.11 \times 10^{-3} \times \mathrm{T} + 1.74 \quad (3\text{-}52)$$

$$C_{pm,g} = 18.29 \times \mathrm{T} + 26\,019.22 \quad (3\text{-}53)$$

$$\mu_g = 4.47 \times 10^{-8} \times \mathrm{T} + 1.88 \times 10^{-6} \quad (3\text{-}54)$$

3.2.7. Effective thermal conductivity

The assumptions made on the different coefficients used in the heat and mass transfer equations, significantly affect the results. The effective thermal conductivity (k_{eff}) is one of the main coefficients of the model. The correlation adapted to predict k_{eff} mainly affects the frost thickness. In fact, several correlations for predicting k_{eff} exist. However, most of them are developed based on experimental studies for water vapor in moist air. Thus, it is not evident if they can be used to accurately predict the effective thermal conductivity of benzene and water frost layers, in which the pores are filled with producer gas, as well as other condensable compounds. Eq. (3-55) developed by Lee et al. [114], and eq. (3-56) developed by Sanders [136] are the most well-known correlations for k_{eff}. Both equations are valid for frost densities below 500 kg.m^{-3}. Eq. (3-56) is valid for air temperatures ranging between -10°C and 0°C, and for wall temperatures ranging between -19°C and -11°C. Yonko and Sepsy [137] also developed a correlation for predicting k_{eff} of the frost, function of the frost density, given in eq. (3-57). This latter is valid for frost densities lower than 580 kg.m^{-3}, for air temperatures ranging between 20°C and 23°C, and for wall temperatures ranging between -30°C and -20°C.

Le Gall and Grillot [138] developed a model that calculates the frost effective thermal conductivity as in eq. (3-58). The latter is used in this thesis since the effective thermal conductivity is calculated based on the thermal conductivity of the solid phase, the gas phase and the frost porosity. Therefore, it can be adapted to cover frost growth processes dealing with components other than moist air.

$$k_{eff} = 0.132 + 3.13 \times 10^{-4}.\rho_{fr} + 1.6 \times 10^{-7}.\rho_{fr}^2 \quad (3\text{-}55)$$

$$k_{eff} = 0.001202.\rho_{fr}^{0.963} \quad (3\text{-}56)$$

$$k_{eff} = 0.024248 + 7.2311 \times 10^{-4}.\rho_{fr} + 1.183 \times 10^{-6}.\rho_{fr}^2 \quad (3\text{-}57)$$

$$k_{eff} = 1 \Big/ \left(a \Big/ k_{per} + (1-a) \Big/ k_{par} \right)$$

where :

$$k_{per} = 1 \Big/ \left(\varepsilon \Big/ k_g + (1-\varepsilon) \Big/ k_{solid} \right), \quad (3\text{-}58)$$

$$k_{par} = \varepsilon \Big/ k_g + (1-\varepsilon) \Big/ k_{solid},$$

$$a = 0.42(0.1 + 0.995^{\rho_{fr}})$$

Two different studies tackling the solid benzene thermal conductivity are available in the literature. The first one [107] considers a constant solid benzene thermal conductivity of 0.251 W.m^{-1}.K^{-1}. Another study [139] that analyzes the thermal properties of solid benzene developed the variation of its thermal conductivity function of the temperature based on isobaric case. Moreover, the variation of the solid benzene thermal conductivity function of the temperature is also developed on Aspen Properties while considering it in the liquid phase, and it is expressed:

$$k_{benz} = -3.06 \times 10^{-4} T + 0.234 \quad (3\text{-}59)$$

The variation of three different solid benzene thermal conductivities function of the temperature is compared as seen in Figure 3-8. It can be seen that the correlation developed on Aspen properties yields average values between the two correlations found in the literature. Consequently, the solid benzene thermal conductivity is computed using eq. (3-59).

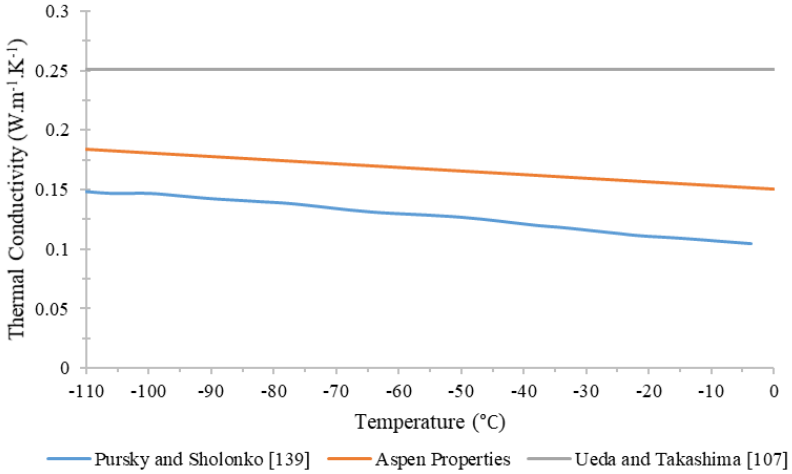

Figure 3-7: Variation of the solid benzene thermal conductivity (k_{benz}) function of the temperature based on three different correlations.

Equations for the thermal conductivity of the gas (k_g) and the porosity (ε), were previously mentioned in eqs. (3-51) and (3-1), respectively.

The ice thermal conductivity (k_{ice}) is calculated function of the temperature (in K) [138]:

$$k_{ice} = 630/T \tag{3-60}$$

The presence of liquid toluene inside the frost pores affects the effective thermal conductivity. Therefore, the equation used to predict the effective thermal conductivity, in the presence of a liquid phase inside a porous media, is given in eq. (3-61) [127,140]. This equation is based on the volumetric average method. It is function of the thermal conductivities of the three co-existing phases, the porosity and the liquid saturation (S_l). The porosity reflects the fraction of the solid and the void in the frost, while the liquid saturation reflects the fraction of the void filled by the liquid toluene. The saturation is the ratio of the liquid volume (toluene) in a porous media (frost) over the volume of the pores in the same medium. Therefore, the liquid saturation is equal to v_{tol}, previously given in eq. (3-24). The thermal conductivity of the liquid toluene is given in eq. (3-62).

$$k_{eff} = k_g \varepsilon (1 - S_l) + k_l \varepsilon S_l + k_{solid}(1 - \varepsilon) \tag{3-61}$$

$$k_l = -2.42 \times 10^{-4}.T + 0.204 \tag{3-62}$$

Figure 3-8 (a) and (b) respectively present a comparison between the effective thermal conductivities predicted using the main correlations, for ice and benzene frost layers. It can be seen that, for both frost layers, the effective thermal conductivity increases when the frost density increases.

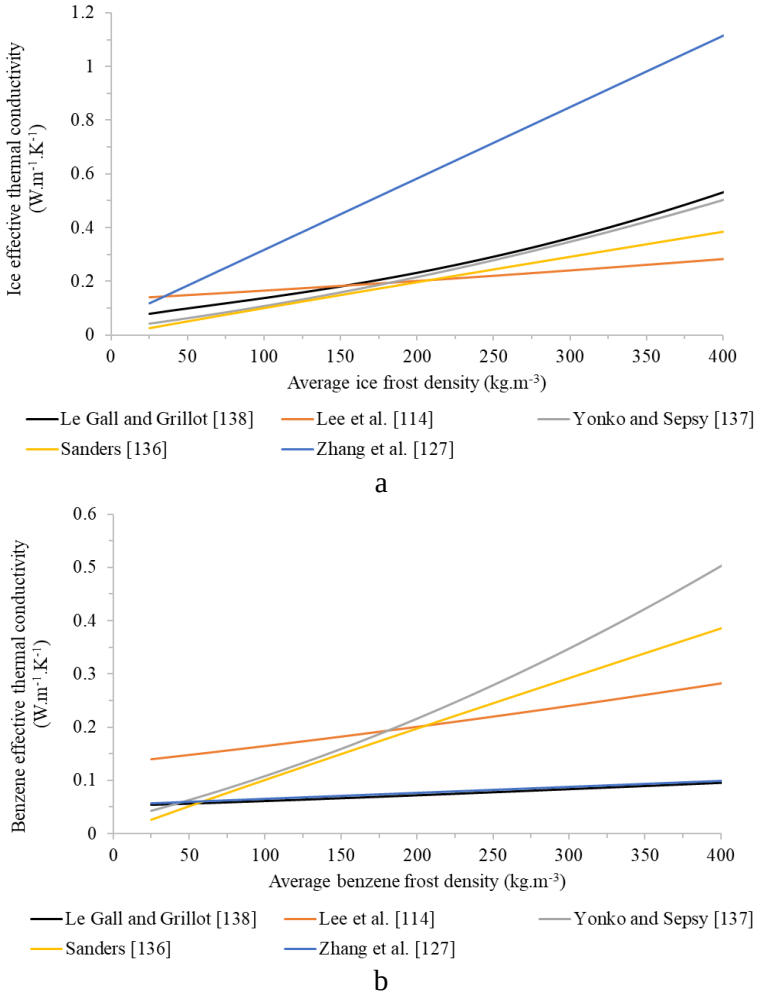

Figure 3-8: Variation of the effective thermal conductivities of the a) ice and b) benzene frost layers, function of the average frost densities, for the main correlations.

By comparing Figure 3-8 (a) and Figure 3-8 (b), it can be deduced that, eqs. (3-55) to (3-56) result in the same effective thermal conductivity for ice and benzene frost layers. Therefore, those equations were not considered in the model since they are only function of the frost density. On the contrary, eqs. (3-58) and (3-61) are function of the thermal conductivities, the frost density and the porosity. Thus, they lead to different effective thermal conductivities, for ice and benzene frost layers. The effective thermal conductivity of the benzene frost layer is lower than that of the ice frost layer. Consequently, the benzene frost layer has a higher thermal resistivity. In general, the thermal conductivity of the organic compounds is lower than that of inorganic compounds. It can be observed from Figure 3-8 (a) that the effective thermal conductivity of the ice frost layer computed using eq. (3-61), is higher than the one calculated using eq. (3-58). The effective thermal conductivities of the benzene frost layer, calculated using eqs. (3-58) and (3-61), are almost the same.

3.2.8. Diffusion and effective diffusion coefficients

The effective diffusion coefficient (D_{eff}) is also a crucial coefficient that affects the model results. It is a function of the diffusion coefficient of "i" in the gas mixture (D_{im}) and the diffusion resistance factor (μ), expressed in eq. (3-63). According to Jeong and Levy [130], D_{im} can be deduced from the diffusion coefficient of "i" in the air (D_{i-air}) at the same temperature, as in eq. (3-64). Eq. (3-65) is used to calculate the thermal diffusivities of the producer gas (α_{gas}) and the air (α_{air}). Usually, the diffusion coefficient of "i" in the air is available at atmospheric pressure and room temperature. Eq. (3-66) is used

to compute the diffusion coefficient of "i" in "j" (D_{ij}) at different operating conditions of temperature and pressure (P) [141]. The diffusion coefficients for the benzene, the toluene and the water vapor in the air, at normal conditions, are presented in Table 3-2.

$$D_{eff,im} = \mu_i . D_{im} \tag{3-63}$$

$$D_{im\,@\,T} = \frac{\alpha_{gas}}{\alpha_{air}} . D_{i-air\,@\,T} \tag{3-64}$$

$$\alpha_{gas} = \frac{k_g}{\rho_g C_{p,g}} \tag{3-65}$$

$$\frac{D_{ij,1}}{D_{ij,2}} = \frac{P_2}{P_1} . \left(\frac{T_1}{T_2}\right)^{3/2} \tag{3-66}$$

Table 3-2: Diffusion coefficients, in $m^2.s^{-1}$, of the different components in the air at atmospheric pressure.

Component "i"	Component "j"	D_{ij} ($m^2.s^{-1}$)	T (°C)	Reference
Benzene	Air	0.88×10^{-5}	25	[141]
Water Vapor	Air	2.5×10^{-5}	25	[141]
Toluene	Air	0.87×10^{-5}	23	[142]

Another method to compute the diffusion coefficient in multicomponent gas systems (D_{im}), of a component 'i' in a gas mixture, consists in using Blanc's law, based on the Stefan-Maxwell equation [143]:

$$D_{im} = \left(\sum_{j=1}^{n} \frac{x_j}{D_{ij}}\right)^{-1} \tag{3-67}$$

where x_j is the mole fraction of component j, D_{ij} is the binary diffusion coefficient of the *ij* system and n is the number of components in the mixture.

The binary diffusion coefficient is computed according to the equation developed by Fuller et al. [144]:

$$D_{ij} = \frac{0.00143 T^{1.75}}{P {M_{ij}}^{1/2} \left[(\sum)_i^{1/3} + (\sum)_j^{1/3}\right]^2} \tag{3-68}$$

$$M_{ij} = \frac{2}{(1/M_i) + (1/M_j)} \tag{3-69}$$

where D_{ij} is the binary diffusion coefficient of the *ij* system in $cm^2.s^{-1}$, T is the temperature in K, P is the pressure in bar, M_i and M_j are the molecular weights of "i" and "j" in $g.mol^{-1}$ and $\sum \upsilon$ is the sum of the atomic diffusion volumes for each component.

A comparison between the diffusion coefficients of the condensable components in the producer gas, computed according to eqs. (3-64) and (3-67), is performed. Figure 3-9 illustrates the variation of the diffusion coefficients of benzene (a), toluene (b) and water vapor (c) in the producer gas, function of the temperature, based on the two described calculation methods [130,143]. It can be observed that the correlation developed by Jeong and Levy [130] results in a higher diffusion coefficient, for all the components. It can be also noticed that, for both equations, the diffusion coefficient decreases when the temperature decreases. Note that he equation used by Jeong and Levy [130] is based on the assumption of a constant Lewis number, which is equal to one for the air. However, the Lewis number varies between the gases. Therefore, eqs. (3-67) to (3-69) are used to compute the diffusion coefficient in

multicomponent gas systems. The composition of the producer gas considered in eq. (3-67), is presented in the last column of Table 2-6.

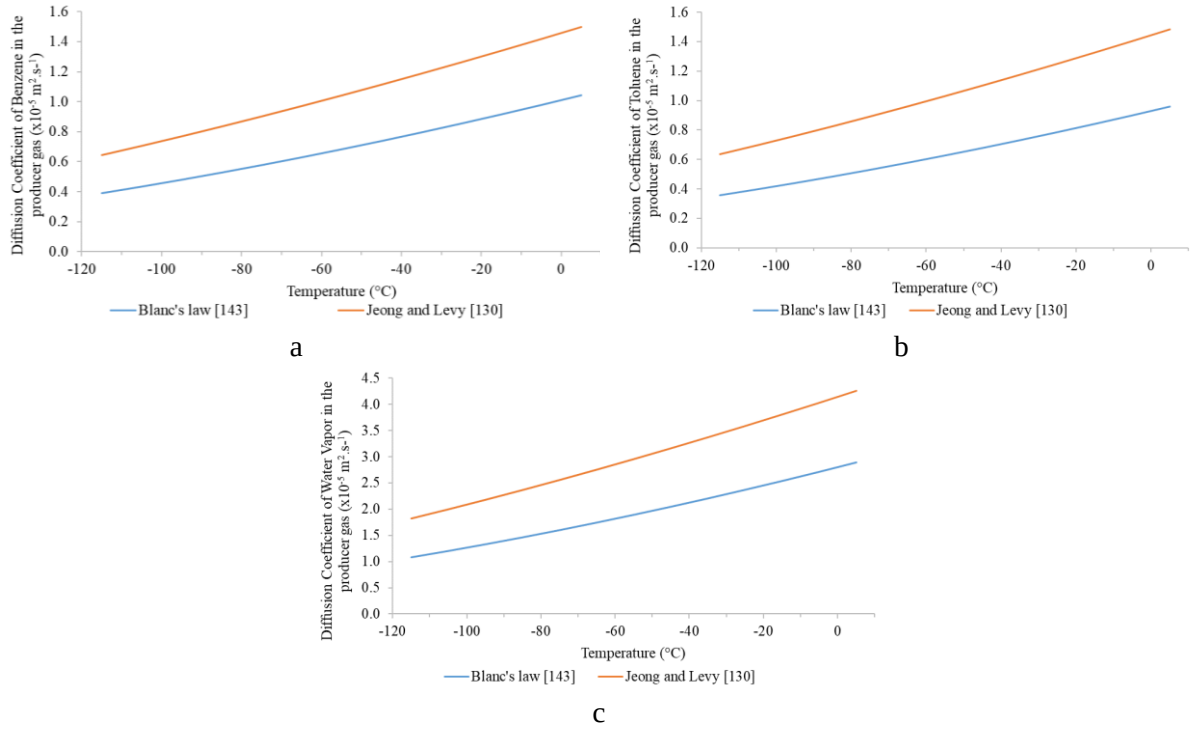

Figure 3-9: Variation of the diffusion coefficients of the benzene (a), toluene (b) and water vapor (c) in the producer gas, function of the temperature, for the two calculation methods [130,143].

As for the diffusion resistance factor, it depends on the porosity and tortuosity (τ):

$$\mu_i = {}^{\varepsilon_i}/_{\tau_i} \tag{3-70}$$

Several correlations for predicting the tortuosity, and therefore the diffusion resistance factor, have been proposed in different studies. Most of those studies are based on experiments [111], either over porous mediums such as catalyst, sand or glass spheres, or over a frost layer [145].

Some of the correlations lead to a diffusion resistance factor strictly lower than one, while other correlations result in a diffusion resistance factor higher than one. Note that a diffusion resistance factor of one corresponds to the diffusion of the vapor through the gas ($D_{eff,im} = D_{im}$). For instance, eqs. (3-71) and (3-72) respectively developed by Sanders [136] and Auracher [146], experimentally, lead to a diffusion resistance factor strictly lower than one. Therefore, the effective diffusion coefficient is strictly lower than the diffusion coefficient. According to Na and Webb [122], the diffusion resistance factor should be always lower than one, since the porosity cannot exceed a value of one and the tortuosity is always higher than one. On the contrary, eqs. (3-73) and (3-74) respectively developed by Le Gall and Grillot [138], and Tao et al. [147], lead to a diffusion resistance factor higher than one, for low frost densities. Therefore, the effective diffusion coefficient is higher than the diffusion coefficient. This phenomenon is known as the "hand-to-hand" diffusion, in which the diffusing substance and the solid are the same [138]. The described tortuosity correlations are given by:

$$\tau_i = \frac{\varepsilon_i}{1-(1-\varepsilon_i)^{0.5}} \tag{3-71}$$

$$\tau_i = 1 - 0.58(1-\varepsilon_i) \tag{3-72}$$

$$\tau_i = \frac{\varepsilon_i}{\frac{\varepsilon_i}{1 - C_0(1-\varepsilon_i)} + F_\mu k (1-\varepsilon_i)\varepsilon_i^k} \quad ; \quad C_0 = 0.58, k = 10, 0 \leq F_\mu \leq 10 \tag{3-73}$$

$$\tau_i = \frac{1}{1+F} \quad ; \quad 1 \leq F \leq 2 \tag{3-74}$$

Figure 3-10 illustrates a comparison between the different correlations used to predict the tortuosity, and therefore the diffusion resistance factor, function of the average frost density. It can be observed that each correlation results in a different diffusion resistance factor. The latter, if computed according to eqs. (3-71), (3-72) and (3-74), decreases as the average frost density increases. However, eq. (3-74) leads to diffusion resistance factors higher than 1. Eq. (3-73) is a compromise between the correlations developed by Auracher [146] and Tao et al. [147]. Initially, the diffusion resistance factor is equal to one. As the average frost density increases, the diffusion resistance factor increases, until reaching a maximum of 1.48 and 2.71 for $F_\mu = 1.5$ and $F_\mu = 5$, respectively. Afterwards, the diffusion resistance factor starts to decrease and becomes lower than 1 for an average frost density of 265 kg.m^{-3} and 340 kg.m^{-3} for $F_\mu = 1.5$ and $F_\mu = 5$, respectively.

In this thesis, the tortuosity is calculated based on eq. (3-72), which is the most used correlation for tortuosity prediction [136], unless stated otherwise.

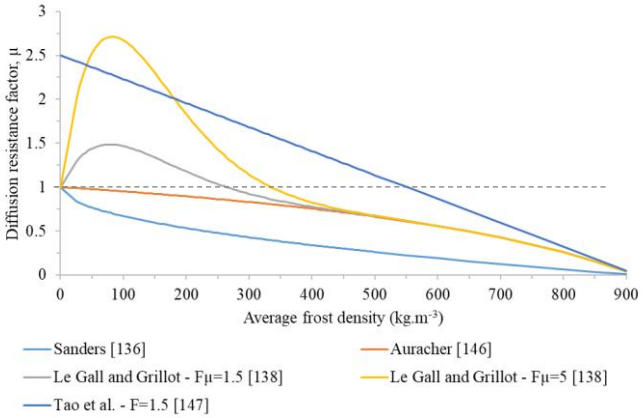

Figure 3-10: Variation of the diffusion resistance factor for several correlations, function of the average frost density.

3.2.9. Saturation mass fraction

The calculation procedure of the saturation mass fraction for benzene, toluene and water vapor in the producer gas, is previously developed in section 2.2. Note that the same calculation procedure is followed. However, the saturation line is not the same as the one presented in section 2.2., since an important water vapor fraction was removed in the scrubbers. Therefore, the equilibrium state is recalculated based on the new producer gas composition. A correlation for the variation of the mass fraction, function of the temperature, is then developed using the fitting function of excel. Several polynomial and logarithmic correlations were evaluated and compared with the original results previously obtained by calculations. The ones having the lowest error, thus the highest accuracy, were selected to be implemented in the model.

$$\log(w_{benz}) = 1.08 \times 10^{-6} T^3 - 9.60 \times 10^{-4} T^2 + 0.30T - 34.37 \tag{3-75}$$

$$\log(w_{wat}) = 2.43 \times 10^{-6} T^3 - 2.01 \times 10^{-3} T^2 + 0.58T - 60.60 \tag{3-76}$$

$$\log(w_{tol}) = -5.02 \times 10^{-8}T^4 + 5.10 \times 10^{-5}T^3 - 1.95 \times 10^{-2}T^2 + 3.34T - 221.43 \quad (3\text{-}77)$$

In fact, the values in eqs. (3-75) to (3-77) are obtained by rounding the practically used values, that are with 14 decimal numbers.

3.2.10. Heat transfer coefficient

Several correlations for computing the convective heat transfer coefficient in frosting applications are found in the literature [111,132]. These equations are summarized in Table 3-3. The most used correlations are given in eqs. (3-78) and (3-79). Eq. (3-78) is basically used for laminar flow over smooth flat plates, while eq. (3-79) is used for frosting over two parallel flat plates. In fact, in almost all the experimental studies, the producer gas is cooled by flowing inside a duct having the bottom wall cooled to a low temperature. For this purpose, eqs. (3-80) to (3-82) are also used. Eq. (3-80) and eq. (3-81) are developed for smooth surfaces, while eq. (3-82) considers rough surfaces.

Table 3-3: Summary of the convection correlations.

Nusselt number equation	Reference	
$Nu_x = 0.332 Re_x^{\frac{1}{2}} Pr^{\frac{1}{3}}$, Smooth flat plate, $\mathrm{Re} < 5 \times 10^5$	[148]	(3-78)
$Nu_{Dh} = 0.0342 Re_{Dh}^{0.8}$, Two parallel flat plate with frost, $6000 < \mathrm{Re} < 50000$	[114]	(3-79)
$Nu_{Dh} = \begin{cases} 0.0214\left(Re_{Dh}{}^{0.8} - 100\right)Pr^{0.4}, \\ 0.5 < Pr < 1.5 \; and \; 10^4 < Re_{Dh} < 5 \times 10^6 \\ 0.012\left(Re_{Dh}{}^{0.87} - 280\right)Pr^{0.4}, \\ 1.5 < Pr < 500 \; and \; 3000 < Re_{Dh} < 10^6 \end{cases}$	[148]	(3-80)
$Nu_{Dh} = 0.023 Re_{Dh}^{0.8} Pr^{0.3}$	[148]	(3-81)
$Nu_{Dh} = \dfrac{\left(\frac{f}{8}\right)(Re^{0.8} - 1000)Pr}{1 + 12.7\left(\frac{f}{8}\right)^{\frac{1}{2}}\left(Pr^{\frac{2}{3}} - 1\right)}$, Rough duct, $3000 < \mathrm{Re} < 5 \times 10^6$	[149]	(3-82)

Those equations are originally developed for tube flow but they can be also applied for rectangular ducts by using the hydraulic diameter:

$$D_h = {}^{4A}/_{P} \quad (3\text{-}83)$$

where *A* is the flow cross-sectional area and *P* is the wetted perimeter.

Note that the hydraulic diameter and the cross-sectional area are not constant due to the frost accumulation over the time. Therefore, the effective hydraulic diameter ($D_{h,eff}$) and the effective cross-sectional area (A_{eff}) are introduced in order to take into consideration the reduction in the gas passage. The effective cross-sectional area of the duct can be expressed by eq. (3-84). $D_{h,eff}$ is then computed function of A_{eff}, according to eq. (3-83). The latter is also used to compute the variation of the gas velocity along the x-axis due to the frost accumulation.

$$A_{eff} = \left(h_p - \delta_{fr,wat} - \delta_{fr,benz}\right).w_{plate} \quad (3\text{-}84)$$

The appropriate Nusselt number equation is selected depending on the values of Reynold's number $\left(Re = {\rho_g v_g D_h}/{\mu_g}\right)$ and Prandtl number $\left(Pr = {\mu_g C_{p,g}}/{k_g}\right)$. The convective heat transfer coefficient $\left(h_{c,g}\right)$ is then calculated as:

$$h_{c,g} = {Nu.\,k_g}/{D_{h,eff}} \quad (3\text{-}85)$$

3.2.11. Mass transfer coefficient

The mass transfer coefficient (k_m) is calculated according to the heat and mass transfer analogy, also known as Chilton-Colburn analogy, based on Lewis number (Le):

$$k_{m,A} = {h_{c,g}}/{\rho_g C_{p,g} {Le_A}^{2/3}} \quad (3\text{-}86)$$

where:

$$Le_A = {k_g}/{\rho_g C_{p,g} D_{A-gas}} \quad (3\text{-}87)$$

Note that, in eqs. (3-86) and (3-87), the subscript 'A' ($A \in \{benzene, water\ vapor, toluene\}$) is used to avoid repetition.

Other mass transfer coefficient computation approaches were developed for the specific case of frost formation. However, these approaches are not widely used because they are limited to the operating conditions of the experimental setup and to the water vapor frosting from moist air. For instance, Tokura et al. [150] developed an equation that correlates the Sherwood number (Sh) to the Reynolds number based on experimental measurement at a length x, in order to calculate the mass transfer coefficient:

$$Sh_{x,A} = \frac{k_{m,A} x}{D_{A-gas}} = 1.72 \times 10^{-2} Re_x^{0.8} \quad (3\text{-}88)$$

Consequently, the heat and mass transfer analogy, presented in eq. (3-86), is used to calculate the mass transfer coefficient.

3.3. Carbon dioxide frosting

The tar removal requirement of temperature reduction to -110°C leads to the simultaneous CO_2 frosting, depending on the producer gas composition. The CO_2 dew point depends on the initial CO_2 content present in the gas. Figure 3-11 presents the carbon dioxide phase diagram. Based on the producer gas composition previously described in Table 1-3, the molar fraction of CO_2 initially present in the gas, after drying, does not exceed 0.3. Therefore, it can be seen in Figure 3-11 that, for the highest CO_2 initial content, the frosting starts for wall temperatures below -92°C. For instance, for the composition considered in Table 2-6 which corresponds to a CO_2 molar fraction of 0.2, the CO_2 frosting starts at wall temperatures below -96°C, as seen in Figure 3-11. Therefore, the last stage of tar removal at low temperatures involves a partial CO_2 frosting that cannot be avoided.

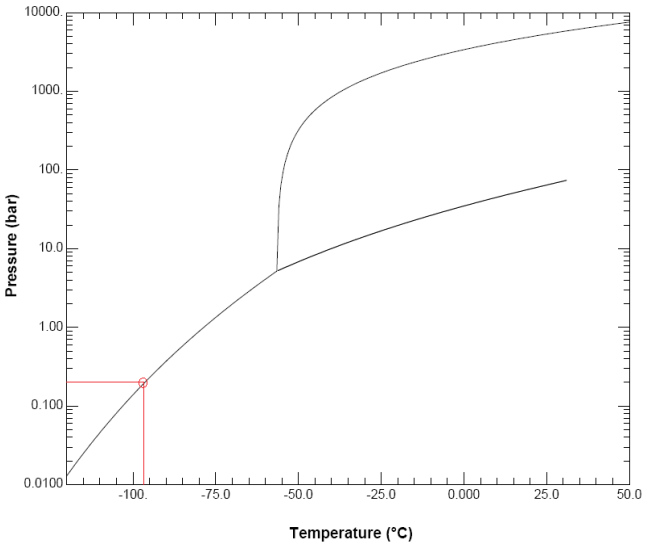

Figure 3-11: Carbon dioxide phase diagram [151].

The CO_2 frosting model and the CO_2 properties were intensively studied by previous researchers in the research center [152]. Therefore, they are not detailed in this thesis. However, the previous CO_2 frost growth models were developed based on a 1D analysis, while in this thesis, the model has been modified to a 2D frost growth analysis. In order to take into consideration the CO_2 frost formation at low temperatures, it is assumed that an additional carbon dioxide frost layer is built-up on the top of the frost layers of ice and benzene. The same equations detailed in section 3.2.3.4 apply for the CO_2 frost layer. A new interface between the water and the carbon dioxide layers is considered. The overall heat balance around each control volume in the gas phase is modified to cover the CO_2 frosting:

$$\dot{Q}_{total} = \dot{Q}_{sens} + \dot{m}_{s,benz}.L_{sv,benz} + \dot{m}_{s,wat}.L_{sv,wat} + \dot{m}_{s,tol}.L_{vap,tol} + \dot{m}_{s,CO_2}.L_{sv,CO_2} \quad (3\text{-}89)$$

$$\dot{m}_{s,CO_2} = k_{m,CO_2}.S.\rho_g.\left(w_{g,CO_2} - w_{s,CO_2}\right) \quad (3\text{-}90)$$

where $\dot{m}_{s,CO_2}$ is the total mass flow rate of carbon dioxide transferred from the producer gas to the frost surface, k_{m,CO_2} represents the mass transfer coefficients of CO_2 in $m.s^{-1}$, w_{g,CO_2} and w_{s,CO_2} are respectively the mass fraction of the CO_2 in the gas and at the frost surface, and L_{sv,CO_2} is the latent heat of CO_2 sublimation, in $J.kg^{-1}$.

It is important to mention that the CO_2 removal in the process of combining biomass gasification with producer gas methanation is a necessary step. Therefore, the CO_2 frosting within the tar removal at low temperatures might be advantageous on the overall process of converting the biomass into biomethane. It was previously seen in Figure 1-22 that, the CO_2 removal in the GoBiGas project is performed in two steps. A fraction of CO_2 is removed in unit (14), after the tar removal units (7 and 8), and before the water gas shift reaction unit (16) which targets the removal of hydrogen sulphides. The remaining fraction of CO_2, in addition to the CO_2 regenerated in the water gas shift reaction, are then removed in unit (18) before the methanation unit. The details of the CO_2 removal within the gasification process and the impact of the partial CO_2 removal, are out of the scope of this thesis. Only the impact of the simultaneous CO_2 removal on the energy required in the tar removal process is included. Note that reducing the CO_2 content before the WGS reaction is advantageous since it favors the reaction towards the formation of H_2, which is then converted into CH_4, as shown in Appendix B.

3.4. Model validation

Models that handle a simultaneous multi-component frosting and condensation do not exist. Thus, the heat and mass transfer equations were first validated by comparing the model results to different previously developed studies, for the case of water vapor frosting in humid air and for the case of carbon dioxide frosting from CO_2-N_2 mixture.

3.4.1. One-dimensional: water vapor frosting from humid air

In this section, a comparison between the results obtained by the proposed model and the ones retrieved from Lee et al. [121], is conducted. Note that the latter experiment is chosen to compare with since it constitutes a basis for models validation in the literature [111,120,132].
As a first step, the model is validated for a one-dimensional frost growth, which varies only along the y-axis. Note that the water vapor properties remain the same for the validation, while the air properties are considered instead of those of the producer gas in order to have good inputs for the result comparison.

The following plate dimensions are used: $L_p = 300\ mm, w_p = 150\ mm$ and $h_p = 150\ mm$. Several operating conditions, presented in Table 3-4, are considered to validate the model.

Table 3-4: Operating conditions used in the experiments of Lee et al. [121].

	T_{wall} (°C)	T_g (°C)	X_{wat} $(kg.kg^{-1})$	V_g $(m.s^{-1})$
Case 1	-20	10	0.00528	1.75
Case 2	-15	15	0.00633	2.5
Case 3	-15	5	0.00322	1

The initial conditions are previously mentioned in section 3.2.5. Eq. (3-57) is used for the calculation of the effective thermal conductivity. Eq. (3-72) is used to compute the tortuosity for the effective diffusion coefficient calculation. A sensitivity study is performed to assess the effect of the number of meshes on the results. This study is shown in Appendix C. Based on the latter, and since the simulation time did not significantly vary, 50 meshes are considered for a more robust model and a higher comparison accuracy.

Figure 3-12, Figure 3-13, Figure 3-14 and Figure 3-15 illustrate a comparison between the proposed model and the experimental results [121] for the temporal variation of the frost layer thickness, the frost surface temperature, the average frost density and the heat fluxes, respectively. It can be observed in these figures that the results show a good agreement between the model and the experiments for the frost thickness, the frost surface temperature and the heat fluxes, while the model overestimates the average frost density. Note that in Figure 3-14, the modeled frost density corresponds to the average frost density, while in the experimental results of Lee et al. [121], the location of the measured frost density was not mentioned. This might be the reason of the deviation between the results. In Figure 3-15, the total heat flux is divided between latent heat and sensible heat fluxes. No important variation is observed in the latent heat. The sensible heat flux decreases with time, resulting in a decreasing total heat flux. It can be noticed from the figures that, although there is an agreement between the frost thickness and the heat fluxes, the frost density was overestimated. This might be caused by the lack of information on several parameters such as the heat transfer coefficient and the effective diffusion coefficient, which highly affects the result. Another reason could be the deviations between the thermo-physical properties of air and water vapor. Finally, it can be deduced that the proposed model results in an accurate prediction of the heat and mass transfer during the one-dimensional frost growth, over a wide range of operating conditions.

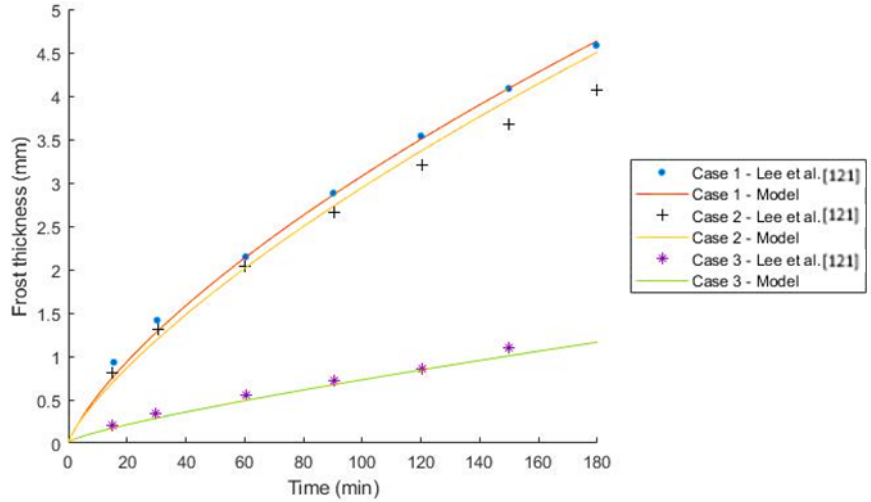

Figure 3-12: Validation of the 1D frost growth model for the variation of the frost layer thickness over time, based on a comparison with Lee et al. [121].

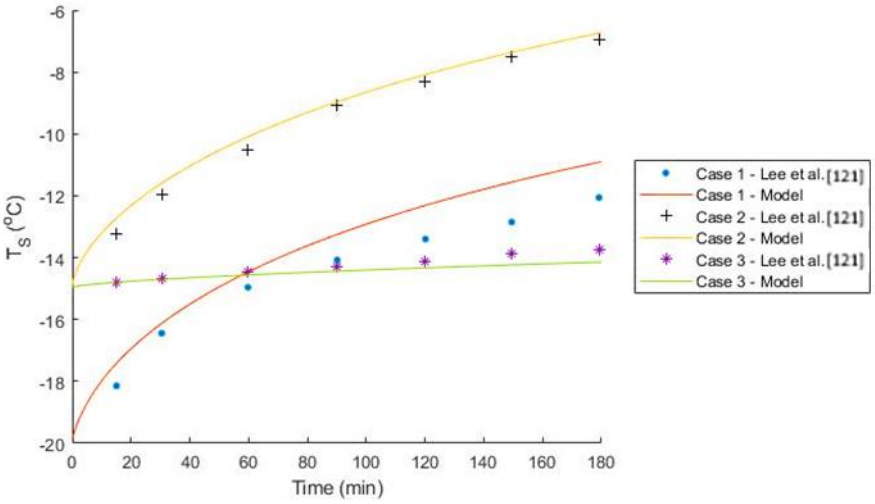

Figure 3-13: Validation of the 1D frost growth model for the variation of the frost surface temperature over time, based on a comparison with Lee et al. [121].

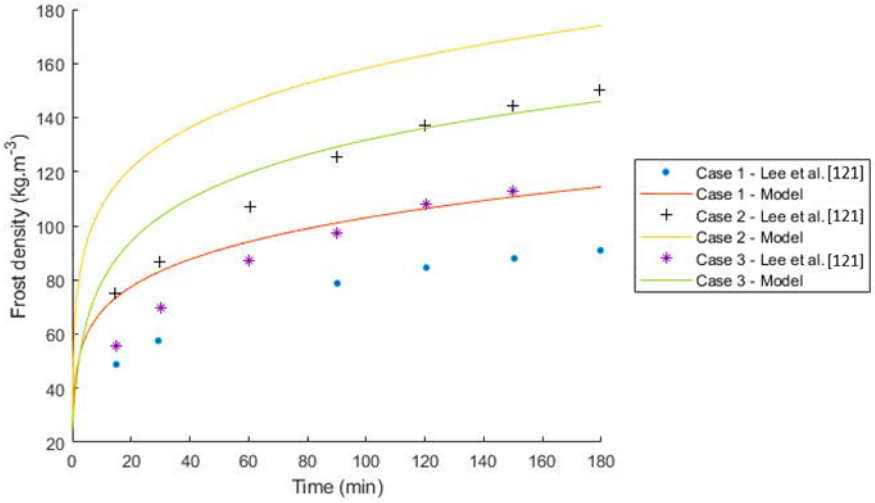

Figure 3-14: Validation of the 1D frost growth model for the variation of the average frost layer density over time, based on a comparison with Lee et al. [121].

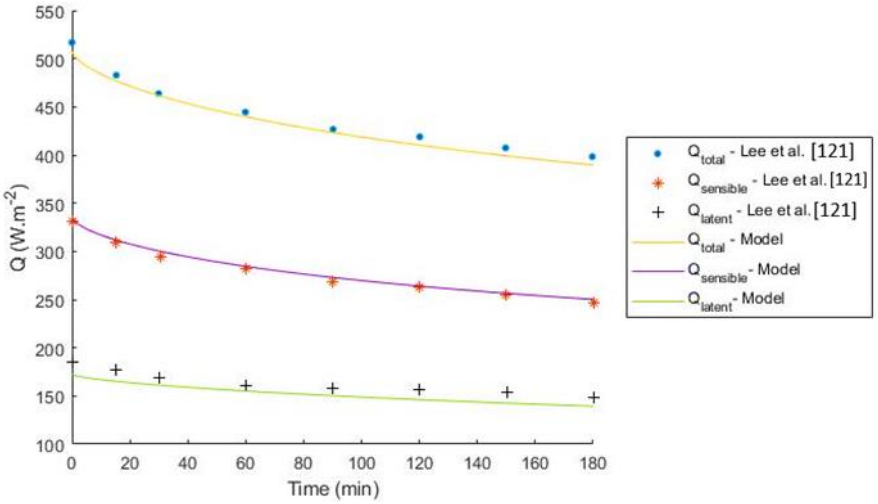

Figure 3-15: Validation of the 1D frost growth model for the variation of the heat flux over time for Case 2 in Table 3-4, based on a comparison with Lee et al. [121].

3.4.2. Two-dimensional

3.4.2.1 Water vapor frosting from humid air

After validating the model for one-dimensional frost growth, a more advanced step for the model validation in two-dimensional frost growth is conducted. The model results are compared with Lee et al. [120] for water vapor frosting from humid air. The results found in the literature for the two-dimensional frost growth are CFD-based models.

Note that the following plate dimensions are used in this section: $L_p = 50\ mm, w_p = 5\ mm$ and $h_p = 5\ mm$. It is important to mention that the correlations of the computation of several parameters, such as the effective diffusion coefficient and the heat transfer coefficient, are not detailed in the literature [120]. This might lead to important deviations between the proposed model results and those retrieved from the published paper. Eqs. (3-57) and (3-72) are used for the calculation of the effective thermal conductivity and the tortuosity, respectively. The operating conditions are: $T_{wall} = -40$°C, $T_g = 8$°C, $X_{wat} = 0.0033\ kg.kg^{-1}$ and $V_g = 1.5\ m.s^{-1}$. Note that a meshing of 20 x 20 is considered.

Figure 3-16 presents a comparison between the variation of the frost thickness and the frost density, along the plate length after 20 min, 40 min and 60 min of cooling, obtained by the proposed model (a) and by Lee el al. [120] (b). It can be observed that the model underestimates the frost thickness. The representation found in the literature is used in these figures. The frost density has the same behavior in the proposed model and in the one of the literature, where the frost layer density increases with time. The frost density varies between 40 and 150 kg.m^{-3}, the highest frost density is encountered at the first 10 mm of the plate and at the lower part of the frost. Finally, the frost density decreases along the frost thickness and along the plate length.

a

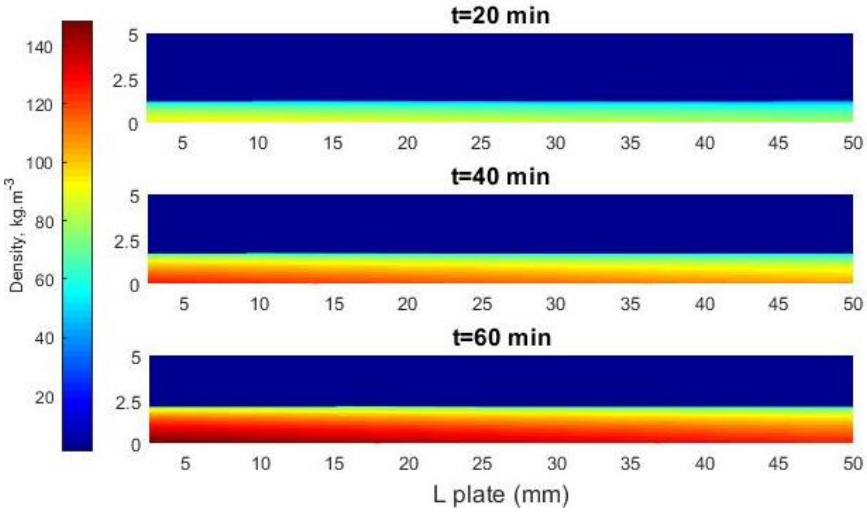

b

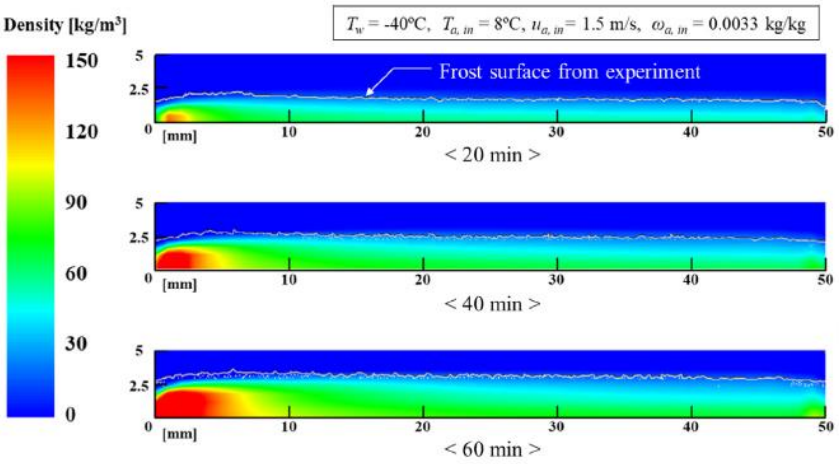

Figure 3-16: Validation of the 2D frost growth model: frost density and frost thickness obtained by the proposed model (a) and by Lee et al. [120] (b).

Figure 3-17 and Figure 3-18 illustrate a comparison between the model and the literature results for the temporal variation of the frost surface temperature and the total heat flux, respectively. It can be observed that the proposed model succeeds in computing the frost surface temperature. The temporal variation of the heat flux is slightly overestimated by the model. This might be the result of using different correlations for the computation of the heat and mass transfer coefficients.

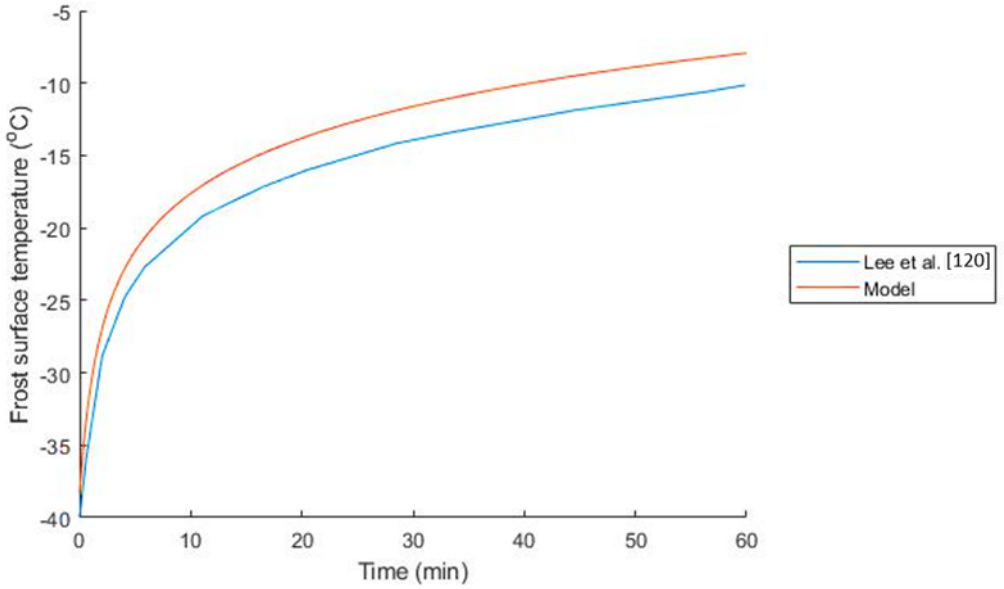

Figure 3-17: Validation of the 2D frost growth model based on a comparison with Lee et al. [120], for the variation of the frost surface temperature over time.

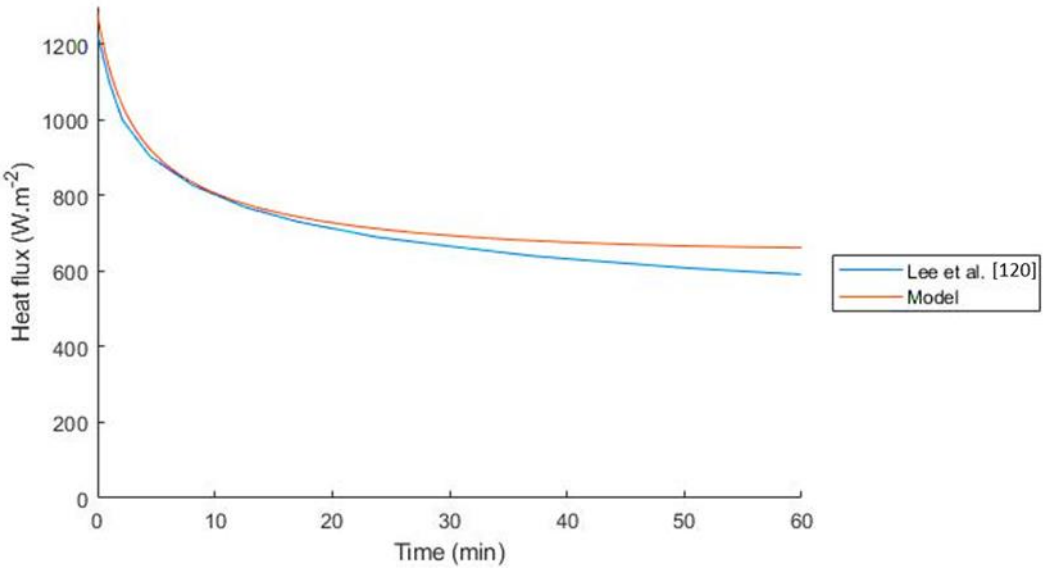

Figure 3-18: Validation of the 2D frost growth model based on a comparison with Lee et al. [120], for the variation of the heat flux over time.

3.4.2.2 CO_2 frosting from CO_2-N_2 mixture

In this section, a comparison between the results obtained by the proposed model and the experimental results retrieved from Shchelkunov et al. [153], for the frosting of CO_2 from a CO_2-N_2 mixture, is conducted. The case of CO_2 is also considered since it takes place at temperatures lower than those required for the H_2O frosting, which corresponds to the case of benzene frosting.

The model is validated for a 2D CO_2 frost growth, which varies along the x-axis and y-axis. It is important to mention that the CO_2 properties are considered in this section for the frost layer, while the N_2 properties are used for the gas phase in order to have good inputs for the results comparison.
The following plate dimensions are used in this section: $L_p = 56\ mm$ and $w_p = 56\ mm$. Different operating conditions are considered to validate the model, including the wall temperature, the gas temperature, the initial CO_2 content and the gas velocity. The different cases studied in the model

validation are summarized in Table 3-5. The mass fraction of CO_2 is calculated using Dalton's law, for a total pressure of 0.1 MPa. The initial conditions are previously mentioned in section 3.2.5. The effective thermal conductivity is computed using the correlation developed by Haddad et al. [154], based on the experimental results of Shchelkunov et al. [153]:

$$k_{eff} = \frac{0.27\rho_{fr,avg}}{2386.037 - \rho_{fr,avg}} \tag{3-91}$$

Eq. (3-72) and (3-81) are used to compute the tortuosity for the calculation of the effective diffusion coefficient and the heat transfer coefficient, respectively.

Table 3-5: Operating conditions for the experiments conducted by Shchelkunov et al. [153].

	T_{wall} (°C)	T_g (°C)	$VP_{CO_2}(kPa)$	$X_{CO_2}(kg.kg^{-1})$	$V_g\,(m.s^{-1})$
Case 1	-128	-80	4.35	0.0715	3
Case 2	-128	-80	4.35	0.0715	0.5
Case 3	-122	-74	8.76	0.1510	3

Figure 3-19 and Figure 3-20 illustrate a comparison between the model and the experimental results for the temporal variation of the frost density and the frost layer thickness, respectively. It can be observed from these figures that the results show a good agreement between the model and the experiments for the frost density, while the model underestimates the average frost thickness. Note that, the model results shown in the figures correspond to the averaged values along the plate length and the frost thickness, for the sake of comparison with the published experimental data. Shchelkunov et al. [153] mentioned that the distribution of the frost thickness along the plate length is not uniform, and it varies within a range of 1 to 3 mm. Therefore, the deviation between the results obtained by the proposed model and the experimental results might be due to the non-uniform frost thickness distribution in the experiment.

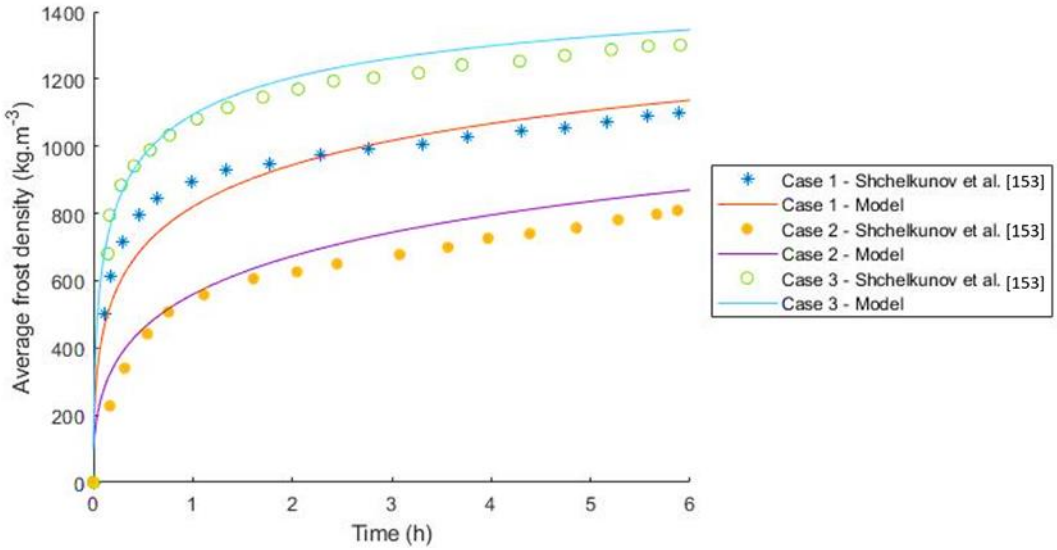

Figure 3-19: Validation of the 2D frost growth model based on a comparison with Shchelkunov et al [153], for the variation of the CO_2 average frost density over the time.

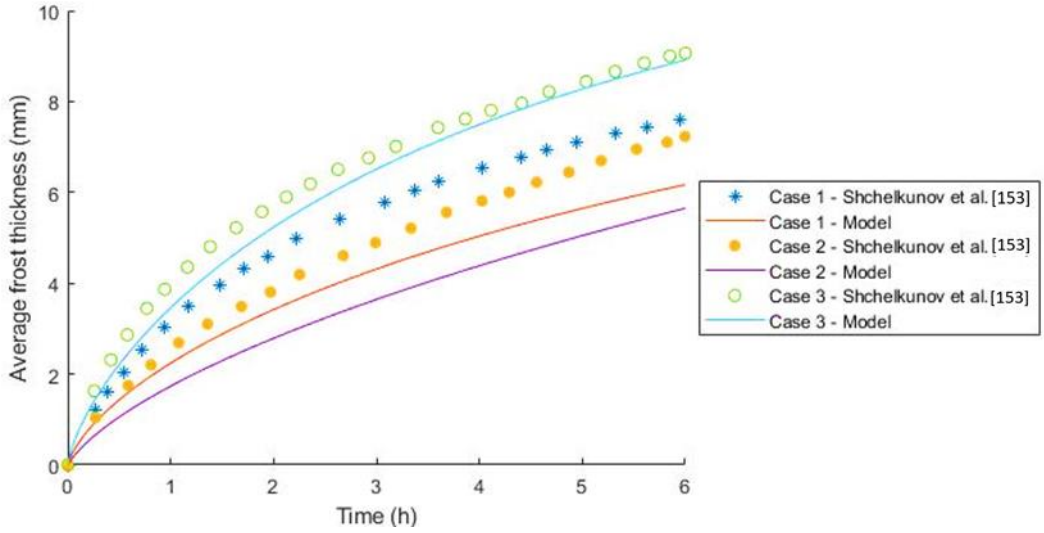

Figure 3-20: Validation of the 2D frost growth model based on a comparison with Shchelkunov et al [153], for the variation of the CO_2 average frost layer thickness over the time.

It can be observed that, for the three studied cases, the frost density highly increases at the beginning and then it becomes almost constant after two hours of operation. This is related to the thermal resistivity increase, and thus the increase in the frost surface temperature. As for the frost thickness, the latter increases as the time increases. However, the frost growth rate varies along the frosting process, and it becomes slower as the operational time increases. The increase in the CO_2 frost thickness has the same shape of the H_2O frosting (cf. Figure 3-12). However, the densification process, which is a result of the internal diffusion, is more important in the case of CO_2 frosting. This is a result of the higher initial partial pressure of CO_2. Note that by reducing the gas velocity (case 2), the heat transfer coefficient decreases and results in a lower frost density and frost thickness. Furthermore, the highest frost density and frost thickness are achieved for case 3, which corresponds to a higher CO_2 initial partial pressure.

It can be deduced that the proposed model results in an accurate prediction of the heat and mass transfer for 1D and 2D frost growth, over a wide range of operating conditions for H_2O and CO_2 frosting. In the next section, besides the frost growth of water vapor and carbon dioxide, the model is extended to cover the frost growth of benzene and the condensation of toluene.

3.5. Model results and discussion

This section deals with the tar components (benzene and toluene) removal, by simultaneous deposition (from gas to solid) and condensation (from liquid to solid), at low temperature. This drives the water vapor present in the producer gas to form an additional frost layer. Heat and mass transfer equations are previously detailed in section 3.2. The producer gas temperature, its flow rate, the wall temperature, the surface area and the tar content are the parameters affecting the tar components transfer from the gas phase to the condensate. Those parameters must be studied in order to optimize the tar removal process. In this section, the model is developed based on a constant wall temperature. A two-dimensional frost growth is considered. Based on a sensitivity study, the meshing is considered equal to 20x20 for each of the benzene and ice frost layers.

The initial inlet gas temperature and composition are considered as fixed parameters, since they result from the water scrubber simulations previously described in section 2.3. Therefore, the main parameters that can be varied are the wall temperature, the gas velocity and the plate dimensions. A parametric study is then conducted in order to assess the parameters impact on the tar removal, more precisely on the frost growth thickness, the frost density, the gas temperature and the heat fluxes.

After assessing the impact of the different parameters on the frost growth and on the tar removal, several plates, placed in series, are considered with a decreasing wall temperature. After simulating the first plate, its outlet conditions are used as input parameters for the second plate until reaching the desired outlet temperature.

Figure 3-21 summarizes the followed steps in order to solve the mathematical model. As for the single plate analysis, the model stops after a single run at the output. When several plates are placed in series, the process targets to reach the desired tar content, and thus one plate is added at each run until reaching the final objective.

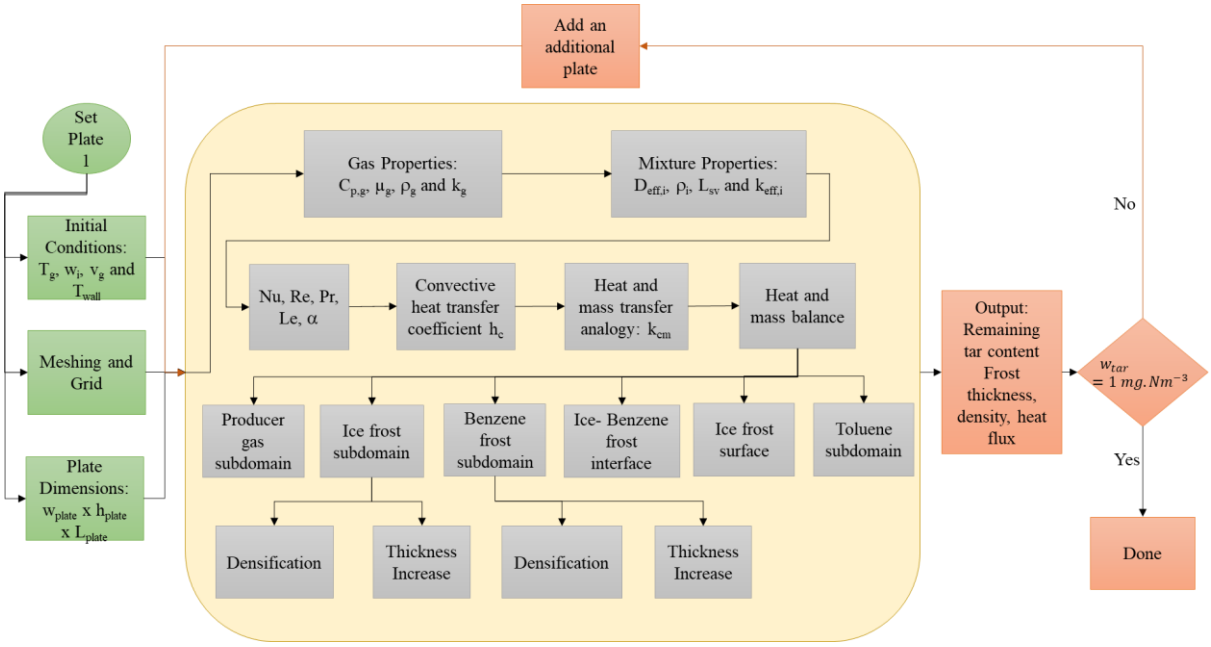

Figure 3-21: Schematic representation of the considered procedure to solve the mathematical model on Dymola.

3.5.1. Single plate

The parametric study is done for only one plate. This allows analyzing the impact of each parameter on the obtained results. Table 3-6 summarizes the different operating conditions considered for the parametric study. It can be seen that the initial gas temperature is fixed for all the cases. This temperature is equal to the outlet temperature of the pre-treatment section.

Table 3-6: Inlet conditions of the first plate.

Plate 1	T_{wall} (°C)	T_g (°C)	X_{benz} $(kg.kg^{-1})$	X_{tol} $(kg.kg^{-1})$	X_{wat} $(kg.kg^{-1})$	V_g $(m.s^{-1})$	Plate dimensions $w_p \times h_p \times L_p$ (m^3)
Case 1	-20	5	0.089	0.0142	0.0075	0.6	$0.05 \times 0.05 \times 5$
Case 2	-20	5	0.089	0.0142	0.0075	1.5	$0.05 \times 0.05 \times 5$
Case 3	-25	5	0.089	0.0142	0.0075	1	$0.05 \times 0.05 \times 5$
Case 4	-25	5	0.063	0.0092	0.0075	1	$0.05 \times 0.05 \times 5$
Case 5	-25	5	0.063	0.0092	0.0075	0.6	$0.05 \times 0.025 \times 5$
Case 6	-25	5	0.063	0.0092	0.0075	1	$0.05 \times 0.025 \times 5$
Case 7	-25	5	0.063	0.0092	0.0075	2	$0.05 \times 0.025 \times 5$
Case 8	-30	5	0.063	0.0092	0.0075	1	$0.05 \times 0.025 \times 5$
Case 9	-30	5	0.063	0.0092	0.0075	1	$0.15 \times 0.15 \times 5$

In cases 1, 2 and 3, the sum of the initial benzene and toluene contents is considered equal to 100 $g.Nm^{-3}$. The latter corresponds to the highest possible tar content after the gasifier. In the other cases,

the initial benzene and toluene contents are considered equal to their remaining contents at the exit of the scrubbers (cf. Table 2-6). In cases 1 to 4, a square duct is considered where the width of the plate is equal to the height of the gas channel. In cases 5 to 8, a rectangular duct is assessed by reducing the height of the channel by two. In the last case, a larger square duct is considered to assess the impact of the geometry on the heat and mass transfer between the gas and the surface. A comparison between case 2 and case 4, and between cases 5, 6 and 7, allows to evaluate the impact of the velocity, and thus the mass flow rate, on the frost growth. The impact of the duct height is evaluated by comparing case 4 with case 6, the impact of the initial benzene and toluene contents is analyzed by comparing case 3 with case 4, and the impact of the wall temperature is assessed by comparing case 6 with case 8. The plate dimensions are selected based on the ones used in the literature [110,121].

3.5.1.1 Gas temperature

Figure 3-22 illustrates the variation of the gas temperature function of the plate length and the time, for the different inlet conditions shown in Table 3-6. It can be observed that, in all the cases, the gas temperature is decreasing along the plate length while it is increasing with respect to the operating time. The lowest gas temperature at the end of the plate is reached in case 5, while the highest one is obtained in case 9. In addition, the gas temperature variations in case 1 and case 2 are close. However, it can be seen that in case 1, the increase rate of the gas temperature at the end of the plate, function of time, is lower than that of case 2. Reducing the wall temperature in cases 3 and 4, results in a lower gas temperature, by increasing the temperature difference between the producer gas and the plate. A lower benzene and toluene initial content slightly affects the gas temperature, as observed when comparing case 3 with case 4. Moreover, it can be noticed by comparing case 4 with case 6 that, by reducing the duct height and thus the mass flow rate, while keeping a constant velocity, the gas temperature highly decreases at the end of the plate. According to cases 5, 6 and 7, increasing the gas velocity leads to a higher increase rate of the gas temperature. Furthermore, reducing the wall temperature in case 8 results in a lower gas temperature at the end of the plate. Finally, increasing the duct height highly reduces the heat transfer between the gas and the plate, leading to a higher gas temperature even for a lower wall temperature. Note that, analyzing the parameters impact on the gas temperature is crucial, since the main objective of this thesis is to reduce the tar content, which is directly related to the gas temperature.

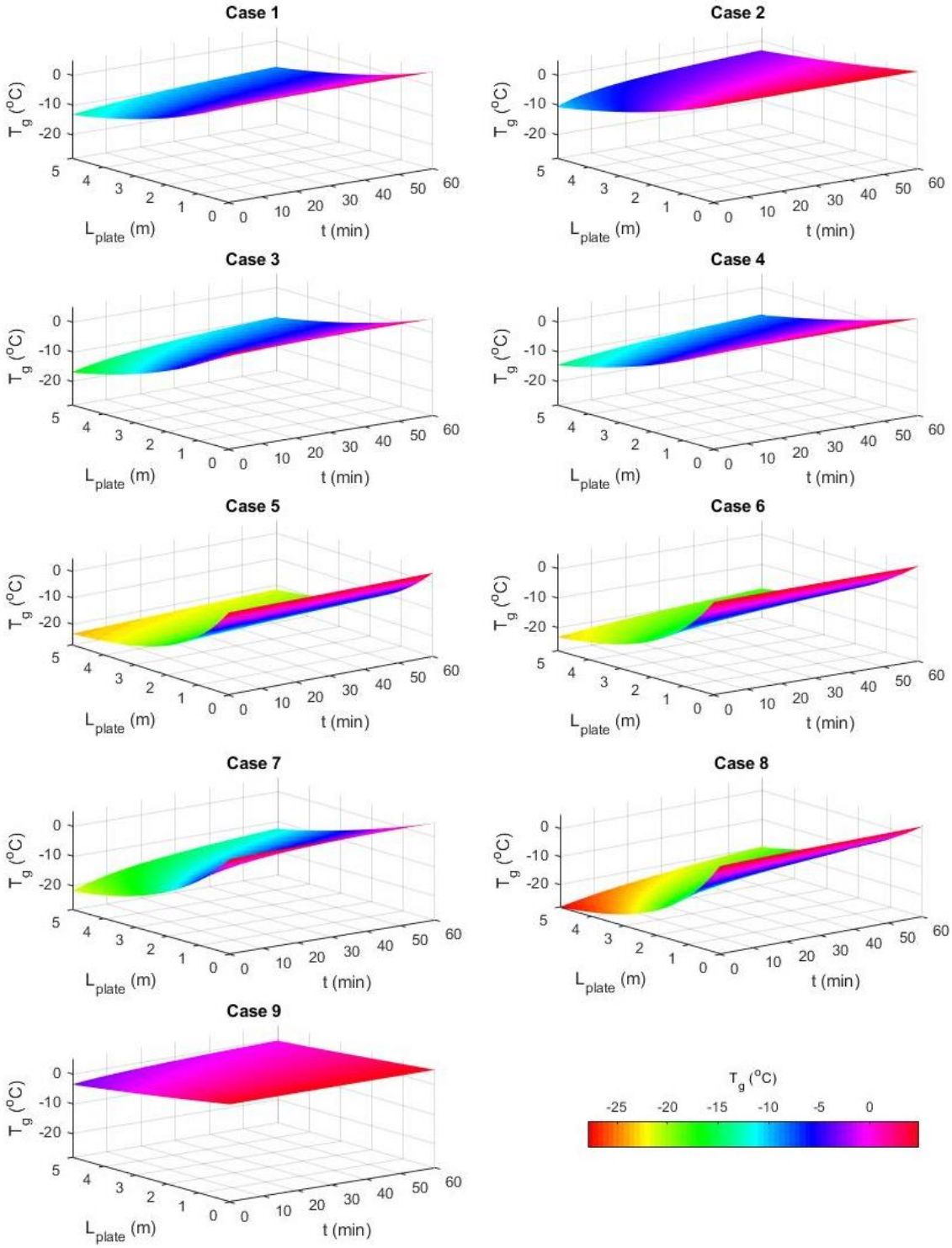

Figure 3-22 : Variation of the gas temperature function of the plate length and the time, for different initial conditions.

3.5.1.2 Benzene and toluene remaining content

Figure 3-23 illustrates the variation of the benzene mass fraction (X_{Benz}) remaining in the producer gas, function of the plate length and the time, for the different inlet conditions shown in Table 3-6. It can be observed that, in all the cases, X_{Benz} is decreasing along the plate length while it is slightly increasing with respect to the operating time.

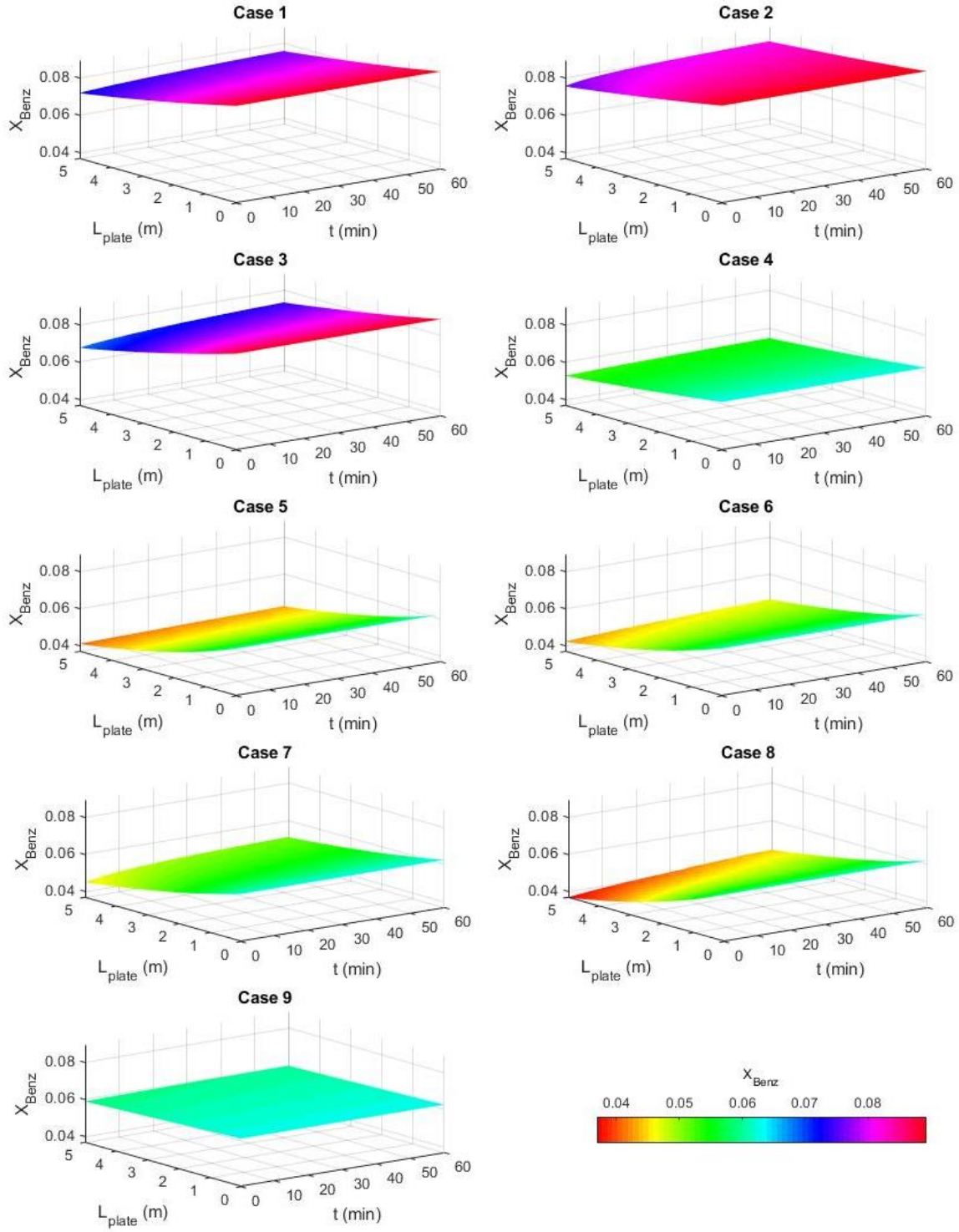

Figure 3-23: Variation of the benzene mass fraction remaining in the gas phase, function of the plate length and the time, for different initial conditions.

In addition, by comparing case 1 with case 2, and case 5 with cases 6 and 7, it can be seen that increasing the gas velocity leads to a higher X_{Benz}. This is related to the decreasing residence time of the producer gas inside the duct. Consequently, the highest reduction in the benzene content is achieved in case 1 and case 5 for the square and rectangular ducts, respectively. Moreover, reducing the wall temperature in cases 3 and 8, results in a lower X_{Benz} by increasing the concentration difference between the producer gas and the frost surface. As a result, case 8 leads to the lowest X_{Benz} and the highest reduction rate. It can be also seen that, by comparing case 3 to case 4, a lower initial benzene content leads to a lower

concentration difference between the producer gas and the frost surface. Consequently, a lower benzene reduction is reached, and therefore a higher X_{Benz} in case 4. Furthermore, it can be noticed by comparing case 4 with case 6 that, reducing the duct height, thus reducing the mass flow rate while keeping a constant velocity, leads to a higher benzene content reduction along the plate length. Therefore, a lower X_{Benz} is achieved in case 6. Finally, highly increasing the duct height reduces the mass transfer between the producer gas and the frost surface, leading to almost a constant X_{Benz}.

Figure 3-24 illustrates the variation of the toluene mass fraction (X_{tol}) remaining in the producer gas, function of the plate length and the time, for the different inlet conditions shown in Table 3-6.

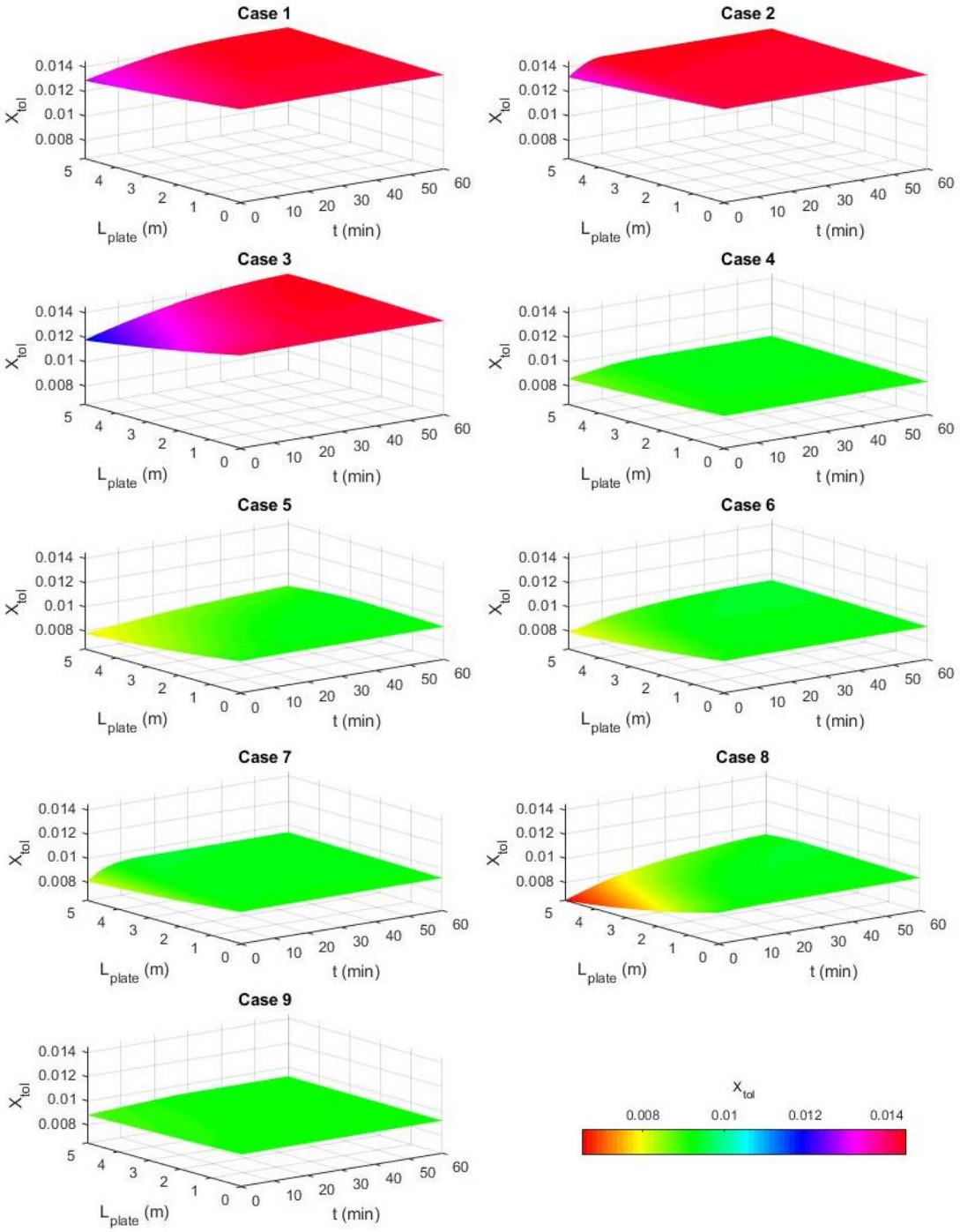

Figure 3-24: Variation of the toluene mass fraction remaining in the gas phase, function of the plate length and the time, for different initial conditions.

It can be observed that, in all the cases, X_{tol} is slightly decreasing with respect to the plate length. For instance, in cases 1, 2, 4, 5, 6, 7 and 9, the toluene content is not affected. In cases 3 and 8, the toluene content slightly decreases at the end of the plate for the first 20 minutes of operation, due to the lower wall temperature. However, the toluene condensation stops after 20 minutes of operation, due to the formation of frost layers, which limits the heat transfer and increases the frost surface temperature.

3.5.1.3 Frost thickness

Figure 3-25 presents the variation of the benzene frost thicknesses function of the plate length and the time, for the different inlet conditions shown in Table 3-6.

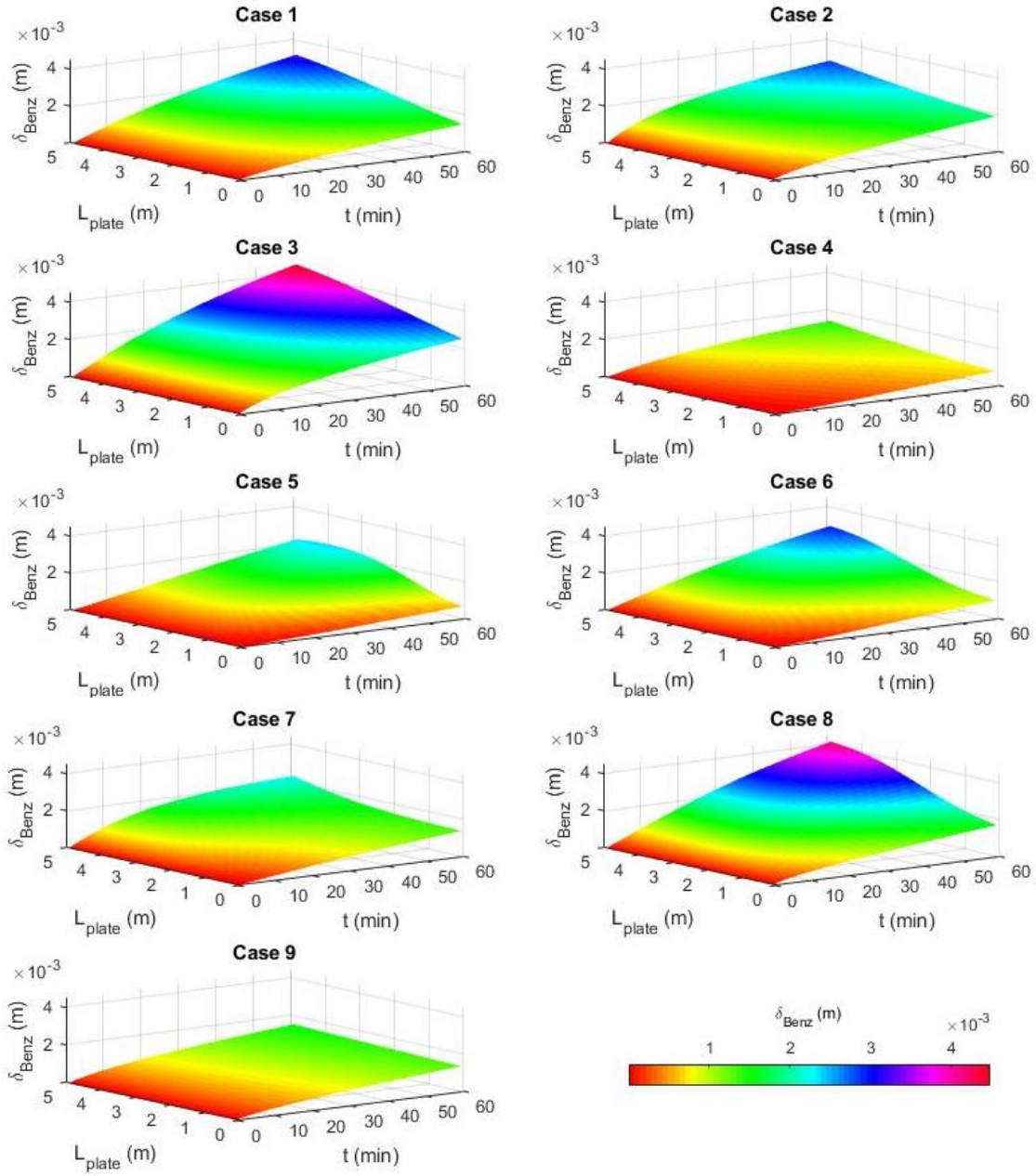

Figure 3-25: Variation of the benzene frost thickness function of the plate length and the time, for different initial conditions.

It can be observed that, in all the cases, the benzene frost thickness is increasing along the plate length and with respect to the operating time. The highest benzene frost thicknesses are encountered in cases

1, 2 and 3, that correspond to a higher initial benzene content. By comparing case 1 with case 2, it can be seen that increasing the gas velocity does not highly affect the frost thickness. To better illustrate the comparison, Figure 3-27 (a) shows the variation of the average value of the benzene frost thickness, function of time, for the different cases. It can be noticed that increasing the gas velocity leads to a higher rate of growth of the frost layer thickness, for the first period of operation. After a certain period of operation (denoted by τ_p), the growth rate of the frost layer thickness decreases, as the frost surface temperature increases and reaches the benzene phase transition equilibrium temperature. Therefore, as the gas velocity increases, τ_p becomes shorter and the rate of growth of the frost thickness decreases earlier. This behavior is also seen by comparing case 5 with cases 6 and 7. More precisely, for the first 25 minutes of operation, the highest benzene frost thickness is encountered in case 7, which corresponds to the highest velocity. After that time, the rate of growth highly decreases, and therefore the frost thickness in cases 5 and 6 becomes higher. In addition, it can be noticed from case 3 that, decreasing the wall temperature leads to a thicker benzene frost layer. This can be also seen by comparing case 6 with case 8, where reducing the wall temperature by 5°C, while keeping a constant gas velocity and a constant initial benzene content, increases the benzene frost thickness. Moreover, reducing the height of the duct leads to a thicker benzene frost layer, which can be deduced by comparing case 4 with case 6. In the last case, it can be seen that the benzene frost layer becomes thinner for higher plate height.

Note that, due to the total frost thickness accumulation during the frost growth, the frost thickness resistivity increases. This increases the gas temperature function of time, as seen in Figure 3-22.

Figure 3-26 presents the variation of the ice frost thicknesses function of the plate length and the time, for the different inlet conditions shown in Table 3-6. It can be observed that the ice frost thickness is decreasing along the plate length while it is increasing with respect to the operating time, in all the cases. The same initial water vapor content is considered in all the cases. In general, the growth rate of the ice frost thickness is higher in the first period of operation, and it decreases as the operating time increases. It can be also seen that the growth rate of benzene frost layer starts to decrease before that of the ice frost layer. This is due to the equilibrium temperature of the phase transition, which is lower for benzene. It can be seen by comparing case 1 with case 2 that the ice frost thickness highly increases with the increase of the gas velocity. To better illustrate the comparison, Figure 3-27 (b) shows the variation of the average value of the ice frost thickness, function of time, for the different cases. The same behavior is encountered by comparing cases 5, 6 and 7. The ice frost thickness increases with the increase of the initial gas velocities. In addition, decreasing the wall temperature in case 3, leads to an ice frost layer thicker than that of case 1. However, the ice frost thickness remains higher in case 2, which corresponds to a higher gas velocity and a higher wall temperature. This can be also seen by comparing case 6 with case 8, where reducing the wall temperature by 5°C while keeping a constant gas velocity, slightly increases the ice frost thickness. Moreover, reducing the duct height leads to a thinner ice frost layer, as seen when comparing case 4 with case 6. More precisely, a similar frost thickness is obtained at the entrance of the plate. However, in case 6, the growth rate decreases more importantly than that of case 4, along the plate length. In the last case, the ice frost layer becomes thicker and the frost growth is almost constant along the plate length for higher plate dimensions. To conclude, the gas velocity affects the ice frost thickness more than the wall temperature. On the contrary, the wall temperature affects the benzene frost thickness more than the gas velocity.

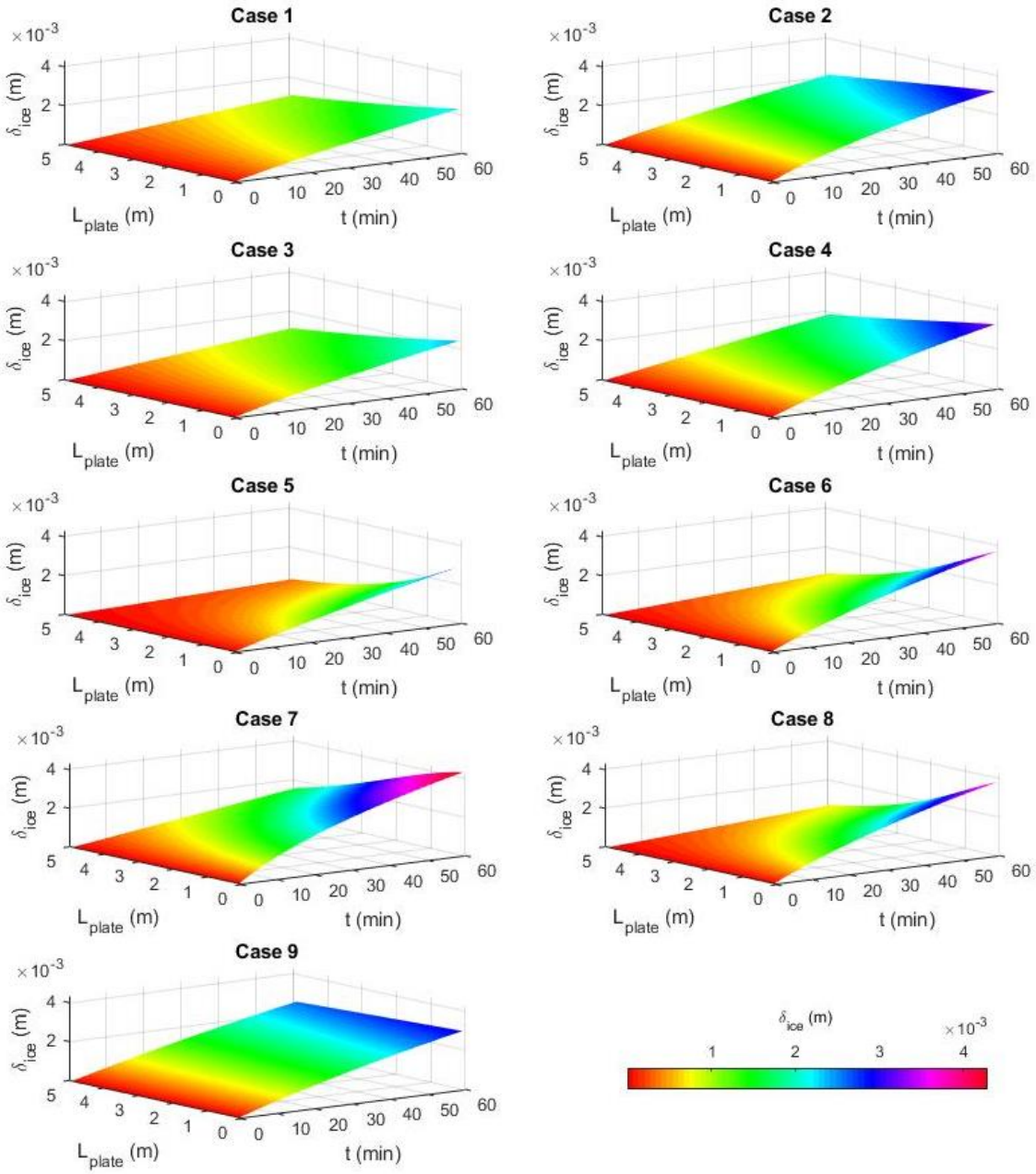

Figure 3-26 : Variation of the ice frost thicknesses function of the plate length and the time, for different initial conditions.

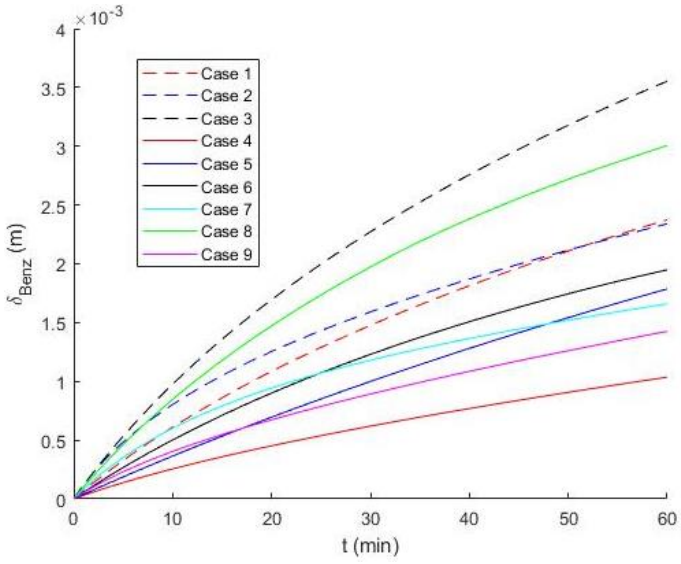

a

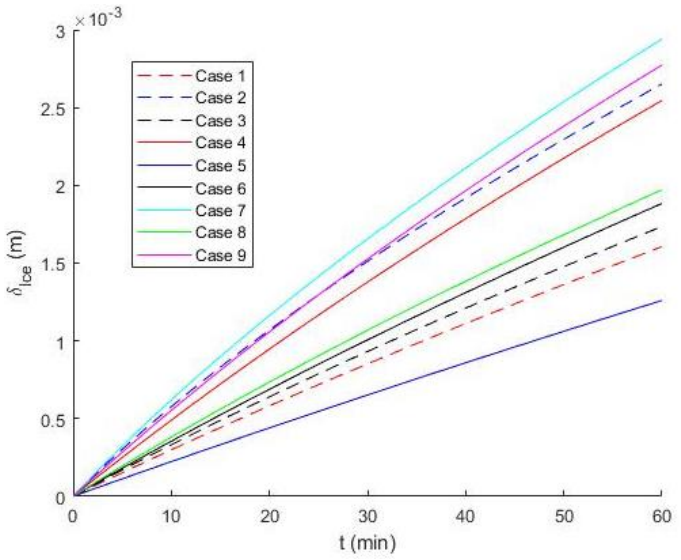

b

Figure 3-27: Variation of the average (a) benzene and (b) ice frost thicknesses function of time, for different initial conditions.

3.5.1.4 Mass flux of the condensable components

Figure 3-28 shows the variation of the benzene, ice and toluene condensable mass fluxes (m'') function of time, for the different inlet conditions shown in Table 3-6. Note that the average values are presented in the plots. It can be observed that, in all the cases, toluene has the lowest condensable total mass flux, followed by water, while benzene has the highest condensable mass flux. Although the total mass fluxes decrease during the frost growth, the densification mass fluxes increase in most of the cases. This is due to the increase in the temperature difference between the wall and the frost surface, as the frost grows. Therefore, the difference between the saturation mass fraction at the wall and that at the frost surface increases. In addition, the condensable mass flux of toluene is significantly reduced as the operating time increases until reaching zero, due to the increase in the frost surface temperature. As for the ice frost layer, it can be seen that for all the cases, the mass flux that increases the frost thickness (m''_δ) is higher than the mass flux that increases the frost density (m''_ρ). On the contrary, for the benzene frost layer, the mass flux that increases the frost density is higher than the mass flux that increases the frost thickness.

Moreover, by comparing case 1 with case 2, increasing the gas velocity increases the initial m'' for all the components. However, as the operational time increases, m'' decreases more significantly for higher gas velocities. This behavior can be also observed by comparing case 5 with cases 6 and 7. Furthermore, by comparing case 3 with cases 1 and 2, and case 6 with case 8, it can be deduced that reducing the wall temperature results in a higher m''_{δ}. Finally, higher total mass fluxes of benzene and toluene are obtained when the initial benzene and toluene contents are high, as observed when comparing case 3 with case 4.

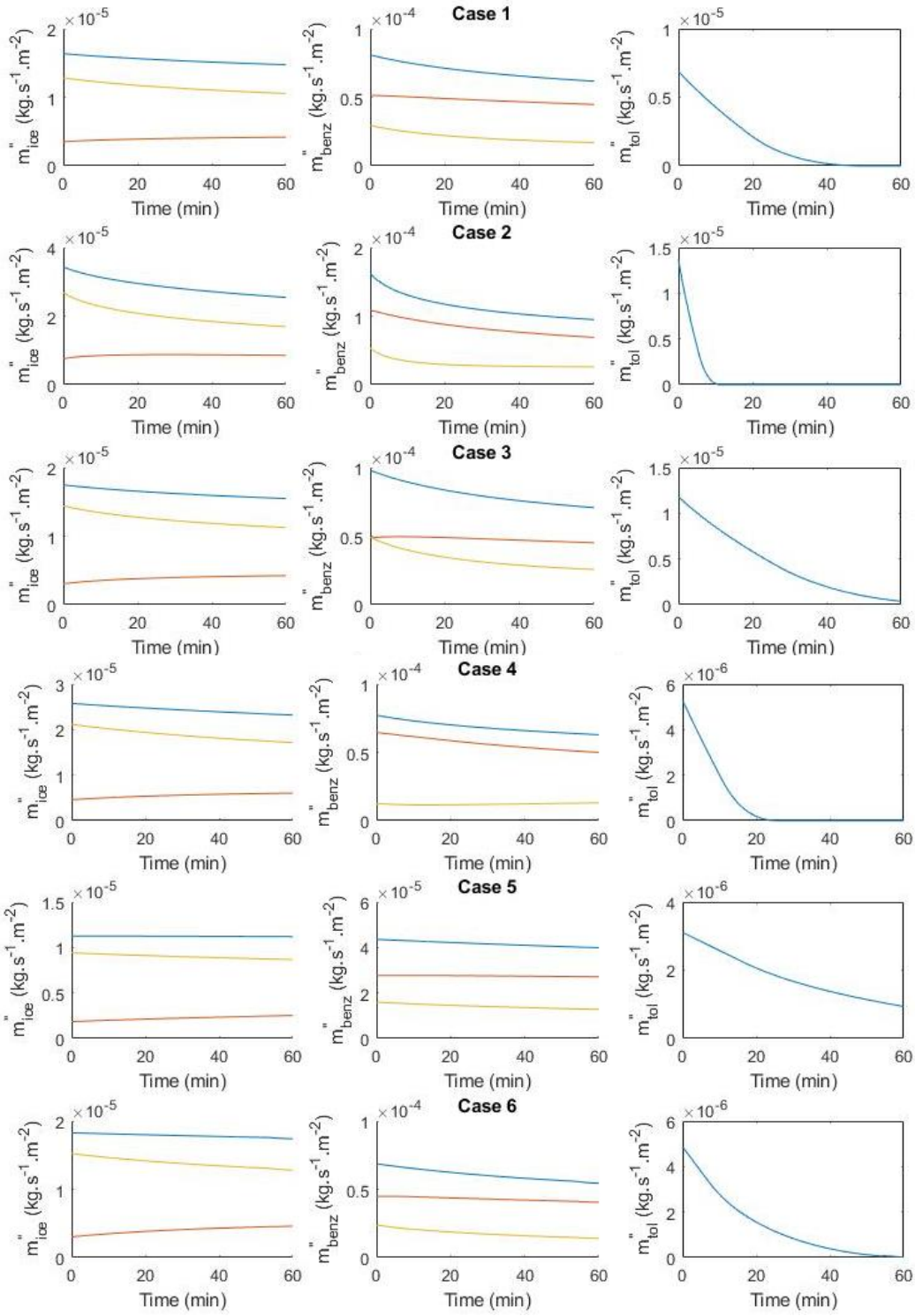

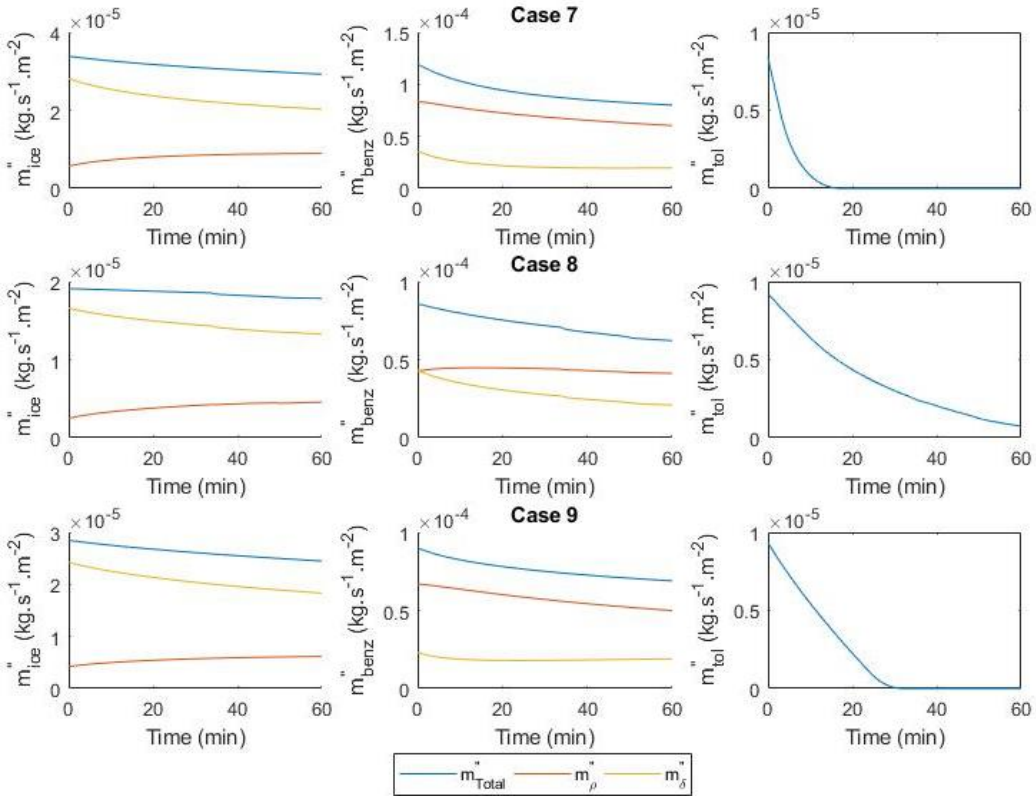

Figure 3-28 : Variation of benzene, ice and toluene condensable mass fluxes function of time, for different initial conditions.

3.5.1.5 Frost density

Figure 3-29 (a) and (b) respectively illustrate the variation of the average benzene and ice frost layers densities, function of the operating time. It can be seen that the average frost density increases during the frost growth. However, the rate of increment decreases as the operating time increases. In addition, it can be noticed that the impact of the parametric study on the benzene and the ice frost densities is the same. It can be observed by comparing case 1 with case 2 that increasing the gas velocity leads to higher frost densities. This behavior is also seen when comparing case 5 with cases 6 and 7. The benzene frost density, after 60 minutes of operation, becomes 2 times denser when the gas velocity is increased from 0.6 to 2 m.s^{-1}. Moreover, reducing the initial benzene content reduces the frost density, as seen when comparing case 3 with case 4. Furthermore, reducing the wall temperature slightly increases the frost density, as seen when comparing case 6 with case 8. Finally, when comparing case 4 with case 6, it can be deduced that reducing the duct height reduces the frost density.

In order to understand the densification process, the distribution of the frost density inside the frost layer should be analyzed. Therefore, Figure 3-30 and Figure 3-31 respectively illustrate the distribution of the benzene and ice frost layers densities in both frost computational sub-domains, for the different inlet conditions shown in Table 3-6 after 60 minutes of operation. It can be observed that the frost density, in both sub-domains, is higher at the front end of the plate where the charged producer gas enters. The density decreases as the plate length tends towards its rear end. In general, the density is higher near the cold surface and decreases as the frost thickness tends towards the frost surface. As the frost layer grows, the distance between the cold surface and the frost surface increases, leading to a thermal resistance increase. In addition, the thermal conductivity increases with the densification phenomenon as it will be seen in the next section. However, the increase of the thermal conductivity that results from the

densification is lower than the increase of the thermal resistance due to the frost thickness growth. Therefore, the frost surface temperature as well as the gas temperature increase with time as previously discussed. This general behavior of densification is encountered in all the cases.

It can be also seen that the benzene frost is denser than the ice frost. This is mainly due to the fact that the initial benzene mass fraction is higher than that of the water vapor. Moreover, in the proposed model, it is assumed that the benzene frost is formed on the top of the cold surface while ice frost is formed on the top of the benzene surface. This results in increasing the cold surface temperature on which ice deposition occurs.

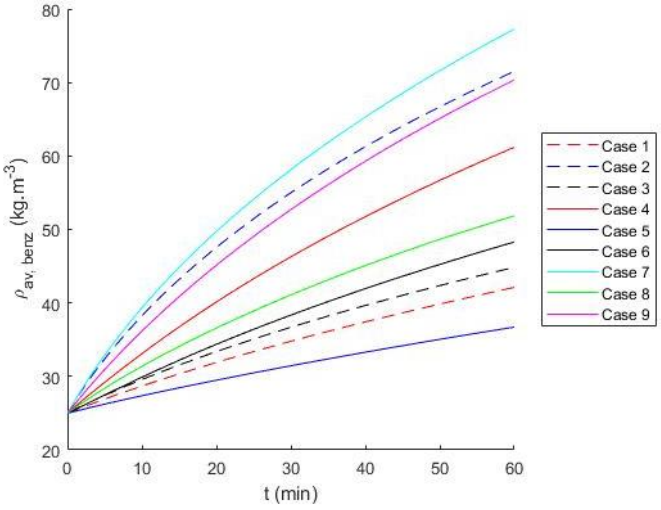

a

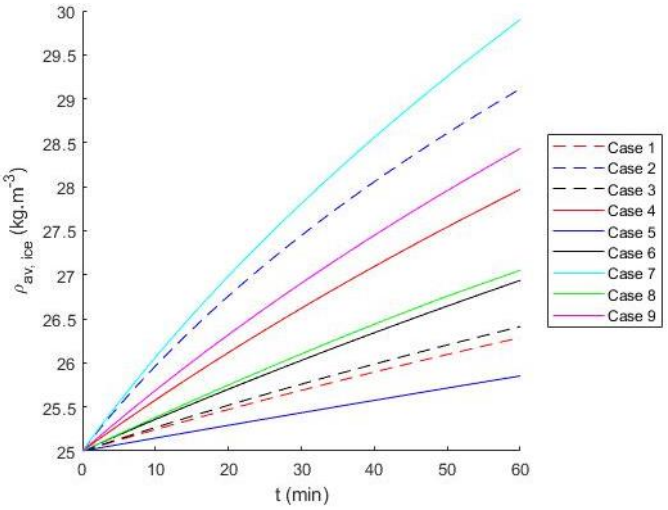

b

Figure 3-29: Variation of the average (a) benzene and (b) ice frost densities function of time, for different initial conditions

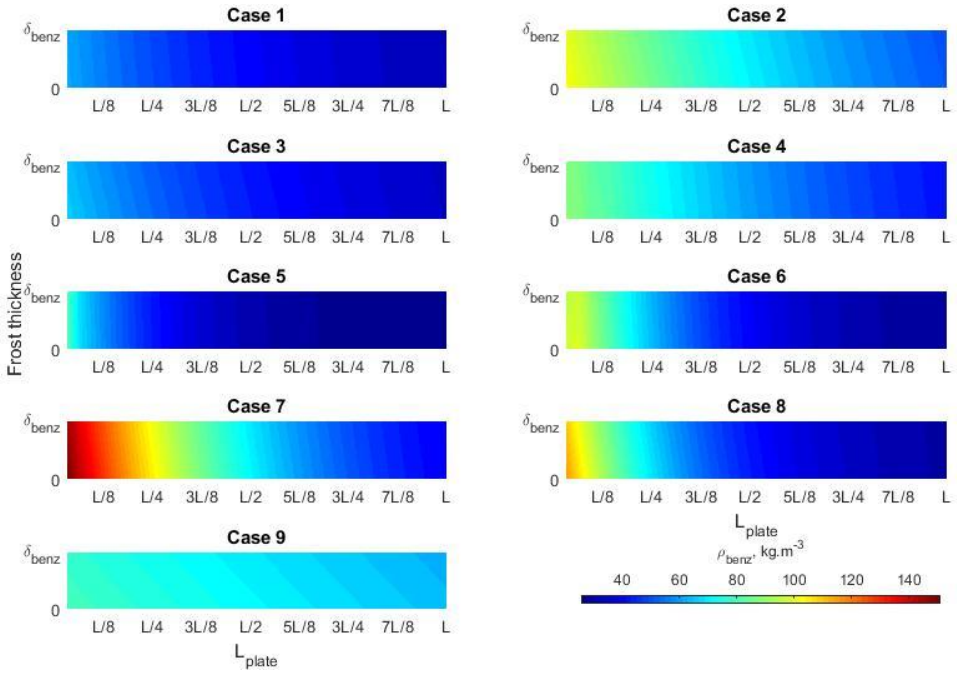

Figure 3-30 :Variation of the benzene frost density along the plate length and the frost thickness, at t=60 min.

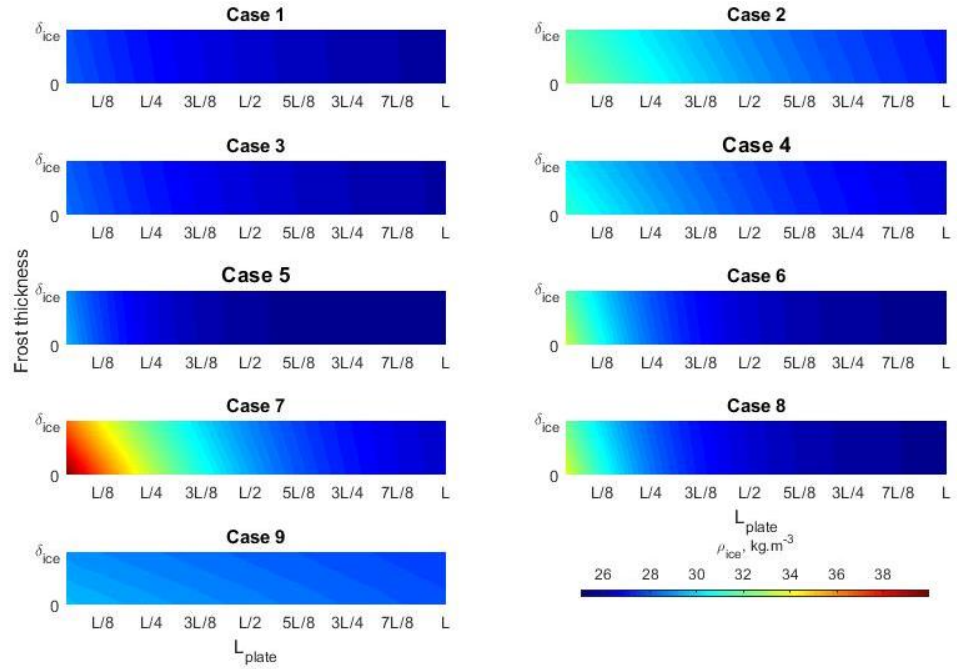

Figure 3-31 : Variation of the ice frost density along the plate length and the frost thickness, at t=60 min.

3.5.1.6 Effective thermal conductivity

Figure 3-32 and Figure 3-33 respectively illustrate the distribution of the benzene and ice effective thermal conductivities in both frost computational sub-domains, for the different inlet conditions shown in Table 3-6 after 60 minutes of operation. It can be observed that the effective thermal conductivity has the same pattern as the frost density, in all the cases. This is expected since the thermal conductivity is calculated function of the frost density, as shown in section 3.2.7. The highest effective thermal conductivity is at the cold surface front end, and it decreases in the direction of the cold surface rear end. The highest effective thermal conductivity is near the cooling surface, and it decreases towards the frost surface, where the density is lower. In addition, the benzene effective thermal conductivity is lower than

that of the ice by 30%. Therefore, the benzene frost layer blocks the heat transfer more than the ice frost layer. Finally, the average effective thermal conductivity increases during the frost growth due to the frost density increase. However, the rate of increment decreases as the operating time increases.

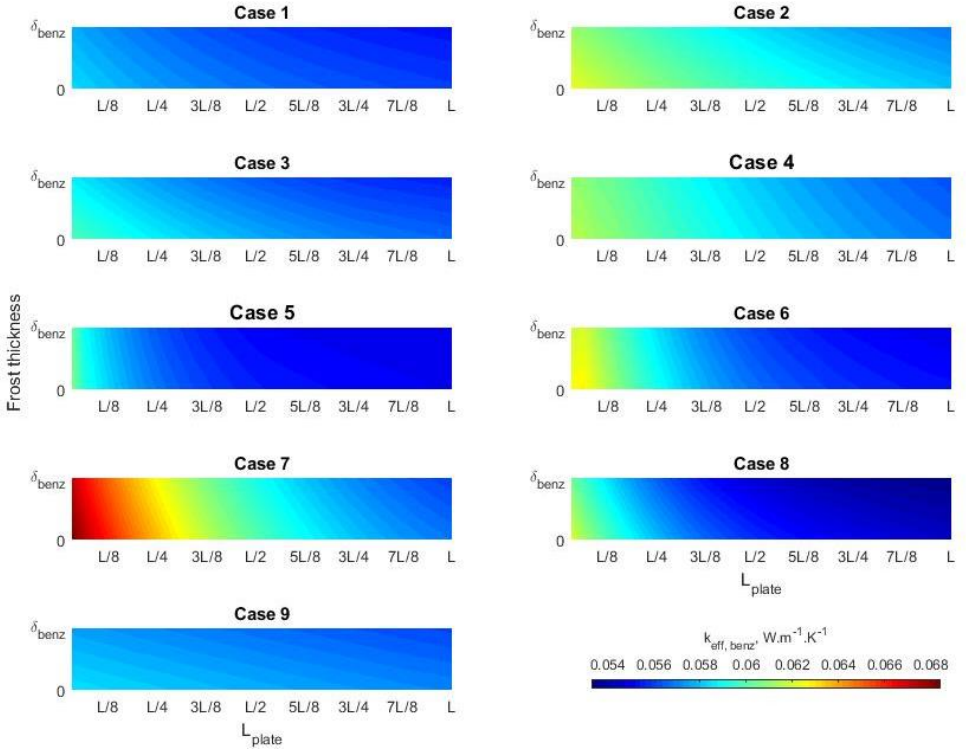

Figure 3-32 : Variation of the benzene effective thermal conductivity along the plate length and the frost thickness, at t=60 min.

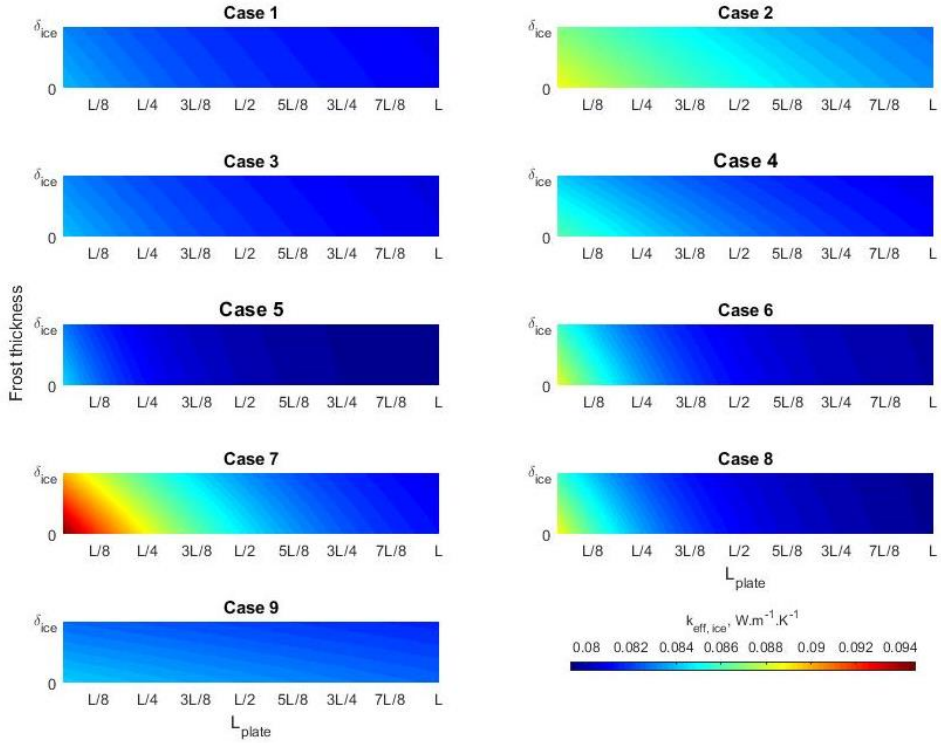

Figure 3-33: Variation of the ice effective thermal conductivity along the plate length and the frost thickness, at t=60 min.

3.5.1.7 Heat fluxes

The frost layer growth behavior is not only function of the frost properties variations, but also of the overall heat and mass transfer characteristics. Therefore, it is important to study the heat and mass transfer. Figure 3-34 presents the variation of the total heat flux, sensible heat flux, and latent heat fluxes of water vapor frosting, benzene frosting and toluene condensation function of time, for the different inlet conditions shown in Table 3-6. Note that the average values of the heat fluxes are plotted. It can be seen that, in all the cases, the total heat fluxes decrease over the time. Similarly, the sensible heat fluxes decrease during the frost growth. This is due to the increase in the thermal resistance over the time, which increases the frost surface temperature, the interface temperature and the gas temperature. On the contrary, the latent heat fluxes slightly decrease at the beginning and then remain almost constant during the frost growth. Only the latent heat flux of toluene condensation is almost null, since the weight of liquid toluene condensed at those conditions is negligible, as previously discussed in section 3.5.1.4. Even though the weight of the deposited benzene is higher than that of ice, the latent heat flux of benzene frosting is lower than or equal to that of water deposition. This can be justified by the high latent heat of water sublimation.

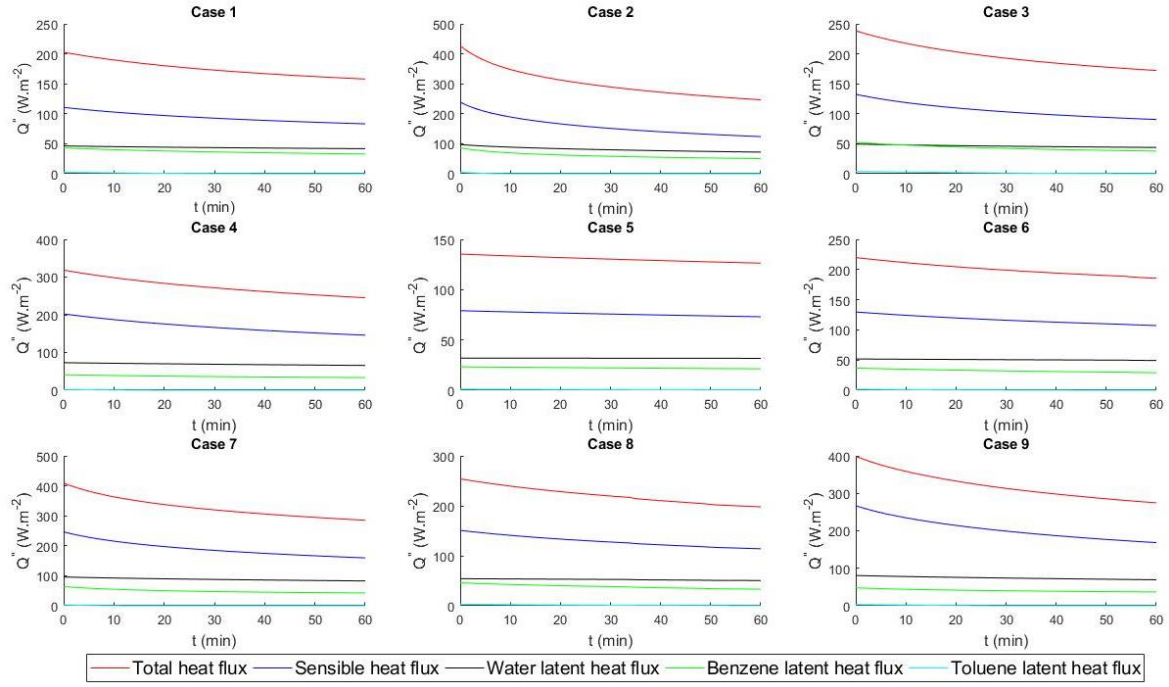

Figure 3-34 : Variation of the total heat flux, sensible heat flux and latent heat fluxes of water vapor frosting, benzene frosting and toluene condensation function of time, for different initial conditions.

Note that the total heat flux consists in adding the sensible heat flux and the different latent heat fluxes. It can be noticed from Figure 3-34 that the variation of the sensible heat fluxes is higher than that of the latent heat fluxes. After 60 minutes of operation, the sensible heat flux is reduced by approximately 30%, while the variations in the latent heat fluxes are much lower. Therefore, the curve of the total heat flux resembles that of the sensible heat flux. It can be seen when comparing case 1 with case 2 that increasing the gas velocity increases simultaneously the sensible heat flux, the latent heat fluxes and thus the total heat flux. Similarly, in cases 5, 6 and 7, a higher initial gas velocity increases the heat fluxes. Moreover, lower benzene and toluene initial contents increase the sensible heat flux, and reduce the latent heat flux of water while the latent heat of benzene and toluene, as observed when comparing case 3 with case 4. This is due to the formation of a thinner benzene frost layer, and thus a lower thermal

resistivity in case 4. Furthermore, it can be seen when comparing case 6 with case 8 that, reducing the wall temperature leads to higher heat fluxes. Finally, reducing the duct height reduces the heat fluxes, as observed when comparing case 4 with case 6.

To better illustrate the variation of the different heat fluxes, Figure 3-35 presents the variation of the total heat flux, the sensible heat flux, latent heat fluxes of water vapor frosting, benzene frosting and toluene condensation function of the plate length and time, for case 7. Note that, only case 7 is shown since the general behavior of the heat fluxes is similar for the different cases. It can be seen that all the heat fluxes decrease along the plate length. The benzene and water latent heat fluxes remain almost constant function of time, as previously seen in Figure 3-34. Finally, the lowest latent heat flux is that of toluene. This latter becomes null after a certain time of operation.

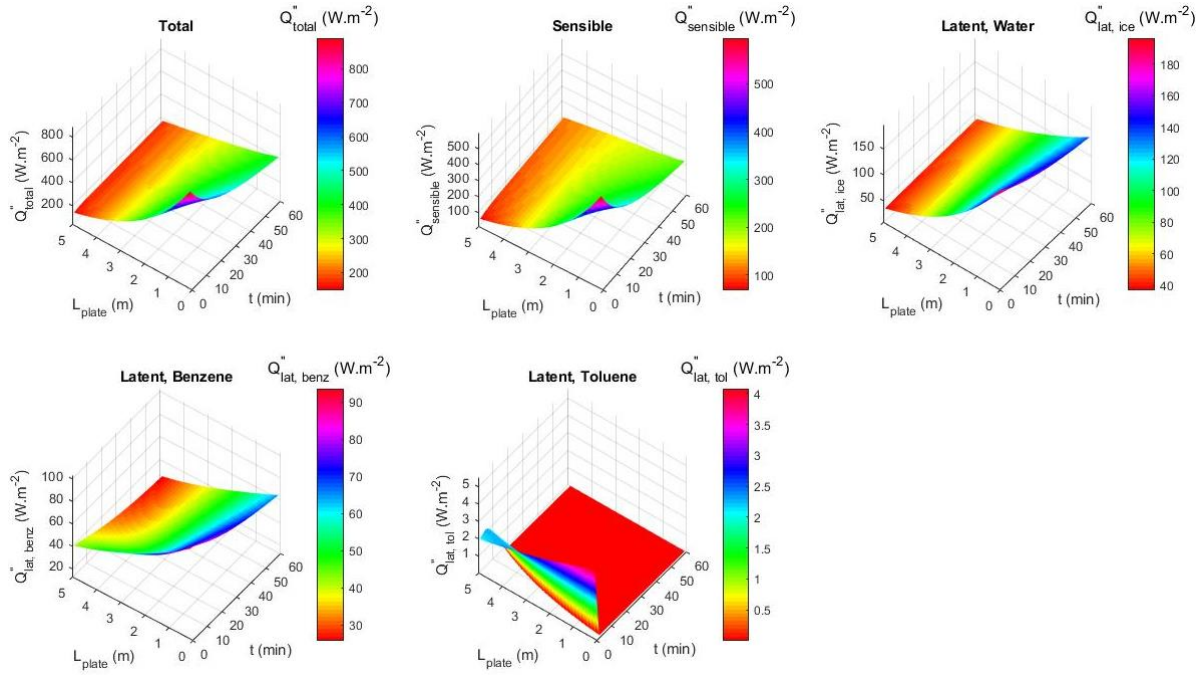

Figure 3-35: Variation of the total heat flux, sensible heat flux and latent heat fluxes of water vapor frosting, benzene frosting and toluene condensation function of the plate length and the time, for case 7.

3.5.2. Several plates placed in series

After benchmarking all the model parameters, it can be deduced from the obtained results shown in the previous section, that case 5 and case 8 outperform the other cases, since they highly reduce the benzene content. Decreasing the wall temperature while keeping a constant inlet gas temperature in case 8, increases the temperature difference and therefore enhances the heat and mass transfer. However, this highly increases the required energy and the exergy destruction. On the contrary, the required energy in case 5 is lower by 50%. Simultaneously, the benzene content is reduced by almost 30% in both cases.

This section aims at reducing the gas temperature to -110°C, as well as the remaining tar content after the pre-treatment process. To do so, an additional plate is added in series at each run until reaching the optimum result. Note that this procedure was done for several cases. Although case 5 outperforms the remaining cases in the first plate, the best results obtained using case 6 with 6 plates placed in series are presented. This is due to the fact that part of the producer gas is condensed in each plate, which leads to a decrease in the gas velocity from one plate to another. Therefore, using a low initial velocity of 0.6 $m.s^{-1}$ in the first plate is disadvantageous for the remaining plates. Table 3-7 presents the different wall

temperatures considered for the six plates. It can be seen that the wall temperature of plates 2, 3 and 4 is reduced by 20°C from one plate to another, while the wall temperature is fixed at -95°C in order to avoid the CO_2 frosting in plate 5. In the last plate, the CO_2 frosting is introduced in the simulations.

Table 3-7: Selected wall temperature for the different plates.

Plate #	1	2	3	4	5	6
T_{wall} (°C)	-25	-45	-65	-85	-95	-115

3.5.2.1 Gas temperature

Figure 3-36 presents two different views of the gas temperature variation function of the plate length and the time, for the six plates placed in series. Note that plates 1 to 6 are respectively shown from the top to the bottom. It is important to mention that a constant plate length is considered for the different plates. It can be observed that all the plates have the same gas temperature behavior. Initially, the gas temperature is close to the cold surface temperature, and then increases over time due to the frost growth. Therefore, an optimal solution could be operating for a short period with several plates. This helps in retaining a low gas temperature.

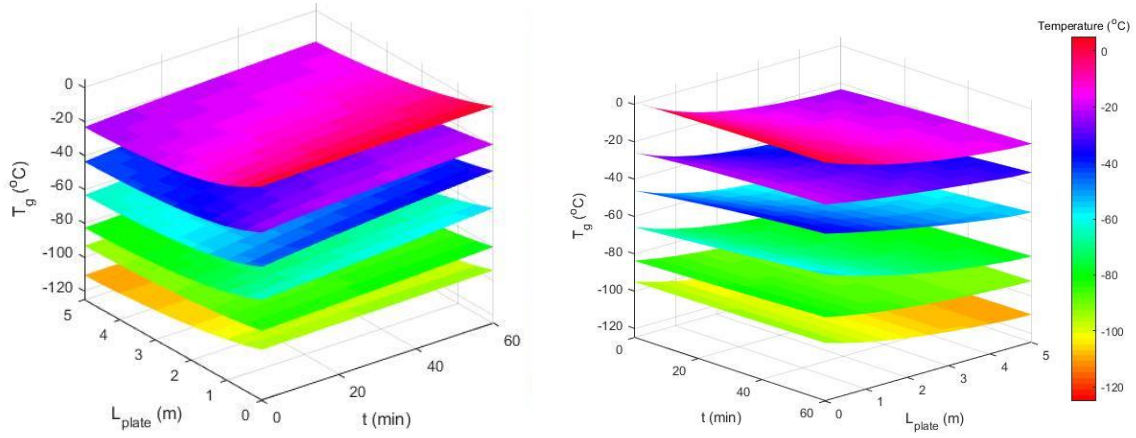

Figure 3-36 : Two different views of the gas temperature variation function of the plate length and the time, for the six plates placed in series.

3.5.2.2 Benzene and toluene remaining content

Figure 3-37 (a) and (b) respectively illustrate the variation of the benzene and toluene mass fractions remaining in the producer gas function of the plate length and the time, for the six plates placed in series. It can be seen that, for all the plates, the remaining benzene and toluene mass fractions decrease function of the plate length, while they slightly increase function of time. The results of the first plate were previously analyzed in section 3.5.1.2. The highest reduction rate of the mass fraction is observed in plate 2 for both benzene and toluene components. As the initial benzene and toluene contents decrease from one plate to another, the reduction rate of their mass fraction decreases. In addition, the remaining mass fraction of benzene and toluene in the last two plates becomes too low, and therefore their variation is not visible.

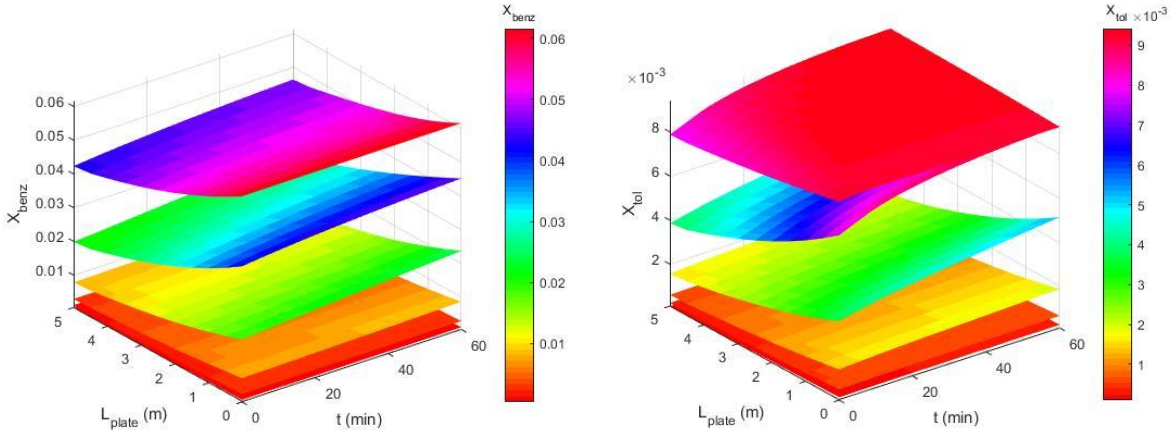

a b

Figure 3-37: Variation of the mass fraction of benzene (a) and toluene (b) remaining in the gas phase, function of the plate length and the time, for the six plates placed in series.

3.5.2.3 Frost thickness

Figure 3-38 and Figure 3-39 respectively illustrate the variation of the benzene and ice frost thicknesses, function of the plate length and the time, for the six plates placed in series.

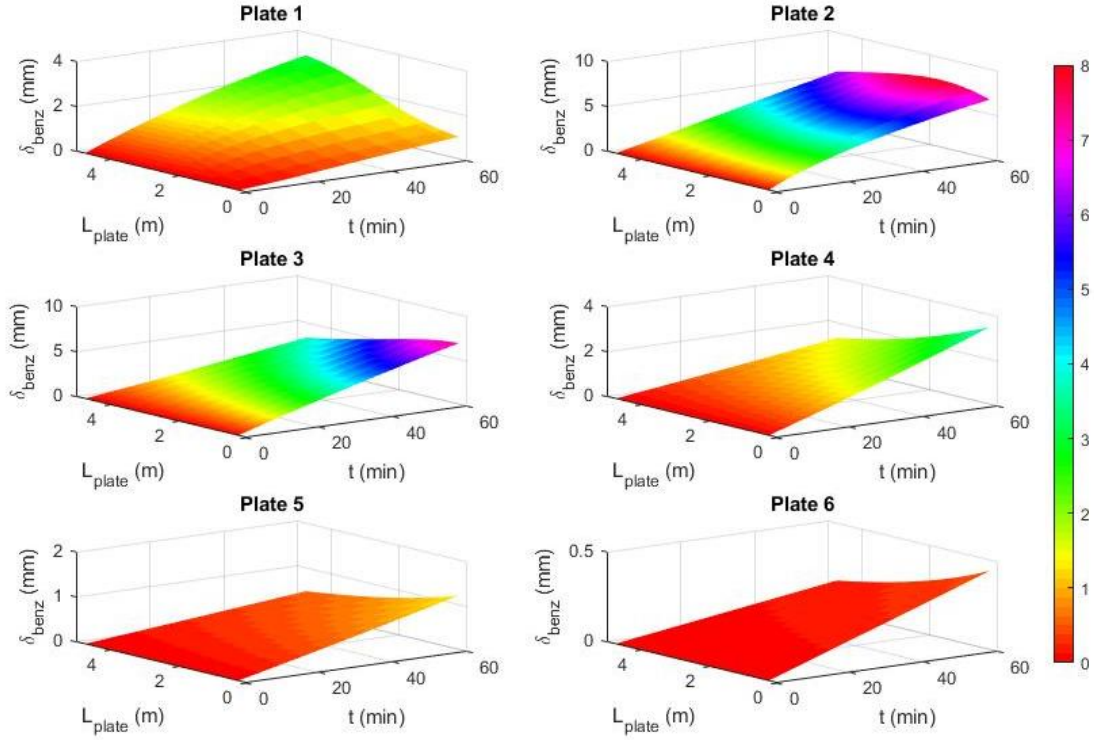

Figure 3-38: Variation of the benzene frost thickness function of the plate length and the time, for the six plates placed in series.

It can be observed that, at the front end of the first plate which has the highest wall temperature, the ice frost layer is thicker than the benzene frost layer. On the contrary, the benzene frost layer becomes thicker than the ice frost layer for the remaining plates. As the wall temperature decreases, the benzene frost layer becomes thicker until reaching a maximum value in the third plate, for a wall temperature of -65°C. On the other hand, the ice frost thickness decreases with the decrease of the wall temperature. In fact, several factors lead to this benzene and ice frost thicknesses behavior. More precisely, for the first

plate, the wall temperature is not low enough to drive the benzene frost layer growth due to its high vapor pressure. As for the remaining plates, when the temperature decreases, the saturation mass fraction at the frost surface becomes lower. Since the initial benzene mass fraction is higher than that of the water, higher benzene frost thicknesses are reached.

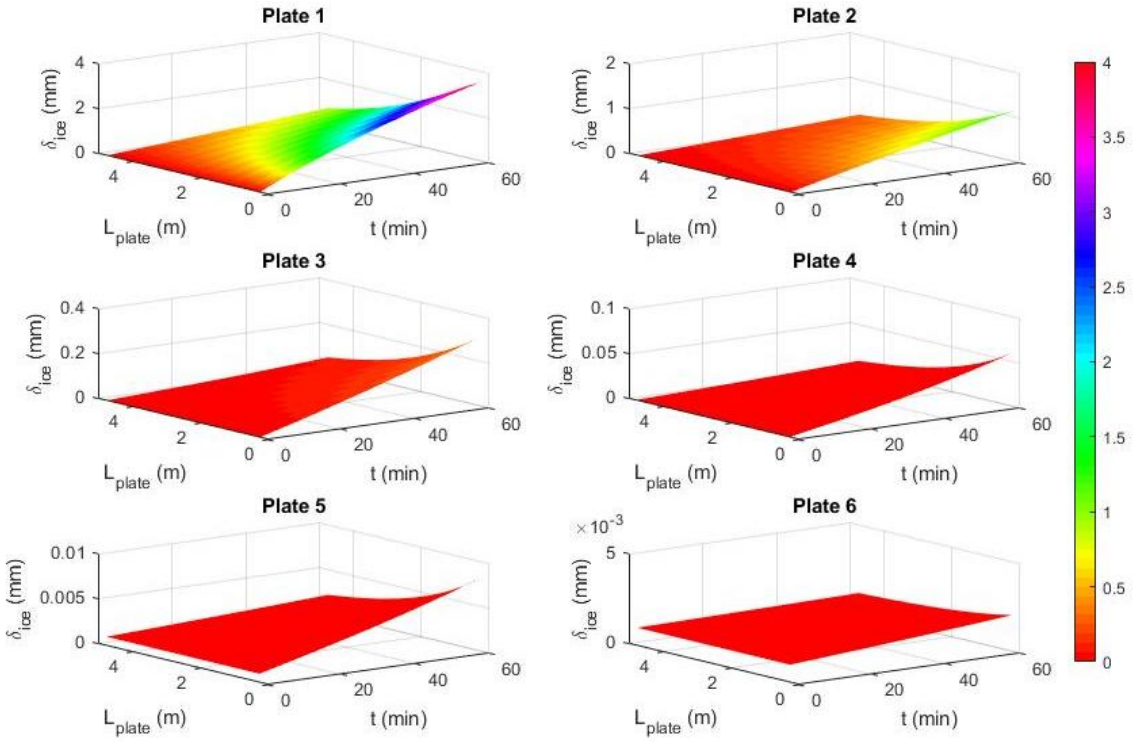

Figure 3-39: Variation of the ice frost thickness function of the plate length and the time, for the six plates placed in series.

3.5.2.4 Mass flux of the condensable components

Figure 3-40 shows the variation of the benzene, ice and toluene condensable mass fluxes (m'') function of time, for plates 2 to 6. Note that the average values are presented in the plots. For the first plate, the variation of the different condensed weights was previously presented in case 6 of Figure 3-28. Benzene has the highest deposited weight for all the plates, since it has the highest initial mass fraction. The weight of benzene and ice frost layers decreases for each added plate. As for the toluene, the condensed liquid weight in the first plate is null because the temperature difference is not sufficient for its condensation. As for plate 2, the temperature difference in the first minutes of operation drives the toluene condensation. The surface temperature increases function of time due to the frost formation, leading to a higher saturation mass fraction at the interface, and therefore reducing the condensation. For the remaining plates, as the wall temperature decreases by adding plates, the mass fluxes of benzene frosting, water vapor frosting and toluene condensation, increases function of time for several reasons. For instance, as the frost thickness increases, the effective hydraulic diameter decreases leading to a higher velocity, which results in higher heat and mass transfer coefficients. Therefore, the mass fluxes increase function of time. Simultaneously, the remaining content of the condensable components in the gas phase decreases from one plate to another. Consequently, the frost layers thermal resistances decrease and the variation of the frost surface temperature decreases. This also results in increasing the mass fluxes function of time.

In addition, as the wall temperature decreases, the mass flux leading to the increase of the frost thickness (m''_δ) becomes higher than the mass flux which increases the frost density (m''_ρ). At wall temperatures

lower than -95°C, the total mass flux (m''_{Total}) and m''_{δ} become almost equal, while m''_{ρ} approaches zero.

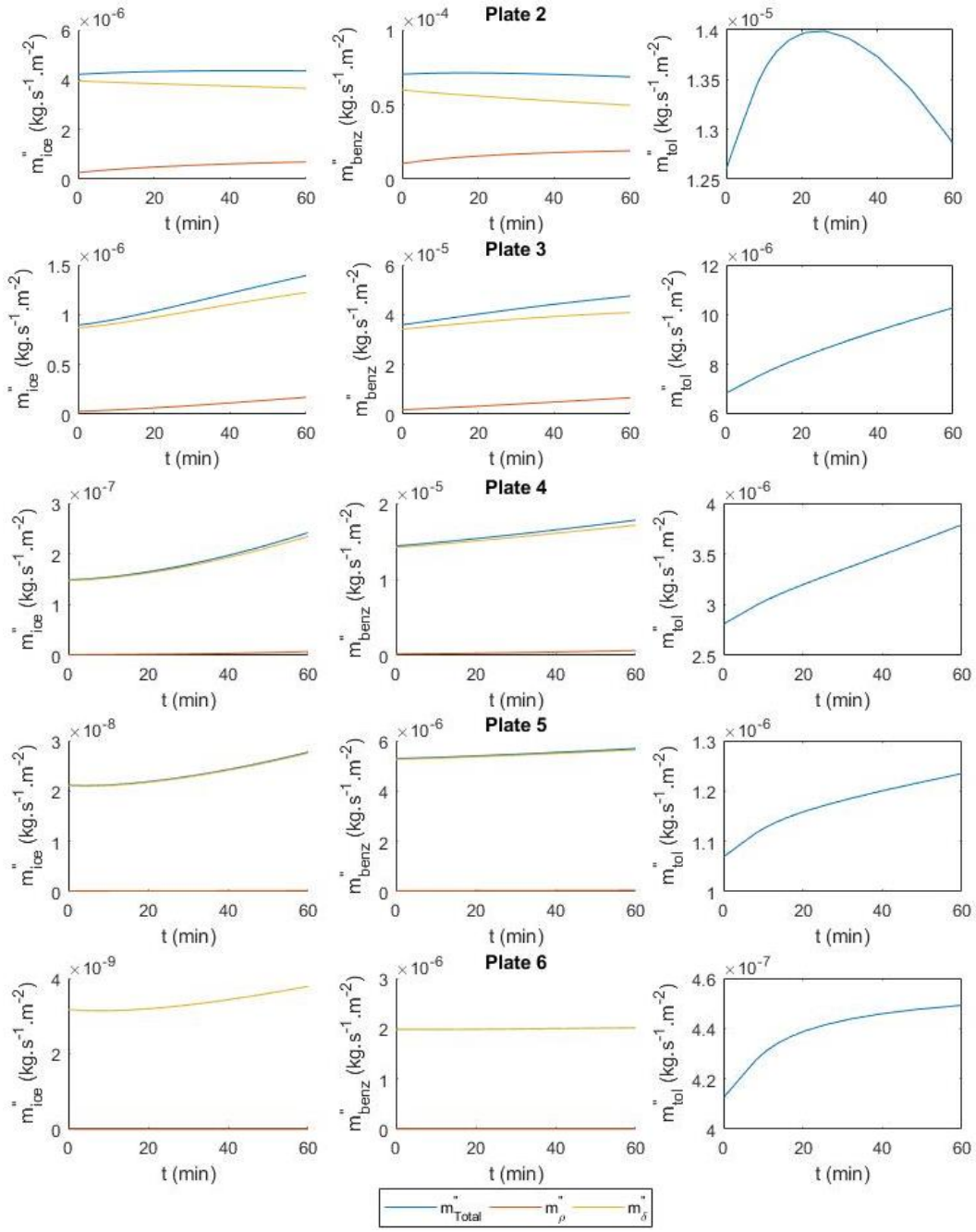

Figure 3-40 : Variation of benzene, ice and toluene mass fluxes function of time, for plates 2 to 6 placed in series.

3.5.2.5 Benzene frost density

Figure 3-41 illustrates the distribution of the benzene frost density in the benzene computational sub-domain, after 60 minutes of operation. It can be seen that reducing the wall temperature results in decreasing the frost density. It can be deduced from Figure 3-38 and Figure 3-41 that decreasing the wall temperature leads to the formation of a thicker frost layer with a lower frost density. The frost layer becomes thicker due to the low saturation benzene mass fraction at the frost surface, that drives the deposition at the surface. On the contrary, the density becomes lower due to the lower saturation benzene

mass fraction gradient inside the frost layer that drives the densification process. This can be also seen in Figure 3-40, where the mass flux that increases the frost density becomes close to zero for the last two plates.

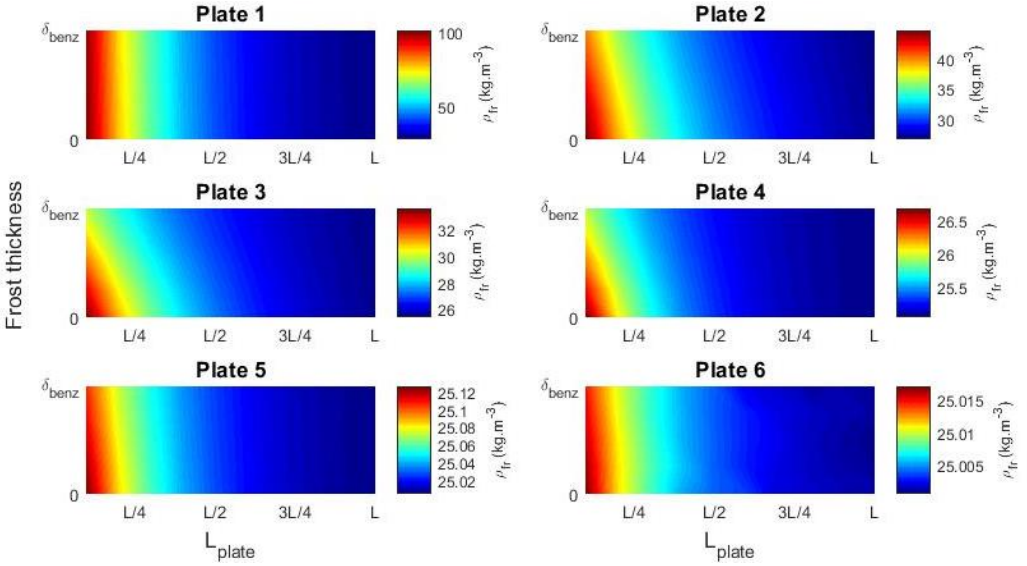

Figure 3-41: Variation of the benzene frost density along the plate length and the frost thickness at t=60min, for the six plates placed in series.

3.5.2.6 Thermal diffusivity

Figure 3-42 and Figure 3-43 respectively illustrate the variation of the thermal diffusivity of the benzene frost layer and the ice frost layer, function of the plate length after 1 minute, 10 minutes, 30 minutes and 60 minutes of operation. The thermal diffusivity is defined as the ability of a material to conduct the thermal energy represented by the effective thermal conductivity, with respect to its ability in storing the thermal energy represented by the frost density that is multiplied by the frost heat capacity [155]. Therefore, the thermal diffusivity reflects a clearer idea about the frosting phenomenon, since the effective thermal conductivity and the frost density are varying function of the plate length and the time.

It can be observed that the thermal diffusivity of the benzene frost layer is lower than that of the ice frost layer. In the first four plates, the thermal diffusivity of the benzene frost layer decreases for longer operating time, while in the last two plates, the thermal diffusivity of the benzene frost layer remains constant function of time. For the first minutes of operation, the thermal diffusivity does not vary importantly along the plate length. However, as the operating time increases, the variation of the thermal diffusivity along the plate length becomes higher, due to the frost formation. Consequently, as the operating time increases, the frost ability to transmit the thermal energy becomes lower than its ability to store it. According to Figure 3-42, the benzene frost thermal diffusivity, after 1 minute of operation, decreases with the decrease of the wall temperature until becoming almost constant for the last two plates. Moreover, as the wall temperature decreases, the variation of the benzene frost thermal diffusivity function of time becomes lower. This results in a constant thermal diffusivity in the two last plates, where the wall temperature is equal to -95°C and -115°C, respectively. As seen in Figure 3-43, the behavior of the ice frost thermal diffusivity is different than that of the benzene frost. The ice frost thermal diffusivity increases as the temperature of the wall decreases. Thus, the ability of the ice frost to transmit the thermal energy becomes higher than its ability to store it.

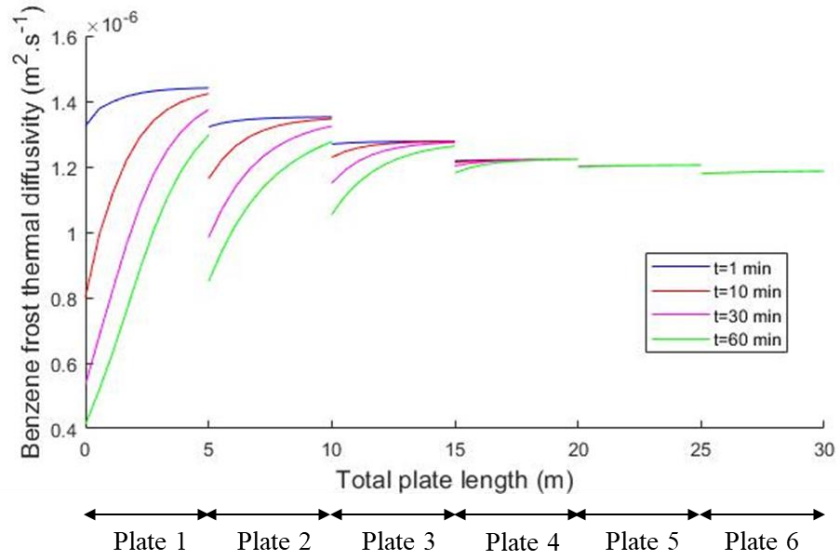

Figure 3-42: Variation of the benzene frost layer thermal diffusivity for the six plates, function of the plate length after 1 min, 10 min, 30 min and 60 min of operation.

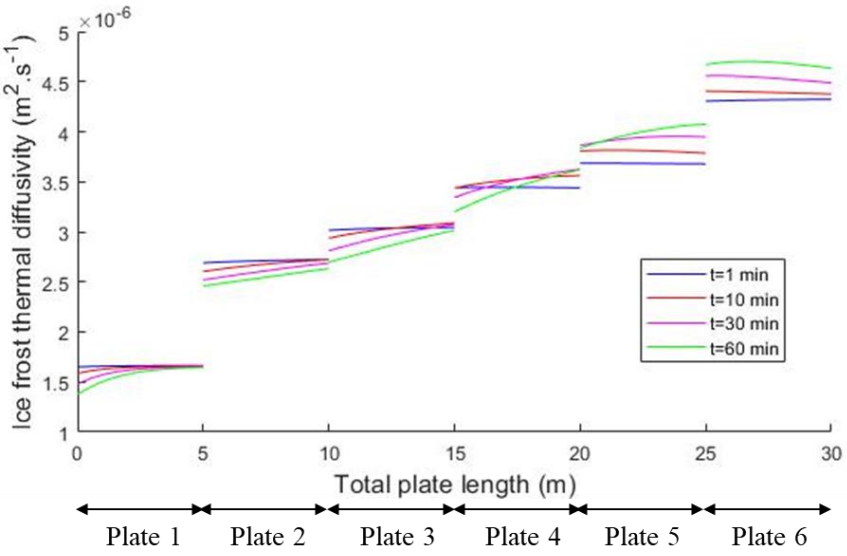

Figure 3-43 : Variation of the ice frost layer thermal diffusivity for the six plates, function of the plate length after 1 min, 10 min, 30 min and 60 min of operation.

3.5.2.7 Heat fluxes

Figure 3-44 presents the variation of the total heat flux, sensible heat flux, and latent heat fluxes of water vapor frosting, benzene frosting and toluene condensation function of time, for plates 2 to 6. Note that the average values of the heat fluxes are plotted. In the last plate, the latent heat flux of CO_2 frosting is added. The variation of the heat fluxes in the first plate are similar to the one previously presented in case 6 of Figure 3-34. It can be seen that the latent heat fluxes are proportional to the condensed weight presented in Figure 3-40. In the first plate, although the mass flux of benzene is higher than that of water vapor, the heat fluxes of benzene and water vapor frosting are similar, since the latent heat of benzene sublimation is lower than that of water vapor sublimation, as previously discussed. As the wall temperature and the initial content of the condensable components are reduced from one plate to another, the latent heat flux of benzene frosting becomes higher than that of water vapor frosting. In the second plate, even though the mass flux of toluene is higher than that of water vapor, the heat flux of water

vapor frosting is higher than that of toluene condensation. This is due to the fact that the latent heat of the toluene condensation is lower than that of the water vapor sublimation. In the third plate, the latent heat fluxes of toluene condensation and water vapor frosting are almost the same. This is due to the fact that the mass flux of the condensed toluene becomes much higher than that of water vapor frosting. The curve of the total heat flux resembles that of the sensible heat flux, as mentioned earlier. In addition, the latent heat fluxes of the different condensable components decrease from plate 2 to plate 6, until becoming almost null in the last plate, due to their decreasing initial content. Consequently, the total heat flux and the sensible heat flux get closer from one plate to another. The wall temperature set in the last plate leads to the CO_2 frosting. Therefore, the latent heat flux of the CO_2 frosting is introduced. It can be seen that the highest latent heat flux is that of the CO_2 frosting. This is due to the high CO_2 mass fraction present in the producer gas. Moreover, the latent heat flux of the CO_2 frosting is 5 times higher than the sensible heat flux. This leads to a high increase in the energy requirement.

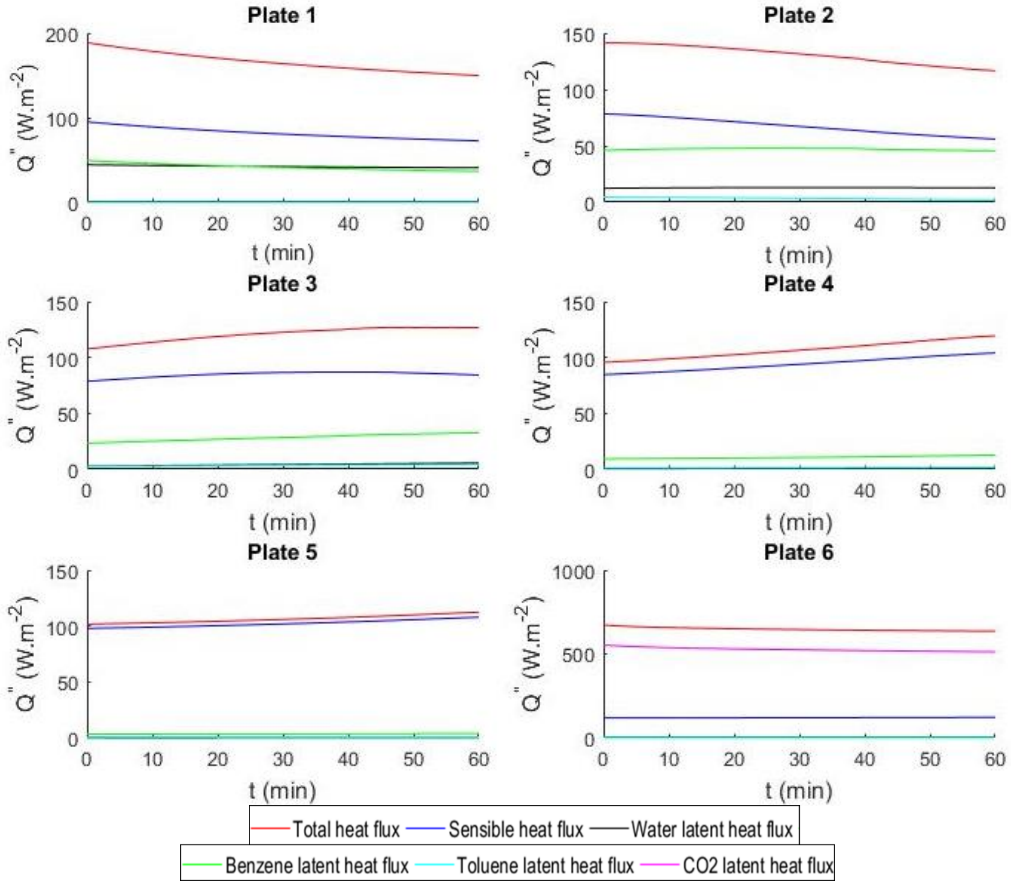

Figure 3-44 : Variation of the total heat flux, sensible heat flux, and latent heat fluxes of water vapor frosting, benzene frosting, toluene condensation and CO_2 frosting, function of time, for plates 1 to 6.

3.6. Regeneration of the plates

In order to ensure a continuous operation of the proposed process, the regeneration of the plates must be studied. The existing methods of regenerations target the defrosting of the built frost layer by thermal methods including on-off defrost, electrical defrost and gas defrost. Table 3-8 present a brief description of the operation, the advantages and disadvantages of the existing defrosting methods.

Table 3-8: Brief description of the different thermal defrosting methods.

On-Off Defrost	Electrical Defrost	Gas Defrost
The refrigeration system is turned off when frost accumulates and the gas continues to pass in the evaporator of the system. Then the refrigeration system is turned on when the frost melts and the refrigerant re-enters the condenser.	Resistive heaters are placed in the evaporator. Electricity is supplied, then heat is created and leads to the frost melting. After a certain time interval the power is cut off and the melted frost is eliminated.	It is the most industrially used method. The evaporator of the system is converted into a condenser. The hot refrigerant leaving the compressor is directed into the evaporator.
No additional heating is required in the process.	Requires less time than the on-off defrosting.	Causes major temperature fluctuations and decreases the system's efficiency.
This method is time consuming.	It has a higher cost since it requires an additional heat source.	Lower defrosting time can be reached.
It is not suitable for low temperature operations.		Costly but yields a higher coefficient of performance.

All the defrosting methods leads to the sublimation of the frost and thus the condensable components will be diluted into a gas stream (the refrigerant that pre-exists in the evaporator). This renders the recovery of the deposited frost components complicated.

As it has been mentioned earlier, one of the targets of this thesis is to recover the deposited benzene and toluene and benefit from their economic or energetic values. This becomes complicated in case where those components are diluted in a gas mixture during the regeneration of the cold plates. Consequently, a mechanical method for regeneration is proposed. The latter implicates the use of blades that pass inside the gas channel after a certain operating time and remove mechanically the deposited frost layer.

3.7. Conclusion

A new method allowing to reduce the tar content initially present in the producer gas, for its integration in a catalytic process, is proposed. This method combines two water scrubbers followed by a low temperature process in which the remaining tar fraction undergoes simultaneous frosting and condensation. Benzene and toluene are the main remaining components after water scrubbing. The producer gas charged with benzene, toluene and water vapor flows over a cold surface in order to reduce their content to the acceptable level. For this purpose, a mathematical model of simultaneous frost growth and condensation was developed on Dymola. The proposed model is then validated by comparing it with models and experiments from the literature, for the deposition of water vapor from humid air, as well as CO_2 from CO_2—N_2 mixtures.

A sensitivity analysis for the variation of the cold surface temperature showed that, by decreasing the wall temperature, the frost surface temperature is reduced and the concentration gradient inside the frost layer becomes lower. Consequently, the deposited mass tends to increase the frost thickness rather than the frost density. In addition, increasing the duct height led to a higher gas temperature at the rear end of the plate. Moreover, when reducing the gas velocity and thus the mass flow rate, the remaining mass fraction in the producer gas of the condensable components becomes lower.

Six plates are placed in series in order to reduce the gas temperature and the tar content. As the operating time increases, the frost thickness and density increase. Therefore, the thermal resistivity increases, which leads to higher frost surface temperatures. It can be also deduced that as the wall temperature decreases from one plate to another, the remaining water mass fraction in the gas phase decreases and becomes much lower than that of benzene. Therefore, the frost layer of ice becomes thinner and almost negligible compared with that of benzene as of the third plate. This is also reflected on the latent heat of water sublimation that becomes lower than that of benzene from the second plate until the last one.

More specifically, the condensation and deposition are function of both sublimation or vaporization temperature and the saturation vapor pressure. Even if the initial benzene and toluene contents are higher than that of water, the benzene and toluene have higher saturation vapor pressure than that of water. This makes benzene and toluene more volatile components, thus benzene deposition and toluene condensation will take place only when their saturation vapor pressure at the cold surface temperature becomes lower than their vapor pressure in the gas phase. As for the water, its vapor pressure is higher than the saturation vapor pressure at the wall temperature of the first plate. This leads to the formation of a thick ice frost layer in the first plate that almost has the same thickness of benzene frost layer depending on the initial conditions but a lower frost density. As the wall temperature becomes lower in the second plate, the benzene frost thickness becomes higher than that of the ice. As for toluene, its content is slightly affected in the first plate and it starts to condense when the wall temperature decreases from the second plate until the last one.

As it is previously discussed, the liquid toluene will take the place of the gas in the pores. The thermal conductivity of liquid toluene (around 0.143 $W.m^{-1}.K^{-1}$) is higher than the thermal conductivity of the producer gas (around 0.053 $W.m^{-1}.K^{-1}$), while it is much lower than that of ice (around 2.5 $W.m^{-1}.K^{-1}$). Therefore, the effective thermal conductivity of ice frost layer increases when toluene condenses. On the contrary, the effective thermal conductivity of benzene frost layer is slightly affected by the presence of toluene since the latter has a thermal conductivity close to that of benzene (around 0.157 $W.m^{-1}.K^{-1}$). Moreover, it can be seen that the effective thermal conductivity of benzene frost layer is lower than that of ice, and that the benzene frost layer is thicker than that of ice. Thus, benzene frost layer has the highest thermal resistance and it is the main reason of blocking the heat transfer. This justify the assumption in which benzene is considered to form the first frost layer since it corresponds to the worst-case scenario.

Finally, to analyze the process feasibility, the next chapter will shed the light on the economic assessment of the proposed tar treatment method while optimizing the required refrigeration cycle.

Chapitre 3 : Condensation de goudron à des basses températures.

1. Introduction

Certains travaux [105] ont mentionné que le développement d'un traitement cryogénique pour l'élimination de la fraction légère restante est important pour certains procédés de gazéification. Cette méthode permet de séparer les composants BTX du gaz produit et de les intégrer dans le processus de gazéification. La phase condensée peut alors être utilisée comme source de chaleur supplémentaire pour le gazéifieur, ou dans une chaudière séparée comme combustible.
A ce stade, il est important de définir une géométrie pour les surfaces froides sur lesquelles il aura la condensation et la déposition simultanée des composants de goudron, à l'addition de la vapeur d'eau. Différentes géométries peuvent être envisagées, comme des tubes ou des plaques, par exemple. Étant donné que la plupart des études précédentes ont été développées sur la base de la géométrie des plaques, les plaques plates sont considérées dans le cadre de cette thèse. Cela permet une validation aisée du modèle développé par comparaison avec des résultats expérimentaux et simulés de la littérature.
Pour faire face au problème de condensation multi-composants et à l'importante énergie requise, le processus de refroidissement est divisé en plusieurs étapes. Cette configuration permet de réduire le nombre de composants traités simultanément, en divisant le problème en plusieurs étapes. Elle réduit également la destruction d'exergie en réduisant la différence de température entre la plaque froide et le flux de gaz.

2. Modèle mathématique pour le givrage/la condensation du goudron

2.1. Théorie

Le gaz produit est refroidi par écoulement sur une plaque froide dont la température est inférieure au point de rosée des composants condensables. Du givre et un film liquide apparaissent lorsque la température de la paroi est inférieure au point de congélation et au point de condensation, respectivement. Comme il n'existe pas d'études abordant ce dépôt-condensation simultané de plusieurs composants, chaque phase est hypothétiquement traitée séparément. Par conséquent, deux couches de givre distinctes sont considérées, la première pour le benzène et la seconde pour la glace, en plus d'un film de toluène liquide qui remplit un certain volume des pores. Dans cette étude, le gaz produit circule dans un conduit où la plaque supérieure est isolée afin d'éviter le transfert de chaleur entre le gaz et l'environnement. Le givrage et la condensation se produisent uniquement sur la plaque inférieure du conduit, qui est maintenue à une basse température constante. Fig. 3.1 décrit le modèle physique de transfert de chaleur et de masse entre le gaz et les composants condensables. Le processus est divisé en six sous-domaines : le gaz, l'interface entre la couche de givre de glace et le gaz, la couche de givre de glace, l'interface entre les couches de givre de glace et de benzène, la couche de givre benzénique et le volume de toluène liquide.

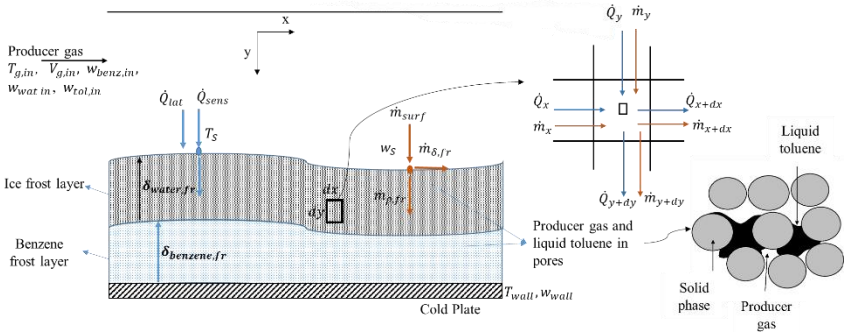

Fig. 3.1: Diagramme du processus de givrage et de condensation

Hayashi et al. [109] sont parmi les premiers à étudier le processus de croissance du givre. Ils ont divisé le processus en trois périodes différentes ; « la période de formation des cristaux », suivie par la « période de croissance du givre », et enfin « la période de développement complet du givre ». La première période correspond aux premiers instants de formation de givre sous forme de colonne de givre. Elle a relativement un temps court par rapport à l'ensemble du processus de formation du givre. Afin de considérer l'impact de cette période sur la croissance du givre, des conditions initiales appropriées, pour l'épaisseur de givre $\left(\delta_{fr,int} = 2 \times 10^{-5}\, m\right)$ et pour la densité de givre $\left(\rho_{fr,int} = 25\, kg.m^{-3}\right)$, sont considérées [110].

La période la plus étudiée est celle de croissance de givre sous la forme d'une structure poreuse formée d'une phase solide poreuse contenant des interstices comblés par le gaz produit. Au cours de cette phase, la masse transférée de la phase gazeuse à la surface froide est divisée en deux parties. La première partie se dépose sur la surface du givre et tend à augmenter son épaisseur, tandis que la deuxième partie diffuse à travers le givre et contribue à l'augmentation de la densité du givre [132]. Cela continue jusqu'à ce que la température de la surface du givre atteigne le point de fusion des composants condensables, indiquant le début de la période de développement complet du givre. Le modèle mathématique développé est formulé en utilisant le système de coordonnées cartésiennes 1D pour le côté gaz, et le système de coordonnées cartésiennes 2D pour le condensat. Il est discrétisé selon la méthode des volumes finis (FVM) et implémenté à l'aide de Dymola.

2.2. Les sous-domaines considérés

Afin de résoudre le système des équations de transfert de masse et de chaleur présenté ci-dessous, la modélisation est faite sur Dymola, basé sur le langage Modelica. La FVM est utilisée pour modéliser la croissance du givre en 2D, où le volume total de givre est discrétisé en des plus petits volumes de contrôle, appelés cellules. Les équations différentielles gouvernantes, présentées précédemment, sont appliquées pour chaque volume de contrôle.

2.2.1. Coté gaz produit

En partant du sous-domaine du gaz produit, la chaleur sensible transférée par convection du gaz produit à la surface du givre $\left(\dot{Q}_{sens}\right)$, est calculée comme suit :

$$\dot{Q}_{sens} = h_{c,g}.S.(T_g - T_{fr,s}) \qquad \textit{Eq. 3.1}$$

Les débits massiques totaux $\left(\dot{m}_{s,j}\right)$ de benzène, de vapeur d'eau et de toluène, transférés du gaz produit à la surface du givre, sont calculés selon l'analogie de transfert de chaleur et de masse définie dans l'Eq. 3.2 où j ∈{benzène, toluène, vapeur d'eau}. Ces débits massiques subiront un changement de phase. Le benzène et la vapeur d'eau sont sujets au givrage tandis que le toluène est sujet à la condensation.

$$\dot{m}_{s,j} = k_{m,j}.S.\rho_g.\left(w_{g,j} - w_{s,j}\right) \qquad \textit{Eq. 3.2}$$

A noter que la surface du givre est considérée à l'équilibre thermodynamique. Ainsi, la fraction massique à la surface du givre peut être liée aux courbes de saturation développées dans le chapitre 2 pour chaque composant à la température de surface comme suit :

$$w_{s,j} = f(T_{fr,s}) \qquad \textit{Eq. 3.3}$$

2.2.2. Surface du givre

Comme mentionné précédemment, le débit massique total transféré du gaz à la surface du givre ($\dot{m}_s$) est divisé en deux termes. Le premier terme ($\dot{m}_\delta$) correspond au débit massique qui augmente l'épaisseur

du givre par dépôt sur la surface, tandis que le deuxième terme ($\dot{m}_\rho$) est le débit massique qui augmente la densité du givre par diffusion à l'intérieur du givre. Eq. 3.4 s'applique aux deux couches de givres de benzène et de glace.

$$\dot{m}_s = \dot{m}_\delta + \dot{m}_\rho \qquad \textit{Eq. 3.4}$$

Le débit massique qui augmente la densité du givre par diffusion à l'intérieur du givre, peut être calculé en fonction de la variation de la fraction massique de vapeur d'eau selon l'axe des y à la surface ($\partial w_{water}/\partial y$), et du coefficient de diffusion effectif de la vapeur d'eau dans le gaz des pores du givre $\left(D_{eff,water}\right)$, comme dans l'Eq. 3.5. Il est à noter que le coefficient de diffusion effectif est égal au coefficient de diffusion multiplié par le facteur de résistance à la diffusion (μ) [138].

$$\dot{m}_{\rho,wat} = -D_{eff,wat}.S.\rho_g.(\partial w_{wat}/\partial y)_s \qquad \textit{Eq. 3.5}$$

Une fois le débit massique diffusant est calculé, le débit massique qui augmente l'épaisseur peut être déduit de l'Eq. 3.4. La variation de l'épaisseur de la couche de givre peut être alors calculée par :

$$\dot{m}_\delta = \rho_{frost}.S.(d\delta/dt) \qquad \textit{Eq. 3.6}$$

Le transfert de chaleur à la surface du givre peut être exprimé par l'Eq. 3.7. Le débit de transfert de chaleur par conduction à la surface est calculé en fonction de la variation de température du givre lorsque y tend vers $\delta_{fr,wat}$, et de la conductivité thermique effective du givre $\left(k_{eff}\right)$ comme dans l'Eq. 3.8.

$$\dot{Q}_{cond,wat,s} = \dot{Q}_{sens} + \dot{m}_{\delta,wat}L_{sv,wat} + \dot{m}_{s,tol}L_{vap,tol} \qquad \textit{Eq. 3.7}$$

$$\dot{Q}_{cond,wat,s} = -k_{eff,wat}.S.(\partial T/\partial y)_s \qquad \textit{Eq. 3.8}$$

2.2.3. L'interface entre la couche de givre de glace et la couche de givre benzénique

Les mêmes équations pour les flux massiques s'appliquent à l'interface benzène-glace. La différence entre eux est que le flux massique conduisant à la densification du givre benzènique, est fonction de la variation de la fraction massique de benzène à l'interface. Le débit massique total de benzène transféré du gaz à la surface du givre de benzène, est calculé selon l'Eq. 3.2. Le débit massique de benzène qui augmente la densité du givre par diffusion à l'intérieur du givre peut être calculé comme suit :

$$\dot{m}_{\rho,benz} = -D_{eff,benz}.S.\rho_{gas}.(\partial w_{benz}/\partial y)_{int} \qquad \textit{Eq. 3.9}$$

Une fois le débit massique diffusant est calculé, le débit massique qui augmente l'épaisseur du givre peut être déduit de l'Eq. 3.4. Ensuite, la variation de l'épaisseur de la couche de givre de benzène $(d\delta/dt)$ peut être calculée selon l'Eq. 3.6.

Le bilan thermique, à l'interface entre les deux couches de givre de benzène et de glace, peut être exprimer par:

$$\left(-k_{eff,wat}.S.(\partial T/\partial y)_{int}\right) = \left(-k_{eff,benz}.S.(\partial T/\partial y)_{int}\right) + \dot{m}_{\delta,benz}L_{sv,benz} \qquad \textit{Eq. 3.10}$$

2.2.4. Les couches de givre

Le bilan massique du benzène ou de la vapeur d'eau à l'intérieur des couches de givre peut être prédit selon la loi de Fick:

$$\frac{\partial}{\partial x}\left(-D_{eff}.\rho_{gas}.\frac{\partial w}{\partial x}\right)+\frac{\partial}{\partial y}\left(-D_{eff}.\rho_{gas}.\frac{\partial w}{\partial y}\right)=-\alpha \qquad \textit{Eq. 3.11}$$

Notez que la condition de saturation est également considérée à l'intérieur de la couche de givre. Ainsi, la même analogie discutée dans la section précédente s'applique au gradient de la fraction massique à l'intérieur de la couche de givre.

La densification des couches de givre peut alors être calculée :

$$d\rho_{frost}/dt=\alpha \qquad \textit{Eq. 3.12}$$

Le bilan énergétique à l'intérieur de la couche de givre est alors appliqué selon l'*Eq. 3.13*. Cette dernière fait le lien entre le transfert de chaleur basé sur la loi de Fourier et la chaleur latente liée à la densification massique.

$$\frac{\partial}{\partial x}\left(-k_{eff}.\frac{\partial T}{\partial x}\right)+\frac{\partial}{\partial y}\left(-k_{eff}.\frac{\partial T}{\partial y}\right)=\alpha.L_{sv} \qquad \textit{Eq. 3.13}$$

2.2.5. Condensation liquide de toluène

La fraction volumique des pores qui sera remplie par le toluène liquide est égale au rapport du volume accumulé du toluène condensé sur le volume total des pores de givre :

$$v_{tol}=\left(\dot{m}_{tol,s}/\rho_{tol}\right).t/\left(\left(\delta_{benz,fr}+\delta_{wat,fr}\right).w_p.L_p.\varepsilon\right) \qquad \textit{Eq. 3.14}$$

3. Givrage du CO_2

L'élimination du goudron exige une réduction de la température jusqu'à -110°C. Cela conduit au givrage simultané du CO_2, en fonction de la composition du gaz produit. Le point de rosée du CO_2 dépend de la teneur initiale de CO_2 présente dans le gaz. Cette dernière ne dépasse pas une fraction molaire de 0.3. A cette fraction molaire, la déposition du CO_2 commence pour des températures inférieures à -92°C. Alors que pour la composition considérée dans cette thèse, qui correspond à une fraction molaire de 0.2, la déposition commence pour des températures inférieures à -96°C. La dernière étape d'élimination du goudron à basse température implique alors une déposition partielle du CO_2, qui ne peut pas être évité.

Le modèle de givrage du CO_2 ainsi que ces propriétés ont été intensivement étudiés par des chercheurs du centre de recherche comme Haddad et al. [154]. Ils ne sont donc pas détaillés dans cette thèse. Cependant, les précédents modèles de croissance du givre du CO_2 ont été développés sur la base d'une analyse 1D, tandis que dans cette thèse, le modèle a été modifié pour une analyse de croissance de givre 2D. Afin de prendre en considération la formation de givre de CO_2 à basse température, il est considéré qu'une couche de givre supplémentaire de CO_2 s'accumule au-dessus des couches de givre de glace et de benzène.

4. Les principales variables

Plusieurs variables figurant dans les équations présentées ci-dessus doivent être calculer afin de les résoudre, y inclut les propriétés thermo-physiques du gaz produit, le coefficient de diffusion $\left(D_{ij}\right)$, le coefficient de conductivité thermique effective $\left(k_{eff}\right)$, le coefficient de transfert de chaleur (h_c), le coefficient de transfert de masse (k_m), etc. Les propriétés thermo-physique du gaz comprennent la conductivité thermique (k_g), la densité (ρ_g), la viscosité (μ_g) et la capacité thermique ($C_{p,g}$). Des

corrélations sont développées pour la prédiction de ses propriétés dans le domaine des conditions opératoires, en utilisant Aspen Properties. Plusieurs corrélations existent dans la littérature pour la prédiction des autres propriétés. Les différentes corrélations sont comparées et celle la plus utilisée ou bien la plus convenable pour l'application de la thèse est sélectionnée comme illustré dans le Tableau 3.1.

Tableau 3.1: Résumé des corrélations principales utilisées pour la prédiction des différents paramètres de givrage.

Propriété	Corrélation	Réf.	Eq.
D_{im}	$D_{im} = \left(\sum_{j=1}^{n} \frac{x_j}{D_{ij}} \right)^{-1}$	[156]	Eq. 3.15
D_{ij}	$D_{ij} = \frac{0.00143T^{1.75}}{PM_{ij}^{1/2}\left[(\sum)_i^{1/3} + (\sum)_j^{1/3}\right]^2}$ où: $M_{ij} = \frac{2}{(1/M_i) + (1/M_j)}$	[144]	Eq. 3.16
D_{eff}	$D_{eff,im} = {\varepsilon_i}/{\tau_i} . D_{im}$ où : $\varepsilon_i = \frac{\rho_{fr,i} - \rho_{solid,i}}{\rho_g - \rho_{solid,i}}$	[157]	Eq. 3.17
τ_i	$\tau_i = 1 - 0.58(1 - \varepsilon_i)$	[146]	Eq. 3.18
k_{eff}	$k_{eff} = {1}/{\left({a}/{k_{per}} + {(1-a)}/{k_{par}}\right)}$ où : $k_{per} = {1}/{\left({\varepsilon}/{k_g} + {(1-\varepsilon)}/{k_{solid}}\right)}$, $k_{par} = {\varepsilon}/{k_g} + {(1-\varepsilon)}/{k_{solid}}$, $a = 0.42(0.1 + 0.995^{\rho_{fr}})$	[138]	Eq. 3.19
h_c	$Nu_{Dh} = 0.023 Re_{Dh}^{0.8} Pr^{0.3}$	[148]	Eq. 3.20
k_m	$k_m = {h_c}/{\rho_g C_{p,g} Le^{2/3}}$	[148]	Eq. 3.21

5. Validation du modèle

Il n'existe pas de modèles gérant un givrage et une condensation simultanés de plusieurs composants. Ainsi, les équations de transfert de chaleur et de masse sont d'abord validées en comparant les résultats avec différentes études antérieures disponibles, pour le cas du givrage de la vapeur d'eau présent dans l'air humide ou pour le givrage de CO_2 des mélanges de CO_2 et N_2.

Dans un premier temps, le modèle est validé pour une croissance de givre unidimensionnelle, qui varie seulement en fonction de l'axe des y. Une comparaison entre les résultats obtenus par le modèle proposé et ceux extraits de Lee et al. [121], est menée. A noter que cette expérience est choisie pour la comparaison car elle constitue une référence de validation des modèles dans la littérature [111,120,132]. Fig. 3.2 présente une comparaison entre les résultats simulés et les résultats expérimentaux de la littérature. On peut voir que les résultats sont très proches et une faible déviation entre les modèles est déduite.

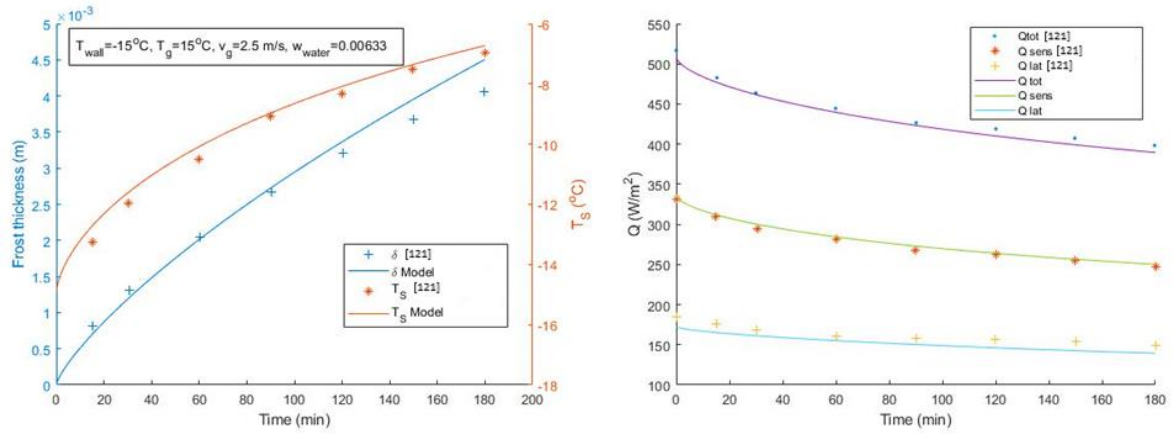

Fig. 3.2: Validation du modèle de croissance du givre basée sur une comparaison avec Lee et al. [121]*, pour la variation de l'épaisseur de la couche de givre, de la température de surface du givre et des flux de chaleur, en fonction du temps.*

Après avoir validé le modèle pour la croissance du givre unidimensionnel, une étape plus avancée pour la validation du modèle avec la croissance du givre bidimensionnel est menée. Les résultats du modèle sont comparés à ceux de Lee et al. [120] pour le givrage de la vapeur d'eau contenue dans l'air humide. Les résultats trouvés dans la littérature pour la croissance du givre bidimensionnel sont obtenus par des modèles basés sur une approche CFD.

Finalement, une comparaison entre les résultats obtenus par le modèle proposé et les résultats expérimentaux extraits de Shchelkunov et al. [153], pour le givrage du CO_2 à partir d'un mélange CO_2-N_2, est menée. Le cas du CO_2 est également considéré puisqu'il se déroule à des températures inférieures à celles requises pour le givrage du H_2O, ce qui correspond au cas du givrage du benzène.

On peut déduire que le modèle proposé aboutit à une prédiction précise du transfert de chaleur et de masse pour la croissance du givre en 1D et 2D, sur une large gamme de conditions opératoires pour le H_2O et le CO_2. Dans la section suivante, le modèle est étendu pour englober la formation de givre de benzène et la condensation de toluène, autre que la formation de givre de vapeur d'eau et de dioxyde de carbone.

6. Résultats et discussion

Cette section traite l'élimination des composants du goudron (benzène et toluène), par dépôt (de gaz vers solide) et condensation (de liquide vers solide) simultanés, à basse température. Cela induit le givrage de la vapeur d'eau présente dans le gaz produit, et alors la formation d'une couche de givre supplémentaire. La température et la composition initiales du gaz sont considérées comme des paramètres fixes, car elles résultent des simulations des colonnes d'absorption à eau précédemment décrites. Les principaux paramètres qui peuvent être modifiés sont la température de la paroi, la vitesse du gaz et les dimensions de la plaque.

6.1. Une seule plaque plane ayant une température constante

Une étude paramétrique pour une seule plaque est ensuite menée afin d'évaluer l'impact des paramètres sur l'élimination de goudron, plus précisément sur la concentration de goudron restante dans le gaz, l'épaisseur du givre, la densité du givre, la température du gaz et les flux thermiques.

Neuf cas différents sont considérés dans l'étude paramétrique. La température initiale du gaz est fixée à 5°C, pour tous les cas. Cette température est égale à la température de sortie des colonnes d'absorption. Dans les cas 1, 2 et 3, la somme des teneurs initiales en benzène et toluène est considérée égale à 100 $g.Nm^{-3}$. Cette dernière correspond à la teneur en goudron la plus haute possible après le gazéifieur. Dans les autres cas, les teneurs initiales en benzène et toluène sont considérées égales à leurs teneurs

résiduelles en sortie des colonnes d'absorption. Dans les 4 premiers cas, un conduit carré est considéré où la largeur de la plaque est égale à la hauteur du canal de gaz. Dans les cas 5 à 8, un conduit rectangulaire est évalué en réduisant de deux la hauteur du canal. Dans le dernier cas, un conduit carré plus grand est envisagé pour évaluer l'impact de la géométrie sur le transfert de chaleur et de masse entre le gaz et la surface. Une comparaison entre cas 2 et cas 4, et entre les cas 5, 6 et 7, permet d'évaluer l'impact de la vitesse, et donc du débit massique, sur la croissance du givre. L'impact de la hauteur du conduit est évalué en comparant cas 4 avec cas 6, tandis que l'impact des teneurs initiales en benzène et toluène est analysé en comparant cas 3 avec cas 4. Finalement, l'impact de la température de la paroi est évalué en comparant cas 6 avec cas 8. La température de la paroi varie entre -20°C et -30°C, la vitesse de gaz varie entre 0.6 et 2 $m.s^{-1}$, et la hauteur du conduit varie entre 0.025 et 0.15 m.

6.1.1. Température du gaz produit

On peut remarquer d'après les résultats que la température du gaz diminue tout au long de la longueur de la plaque, alors qu'elle augmente en fonction du temps. La température du gaz ne varie pas de manière importante en augmentant la vitesse du gaz de 0.6 à 1.5 $m.s^{-1}$. Cependant, dans le cas 1, la vitesse d'augmentation de la température du gaz à l'extrémité de la plaque en fonction du temps est plus basse à des faibles vitesses. Réduire la température de la paroi, se traduit par une température de gaz plus basse puisque la différence de température entre le gaz produit et la plaque augmente. De plus, une teneur initiale plus faible en benzène et toluène affecte légèrement la température du gaz. Par ailleurs, on constate qu'en diminuant la hauteur du conduit et donc le débit massique, tout en gardant une vitesse constante, la température du gaz diminue fortement au bout de la plaque. En outre, l'augmentation de la vitesse du gaz conduit à un taux d'augmentation plus élevé de la température du gaz. Enfin, l'augmentation de la hauteur du conduit réduit fortement le transfert de chaleur entre le gaz et la plaque, conduisant à une température de gaz plus élevée, même pour une température de paroi inférieure.

6.1.2. Teneur restante de benzène et toluène

Dans tous les cas, la fraction massique de benzène restante dans la phase gazeuse (X_{Benz}) est décroissante tout au long de la longueur de la plaque, alors que X_{Benz} augmente légèrement en fonction du temps. De plus, l'augmentation de la vitesse du gaz conduit à X_{Benz} plus élevé. Ceci est lié à la diminution du temps de séjour du gaz produit à l'intérieur du conduit. En outre, la réduction de la température de la paroi se traduit par une X_{Benz} plus faible, suite à l'augmentation de la différence de concentration entre le gaz produit et la surface de givre. Réduire la hauteur du conduit mène à la réduction du débit massique tout en gardant une vitesse constante. Cela conduit à une réduction de la teneur en benzène plus élevée tout au long de la longueur de la plaque. En outre, la fraction massique de toluène restante dans la phase gazeuse (X_{tol}) est toujours intacte dans la plupart des cas, car la température de la paroi n'est pas assez basse pour déclencher la condensation de toluène pour sa teneur initiale.

6.1.3. Epaisseur du givre

Dans tous les cas, l'épaisseur du givre benzénique augmente tout au long de la longueur de la plaque et en fonction du temps. L'augmentation de la vitesse du gaz n'affecte pas fortement l'épaisseur du givre. On peut remarquer que l'augmentation de la vitesse du gaz conduit à un taux de croissance plus élevé de l'épaisseur de la couche de givre, pour la première période de fonctionnement. Après une certaine période de fonctionnement (notée τ_p), la vitesse de croissance de l'épaisseur de givre diminue au fur et à mesure que la température de la surface du givre augmente et atteint la température d'équilibre de transition de phase benzénique. Ainsi, lorsque la vitesse du gaz augmente, τ_p devient plus courte et le taux de croissance de l'épaisseur du givre diminue plus tôt. De plus, la diminution de la température de

la paroi conduit à une couche de givre benzénique plus épaisse. En outre, réduire la hauteur du conduit mène à une couche de givre benzénique plus épaisse.
L'épaisseur du givre de glace diminue tout au long de la longueur de la plaque, alors qu'elle augmente en fonction du temps pour tous les cas. En général, le taux de croissance de l'épaisseur du givre est plus important dans la première période, et il diminue au fur et à mesure que le temps augmente. On peut également observer que le taux de croissance de la couche de givre de benzène commence à diminuer avant celui de la couche de givre de glace. Ceci est dû à la température d'équilibre de la transition de phase, qui est plus faible pour le benzène. L'épaisseur du givre augmente avec l'augmentation des vitesses initiales du gaz, ainsi qu'avec la diminution de la température de la paroi. De plus, la réduction de la hauteur des conduits mène à une couche de givre plus mince. Pour conclure, la vitesse du gaz affecte l'épaisseur de la glace plus que la température de la paroi. Au contraire, la température de la paroi affecte plus l'épaisseur du givre de benzène que la vitesse du gaz.

6.1.4. Flux massique des composants condensables

On peut observer que, dans tous les cas, le toluène a le flux massique total condensable (m'') le plus faible, suivi par l'eau, tandis que le benzène a le flux massique condensable le plus élevé. Bien que les flux massiques totaux diminuent au cours de la croissance du givre, les flux massiques de densification augmentent dans la plupart des cas. Cela est dû à l'augmentation de la différence de température entre la paroi et la surface de givre, au fur et à mesure que le givre se développe. Par conséquent, la différence entre la fraction massique de saturation à la paroi et celle à la surface du givre augmente. De plus, le flux massique condensable de toluène est considérablement réduit au fur et à mesure que le temps augmente jusqu'à devenir nulle, en raison de l'augmentation de la température de la surface du givre. Quant à la couche de givre de glace, on constate que pour tous les cas, le flux massique qui augmente l'épaisseur du givre (m''_{δ}) est supérieur au flux massique qui augmente la densité du givre (m''_{ρ}). Au contraire, pour la couche de givre benzénique, le flux massique qui augmente la densité du givre est supérieur au flux massique qui augmente l'épaisseur du givre. En outre, l'augmentation de la vitesse du gaz augmente m'' pour tous les composants. Cependant, au fur et à mesure que le temps de fonctionnement augmente, m'' diminue de manière plus significative pour des vitesses de gaz plus élevées. De plus, la réduction de la température de la paroi entraîne une augmentation de m''_{δ}. Enfin, des flux massiques totaux de benzène et de toluène plus importants sont obtenus lorsque les teneurs initiales en benzène et toluène sont élevées.

6.1.5. Densité du givre

La densité moyenne du givre augmente au cours de sa croissance. Cependant, le taux d'incrémentation diminue avec le temps. De plus, l'impact de l'étude paramétrique sur les densités de benzène et de glace est le même. L'augmentation de la vitesse du gaz conduit à des densités de givre plus élevées. La réduction de la teneur initiale en benzène réduit la densité du givre. En outre, la réduction de la température de la paroi augmente légèrement la densité du givre. Enfin, la réduction de la hauteur du conduit réduit la densité du givre.
De plus, la densité est plus élevée à l'extrémité avant de la plaque où le gaz produit pénètre. La densité diminue quand la longueur de la plaque tend vers son extrémité arrière. En général, la densité est plus haute près de la surface froide et diminue au fur et à mesure que l'épaisseur du givre tend vers la surface du givre. Quand la couche de givre grandit, la distance entre la surface froide et la surface du givre augmente, entraînant une augmentation de la résistance thermique. De plus, la conductivité thermique augmente avec le phénomène de densification. Cependant, l'augmentation de la conductivité thermique qui résulte de la densification, est inférieure à l'augmentation de la résistance thermique due à la croissance de l'épaisseur du givre. Du coup, la température de la surface du givre ainsi que la température du gaz augmentent avec le temps, comme discuté précédemment. Ce comportement général de

densification est rencontré dans tous les cas. Enfin, le givre benzénique est plus dense que le givre glacé. Ceci est principalement dû au fait que la fraction massique initiale de benzène est supérieure à celle de la vapeur d'eau.

6.1.6. Conductivité thermique effective

La conductivité thermique effective a un comportement similaire à celui de la densité du givre, dans tous les cas, puisqu'elle est calculée en fonction de la densité. De plus, la conductivité thermique effective du benzène est inférieure de 30 % que celle de la glace. Par conséquent, la couche de givre de benzène bloque le transfert de chaleur plus que la couche de givre de glace. Enfin, la conductivité thermique effective moyenne augmente pendant la croissance du givre à cause de l'augmentation de la densité du givre. Cependant, le taux d'incrémentation diminue au fur et à mesure que le temps augmente.

6.1.7. Flux de chaleur

Les flux de chaleur totaux et le flux de chaleur sensible diminuent au cours du temps. Ceci est dû à l'augmentation de la résistance thermique au cours du temps, ce qui augmente la température de surface du givre, la température d'interface et la température du gaz. Au contraire, les flux de chaleur latente diminuent légèrement au début puis restent quasiment constants au cours de la croissance du givre. Seul le flux de chaleur latente de condensation du toluène est presque nul, puisque le poids de toluène liquide condensé dans ces conditions est négligeable. Même si le poids du benzène déposé est supérieur à celui de la glace, le flux de chaleur latente du givrage du benzène est inférieur ou égal à celui du dépôt d'eau. Cela peut être justifié par la chaleur latente élevée de la sublimation de l'eau.

6.2. Placement de plusieurs plaques planes en série

Après avoir étalonné tous les paramètres du modèle, on peut déduire que les conditions opératoires suivantes présentent les meilleurs résultats : $T_{wall} = -25℃$, $T_g = 5℃$, $X_{benz} = 0.063$, $X_{tol} = 0.0092$, $X_{wat} = 0.0075$, $V_g = 1\ m.s^{-1}$ et $w_p \times h_p \times L_p = 0.05 \times 0.025 \times 5$. Le Tableau 3.2 présente les différentes températures de paroi considérées pour six plaques placées en série. On peut voir que la température de paroi des plaques 2, 3 et 4 est réduite de 20°C d'une plaque à l'autre, tandis que pour la cinquième plaque, la température de paroi est fixée à -95°C afin d'éviter le givrage de CO_2. Dans la dernière plaque, le givrage du CO_2 est introduit dans les simulations.

Tableau 3.2: Température de paroi sélectionnée pour les différentes plaques.

Plate #	1	2	3	4	5	6
T_{wall} (°C)	-25	-45	-65	-85	-95	-115

6.2.1. Température du gaz produit et fraction massique de benzène et de toluène

Fig. 3.3 présente la variation de la température du gaz (gauche) et de la fraction massique de benzène restante dans la phase gazeuse (droite), en fonction de la longueur de la plaque et du temps, pour les six plaques placées en séries. Il est à noter que les plaques 1 à 6 sont respectivement représentées de haut en bas. On peut observer que, pour toutes les plaques, la température du gaz est initialement proche de la température de paroi, puis elle augmente avec le temps en raison de la croissance du givre. De même, les fractions massiques de benzène et de toluène restantes diminuent en fonction de la longueur des plaques, alors qu'elles augmentent légèrement en fonction du temps. Au fur et à mesure que les teneurs initiales en benzène et toluène diminuent d'une plaque à l'autre, le taux de réduction de leur fraction massique diminue.

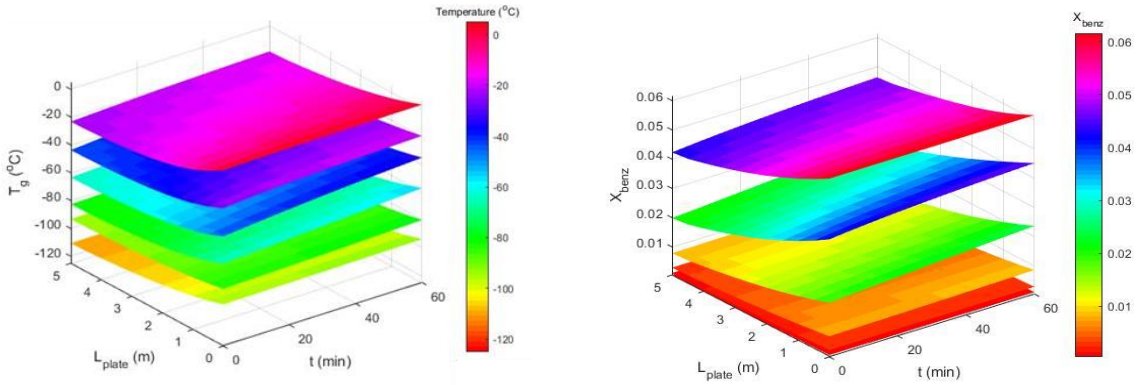

Fig. 3.3: Variation de la température du gaz produit (gauche) et de la fraction massique de benzène restante dans la phase gazeuse (droite), en fonction de la longueur de la plaque et du temps, pour les six plaques placées en séries.

6.2.2. Epaisseur du givre

La couche de givre de glace est plus épaisse que celle du benzène à l'extrémité avant de la première plaque qui a la température de paroi la plus élevée. Cela est due à la température de paroi qui n'est pas assez basse pour entraîner la croissance de la couche de givre de benzène, en raison de sa pression de vapeur élevée. Au contraire, la couche de givre de benzène devient plus épaisse que la couche de givre de glace pour les plaques restantes. Au fur et à mesure que la température de la paroi diminue, la couche de givre benzénique s'épaissit jusqu'à atteindre une valeur maximale dans la troisième plaque, pour une température de paroi de -65°C. D'autre part, l'épaisseur du givre diminue avec la diminution de la température de la paroi.

6.2.3. Flux massique des composants condensables

Le benzène a le poids déposé le plus élevé pour toutes les plaques, car sa fraction massique initiale est la plus élevée. Le poids des couches de givres de benzène et de glace diminue pour chaque plaque ajoutée. Quant au toluène, le poids du liquide condensé dans la première plaque est nul car la différence de température n'est pas suffisante pour sa condensation. En outre, la condensation du toluène se déclenche dans la deuxième plaque pour des températures plus basses. De plus, au fur et à mesure que la température de la paroi diminue d'une plaque à une autre, les flux massiques augmentent en fonction du temps. En outre, quand la température de la paroi diminue, le flux massique qui augmente l'épaisseur du givre (m''_{δ}) devient supérieur à celui qui augmente la densité du givre (m''_{ρ}).

6.2.4. Densité du givre

En général, la diminution de la température des parois conduit à la formation d'une couche de givre plus épaisse ayant une densité plus faible. La couche de givre devient plus épaisse en raison de la faible fraction massique de saturation de benzène à la surface du givre, qui entraîne le dépôt à la surface. Au contraire, la densité devient plus faible puisque le gradient de la fraction massique de saturation à l'intérieur de la couche de givre diminue.

6.2.5. Flux de chaleur

La courbe du flux de chaleur total ressemble à celle du flux de chaleur sensible. De plus, les flux de chaleur latente des différents composants condensables diminuent d'une plaque à l'autre jusqu'à devenir quasi nuls dans la dernière plaque, du fait de leur teneur initiale décroissante. La température de paroi réglée dans la dernière plaque entraîne le givrage du CO_2. Le flux de chaleur latente du givrage du CO_2 est alors introduit. On constate que le flux de chaleur latente le plus élevé est celui du givrage du CO_2. Cela est dû à la fraction massique élevée de CO_2 présente initialement dans le gaz produit. De plus, le flux de chaleur latente du givrage du CO_2 est cinq fois supérieur au flux de chaleur sensible. Cela entraîne une forte augmentation des demandes énergétiques.

7. Conclusion

Une nouvelle méthode permettant de réduire la teneur en goudron initialement présente dans le gaz produit, pour son intégration dans un procédé catalytique, est proposée. Le gaz produit chargé de benzène, de toluène et de vapeur d'eau s'écoule sur une surface froide afin de réduire cette teneur à un niveau acceptable. À cette fin, un modèle mathématique de croissance simultanée du givre et de condensation, a été développé sur Dymola. Le modèle proposé est ensuite validé en le comparant avec des modèles et des expériences de la littérature, pour le givrage de la vapeur d'eau de l'air humide, ainsi que pour celui du CO_2 des mélanges CO_2-N_2.

Une analyse de sensibilité a montré qu'en diminuant la température de paroi, la température de surface de givre diminue ainsi que le gradient de concentration à l'intérieur de la couche de givre. Par conséquent, la masse déposée tend à augmenter l'épaisseur du givre, plutôt que la densité du givre. En outre, réduire la vitesse du gaz et donc le débit massique, réduit la fraction massique des composants condensables restante dans le gaz produit. Ensuite, plusieurs plaques sont placées en série afin de réduire la température du gaz et la teneur en goudron. Au fur et à mesure que le temps augmente, l'épaisseur et la densité du givre augmentent ainsi que la résistivité thermique. Cela conduit à des températures de surface de givre plus élevées.

En résumé, la condensation et le givrage sont fonction à la fois de la température de sublimation ou de vaporisation et de la pression de vapeur de saturation. Même si les teneurs initiales en benzène et toluène sont supérieures à celle de l'eau, le benzène et le toluène ont une pression de vapeur de saturation supérieure à celle de l'eau. Cela rend le benzène et le toluène des composants plus volatils, ainsi le givrage de benzène et la condensation du toluène n'auront lieu que lorsque leur pression de vapeur de saturation à la température de la paroi devient inférieure à leur pression de vapeur en phase gazeuse. Quant à l'eau, sa pression de vapeur est supérieure à la pression de vapeur de saturation à la température de paroi de la première plaque. Cela conduit à la formation d'une épaisse couche de givre de glace dans la première plaque qui a presque la même épaisseur de couche de givre benzénique mais une densité de givre plus faible. Au fur et à mesure que la température de la paroi diminue dans la deuxième plaque, l'épaisseur du givre benzènique devient plus élevée que celle de la glace. Quant au toluène, sa teneur est légèrement affectée dans la première plaque et il commence à se condenser lorsque la température de paroi diminue de la deuxième plaque jusqu'à la dernière.

Chapter 4 : Economic assessment

This chapter aims at evaluating the impact of the suggested tar removal method on the cost of the biomass to biomethane conversion process. The study evaluates the cost of the scrubbing columns and the refrigeration unit required for tar removal. This chapter is divided into three main parts. The first one assesses the impact of the operating conditions on the total cost of the scrubbing columns. The study involves a comparison between the utility costs of the oil-based and water-based scrubbers. The second one analyzes the cost of the refrigeration unit based on several configurations and operating conditions. Energy and exergy analyses are also performed in order to assess and compare the different configurations considered for the refrigeration. Finally, in the last part, the cost of the proposed method at optimal conditions is then compared to the cost of the existing process of tar removal, used in the GoBiGas project, which was previously described in section 1.7. The impact of the plant production capacity on the tar treatment cost is also assessed.

4.1. Reference process

To complete an economic analysis for the proposed tar treatment process, a reference process must be considered. This defines the initial operating conditions and the flow rates of the streams, mainly the producer gas, to be used in the analysis. Therefore, the economic analysis is first conducted for a well-defined biomethane production capacity. Afterwards, the process cost for different production capacities is computed from the reference process cost, based on a scale factor. For this purpose, the GoBiGas plant is set as the reference process since it is the only industrial-scale available plant, which converts the biomass into biomethane while reaching the desired tar content. A detailed economic assessment for the full plant is found in the literature [85]. The latter includes the cost of the tar treatment process adapted in the plant, which combines an RME scrubber with activated carbon beds. The economic analysis in the literature is done for a plant having a production capacity equal to 20 MW of biomethane. Similarly, in the sequel, the calculations are done based on a reference production capacity of 20 $MW_{biomethane}$. The latter corresponds to a DFB biomass gasification unit of 32 MWth [98]. The gasifier converts 150 dry tonnes of biomass per day into 7998 $Nm^3.h^{-1}$ of producer gas (dry flow).

Since this thesis focuses on the tar removal unit, only the cost of this unit is studied in this section. The cost of the remaining units of the plant is considered constant and it is not importantly affected by the tar treatment unit. Table 4-1 summarizes the investment cost of the primary and secondary tar treatment units, in addition to their operating cost.

Table 4-1: Investment and operating costs of the tar treatment system of the GoBiGas plant [85].

Process system	**Investment cost**	
	kSEK	**k€**
Primary producer gas cleaning	23780	2402
Tar adsorption	10620	1072
Related operating cost	**SEK.MWh^{-1}**	**€.h^{-1}**
Electricity	37.6	75.9
RME	31.7	64.0
Activated carbon/BTX removal	8.5	17.2
Other	53.6	108.3

Note that the investment cost of the scrubber alone is not given. The investment cost of the full pre-treatment process, which includes material pre-coating, filter, scrubber, two coolers and analyzers, is presented instead. The tar absorption system includes the activated carbon beds and the regeneration

system. The total investment cost of the plant is equal to 24082 k€. Therefore, the primary producer gas cleaning and the tar adsorption systems contribute in 9.97% and 4.45% from the total investment cost, respectively. The operating cost is calculated based a 20 MW biomethane production plant and 8000 Full Load Hours (FLH) [85]. The "electricity" and the "other" operating costs are those of the full process and not only the tar treatment section. As for the scrubber and the tar adsorption systems, the cost of the consumed RME and AC are considered. However, the electrical consumption of each system is not separately given. Therefore, the electrical consumption of the pumps and the consumptions of the coolers and heaters cannot be computed from the literature. It can be observed in Table 4-1 that the costs of the RME and the AC form 24.1% and 6.5% of the total consumables cost, respectively. Note that the conversion rate from SEK to Euro is taken as 9.9 SEK.€$^{-1}$ (at the date of the article).

4.2. Methodology

The total cost rate $(\dot{Z}_{tot})$ includes the operating costs $(\dot{Z}_{op})$, environmental cost $(\dot{Z}_{env})$, as well as the investment and maintenance cost rate $(\dot{Z}_{Inv})$:

$$\dot{Z}_{tot} = \dot{Z}_{Inv} + \dot{Z}_{op} + \dot{Z}_{env} \tag{4-1}$$

The full process investment cost (Z_{Inv}) is equal to the sum of the investment costs of each process section *j*:

$$Z_{Inv} = \sum_{j} Z_{Inv,j} \tag{4-2}$$

The investment costs for each section are computed, in US$, based on functions found in the literature [158,159]. However, those proposed functions are not up to date. Therefore, the Chemical Engineering Plant Cost Index (CEPCI) is used in order to take into account the price inflation of goods and services in the industry. This method updates the cost published from different years (Z_t) to the present year (Z_{2021}) as:

$$Z_{2021} = Z_t \frac{CEPCI_{2021}}{CEPCI_t} \tag{4-3}$$

The CEPCI coefficient values for the different years from 2001 to 2021 are given in Table 4-2.

Table 4-2: Values of the CEPCI, from 2001 to 2021 [160].

Year	CEPCI	Year	CEPCI	Year	CEPCI
2001	394.3	2008	575.4	2015	556.8
2002	395.6	2009	521.9	2016	541.7
2003	402.0	2010	550.8	2017	567.5
2004	444.2	2011	585.7	2018	603.1
2005	468.2	2012	584.6	2019	607.5
2006	499.6	2013	567.3	2020	596.2
2007	525.4	2014	576.1	2021	655.9

After computing Z_{inv}, the investment and maintenance cost rate $(\dot{Z}_{inv})$ is then computed as:

$$\dot{Z}_{inv} = \frac{Z_{inv} \times \varphi \times CRF}{FLH \times 3600} \tag{4-4}$$

where φ is the maintenance factor and CRF is the Capital Recovery Factor.

The CRF, which is function of the expected equipment lifetime (N) and of the interest rate (i), is computed as:

$$CRF = \frac{i(1+i)^N}{(1+i)^N - 1} \quad (4\text{-}5)$$

The different parameters of eqs. (4-4) and (4-5) are presented in Table 4-3. In this chapter, the annual interest rate is considered as 0.1 for a plant lifetime of 20 years, in order to compare the cost rate of the proposed model to the existing one.

Table 4-3: Values of the economical parameters of eqs. (4-4) and (4-5).

Parameter	Value	Ref.
i	0.1	[85,161]
	0.14	[158,162]
N	15	[158,162]
	20	[85]
FLH	8000	[85]
φ	1.06	[158,162]

The next step consists in computing $\dot{Z}_{op}$ of the process, which includes the cost of the consumables, the cooling, the heating and the electricity consumed by the pumps and the compressors. $\dot{Z}_{op}$ of the scrubbers and the low temperature process are separately detailed in the next sections.

4.3. Scrubbers

The cost of the scrubbers system (cf. section 2.3) is evaluated in this section. The scrubbers investment cost, and their operating cost which includes the consumptions of the pumps, heaters, coolers and scrubbing liquid, are calculated. This section focuses on the operating cost rather than the investment cost, since a pre-treatment method, similar to that of the GoBiGas plant, is used but with a different scrubbing liquid, operating conditions and configurations. Several researchers have studied tar removal by scrubbers. OLGA is one of the most known processes for tar removal by wet scrubbers. Consequently, the proposed water scrubbers process is compared to the oil-based scrubbers placed in series, that were previously described and simulated in section 1.5.2.2. The sensitivity analyses for oil-based and water-based scrubbers, previously presented in sections 1.5.2.2 and 2.3 respectively, are considered in this section in order to analyze their impact on the operating cost.

4.3.1. Investment cost

The investment cost of the proposed pre-treatment method includes the cost of two scrubbers, one stripping column, four heat exchangers and three pumps. This configuration is based on the OLGA process that uses the same equipment with different operating conditions. Therefore, the investment cost of the proposed process is similar to that of the OLGA process. Boerrigter et al. [46] reported an economic assessment of the OLGA process which analyzes the impact of the gasification process size on the specific investment cost. The latter includes the indirect and the onside costs. The indirect costs involve engineering, design and construction supervision costs, while the onside costs include the equipment, installation, instrumentation, control systems and piping costs. It is reported that the specific investment cost decreases as the size of the gasification process increases, until becoming almost constant at 200 €.Nm^{-3} for wet producer gas flow rates higher than 4000 $Nm^3.h^{-1}$.

In a 20 MW biomethane production plant, the wet producer gas flow rate is equal to 11500 $Nm^3.h^{-1}$. Therefore, based on this study, the investment cost of the scrubbing system is equal to 2300 k€. The study of Boerrigter et al. [46] was done in 2005. Therefore, the updated investment cost using eq. (4-3) becomes equal to 3222 k€.

Based on Table 4-1, the updated investment cost of the pre-treatment unit in the GoBiGas plant is equal to 2612 k€. However, the latter only includes the system cost without considering the engineering, the design, the piping and the instrumentation costs, that are separately computed for the whole plant. In general, 30% is added on the investment cost in order to take into account the installation, planning, assembly and indirect costs [163]. This increases the pre-treatment investment cost in the GoBiGas plant to 3396 k€. Therefore, the investment cost of the proposed process and that of the GoBiGas plant are almost similar. More precisely, the investment cost of the proposed pre-treatment process is lower than that of the GoBiGas plant by only 5.4%.

4.3.2. Operating cost

For the sake of comparison, the operating costs of the oil-based scrubbers (cf. section 1.5.2.2) and the water-based scrubbers (cf. section 2.3) are evaluated, in this section. The operating costs of the process is mainly determined by the scrubbing liquid consumption cost and the utilities. The latter is divided into three different parts:

1) The electrical consumption of the three pumps (P-101, P-102 and P-103 in Figure 2-11), that are required for the scrubbing liquid circulation.
2) The amount of steam required to increase the scrubbing liquid temperature.
3) The amount of cooling and refrigeration required to reduce the scrubbing liquid temperature.

A brief description of the different utilities is given in the following. The temperature of the scrubbing liquid leaving the collector is reduced to the desired inlet temperature before re-entering the collector through E-101 (cf. Figure 2-11). The saturated scrubbing liquid leaving the absorber and the regenerated scrubbing liquid leaving the stripper exchange heat in E-104. The rest of the heating is added by steam in E-102, while the additional temperature reduction is achieved by cooling water and/or refrigeration in E-103. Note that the required amount of steam (in E-105) to heat the stripping gas fed to the stripper is not usually considered, since the gasification agent should be heated for its injection in the gasifier independently from the tar removal process. The operating cost of each utility is shown in Table 4-4. As for the coolers and refrigeration, the cost of the cooling water is considered for scrubbing liquid temperatures higher than 30°C, while that of refrigeration is added for lower temperatures (down to 5°C). The utilities costs are calculated per one hour of operation for a wet producer gas flow of 11500 $Nm^3.h^{-1}$ (based on a 20 MW biomethane production plant).

Table 4-4: Pricing of the different process utilities.

Utility	Price
Electricity [164]	0.08 €.kWh^{-1}
Heat [46]	4 €.GJ^{-1}
Cooling water (available at 30°C) [165]	0.012 €.m^{-3}
Refrigeration (water available at 5°C) [165]	0.15 €.m^{-3}

4.3.2.1 Oil-based scrubbers

Figure 4-1 (a) illustrates the variation of the utilities costs in oil-based scrubbers process, function of the L/G ratio in the absorber, while fixing the temperature of the scrubbing liquid to 60°C. The pumps have

the lowest utility cost. It can be seen that the steam consumption for the heaters has the highest share of the utilities cost, for L/G ratios greater than $0.8x10^{-3}$ $m^3.m^{-3}$. The utility cost of pumps, heaters and coolers increases linearly by increasing the L/G ratio. It reaches a total of 14.3 €.h^{-1} for a L/G ratio of $2.66x10^{-3}$ $m^3.m^{-3}$.

Figure 4-1 (b) illustrates the variation of the utilities cost in oil-based scrubbers process, function of the scrubbing liquid temperature, while setting the L/G ratio to $1.82x10^{-3}$ $m^3.m^{-3}$. It can be seen that the heaters have the highest utility cost, followed by the coolers, while the pumps have the lowest utility cost. The electrical consumption is not affected by the scrubbing liquid temperature. Steam and cooling water consumptions increase as the scrubbing liquid temperature decreases. The highest total utilities cost is equal to 11.03 €.h^{-1} for a scrubbing liquid temperature of 40°C.

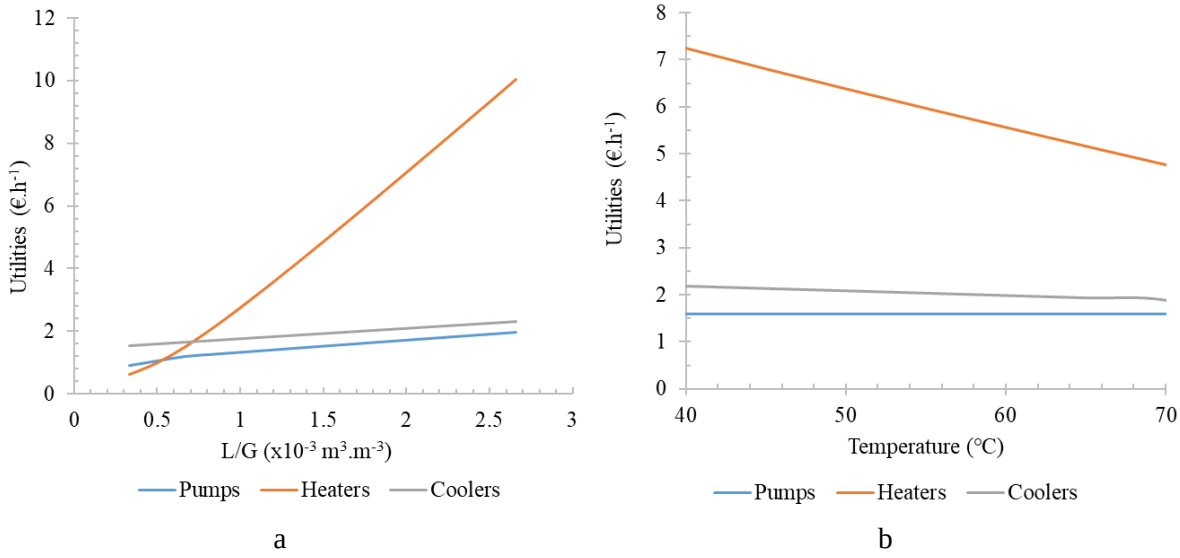

Figure 4-1: Variation of the utilities cost in oil-based scrubbers process, function of a) the L/G ratio in the absorber at 60°C b) the scrubbing liquid temperature fed to the absorber for a L/G ratio of $1.82x10^{-3}$ $m^3.m^{-3}$.

4.3.2.2 Water-based scrubbers

Figure 4-2 (a) illustrates the impact of the L/G ratio in the collector on the utilities costs in the water scrubbers process, for a scrubbing liquid temperature of 25°C. For the first analysis, the L/G ratio and the scrubbing liquid temperature are respectively fixed to $3.06x10^{-3}$ $m^3.m^{-3}$ and 20°C, in the absorber. Figure 4-2 (b) shows the variation of the utilities cost in the water scrubbers process, function of the liquid to gas ratio, for a scrubbing liquid temperature of 20°C. In the second analysis, the liquid to gas ratio and the temperature in the collector are fixed to $0.89x10^{-3}$ $m^3.m^{-3}$ and 25°C, respectively. Finally, the variation of the utilities costs in the water scrubbers, function of the scrubbing liquid temperature in the absorber, is illustrated in Figure 4-2 (c). In the third analysis, the L/G ratios in the collector and in the absorber are set to 0.89 $x10^{-3}$ $m^3.m^{-3}$ and $2.57x10^{-3}$ $m^3.m^{-3}$, respectively. The temperature of the water fed to the collector is set to 25°C. It can be seen that in the three cases, the electrical consumption has the lowest share in the utilities cost and it varies between 0.38 and 0.73 €.h^{-1}. Moreover, the consumption of the heaters, cooler and refrigeration increase with the L/G ratio in both columns. The L/G ratio in the collector has a low impact on the cooling cost. On the contrary, increasing the L/G ratio in the absorber importantly increases the utility cost. In the collector, increasing the L/G ratio increases the steam consumption and therefore the heaters utility cost until becoming constant around a L/G ratio of 1.3 $x10^{-3}$ $m^3.m^{-3}$. Steam consumption for the heaters linearly increases with the L/G ratio in the absorber. It can

be seen from Figure 4-2 (c) that, reducing the scrubbing liquid temperature increases the steam, the cooling water and the refrigeration consumptions, simultaneously. It can be also seen that operating at temperatures lower than 30°C, importantly increases the coolers and refrigeration cost. This refers to the additional refrigeration required to reduce the water temperature from 30°C to the suitable operating temperature. However, decreasing the scrubbing liquid temperature yields a higher tar removal efficiency. For a scrubbing liquid temperature of 5°C, the total utilities cost is 32.8 €.h^{-1}.

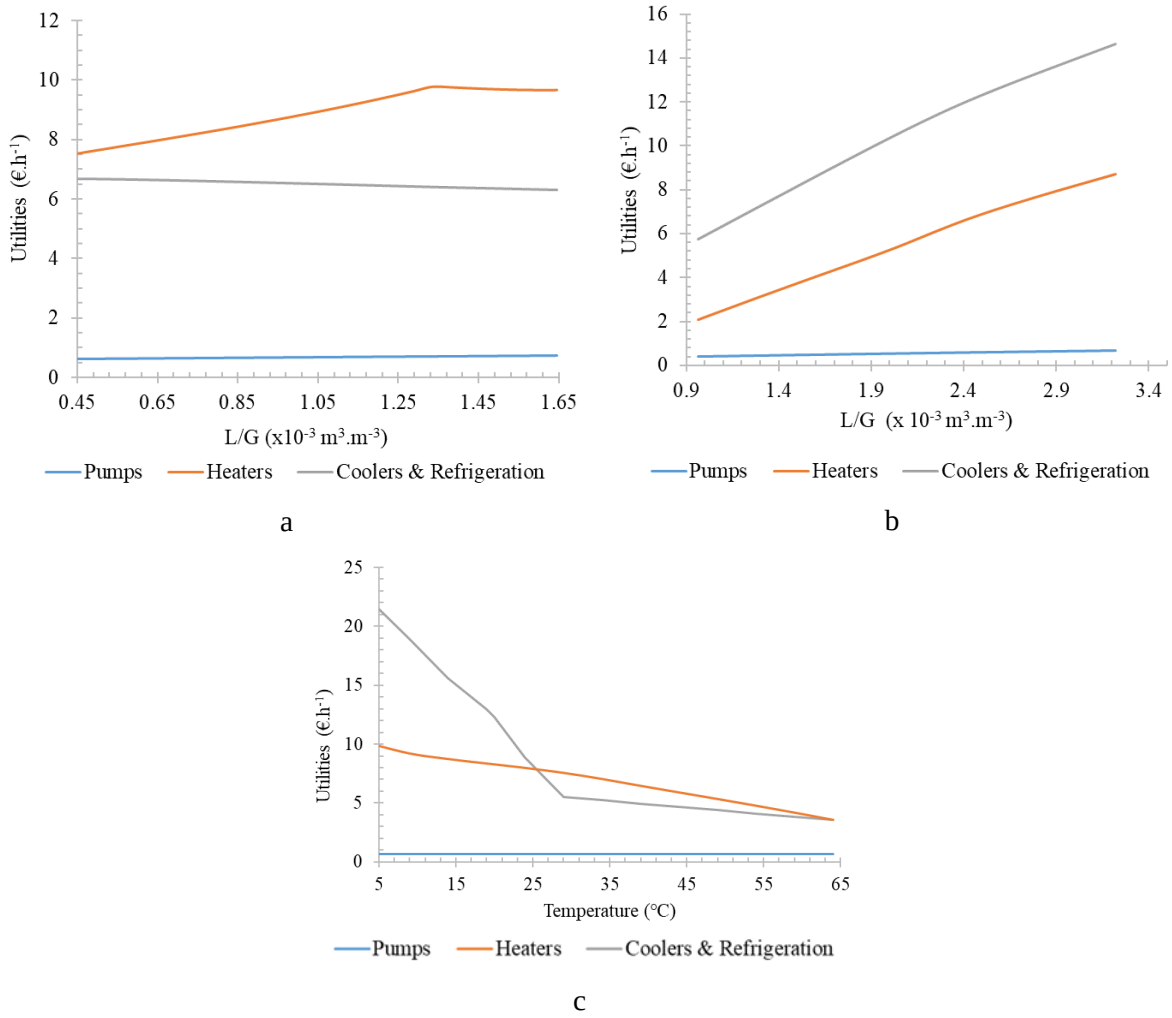

Figure 4-2: Variation of the utilities cost in the water scrubbers process, function of a) the L/G ratio in the collector, for a water temperature of 25°C, b) the L/G in the absorber, for a water temperature of 20°C and c) the water temperature, for a L/G ratio of 2.57x10^{-3} m^3.m^{-3}.

In other words, increasing the L/G ratio and decreasing the scrubbing liquid temperature result in a higher tar removal efficiency, at the expense of a higher utility cost. Therefore, the selection of the optimal operating conditions is crucial.

Finally, it can be deduced that the utilities cost for the water scrubbers is higher than that of the RME scrubbers. However, the difference between the scrubbing liquids prices makes the water scrubbers an appropriate alternative option. The price of water, used as a scrubbing liquid, depends on the considered country. For instance, in France, a cubic meter of water costs around 3.42€ [166]. While the RME is more expensive than water. An RME cubic meter costs around 970 € [167].

For the GoBiGas plant, 70 kg.h^{-1} of fresh RME are required during the stable operation of the 20MW biomethane production plant [98]. The operating cost of the fresh RME added during the stable operation is equal to 3.2 €.MWh^{-1}, which is equivalent to 60.04 €.h^{-1} for $P = 20MW$. Therefore, the RME cost is considered equal to 0.914 €.MWh^{-1}, which is 16% lower than the one found in the literature [164,167]. The same scrubbing liquid recycle ratio is considered in the water-based scrubber, in order to compute the cost of the fresh water added during the stable operation. This yields a fresh water stream of 250 kg.h^{-1}, which is equivalent to 0.827 €.h^{-1} for $P = 20MW$. Therefore, the operating cost of the scrubbing process is highly reduced when using water instead of RME, as scrubbing liquid.

The selection of the suitable scrubbing liquid and the suitable operating conditions depends on several factors; the tar removal efficiency, the required limit for the producer gas application, the operating cost that combines the utilities and the scrubbing liquid prices. In the case of the low temperature process, the water scrubbers are used as a pre-treatment process in order to reduce the water content and the temperature of the producer gas. This decreases the energy required in the low temperature process by limiting the formation of a thick and dense ice frost layer due to the high initial water vapor content.

4.4. Low temperature process

It was previously seen in Chapter 3 that reducing the tar content to 1 mg.Nm^{-3} by simultaneous frosting and condensation over cold surfaces, is feasible when reducing the wall temperature to -115°C. A suitable refrigeration system is required to reach this temperature. Consequently, in this section, different refrigeration systems are compared while performing an energy, exergy and economic analyses for each configuration.

4.4.1. Studied configurations of refrigeration utilities

The refrigeration system mainly aims at reducing the producer gas temperature to -110°C. However, the producer gas is not required to be at low temperature in the methanation process. For this purpose, the cold of the producer gas is recuperated by its integration in the refrigeration process, in which the cold of the producer gas is used to reduce the refrigerant temperature after its compression. This decreases the cost and the energy required in the refrigeration cycle.

As a first step, a simple refrigeration cycle formed of a compressor, condenser, expansion valve and evaporator, is evaluated. This refrigeration cycle is illustrated in Figure 4-3. Firstly, the compressor, which is the heart of the refrigeration system, increases the pressure of the refrigerant. The refrigerant, leaving the compressor at high temperature, is cooled in the condenser (denoted by $HX - COND$) through a countercurrent flow of the cold producer gas. The refrigerant undergoes then an isenthalpic expansion, through a throttle valve, in order to reduce its pressure. Afterwards, the refrigerant enters the evaporator (denoted by $HX - EVAP$), which corresponds to the low temperature process. In the evaporator, the producer gas leaving the scrubber is cooled by means of the cold refrigerant. Several refrigerants are simulated using several operating conditions, including nitrogen, methane and a mixture of nitrogen and methane. Those refrigerants are considered according to the required temperature range in the process, for which a temperature below -110°C must be achieved while operating at pressure higher than the atmospheric. Note that the duty of the evaporator is higher than that of the condenser, since the tar components, the water vapor and a CO_2 fraction undergo a phase change. Therefore, those components are removed from the producer gas and their latent heat of phase change is no longer available in the condenser. As a result, the lowest achievable producer gas temperature, through the simple refrigeration cycle, is equal to -60°C. Therefore, the target of reducing the producer gas temperature to -110°C cannot be achieved due to the fact that the cold of the producer gas is not sufficient

to cool the refrigerant to the required temperature in the condenser. For this purpose, the refrigeration cycle is modified in a way to increase the cooling capacity of the cycle. Figure 4-4, Figure 4-6 and Figure 4-7 show the three modified configurations of the considered refrigeration cycles and their respective P-h diagrams.

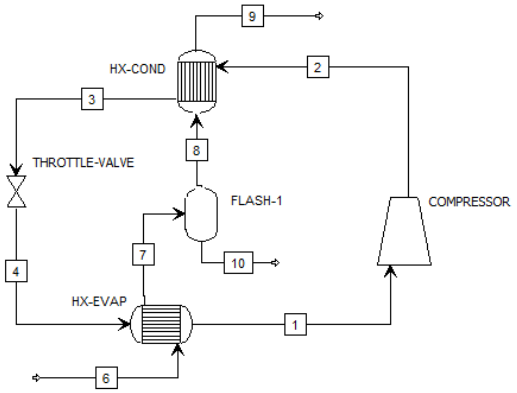

Figure 4-3: Simple refrigeration cycle with heat integration formed of a compressor followed by a cooler or a condenser, then a throttle valve and finally a heater or an evaporator.

It can be seen that in the three configurations, a cooling stage is added prior to the condenser. In this cooler, the refrigerant temperature is reduced to 30°C, using cooling water. Consequently, the condenser duty is reduced and a lower refrigerant temperature can be reached after the condenser. In addition, in the methanation process, the producer gas is compressed after the tar removal unit. Therefore, the temperature of the hot producer gas leaving the condenser should not be too high. By decreasing the temperature of the refrigerant to 30°C in the cooler, the temperature of the hot producer gas leaving the condenser is limited to 27°C. This is done by setting a minimum temperature approach of 3°C in the condenser.

In the first configuration ($Conf1$), presented in Figure 4-4 (a), a pre-cooling stage is added prior to the evaporator. This is based on the fact that the refrigeration cycles that are capable of reducing the temperature to -50°C are well developed and commercially available with a low cost, while reaching temperatures of -110°C is more costly and less developed. Accordingly, the low temperature process combines the pre-cooler and the evaporator units. The producer gas temperature is reduced in the pre-cooler to a minimal temperature of -50°C before entering the evaporator. Therefore, the condenser duty is reduced by decreasing the inlet temperature of the hot producer gas side. Moreover, the refrigerant cooled by the producer gas becomes able to reduce the producer gas temperature to -110°C. Two different refrigerants are considered in $Conf1$. Figure 4-4 (b) and (c) respectively illustrate the P-h diagram of nitrogen and methane. Moreover, a N_2-CH_4 mixture is also considered. In the refrigeration cycle, the nitrogen does not undergo a phase change. Only the sensible heat of the nitrogen is used. On the contrary, part of the methane liquefies either in the condenser or by expansion. Therefore, in the evaporator, both sensible and latent heat transfer take place on the refrigerant side. The P-h diagrams of nitrogen and methane are presented in Appendix D.

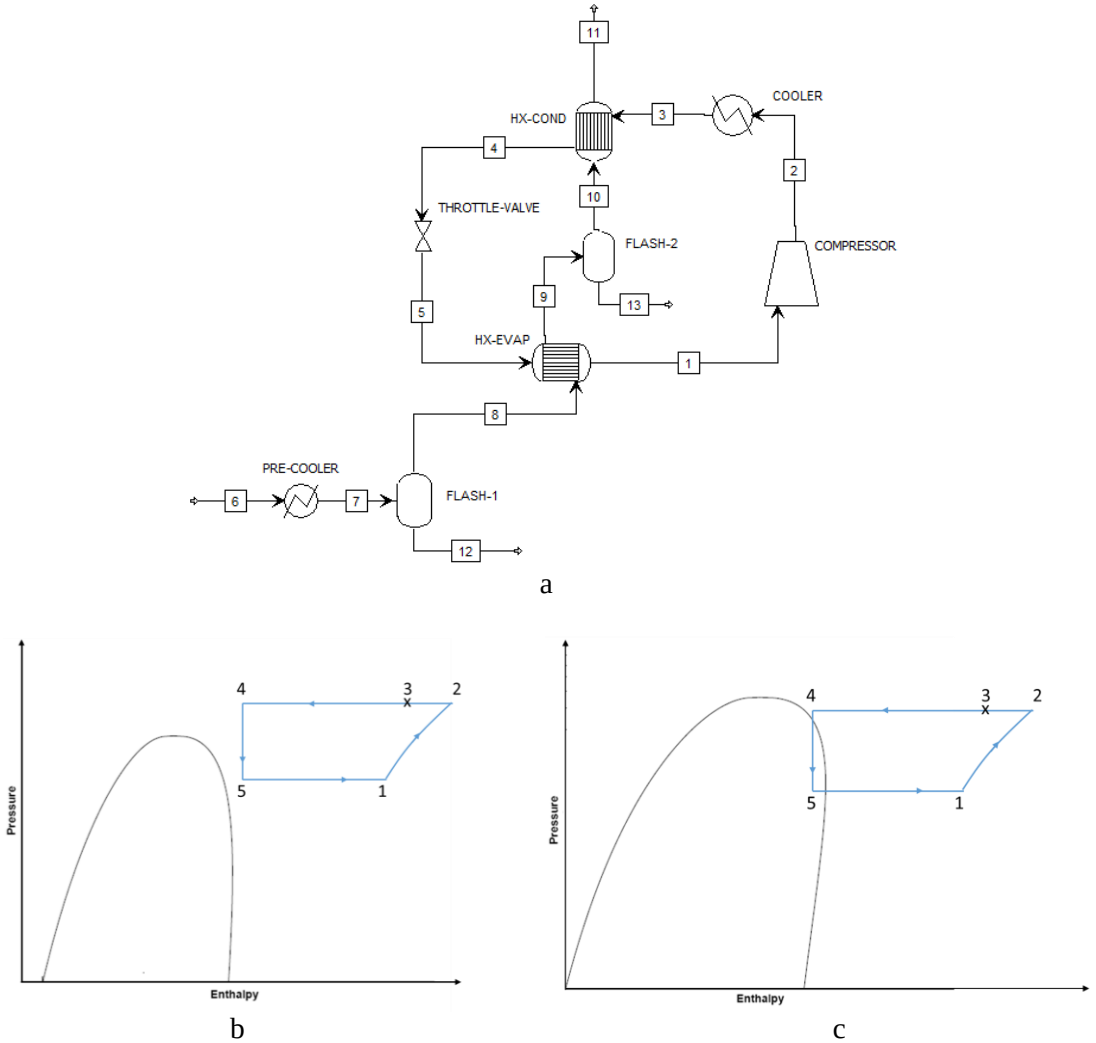

Figure 4-4: Schematic diagram of the refrigeration cycle "Conf1" (a), P-h diagrams of nitrogen (b) and methane (c).

Since the refrigeration cycle of the described pre-cooler is industrially available, the BITZER software [168] is used to configure the refrigeration system by defining the refrigerant, the compressor type, the cooling capacity, the evaporating and the condensing temperatures. The software returns the compressor model, the exact cooling capacity, the required power input, the Coefficient of Performance (COP), the mass flow rate and the temperature of each stream. Therefore, the cycle operating cost is computed based on the required power input, while the investment cost is calculated based on the purchase cost of the compressor model and the remaining components from online catalogs [169]. Note that two types of compressors are available. The first type, presented in Figure 4-5 (a), is a 1-stage semi-hermetic reciprocating compressor. The second type, presented in Figure 4-5 (b), is a 2-stage semi-hermetic reciprocating compressor. For both compressor types, the R404A refrigerant is used. The R404A is considered as a base case in the study. However, future work will replace the R404A by R448A since all the refrigerants having a Global Warming Potential (GWP) higher than 2500 are no longer allowed to be used in new applications in the European Union since January 2020 [170]. The R448A can be used as a substitute to the R404A using the existing system while considering a temperature glide of 5°C [168]. The limits of the evaporating temperature (to) and condensing temperature (tc) are also presented in Figure 4-5. It can be seen that a lower temperature can be reached in the evaporator in the 2-stage compressor type, for the same refrigerant. The evaporator of the cycle corresponds to the pre-cooler, in which the cold of the R404A is exchanged with the producer gas. A minimum temperature approach of

5°C is considered in the pre-cooler. For instance, for temperatures lower than -40°C, a 2-stage semi-hermetic reciprocating cooler should be used. However, the evaporating capacity of the system decreases with the decrease of the outlet producer gas. Note that, in order to reach the required cooling capacity, several refrigeration cycles are placed in parallel since the cooling capacity of a single refrigeration cycle is lower than the required one. Therefore, the required total number of the required cycles (n) is computed by dividing the required cooling capacity $(\dot{Q}_{pre-cool})$ by the cooling capacity of each cycle $(\dot{Q}_{cycle,BITZER})$:

$$n = \dot{Q}_{pre-cool} / \dot{Q}_{cycle,BITZER} \quad (4\text{-}6)$$

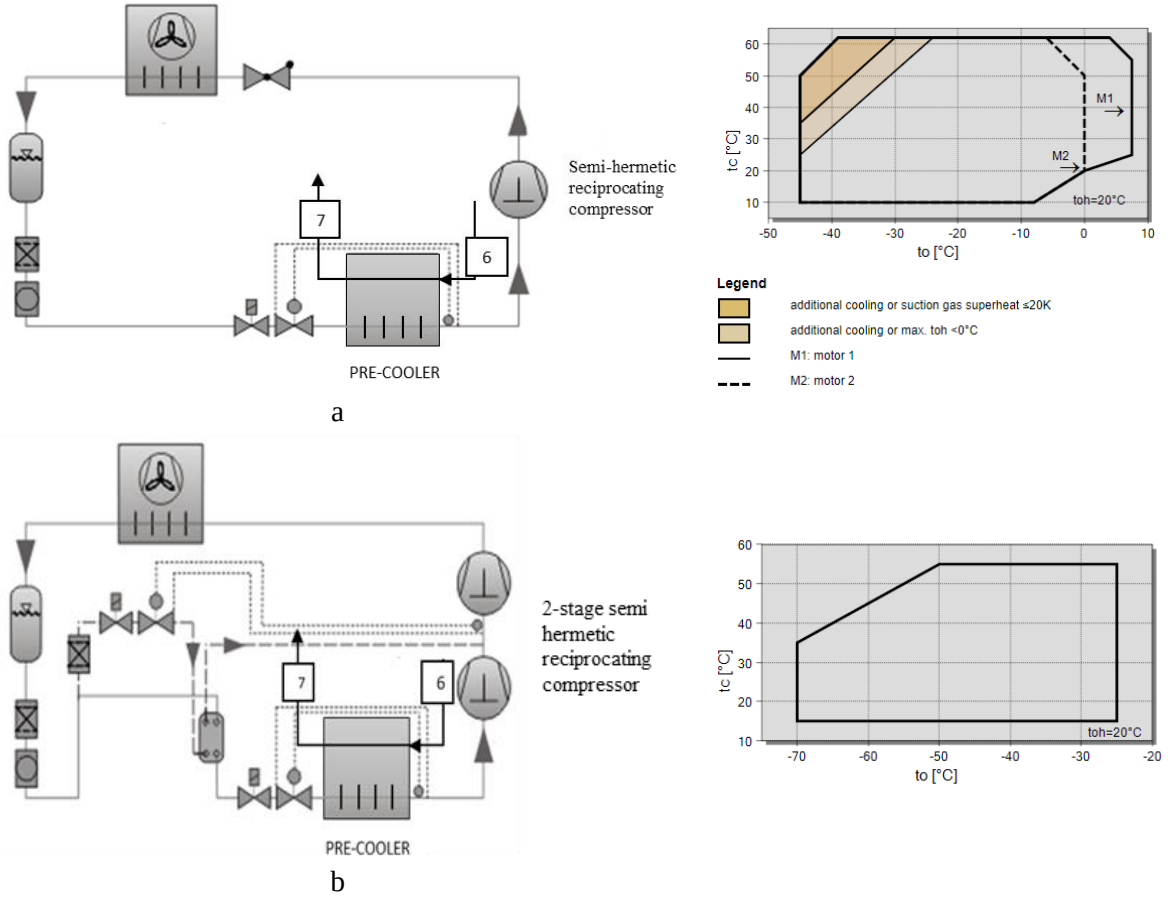

Figure 4-5: Refrigeration cycles of the pre-cooling unit based on single stage (a) and two-stages (b) semi-hermetic reciprocating compressors, in addition to their application limits for the R404A refrigerant [168].

As in $Conf1$, a pre-cooling stage is also added in the second configuration ($Conf2$), prior to the evaporator. Figure 4-6 (a) and (b) respectively illustrate the schematic diagram of the second configuration and the P-h diagram of nitrogen. In $Conf2$, the isenthalpic throttle valve is replaced by a gas turbine. Due to the isentropic expansion, lower refrigerant temperatures can be reached. The work released from the turbine is used in the compressor. Only nitrogen is suitable for this configuration. The methane can no longer be used in this configuration, since part of it is liquefied under those operating conditions.

Finally, the third configuration ($Conf3$) is presented in Figure 4-7. In this configuration, the producer gas is not cooled before entering the evaporator. Therefore, the tar removal takes place only in the evaporator. In order to have an additional temperature reduction after the expansion, the isenthalpic throttle valve is replaced by a gas turbine. The P-h diagram of $Conf3$ is similar to that of $Conf2$. Similarly, only nitrogen is used as a refrigerant in this configuration, in order to avoid the formation of

a liquid condensation in the turbine. Note that $Conf2$ and $Conf3$ are modified versions of the reversed Brayton cycle.

In order to design, select and optimize the refrigeration cycle, multiple criteria should be analyzed. For instance, the economic and the thermodynamic criteria are considered. In some studies [161,171], the environmental aspect is also considered by computing the CO_2 emissions in order to assess the impact of the system on the environment. The main objective of the analysis presented here is to select the appropriate refrigeration configuration, while reducing the exergy destruction, the investment and operation costs, as well as the environmental cost.

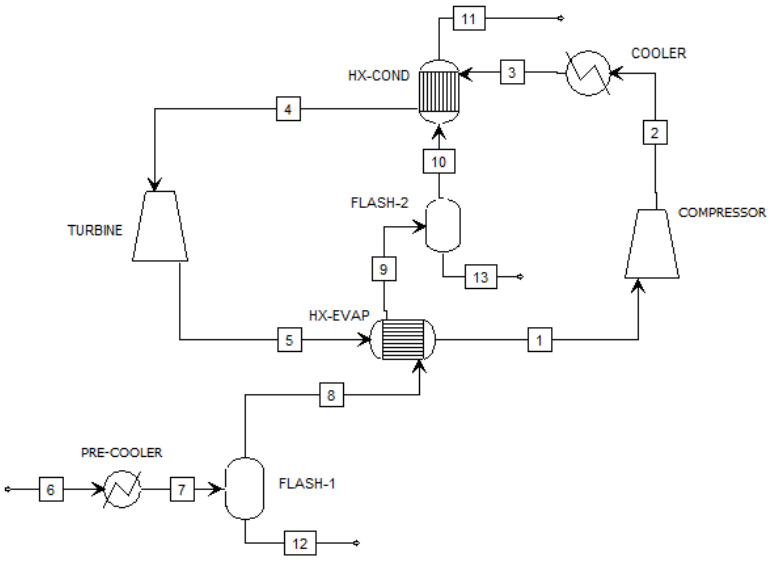

a

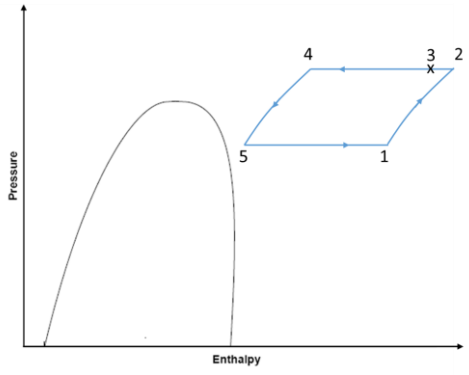

b

Figure 4-6: Schematic diagram of the refrigeration cycle "Conf2" (a), and P-h diagrams of nitrogen (b).

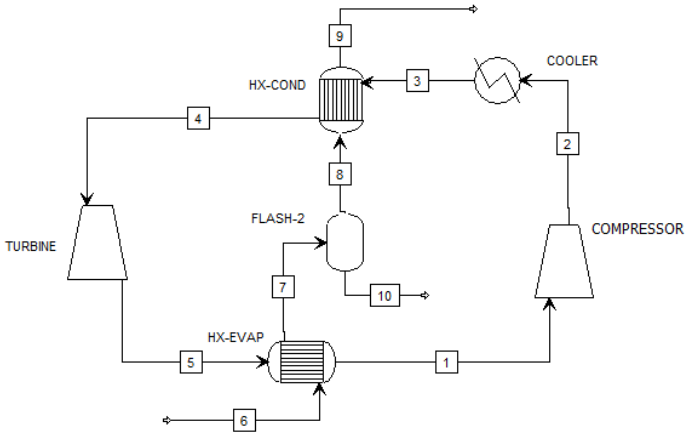

Figure 4-7: Schematic diagram of the refrigeration cycle "Conf3".

Note that the flash drums are not studied in details, since the condensable fraction will be retained in the evaporator by frosting. Therefore, no real separation will take place in the flash drum in a fluid phase. However, it is placed in order to avoid any condensate dragging in the gas stream.

4.4.2. Thermodynamic analysis

The thermodynamic analysis generally includes an energetic analysis (first law), and an exergetic analysis (second law). The energetic analysis is performed in order to analyze the cooling capacity of the refrigeration cycle, function of several parameters. The exergetic analysis is performed in order to compute the exergy destruction of the cycle and modify the parameters in a way to reduce it, while conserving a high cooling capacity with a low total cost rate.

In order to simplify the thermodynamic analysis, several assumptions are considered:

- The system is considered in steady state.
- A steady flow is considered in the process.
- The pressure drop and the heat losses in the pipes of the system are neglected.
- The potential and kinetic energy effects are neglected.

4.4.2.1 Energy Analysis

REFPROP [151] is used to determine the thermodynamic properties of the considered refrigerants, that are CH_4 and N_2.

The compressor power consumption ($\dot{W}_{comp}$) is calculated function of the refrigerant mass flow rate ($\dot{m}_r$), the enthalpy change and the compressor isentropic efficiency $(\eta_{isen,comp})$:

$$\dot{W}_{comp} = \frac{\dot{m}_r(h_{2,s} - h_1)}{\eta_{isen,comp}} \quad (4\text{-}7)$$

The heat rate transferred from the refrigerant to the cooling water in the cooler $(\dot{Q}_{cooler})$, is expressed by eq. (4-8). The refrigerant mass flow rate and enthalpy change are used for computing $\dot{Q}_{cooler}$. The cooling water mass flow rate $(\dot{m}_{CW})$ is then calculated from the same equation by considering a temperature difference of 10°C $(T_{CW,out} - T_{CW,in} = 10°C)$.

$$\dot{Q}_{cooler} = \dot{m}_r(h_2 - h_3) = \dot{m}_{CW} \times Cp_{CW}(T_{CW,out} - T_{CW,in}) \quad (4\text{-}8)$$

The heat rate exchanged from the refrigerant to the cold producer gas in the condenser $(\dot{Q}_{cnd})$, is calculated according to eq. (4-9) for $Conf1$ and $Conf2$, and according to eq. (4-10) for $Conf3$.

$$\dot{Q}_{cnd} = \dot{m}_{g,10}(h_{11} - h_{10}) = \dot{m}_r(h_3 - h_4) \quad (4\text{-}9)$$

$$\dot{Q}_{cnd} = \dot{m}_{g,8}(h_9 - h_8) = \dot{m}_r(h_3 - h_4) \quad (4\text{-}10)$$

where $\dot{m}_g$ is the producer gas mass flow rate in kg.s^{-1}.

As for the expansion device in $Conf1$, the throttle valve is assumed to be isenthalpic, so the energy balance can be expressed by:

$$h_4 = h_5 \quad (4\text{-}11)$$

As for $Conf2$ and $Conf3$, the real turbine work ($\dot{W}_{turb}$) is calculated function of the refrigerant mass flow rate, the enthalpy change and the turbine isentropic efficiency $(\eta_{isen,turb})$:

$$\dot{W}_{turb} = \left(\dot{m}_r(h_4 - h_5)\right)\eta_{isen,turb} \quad (4\text{-}12)$$

The isentropic efficiency of the compressor and the turbine are considered constant and equal to 72%.

The pre-cooler energy balance, expressed by eq. (4-13), is only used in $Conf1$ and $Conf2$.

$$\dot{Q}_{pre-cool} = \dot{m}_{g,6}h_6 - \dot{m}_{g,7}h_7 \quad (4\text{-}13)$$

The heat rate exchanged from the producer gas to the refrigerant in the evaporator $(\dot{Q}_{evap})$, is calculated according to eq. (4-14) for $Conf1$ and $Conf2$, and according to eq. (4-15) for $Conf3$.

$$\dot{Q}_{evap} = \dot{m}_{g,8}h_8 - \dot{m}_{g,9}h_9 = \dot{m}_r(h_5 - h_1) \quad (4\text{-}14)$$

$$\dot{Q}_{evap} = \dot{m}_{g,6}h_6 - \dot{m}_{g,7}h_7 = \dot{m}_r(h_5 - h_1) \quad (4\text{-}15)$$

The refrigeration unit COP is calculated according to eq. (4-16) for $Conf1$, and according to eq. (4-17) for $Conf2$ and $Conf3$.

$$COP = \frac{\dot{Q}_{evap}}{\dot{W}_{comp}} = \frac{\dot{Q}_{evap}}{\dot{Q}_{cond} + \dot{Q}_{cooler} - \dot{Q}_{evap}} \quad (4\text{-}16)$$

$$COP = \frac{\dot{Q}_{evap}}{\dot{W}_{comp} - \dot{W}_{turb}} \quad (4\text{-}17)$$

4.4.2.2 Exergy analysis

In general, mass and energy are conserved in thermodynamic processes. On the contrary, the exergy is destructed in a thermodynamic process, due to the system irreversibility. The exergy analysis consists in computing the exergy of each stream in the process, then the exergy loss and the exergy destruction $(\dot{E}x_D)$ are calculated for each component in the cycle [171].

The exergy balance around a closed control volume is expressed by:

$$\dot{m}_{out}\dot{ex}_{out} - \dot{m}_{in}\dot{ex}_{in} = \dot{E}x^Q - \dot{E}x^W - \dot{E}x_D \quad (4\text{-}18)$$

where $\dot{ex}_{in}$ and $\dot{ex}_{out}$ are respectively the exergy of the inlet and outlet streams of the control volume, in kJ.kg^{-1}, $\dot{m}_{in}$ and $\dot{m}_{out}$ are respectively the mass flow rate of the inlet and outlet streams of the control volume, in kg.s^{-1}, $\dot{E}x^{Q}$ is the exergy transfer rate accompanying the heat transfer and equal to $\dot{Q}(1 - T_0/T)$, $\dot{E}x^{W}$ is the exergy transfer rate associated with the work and equal to $\dot{W}$, and $\dot{E}x_D$ is the exergy destruction rate. Note that $\dot{E}x^{Q}$, $\dot{E}x^{w}$ and $\dot{E}x_D$ are expressed in kW.

The exergy of a stream n $(\dot{ex}_n)$ can be calculated, function of the enthalpy and entropy (s) at the reference state 0, as follows:

$$\dot{ex}_n = (h_n - h_0) - T_0(s_n - s_0) \tag{4-19}$$

$\dot{E}x_D$ in each system component is deduced by developing the exergy balance around each one. The exergy destruction of the compressor $(\dot{E}x_{D,comp})$ is computed as:

$$\dot{E}x_{D,comp} = \dot{m}_r(\dot{ex}_1 - \dot{ex}_2) + \dot{W}_{comp} \tag{4-20}$$

The cooler exergy destruction $(\dot{E}x_{D,cooler})$ is given by:

$$\dot{E}x_{D,cooler} = \left(\dot{m}_r\dot{ex}_2 + \dot{m}_{CW}\dot{ex}_{CW,in}\right) - \left(\dot{m}_r\dot{ex}_3 + \dot{m}_{CW}\dot{ex}_{CW,out}\right) \tag{4-21}$$

The condenser exergy destruction $(\dot{E}x_{D,cnd})$ is calculated according to eq. (4-22) for $Conf1$ and $Conf2$, and according to eq. (4-23) for $Conf3$.

$$\dot{E}x_{D,cnd} = \left(\dot{m}_r\dot{ex}_3 + \dot{m}_g\dot{ex}_{10}\right) - \left(\dot{m}_r\dot{ex}_4 + \dot{m}_g\dot{ex}_{11}\right) \tag{4-22}$$

$$\dot{E}x_{D,cnd} = \left(\dot{m}_r\dot{ex}_3 + \dot{m}_g\dot{ex}_8\right) - \left(\dot{m}_r\dot{ex}_4 + \dot{m}_g\dot{ex}_9\right) \tag{4-23}$$

As for the expansion device in $Conf1$, the throttle valve is assumed to be isenthalpic, and therefore the exergy destruction $(\dot{E}x_{D,TV})$ can be expressed as:

$$\dot{E}x_{D,TV} = \dot{m}_r(\dot{ex}_4 - \dot{ex}_5) \tag{4-24}$$

As for $Conf2$ and $Conf3$, the turbine exergy destruction $(\dot{E}x_{D,turb})$ is given by:

$$\dot{E}x_{D,turb} = \dot{m}_r(\dot{ex}_4 - \dot{ex}_5) - \dot{W}_{turb} \tag{4-25}$$

The pre-cooler exergy destruction $(\dot{E}x_{D,pre-cool})$, expressed by eq.(4-26), is only used in $Conf1$ and $Conf2$. $\dot{E}x_{D,pre-cool}$ is calculated function of the mass flow rate of the R404A refrigerant $(\dot{m}_{R404A})$, the set evaporation temperature (T_{R404A}) and the heat transfer rate in the pre-cooler.

$$\dot{E}x_{D,pre-cool} = \dot{m}_{R404A}\left(\dot{ex}_{R404A,in} - \dot{ex}_{R404A,out}\right) - \left(1 - \frac{T_0}{T_{R404A}}\right)\dot{Q}_{pre-cool} \tag{4-26}$$

The evaporator exergy destruction $(\dot{E}x_{D,evap})$ is calculated according to eq. (4-27) for $Conf1$ and $Conf2$, and according to eq. (4-28) for $Conf3$.

$$\dot{E}x_{D,evap} = \left(\dot{m}_r\dot{ex}_5 + \dot{m}_{g.8}\dot{ex}_8\right) - \left(\dot{m}_r\dot{ex}_1 + \dot{m}_{g,9}\dot{ex}_9\right) \tag{4-27}$$

$$\dot{E}x_{D,evap} = \left(\dot{m}_r\dot{ex}_5 + \dot{m}_{g,6}\dot{ex}_6\right) - \left(\dot{m}_r\dot{ex}_1 + \dot{m}_{g,7}\dot{ex}_7\right) \tag{4-28}$$

The exergy efficiency of the pre-cooling unit is not considered since the latter is not designed nor optimized. However, an online software was used to extract the main parameters of the pre-cooling unit, as previously mentioned. Therefore, the exergy efficiency of the refrigeration cycle $\left(\eta_{\dot{E}_{tot}}\right)$ is only considered in the sequel. $\eta_{\dot{E}_{tot}}$ is defined as the ratio of the desired output exergy $\left(\dot{E}x_{desired}\right)$ to the used exergy $\left(\dot{E}x_{used}\right)$ [172], as in eq. (4-29). $\dot{E}x_{desired}$ is the sum of the desired output exergy rates transferred from the system, in addition to any by-product produced in the system, while the used exergy presents the required input exergy rate for the system.

$$\eta_{\dot{E}_{tot}} = \frac{\dot{E}x_{desired}}{\dot{E}x_{used}} \tag{4-29}$$

In the refrigeration cycle, $\dot{E}x_{desired}$ is equal to $\dot{m}_g(\dot{ex}_9 - \dot{ex}_8)$ in $Conf1$ and $Conf2$, while it is equal to $\dot{m}_g(\dot{ex}_7 - \dot{ex}_6)$ in $Conf3$. $\dot{E}x_{used}$ is equal to the net work required by the refrigeration cycle $\left(\dot{W}_{net}\right)$. The latter is equal to $\dot{W}_{comp}$ in $Conf1$, while it is equal to $\dot{W}_{comp} - \dot{W}_{turb}$ in $Conf2$ and $Conf3$. Therefore, $\eta_{\dot{E}_{tot}}$ can be rearranged into the following:

$$\eta_{\dot{E}_{tot}} = \frac{\dot{m}_g\left(\dot{ex}_{g,out} - \dot{ex}_{g,in}\right)}{\dot{W}_{net}} \tag{4-30}$$

4.4.3. Economic analysis

The economic analysis includes the investment, the maintenance and the operating costs as previously discussed in section 4.2.

4.4.3.1 Investment cost

The capital cost of the different components of the refrigeration cycle are calculated according to the functions presented in Table 4-5. These functions are used to compute the capital cost in USD. A conversion rate of $0.85\ €.USD^{-1}$ is considered to convert the prices to euros.

Table 4-5: Functions for estimating the capital cost of the different components in the refrigeration cycle [159,173,174].

Component	Function of cost	Eq #
Compressor	$Z_{comp} = 10167.5 \times \dot{W}_{comp}$	(4-31)
Throttle Valve	$Z_{TV} = 114.5 \times \dot{m}_r$	(4-32)
Turbine	$Z_{turb} = 10167.5 \times \dot{W}_{turb}$	(4-33)
Condenser	$Z_{cnd} = 516.621 \times A_{cnd} + 268.45$	(4-34)
Evaporator	$Z_{evap} = 309.143 \times A_{evap} + 231.915$	(4-35)
Heat exchangers	$Z_{HX} = 130 \times \left(\frac{A_{HX}}{0.093}\right)^{0.78}$	(4-36)

It can be seen that the same function is used to compute the compressor and the turbine costs, function of the work. The capital cost of the heat exchangers including the condenser and the evaporator are computed function of the heat transfer area (A). Therefore, the LMTD method is used to find the required area of the heat exchangers:

$$A = \frac{\dot{Q}}{U \times LMTD} \tag{4-37}$$

For $Conf1$ and $Conf2$, the cost of the pre-cooler with its refrigeration system is computed based on the catalogs [169].

After computing the capital cost, eq. (4-4) is used to find the investment cost rate of each component, which includes the maintenance cost rate. Afterwards, the total investment cost rate is computed as in eq. (4-2).

4.4.3.2 Operating cost

The operating cost $(\dot{Z}_{op})$ of the refrigeration process is expressed in eq. (4-38). The latter includes the electrical consumption of the compressor $(\dot{Z}_{elec,comp,r})$ for the three configurations. In $Conf1$ and $Conf2$, the electrical consumption of the compressor in the pre-cooling refrigeration system $(\dot{Z}_{elec,comp,pre-cooler})$, is also included. In $Conf2$ and $Conf3$, the work of the turbine is reduced from the required work of the compressor. The cost of the closed cooling water cycle $(\dot{Z}_{CW})$ used in the cooler is also considered for the three configurations. The electrical cost (C_{elec}) and the cooling water cost (C_{CW}) are presented in Table 4-4.

$$\dot{Z}_{op} = \dot{Z}_{elec,comp,r} + \dot{Z}_{elec,comp,pre-cooler} + \dot{Z}_{CW} \tag{4-38}$$

The operating cost of the compressor is computed according to eq. (4-39) for $Conf1$, and according to eq. (4-40) for $Conf2$ and $Conf3$. The electrical consumption of the compressor in the pre-cooling refrigeration system of $Conf1$ and $Conf2$, is calculated according to eq. (4-41).

$$\dot{Z}_{elec,comp,r} = \dot{W}_{comp} C_{elec} \tag{4-39}$$

$$\dot{Z}_{elec,comp,r} = (\dot{W}_{comp} - \dot{W}_{turb}) C_{elec} \tag{4-40}$$

$$\dot{Z}_{elec,comp,pre-cooler} = \dot{W}_{comp,pre-cooler} C_{elec} \tag{4-41}$$

The operating cost of the cooling water is calculated function of the cooling water mass flow rate:

$$\dot{Z}_{CW} = \dot{m}_{CW} C_{CW} \tag{4-42}$$

4.4.4. Environmental analysis: CO_2 emissions

Due to the growing interest in limiting the global warming, which is directly related to the carbon dioxide emissions, the environmental analysis is a key factor in the selection of the optimal refrigeration cycle.

For this purpose, the amount of released CO_2 is an important factor to consider for selecting the suitable refrigeration configuration. The amount of CO_2 that is annually released to the atmosphere $(\dot{m}_{CO_2})$ due to the electrical consumption of the compressors, is expressed in eq. (4-43). The latter is calculated function of the annual electrical consumption (W_{annual}), and the emission conversion factor (μ_{CO_2}) that varies from one country to another. For instance in the European Union, the lowest μ_{CO_2} of $0.0118\ kg.kWh^{-1}$ is achieved in Switzerland, while the highest values $0.791\ kg.kWh^{-1}$ is encountered in Poland. The average μ_{CO_2} in the United States is equal to $0.432\ kg.kWh^{-1}$ [175]. Consequently, the average μ_{CO_2} in the European Union, which is equal to $0.4218\ kg.kWh^{-1}$ is considered in the sequel.

$$\dot{m}_{CO_2} = \mu_{CO_2} W_{annual} \tag{4-43}$$

The W_{annual} is computed depending of the appropriate configuration as follows:

$$W_{annual} = \begin{cases} \left(\dot{W}_{comp,r} + \dot{W}_{comp,pre-cool}\right) \times FLH, & Conf1 \\ \left(\dot{W}_{comp,r} - \dot{W}_{turb} + \dot{W}_{comp,pre-cool}\right) \times FLH, & Conf2 \\ \left(\dot{W}_{comp,r} - \dot{W}_{turb}\right) \times FLH, & Conf3 \end{cases} \quad (4\text{-}44)$$

The penalty cost rate of CO_2 emissions $\left(\dot{Z}_{env}\right)$ is then determined based on the amount of CO_2 emissions:

$$\dot{Z}_{env} = \frac{\dot{m}_{CO_2} C_{CO_2}}{FLH \times 3600} \quad (4\text{-}45)$$

where C_{CO_2} is the penalty cost of CO_2 emissions, which is equal to $0.076\ €.kg_{CO_2}{}^{-1}$ [158,162,176].

4.4.5. Design parameters

Several parameters are involved in the refrigeration system design. In order to analyze the impact of each parameter on the refrigeration cost, a sensitivity study on each parameter is performed. Some parameters are fixed and cannot be changed. For instance, the temperature of the producer gas (T_6), entering the pre-cooler in $Conf1$ and $Conf2$, and the evaporator in $Conf3$, is fixed to 5℃. The latter is equivalent to the temperature of the producer gas leaving the water-based scrubbers. Similarly, the producer gas mass flow rate $\left(\dot{m}_{g,6}\right)$, entering the pre-cooler in $Conf1$ and $Conf2$, and the evaporator in $Conf3$, is fixed to $1.866\ kg.s^{-1}$. Moreover, the temperature of the refrigerant leaving the cooler (T_3) is fixed to 30℃. Furthermore, the main system target is to reduce the temperature of the producer gas leaving the evaporator to -110℃. Therefore, the objective of the parametric variation is to reach this temperature while reducing the energy consumption, the exergy destruction, the environmental impact and the total cost rate of the process. For this purpose, the parametric study is not only performed to assess the cost and the exergy of the process but also to select the operating conditions and the configurations, which sufficiently reduces the temperature.

The remaining parameters that are varied and that affect the results are:

- The refrigerant mass flow rate ($\dot{m}_r$), which affects the cooling and heating capacities of the refrigerant.
- The high pressure (HP), which affects the refrigerant temperature at the compressor exit.
- The low pressure (LP), which affects the refrigerant temperature at the expansion exit.
- The condenser constraint: either the desired refrigerant temperature at the condenser exit (T_4), or the temperature difference between the hot producer gas leaving the condenser and the hot refrigerant entering the condenser ($T_3 - T_{11}$).
- The outlet temperature of the pre-cooler (T_7), in $Conf1$ and $Conf2$, which affects the heat transfer rate in the evaporator as well as the refrigerant temperature at the compressor inlet.

Finally, several design constraints should be considered:

- The ratio of the high pressure to the low pressure should be lower than 3: $HP/LP \leq 3$.
- The refrigerant temperature leaving the compressor should be lower than 150℃: $T_2 < 150$℃ .
- A minimum temperature approach of 3℃ is considered for all the heat exchangers including the condenser and the evaporator.
- In some cases, the temperature difference between the refrigerant leaving the evaporator and the producer gas entering the evaporator is set to 3℃, in the evaporator. In other cases, the

temperature of the cold producer gas is set to -110℃, in order to avoid having any additional CO_2 frosting at lower temperatures, and avoid increasing the heat transfer rate.

The overall heat transfer coefficient in the condenser is considered equal to that of the cooling air or the flue gas, which ranges between 60 and 180 $W.m^{-2}.K^{-1}$ [177]. In the sequel, an average value of 120 $W.m^{-2}.K^{-1}$ is considered in the condenser. In the evaporator, the overall heat transfer coefficient is lower due to the frost layers formation, which limits the heat transfer. Therefore, in order to account for the frost formation, the average overall heat transfer coefficient in the evaporator is modeled using the equations mentioned in section 3.2.3.6. Accordingly, an average value of 17 $W.m^{-2}.K^{-1}$ is considered. The cooler is considered as a tubular heat exchanger in which the refrigerant (gas at high pressure) flows inside the tubes while the liquid (cooling water) flows outside the tubes. The average heat transfer coefficient in those types of heat exchangers ranges between 200 and 400 $W.m^{-2}.K^{-1}$ [177]. An average value of 300 $W.m^{-2}.K^{-1}$ is considered in the sequel.

4.4.6. Results and discussion

4.4.6.1 Producer gas temperature

Firstly, the impact of the different variables on the refrigeration cycle capacity in reducing the producer gas temperature is analyzed. To do so, several values for LP, HP, T_7 and $\dot{m}_r$ are considered. Table 4-6 summarizes the different cases considered in the parametric analysis for $Conf1$. Nitrogen, methane as well as a mixture of methane and nitrogen are tested as refrigerants in $Conf1$.

Figure 4-8 and Figure 4-9 present the variation of the producer gas temperature leaving the evaporator (T_9) for the different considered cases in $Conf1$, when nitrogen and methane are used as refrigerants, respectively.

Nitrogen is used as a refrigerant in cases 1 to 26 of Table 4-6. It can be seen from Figure 4-8 that, in cases 1 to 4, decreasing the HP while fixing LP, T_7 and $\dot{m}_r$, increases the producer gas temperature leaving the evaporator. In addition, in cases 5 to 8, increasing the LP while fixing HP, T_7 and $\dot{m}_r$, also increases the producer gas temperature leaving the evaporator. Thus, it can be deduced from cases 1 to 8 that decreasing the HP/LP reduces the heat transfer and therefore increases T_9. However, for the operating conditions of cases 1 to 8, the required producer gas temperature leaving the evaporator is not achieved. Even though T_7 is increased in case 9, a temperature lower that -110°C is achieved by increasing $\dot{m}_r$, LP and HP. In case 10, reducing $\dot{m}_r$ while reducing LP and thus increasing HP/LP, results in highly increasing T_9. For this purpose, in case 11, $\dot{m}_r$ is increased while HP/LP is reduced by increasing LP. This leads to a high reduction in T_9. Therefore, the mass flow rate has a high impact on the producer gas temperature. However, increasing the mass flow rate increases $\dot{Z}_{op}$ as it will be seen in the next section. In cases 12 to 14, only the $\dot{m}_r$ is being varied, while LP, HP and T_7 are fixed. It can be seen that the lowest T_7 is achieved for the highest $\dot{m}_r$. This can also be seen in cases 18 and 19, where increasing $\dot{m}_r$ by 0.14 kg.s^{-1}, while fixing the rest of the parameters, decreases T_9 by 3.6℃. However, the temperature reduction is not sufficient in both cases due to the low considered values of LP and HP. In cases 15 to 17 and cases 23 to 26, only T_7 is fixed. However, lower T_7 values are considered in cases 23 to 26. It can be seen that higher LP and HP should be considered by increasing T_7 from -46℃ to -35℃, in order to reach a T_9 of -110℃. When the same LP and HP are considered, a higher $\dot{m}_r$ is required for $T_7 = -38$℃, as it can be seen when comparing case 17 with case 20.

Table 4-6: The different cases considered to analyze the impact of LP, HP, T_7 and $\dot{m}_r$, on the refrigeration cycle design of $Conf1$, for nitrogen and methane.

$Case\ \#$	$LP\ (bar)$	$HP\ (bar)$	T_7 (℃)	$\dot{m}_r\ (kg.s^{-1})$
		$Nitrogen$		
1	10	30	-46	1.73
2	10	25	-46	1.73
3	10	20	-46	1.73
4	10	15	-46	1.73
5	17	50	-46	1.73
6	20	50	-46	1.73
7	25	50	-46	1.73
8	30	50	-46	1.73
9	30	70	-38	1.88
10	24	70	-38	1.60
11	35	70	-38	2.00
12	17	50	-46	1.90
13	17	50	-46	2.00
14	17	50	-46	1.95
15	10	30	-46	2.30
16	12	35	-46	2.20
17	30	70	-46	1.75
18	10	20	-46	2.36
19	10	20	-46	2.50
20	30	70	-38	1.90
21	30	70	-35	1.92
22	28	70	-35	1.90
23	22	60	-35	2.01
24	16	45	-35	2.15
25	15	45	-35	2.21
26	30	70	-35	1.81
		$Methane$		
27	14	40	-35	1.11
28	20	40	-35	1.11
29	25	40	-35	1.11
30	10	20	-35	1.20
31	7	20	-35	1.17
32	15.5	46	-35	1.11
33	14	30	-35	1.11
34	14	30	-32	1.11
35	12	30	-30	1.11
36	12	25	-35	1.14
37	11	25	-32	1.15
38	13	25	-35	1.20
		$20\%\ Nitrogen + 80\%\ Methane$		
39	13.5	40	-35	1.25

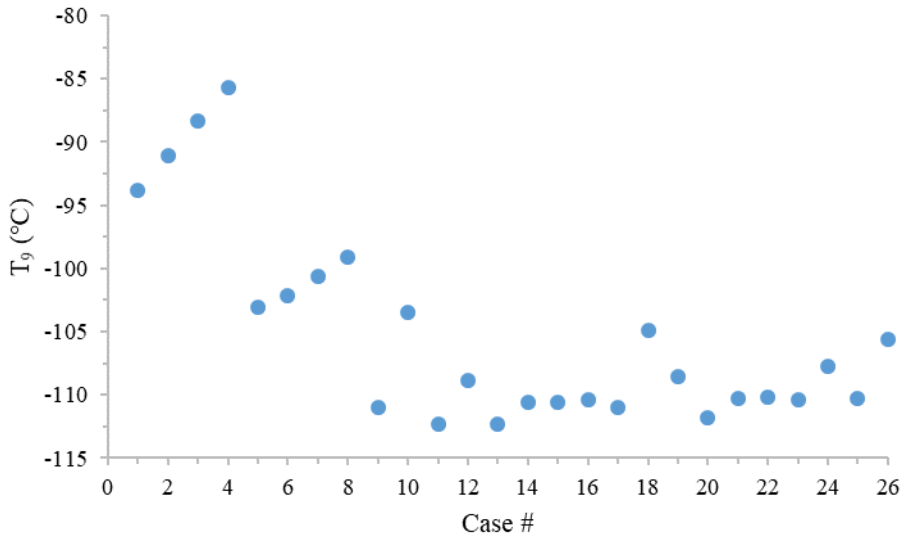

Figure 4-8: Variation of the temperature of the clean producer gas leaving the evaporator (T_9), for the different considered cases in $Conf1$, while using nitrogen as a refrigerant.

As previously mentioned, methane is used as a refrigerant only in $Conf1$. The different operating conditions are presented in cases 27 to 38 of Table 4-6. Finally, the last case (case 39) corresponds to the use of a mixture of 20% nitrogen and 80% methane, by weight, as a refrigerant. The mass flow rate of methane is 40% lower than that of nitrogen, since it undergoes a phase change. A fraction of the methane is liquefied in the condenser and the expansion valve. Therefore, its latent heat of vaporization is added. Moreover, the specific heat capacity of the methane is higher than that of nitrogen. It can be also seen that the considered LP and HP values for the methane are lower than those considered for the nitrogen.

According to Figure 4-9, increasing the LP while fixing HP, T_7 and $\dot{m}_r$, in cases 27 to 29, increases the producer gas temperature leaving the evaporator. In addition, for $T_7 = -35℃$, the HP/LP must be greater than 2 to reach the desired T_9. For instance, cases 28 and 29 do not ensure a sufficient refrigeration. Even though a higher mass flow rate is considered in case 30, T_9 does not reach $-110℃$ since the HP/LP is equal to 2. In case 31, increasing the HP/LP to 2.86 while reducing $\dot{m}_r$ enhances the refrigeration capacity of the cycle, and thus T_9 reaches $-110℃$. Moreover, the required value of $-110℃$ is achieved in cases 32 to 36. Among these cases, case 32 has the highest values of LP and HP. Cases 33 and 34 consider similar LP, HP and $\dot{m}_r$. Although the T_7 value set in case 34 is higher than that of case 33, both cases ensure sufficient cooling. Case 35 has the highest T_7 with the lowest LP. In case 36, a higher $\dot{m}_r$ is set. Although the refrigerant mass flow rate is increased, the operating conditions considered in cases 37 and 38 are not suitable for the refrigeration process. Finally, considering a mixture of nitrogen and methane as refrigerant is also an appropriate option, as seen in case 39.

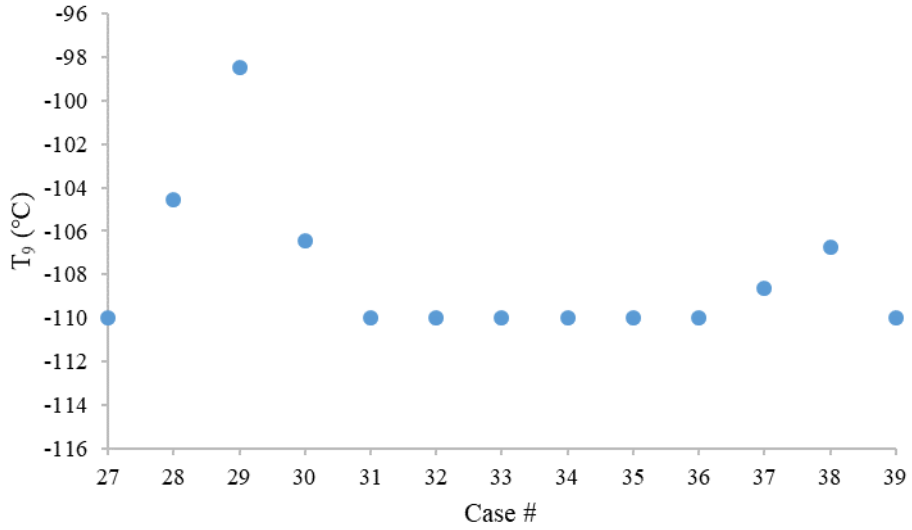

Figure 4-9: Variation of the temperature of the clean producer gas leaving the evaporator (T_9), for the different considered cases in $Conf1$, while using methane and the mixture of nitrogen and methane as refrigerants.

As previously mentioned, the difference between $Conf1$ and $Conf2$ is the replacement of the throttle valve by a turbine. In $Conf2$, only nitrogen is used as refrigerant. In general, the mass flow rate considered in $Conf2$ is higher than that in $Conf1$. On the contrary, the temperature of the producer gas leaving the pre-cooler considered in $Conf2$ is lower than that in $Conf1$. Table 4-7 summarizes the different cases considered in the parametric analysis for $Conf2$.

Table 4-7: The different cases considered to analyze the impact of LP, HP, T_7 and $\dot{m}_r$, on the refrigeration design of $Conf2$, for nitrogen.

$Case\ \#$	$LP\ (bar)$	$HP\ (bar)$	T_7 (°C)	$\dot{m}_r\ (kg.s^{-1})$
40	10	30	-20	2.50
41	13	30	-20	2.50
42	10	30	-20	2.80
43	15	30	-20	3.00
44	25	50	-20	2.40
45	20	50	-20	2.50
46	17	50	-20	2.36
47	30	50	-20	2.50
48	30	70	-20	2.31
49	25	70	-20	2.25
50	34	70	-20	2.50
51	34	70	-20	2.25
52	34	70	-23	2.25
53	34	70	-25	2.25
54	40	70	-27	2.25
55	26	45	-27	2.36
56	16	30	-27	2.50

Figure 4-10 present the variation of the producer gas temperature leaving the evaporator for the different cases considered in $Conf2$, for nitrogen. According to Figure 4-10, the temperature of the clean producer gas leaving the evaporator is reduced to below -110°C, in most of the cases. By comparing case 40 with case 41, it can be seen that increasing the LP while fixing HP, T_7 and $\dot{m}_r$, increases T_9. This behavior is also encountered when comparing case 45 with case 47. Considering a higher $\dot{m}_r$ in case 42, while fixing the other variables, decreases T_9. Even though the $\dot{m}_r$ considered in case 42 is higher than that in case 40, both cases yield a similar T_9. In fact, increasing $\dot{m}_r$ while fixing the

remaining variables, increases the temperature of the refrigerant leaving the condenser (T_4). Consequently, the temperature of the refrigerant leaving the turbine (T_5) increases. However, since a higher $\dot{m}_r$ is considered, the heat transfer rate in the evaporator remains almost constant. In addition, increasing the LP and thus reducing the HP/LP, while increasing the $\dot{m}_r$, highly increases T_9, in case 43. It can be also deduced that for $T_7 = -20$℃, the HP/LP should be greater than 2 while considering the appropriate $\dot{m}_r$, in order to reach the required T_9. This also applies for cases 44 to 50. According to cases 51, 52 and 53, reducing T_7 while fixing the remaining variables, results in reducing T_9. In cases 54, 55 and 56, T_9 is fixed at -110℃ instead of fixing a temperature difference of 3℃ between the producer gas entering the evaporator and the refrigerant leaving it. This avoids any additional unnecessary cooling and therefore additional CO_2 frosting. Consequently, the energy consumption is reduced. The impact of this reduction on the $\dot{Z}_{tot}$ is assessed in the next section.

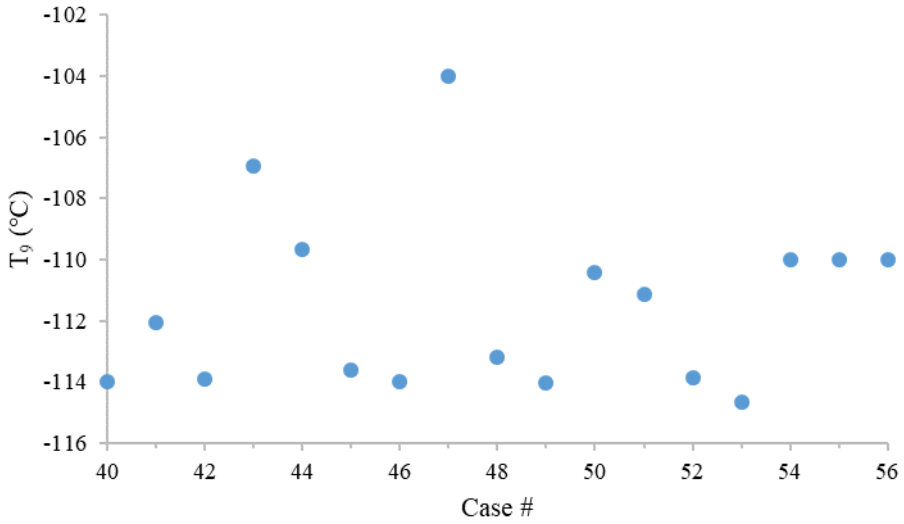

Figure 4-10: Variation of the temperature of the clean producer gas leaving the evaporator (T_9), for the different cases considered for $Conf2$, while using nitrogen as a refrigerant.

Table 4-8 summarizes the different cases considered in the parametric analysis for $Conf3$. Note that in $Conf3$, the temperature of the producer gas leaving the pre-cooler does not exist. Therefore, the initial producer gas temperature (T_6), which is constant, is considered instead. Only nitrogen is used as a refrigerant in $Conf3$.

Figure 4-11 present the variation of the producer gas temperature leaving the evaporator for the different cases considered in $Conf3$, for nitrogen. As previously mentioned, the difference between $Conf2$ and $Conf3$ is the removal of the pre-cooling unit in $Conf3$. Similarly to $Conf2$, only nitrogen can be used as refrigerant. In general, the mass flow rate considered in $Conf3$ is higher than that of $Conf2$. Table 4-8 shows the initial producer gas temperature entering the evaporator (T_6), which is constant for all the cases. It can be seen from Figure 4-11 that the temperature of the clean producer gas leaving the evaporator (T_7) is reduced to below -110℃, in cases 61, 69 and 70 only. In the latter, HP/LP and $\dot{m}_r$ are greater than or equal to 2.917 and 3.18, respectively. The general behavior of T_7 is also encountered in $Conf3$. Reducing HP/LP while fixing the remaining parameters increases T_7. Similarly, reducing $\dot{m}_r$ while fixing the remaining variables increases T_7.

Table 4-8: The different cases considered to analyze the impact of LP, HP and $\dot{m}_r$ on the refrigeration design of $Conf3$, for nitrogen.

$Case\ \#$	$LP\ (bar)$	$HP\ (bar)$	T_6 (°C)	$\dot{m}_r\ (kg.s^{-1})$
57	10	30	5	2.50
58	20	60	5	2.30
59	20	55	5	2.50
60	20	50	5	2.50
61	20	60	5	3.25
62	25	70	5	3.00
63	25	70	5	2.50
64	30	70	5	2.80
65	25	70	5	3.10
66	25	70	5	3.05
67	24	70	5	3.00
68	25	70	5	3.20
69	24	70	5	3.18
70	15	45	5	3.30
71	18	45	5	3.20
72	15	45	5	2.50
73	14	40	5	3.50
74	18	40	5	3.10
75	20	40	5	3.30

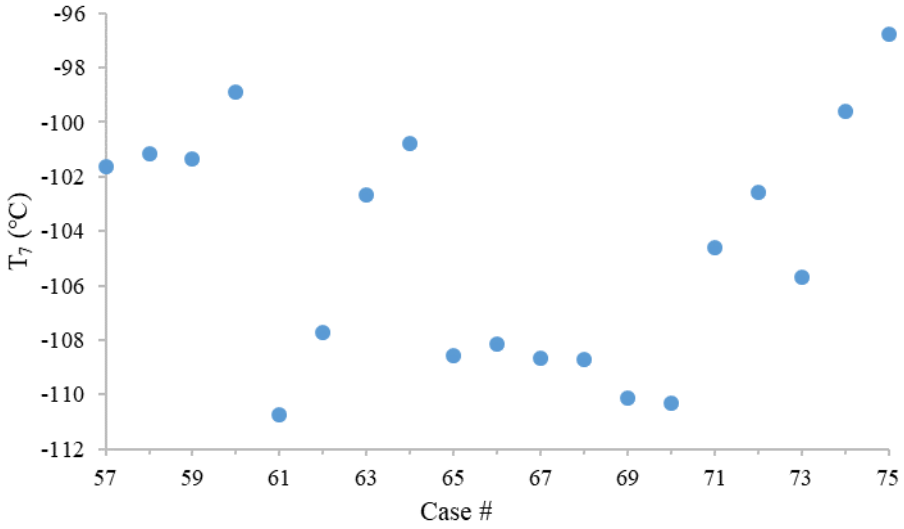

Figure 4-11: Variation of the temperature of the clean producer gas leaving the evaporator (T_6), for the different cases considered for $Conf3$, while using nitrogen as a refrigerant.

The COP for the cases that are able to reduce the producer gas temperature to -110°C, is only analyzed in the next section.

4.4.6.2 Coefficient of performance (COP)

The COP is another important parameter that should be analyzed for selecting the appropriate refrigeration cycle. For this purpose, Figure 4-12 illustrates the COP variation function of the different considered cases, in the three studied configurations. According to eqs. (4-16) and (4-17), the COP increases with the increase of $\dot{Q}_{evap}$ or with the decrease of $\dot{W}_{net}$. $\dot{W}_{net}$ of $Conf2$ is lower than that of $Conf1$, due to the work produced by the turbine. On the contrary, $\dot{Q}_{evap}$ increases from $Conf1$ to $Conf2$ since the producer gas temperature entering the evaporator increases importantly, while the same

producer gas temperature leaving the evaporator is achieved. Therefore, replacing the throttle valve by a turbine increases the COP from $Conf1$ to $Conf2$. The average COP of $Conf3$ is 6% higher than that of $Conf1$, while it is 35% lower than that of $Conf2$. Although $\dot{Q}_{evap}$ highly increases due to the pre-cooler elimination, $\dot{W}_{net}$ highly increases due to the higher HP/LP considered in $Conf3$.

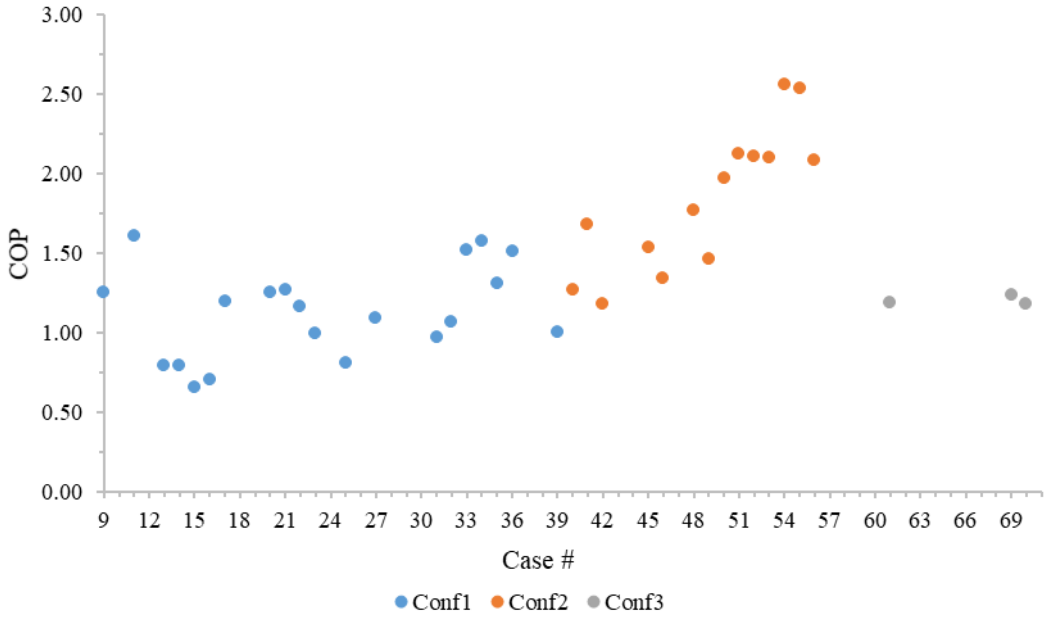

Figure 4-12: COP variation, function of the different considered cases in $Conf1$, $Conf2$ and $Conf3$.

It can be seen that, in $Conf1$, the lowest COP of 0.66 is reached in case 15 for the lowest T_7. The highest COP of 1.61 is reached in case 11, which corresponds to the lowest HP/LP while considering average values of T_7 and $\dot{m}_r$. Increasing T_7 from -46℃ to -38℃ increases the COP by 4.5% for the same HP/LP. In addition, increasing HP/LP from 2.33 to 2.50 increases $\dot{W}_{net}$, and therefore the COP is reduced by 6.4%. In addition, replacing nitrogen by methane decreases $\dot{m}_r$ as well as $\dot{W}_{net}$. Consequently, the refrigeration unit COP increases. In $Conf2$, the lowest COP of 1.18 is reached for the highest HP/LP for case 42. The highest COP of 2.56 is reached in case 54, which corresponds to the lowest $\dot{m}_r$ with an HP/LP of 1.75 while considering a T_7 of -27℃. Reducing T_7 by 2℃ in $Conf2$ reduces the COP by 0.9%. Moreover, reducing $\dot{m}_r$ by 10% while fixing the remaining variables, increases the COP by 8.12%, since $\dot{W}_{net}$ highly decreases while $\dot{Q}_{evap}$ is slightly affected. Furthermore, the COP decreases with the increase of the HP/LP, as in $Conf1$. Finally, the COP in $Conf3$ is almost constant around 1.2 since the HP/LP variation is limited between 2.917 and 3.

$\dot{Z}_{tot}$ for the cases that are able to reduce the producer gas temperature to -110℃, is only analyzed in the next section.

4.4.6.3 Total cost calculation

The $\dot{Z}_{tot}$ is computed in €.s^{-1} for the three configurations based on $\dot{Z}_{Inv}$, $\dot{Z}_{op}$ and $\dot{Z}_{env}$. The impact of each cost on $\dot{Z}_{tot}$ is assessed based on the parametric study. The lifetime of the plant is set to 20 years with 8000 full load operating hours per year with an interest rate of 0.1 [85]. All the cases that did not result in a producer gas temperature lower than or equal to -110℃, are eliminated. Figure 4-13 illustrates the variation of the $\dot{Z}_{Inv}$, $\dot{Z}_{op}$, $\dot{Z}_{env}$ and $\dot{Z}_{tot}$, in €.s^{-1}, for the different considered cases in $Conf1$, $Conf2$ and $Conf3$.

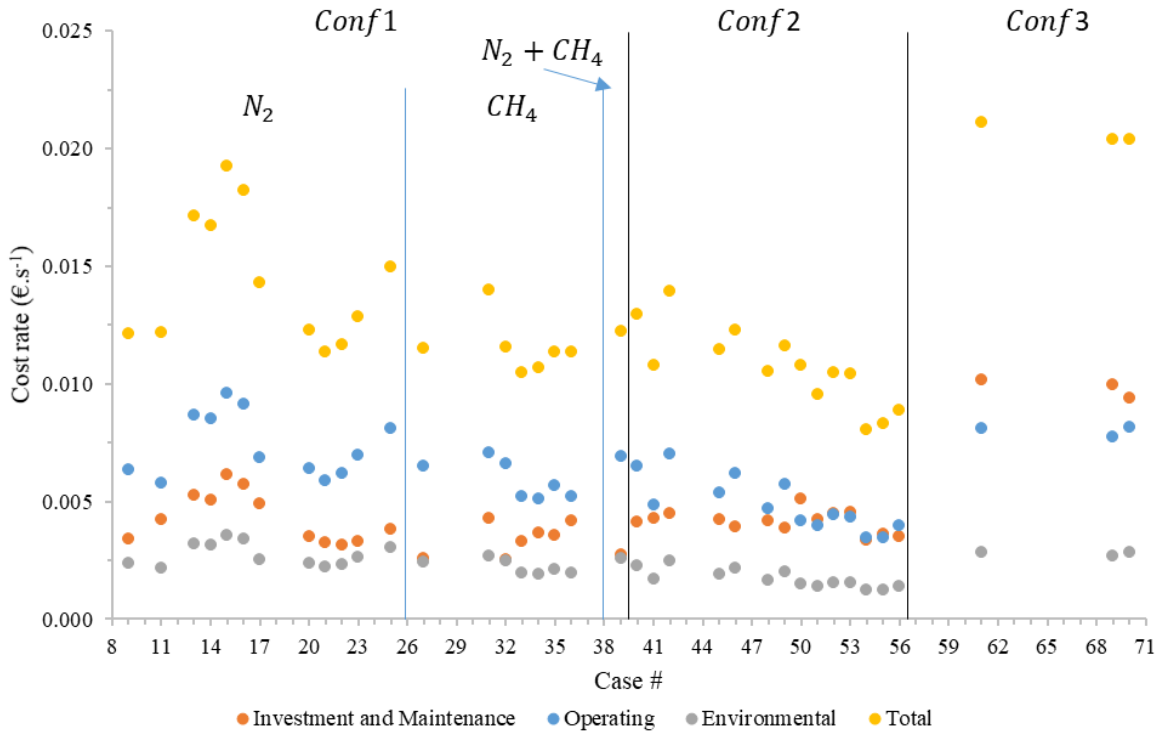

Figure 4-13: Variation of $\dot{Z}_{Inv}$, $\dot{Z}_{op}$, $\dot{Z}_{env}$ and $\dot{Z}_{tot}$ function of the different considered cases in $Conf1$, $Conf2$ and $Conf3$.

It can be seen that for most of the considered cases in $Conf1$ and $Conf2$, $\dot{Z}_{op}$ has the highest share from the $\dot{Z}_{tot}$. The $\dot{Z}_{env}$ has the lowest share from the $\dot{Z}_{tot}$ in the three configurations. On average, $\dot{Z}_{op}$, $\dot{Z}_{Inv}$ and $\dot{Z}_{env}$ respectively form 50.4%, 30.8% and 18.8% of $\dot{Z}_{tot}$, in $Conf1$. The share of $\dot{Z}_{env}$ and $\dot{Z}_{op}$ decreases from $Conf1$ to $Conf2$ while $\dot{Z}_{Inv}$ increases, this is due to the replacement of the throttle valve by a turbine. On the first hand, Z_{turb} is higher than Z_{TV}. On the second hand, the turbine decreases $\dot{W}_{net}$ as well as the $\dot{Q}_{pre-cool}$. On average, $\dot{Z}_{op}$, $\dot{Z}_{Inv}$ and $\dot{Z}_{env}$ respectively form 43.5%, 41.2% and 15.3% of $\dot{Z}_{tot}$, in $Conf2$. As for $Conf3$, $\dot{Z}_{op}$, $\dot{Z}_{Inv}$ and $\dot{Z}_{env}$ respectively form 38.8%, 47.7% and 13.5% of $\dot{Z}_{tot}$, on average. In addition, $Conf3$ has the highest $\dot{Z}_{tot}$. Thus, elimination the pre-cooling unit in $Conf3$ increases $\dot{Z}_{tot}$ by 10%, at least. In fact, as previously mentioned, refrigeration systems that reduces the temperature up to -50°C are well developed and cheaper than refrigeration systems operating at lower temperatures. Moreover, eliminating the pre-cooler increases the evaporator energy requirement. Therefore, $\dot{m}_r$ as well as HP/LP are highly increased in order to compensate the additional required energy. Consequently, $\dot{Z}_{Inv}$ highly increases and becomes higher than $\dot{Z}_{op}$, due to the increase of the required heat transfer area. $\dot{Z}_{op}$ and $\dot{Z}_{env}$ highly increase due to the increase in $\dot{W}_{comp}$.

In general, increasing HP/LP increases Z_{comp} and $\dot{W}_{comp}$. This also leads to a higher gas temperature leaving the compressor. Consequently, the $\dot{Q}_{cooler}$ increases as well as the heat transfer area, which is directly related to its Z_{Inv}. In addition, increasing $\dot{m}_r$ increases simultaneously $\dot{Z}_{tot}$ due to the increase in $\dot{W}_{comp}$ and in the heat exchangers duties. The pre-cooler is the only component that is not affected by the HP/LP nor by $\dot{m}_r$. Moreover, T_7 is the only variable that affects the pre-cooler cost. Furthermore, in some cases, the refrigerant leaves the compressor at temperatures lower than 30°C. Consequently, the cooler after the compressor is no longer required. This leads to a reduction in $\dot{Z}_{Inv}$ and $\dot{Z}_{op}$. In general, this temperature depends on the temperature of the producer gas leaving the pre-cooler, as well as the HP/LP. This is encountered in cases 11, 33 and 36 of $Conf1$, and in cases 54 and 55 of $Conf2$.

Furthermore, the average $\dot{Z}_{tot}$ of $Conf2$ is lower than that of $Conf1$. More precisely, $\dot{Z}_{tot}$ of $Conf1$ varies between 0.0105 and 0.0193 €. s^{-1}, while that of $Conf2$ varies between 0.008 and 0.0139 €. s^{-1}. $Conf1$ corresponds to two different refrigerants. Starting with nitrogen, the lowest $\dot{Z}_{tot}$ of 0.0113 €. s^{-1} is achieved in case 21. The latter corresponds to the highest T_7 with medium values of HP/LP and $\dot{m}_r$. The highest $\dot{Z}_{tot}$ of 0.0193 €. s^{-1} corresponds to case 15, which has the highest HP/LP and $\dot{m}_r$ value combined with a high T_7. Replacing the nitrogen by methane decreases $\dot{Z}_{tot}$. The highest $\dot{Z}_{tot}$ of 0.0140 €. s^{-1} is reached in case 31, and it decreases to 0.0105 €. s^{-1} in case 33 by reducing the HP/LP and the $\dot{m}_r$, while fixing T_7. $\dot{Z}_{tot}$ highly increases in $Conf3$ and reaches 0.021 €. s^{-1}. The general behavior of the different costs can be summarized as follows:

- Increasing $\dot{m}_r$ increases the equipment dimensions and thus increases $\dot{Z}_{Inv}$. In addition, $\dot{W}_{comp}$ increases, and therefore $\dot{Z}_{op}$ and $\dot{Z}_{env}$ increase.
- Increasing HP/LP increases $\dot{W}_{comp}$, and thus $\dot{Z}_{op}$ and $\dot{Z}_{env}$ increase. On the contrary, $\dot{Z}_{Inv}$ remains almost constant since Z_{comp} and Z_{turb} increase, while Z_{evap} decreases.
- Reducing T_7 increases the different pre-cooling unit costs. However, this lowers the refrigeration unit costs by reducing the refrigerant temperature at the compressor inlet. Therefore, the variation of $\dot{Z}_{tot}$ is function of both units.
- Limiting the producer gas temperature leaving the evaporator to -110°C, decreases $\dot{Z}_{op}$ since the refrigerant temperature entering the compressor (T_1) is reduced, which also reduces $\dot{Z}_{env}$.

Figure 4-14 (a), (b) and (c) respectively illustrate the percentage distribution of Z_{Inv} on the different components of $Conf1$, $Conf2$ and $Conf3$. Note that the averaged values of the percentage distribution are presented. The average total Z_{Inv} of $Conf1$, $Conf2$ and $Conf3$ are equal to 908723 €, 957256 € and 2274278 €, respectively.

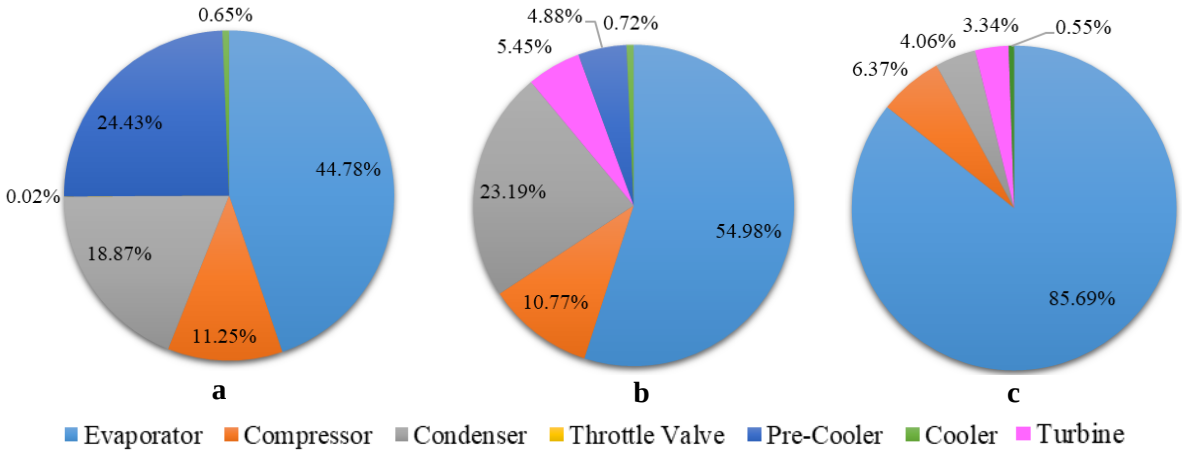

Figure 4-14: Z_{inv} distribution of (a) $Conf1$, (b) $Conf2$ and (c) $Conf3$.

For all the configurations, the evaporator has the highest investment cost. This is due to the fact that the overall heat transfer coefficient is too low due to the frost formation that hinders the heat transfer phenomenon. This increases enormously the required heat transfer area and therefore its Z_{Inv}. It can be seen that the share of the evaporator increases from one configuration to another until reaching 85.7% of the total Z_{inv}. This is related to the decrease in the pre-cooler duty, which is also related to the decrease in the LMTD. It was previously seen in Table 4-6 and Table 4-7 that T_7 ranges between -32°C and -46°C in the first configuration, while it ranges between -20°C and -27°C in the second configuration. Therefore, the pre-cooler duty highly decreases from $Conf1$ to $Conf2$. This is reflected on the pre-cooler share of Z_{inv} that decreases from 24.43% in $Conf1$ to 4.88% in $Conf2$. Consequently, the $\dot{Q}_{evap}$

increases from $Conf1$ to $Conf2$ since the producer gas enters the evaporator at higher temperatures. This explains the increase in the share of Z_{evap}. As for $Conf3$, the pre-cooling unit is eliminated, and therefore $\dot{Q}_{evap}$ highly increases.

The condenser investment cost is lower than that of the pre-cooler in $Conf1$, while in $Conf2$ the condenser investment cost is higher than that of the pre-cooler. This is also related to the higher values of T_7 considered in $Conf2$. This highly decreases the pre-cooler investment cost, and therefore increases the condenser investment cost. As for $Conf3$, the contribution of the condenser in the total investment cost highly decreases to 4.06%. In terms of the cost in €, the condenser cost does not decrease from $Conf1$ and $Conf2$ to $Conf3$. However, due to the high increase in the evaporator and compressor costs, the share of the condenser becomes lower.

The average compressor share is lower than that of the condenser, and it is almost constant around 11%, for the first two configurations. It decreases to 6.37% in the third configuration. However, in $Conf3$, the compressor cost is higher than that of the condenser. This can be explained by the fact that an HP/LP higher than 2.917 is required, which enormously increases the compressor cost.

Among all the components, the throttle valve has the lowest investment cost, as seen in $Conf1$. The turbine investment cost is much higher than that of the throttle valve as reflected in $Conf2$ and $Conf3$. Finally, the cooler investment cost is lower than 1% in the three configurations due to two principal reasons. Firstly, the high overall heat transfer coefficient in the cooler decreases the required heat transfer area, which also decreases the cost, as expressed in eq. (4-36). Secondly, the required temperature reduction in the cooler is not as high as the temperature reduction taking place in the condenser, especially for $Conf1$ and $Conf2$.

Figure 4-15 (a), (b) and (c) respectively illustrate the percentage distribution of $\dot{Z}_{op}$ on the different components of $Conf1$, $Conf2$ and $Conf3$. Note that the averaged values of the percentage distribution are presented.

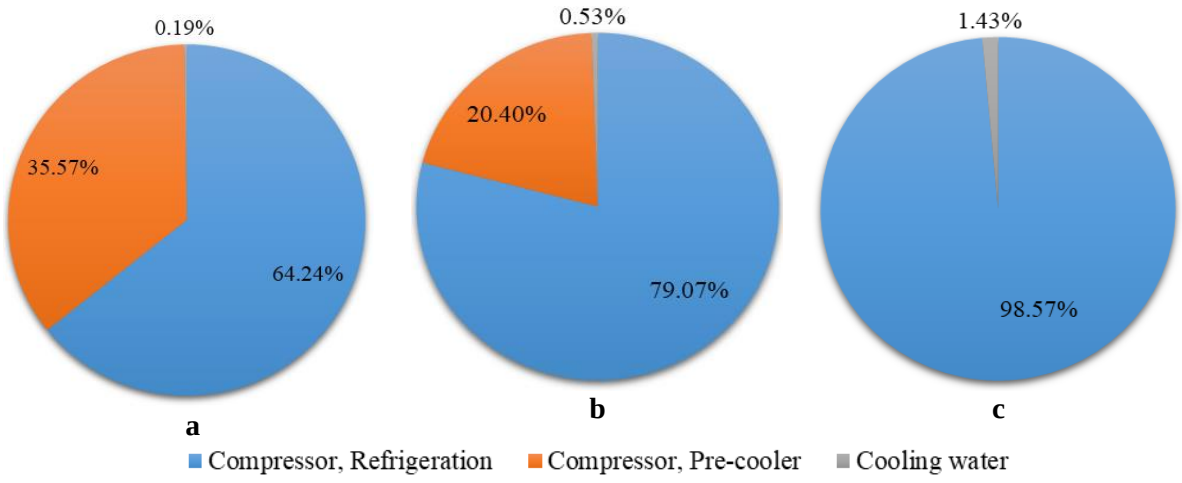

Figure 4-15: Distribution of $\dot{Z}_{op}$ of (a) $Conf1$, (b) $Conf2$ and (c) $Conf3$.

The average $\dot{Z}_{op}$ of $Conf1$, $Conf2$ and $Conf3$ are equal to $25\,€.h^{-1}$, $18\,€.h^{-1}$ and $29\,€.h^{-1}$, respectively. Therefore, $Conf2$ has the lowest $\dot{Z}_{op}$, followed by $Conf1$, while $Conf3$ has the highest $\dot{Z}_{op}$. Note that $\dot{Z}_{op}$ of $Conf2$ is lower than that of $Conf1$ since the turbine decreases the required $\dot{W}_{net}$, and yields a lower temperature at the turbine outlet (T_5) for the same HP and LP considered in a throttle valve. It can be seen that $\dot{Z}_{elect,comp,r}$ has the highest share of $\dot{Z}_{op}$ in the three configurations. It respectively forms 62.2%, 79.1% and 98.6% of $\dot{Z}_{op}$ in $Conf1$, $Conf2$ and $Conf3$. In $Conf1$ and $Conf2$,

$\dot{Z}_{elec,comp,pre-cool}$ is higher than $\dot{Z}_{CW}$. The lower temperatures imposed on the pre-cooler by the use of the throttle valve in $Conf1$, lead to a higher $\dot{Z}_{elec,comp,pre-cool}$. In addition, since T_7 in $Conf1$ is lower than that in $Conf2$, the refrigerant temperature entering the compressor (T_1) in $Conf1$ is lower than that in $Conf2$. Consequently, the refrigerant temperature leaving the compressor (T_2) and thus the required temperature difference in the cooler ($T_2 - T_3$) in $Conf1$ are lower than those in $Conf2$. This increases the required $\dot{m}_{CW}$ in $Conf2$. $\dot{Z}_{op}$ in $Conf3$ is higher by at least 16% than those in the remaining configurations. On the first hand, eliminating the pre-cooler highly increases $\dot{Z}_{CW}$ due to the higher temperature of the refrigerant entering the compressor ($T_1 = 8$°C), which also leads to a higher T_2. On the second hand, the required high HP/LP leads to a higher electrical consumption.

Finally, $\dot{Z}_{env}$ is linked to the electrical consumption as expressed in eqs. (4-43) and (4-45). Therefore, $Conf2$ has the lowest environmental impact, followed by $Conf1$ and $Conf3$.

4.4.6.4 Exergy destruction

Figure 4-16 illustrates a comparison between the average $\dot{E}x_D$ values in the different components of the three studied refrigeration systems $Conf1$, $Conf2$ and $Conf3$. It can be seen that, in $Conf1$, the highest $\dot{E}x_D$ occurs in the throttle valve, followed by the compressor and the evaporator. Replacing the throttle valve by a turbine in $Conf2$ decreases the $\dot{E}x_D$ in the turbine by 64.8%. Consequently, in $Conf2$, the $\dot{E}x_D$ in the compressor becomes the highest one followed by that of the turbine and then the evaporator. Similarly, the $\dot{E}x_{D,comp}$ is the highest one followed by that of the turbine, in $Conf3$. However, $\dot{E}x_{D,cooler}$ and $\dot{E}x_{D,cnd}$ highly increase in $Conf3$, and thus become higher than that of the evaporator. Moreover, $Conf2$ has the lowest total $\dot{E}x_D$, followed by $Conf1$, while $Conf3$ has the highest one. For a better comparison, the $\eta_{\dot{E}_{tot}}$ of each configuration should be computed. Accordingly, the average $\eta_{\dot{E}_{tot}}$ decreases from $Conf1$ to $Conf3$. The highest $\eta_{\dot{E}_{tot}}$ of 60% is achieved in $Conf1$, followed by 54% in $Conf2$, while the lowest $\eta_{\dot{E}_{tot}}$ of 43% is encountered in $Conf3$. Although the $\dot{E}x_D$ of $Conf1$ is higher than that of $Conf2$, $\eta_{\dot{E}_{tot}}$ of $Conf1$ is higher than that of $Conf2$.

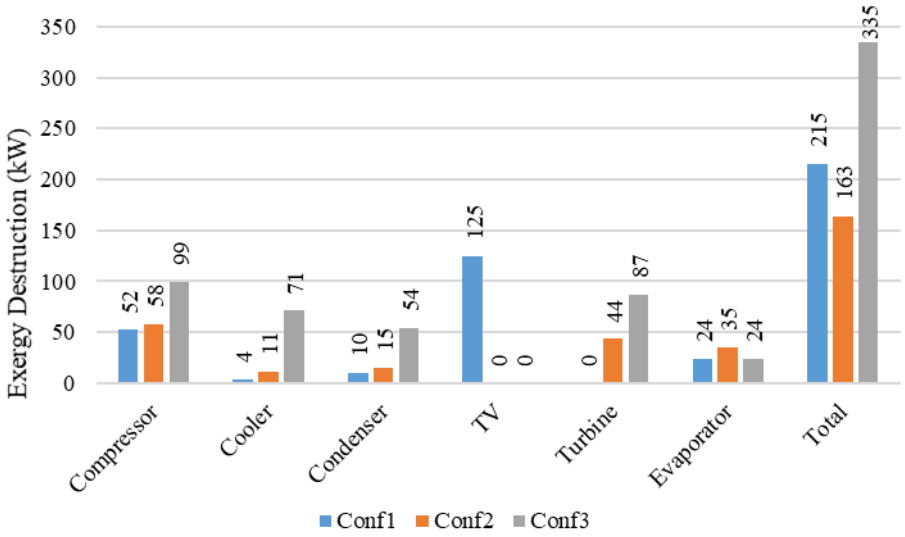

Figure 4-16: Comparison between the $\dot{E}x_D$ values in the different refrigeration system components of Conf1, Conf2 and Conf3.

In general, the average values of the $\dot{E}x_D$ and $\eta_{\dot{E}_{tot}}$ serve to compare the three configurations. However, in order to select the optimal case for each configuration, $\dot{E}x_D$ and $\eta_{\dot{E}_{tot}}$ of each case is separately

analyzed. Consequently, $\eta_{\dot{E}_{tot}}$ has the same behavior as the COP. More precisely, the lowest $\eta_{\dot{E}_{tot}}$ of 37.9% in $Conf1$ is encountered in case 15 which corresponds to the lowest T_7. The highest $\eta_{\dot{E}_{tot}}$ is reached in case 11, which corresponds to the lowest HP/LP while considering average values of T_7 and $\dot{m}_r$. In addition, replacing nitrogen by methane increases $\eta_{\dot{E}_{tot}}$ since $\dot{m}_r$ and therefore $\dot{W}_{net}$ decrease. In $Conf2$, the lowest $\eta_{\dot{E}_{tot}}$ of 34.22% is reached for the highest HP/LP, in case 42. The highest $\eta_{\dot{E}_{tot}}$ is reached in case 54, which corresponds to the lowest $\dot{m}_r$ with an HP/LP of 1.75 while considering a T_7 of -27℃. The $\eta_{\dot{E}_{tot}}$ in $Conf3$ is almost constant around 43% since the HP/LP variation is limited between 2.917 and 3.

To sum up, increasing T_7 while fixing HP/LP decreases $\eta_{\dot{E}_{tot}}$. More precisely, increasing T_7 increases $\dot{E}x_{D,evap}$, which leads to a higher total $\dot{E}x_D$. In addition, increasing HP/LP while fixing the remaining variables, highly reduces $\eta_{\dot{E}_{tot}}$ since the $\dot{E}x_D$ in all the components as well as the required $\dot{W}_{net}$ increase. Moreover, increasing $\dot{m}_r$ while fixing the remaining variables reduces $\eta_{\dot{E}_{tot}}$, especially when a turbine is used instead of a throttle valve.

4.4.7. Optimal configuration

On average basis, $Conf1$ has the lowest $\dot{Z}_{Inv}$, as well as the lowest COP, while it has the highest $\eta_{\dot{E}_{tot}}$. $Conf2$ has the lowest $\dot{Z}_{op}$ and $\dot{Z}_{env}$. On the contrary, it has the highest COP with a high $\eta_{\dot{E}_{tot}}$. $Conf3$ has the highest $\dot{Z}_{Inv}$, the highest $\dot{Z}_{op}$ and $\dot{Z}_{env}$, the lowest $\eta_{\dot{E}_{tot}}$ and a moderate COP value. It can be seen from the obtained results that, although $Conf3$ efficiently reduces the tar content, it is not a suitable alternative for the tar treatment unit due to its high $\dot{Z}_{tot}$, low COP and high $\dot{E}x_D$. On the contrary, $Conf1$ and $Conf2$ are better alternatives for the tar removal unit. In addition, the COP, the different costs and the $\dot{E}x_D$ of the three configurations depend on the initial variables that were previously analyzed by considering several case studies. Therefore, the studied cases for each configuration were compared and the optimal case, presented in Table 4-9, is selected for each configuration.

Table 4-9: Optimum case for each configuration.

Configuration	$Conf1$	$Conf2$	$Conf3$
Refrigerant	CH_4	N_2	N_2
Case	34	54	69
$LP\ (bar)$	14	40	24
$HP\ (bar)$	30	70	70
T_7 (℃)	-32	-27	5
$\dot{m}_r\ (kg.s^{-1})$	1.11	2.25	3.18
Z_{Inv} (€)	850751	780575	230012
$\dot{Z}_{Inv}\ (€.h^{-1})$	13.24	12.14	35.8
$\dot{Z}_{op}\ (€.h^{-1})$	18.34	1.40	27.84
$\dot{Z}_{env}\ (€.h^{-1})$	14.87	10.05	22.25
COP	1.57	2.56	1.24
$\dot{E}x_D\ (kW)$	161	104	324

The selection of the optimal case takes into account the different cost rates, the COP and the $\eta_{\dot{E}_{tot}}$. In the best case scenario, the selected case should have the lowest $\dot{Z}_{tot}$, the highest COP and the lowest $\dot{E}x_D$. However, those conditions are not usually satisfied in one case. Therefore, a compromise between

the three targeted conditions should be considered. For instance, in the first configuration, the highest COP and the lowest $\dot{E}x_D$ are achieved in case 11. However, case 34 yields the lowest $\dot{Z}_{tot}$ while preserving a high COP and a low $\dot{E}x_D$. Consequently, case 34 is selected. In the second and the third configurations, the required conditions are fulfilled by case 54 and case 69, respectively.

4.5. Scale factor

In an economic analysis, it is crucial to assess the impact of the size or the unit capacity on Z_{Inv}. This can be applied to an individual equipment or to an entire plant. Eq. (4-46) links the investment cost of a unit (Z_{Inv}) having a capacity P, to the cost of a reference unit ($Z_{Inv,ref}$) having a capacity of P_{ref}. This equation reflects the non-linearity between the cost and the installation capacity depending on the scale factor (SF). The SF of the different equipment used in the tar treatment process are summarized in Table 4-10.

$$Z_{Inv} = Z_{Inv,ref}\left(\frac{P}{P_{ref}}\right)^{SF} \tag{4-46}$$

The specific investment cost $(Z_{Inv,spec})$ is then calculated function of the investment cost and the bio-methane production capacity:

$$Z_{Inv,spec} = \frac{Z_{Inv}}{P} \tag{4-47}$$

Table 4-10: Scale factors of the different equipment [85].

Equipment	SF	Equipment	SF
Scrubbers	0.70	Throttle Valve	0.67
Compressor	0.95	Heat Exchangers	0.66
Turbine	0.65	Refrigeration cycle	0.70
AC beds	0.80		

The same equation is also used to compute $\dot{Z}_{op}$ of a unit having a capacity P from that of the reference unit having a capacity P_{ref}. The SF of the consumables, including the electricity cost and the cooling water, is considered equal to unity.

Note that $\dot{Z}_{env}$ is only used to select the optimal configuration and the optimal cases. However, it will not be included in this section, since it was not analyzed in the GoBiGas project. This make the comparison between the cost of the designed refrigeration cycle and that of the GoBiGas AC beds more reliable.

Figure 4-17 (a), (b) and (c) respectively illustrate a comparison between the $Z_{Inv,spec}$ variation of the tar removal by adsorption with that of $Conf1$, $Conf2$ and $Conf3$. The bars in this figure present the $Z_{Inv,spec}$ variation in the case where the SF, presented in Table 4-10, varies by +/- 10%. The Z_{Inv} of the tar adsorption by the AC beds is previously presented in Table 4-1 for $P_{ref} = 20MW$. It can be seen that the total $Z_{Inv,spec}$ of $Conf1$ and $Conf2$ are lower than that of the AC beds. On the contrary, the total $Z_{Inv,spec}$ of $Conf3$ is higher than that of the AC beds for all the bio-methane production capacities. In addition, $Z_{Inv,spec}$ strongly depends on the production capacity. $Z_{Inv,spec}$ of the refrigeration systems highly decreases until becoming almost constant for production capacities higher than 200 MW. More precisely, it stabilizes at almost 16900, 15550 and 44920 €. MW^{-1} for $Conf1$, $Conf2$ and $Conf3$, respectively. Similarly, $Z_{Inv,spec}$ of the AC beds becomes almost constant around 31000 €. MW^{-1}, for production capacities higher than 200 MW. Therefore, Z_{Inv} of the tar treatment unit can be significantly

reduced by replacing the AC beds with a refrigeration cycle, according to the first two configurations. However, adapting the third configuration increases Z_{Inv} of the tar removal unit.

a

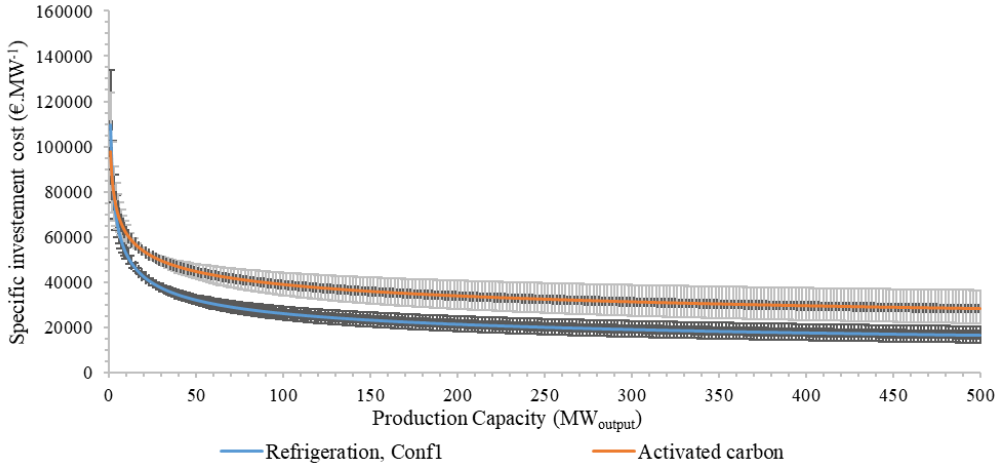

b

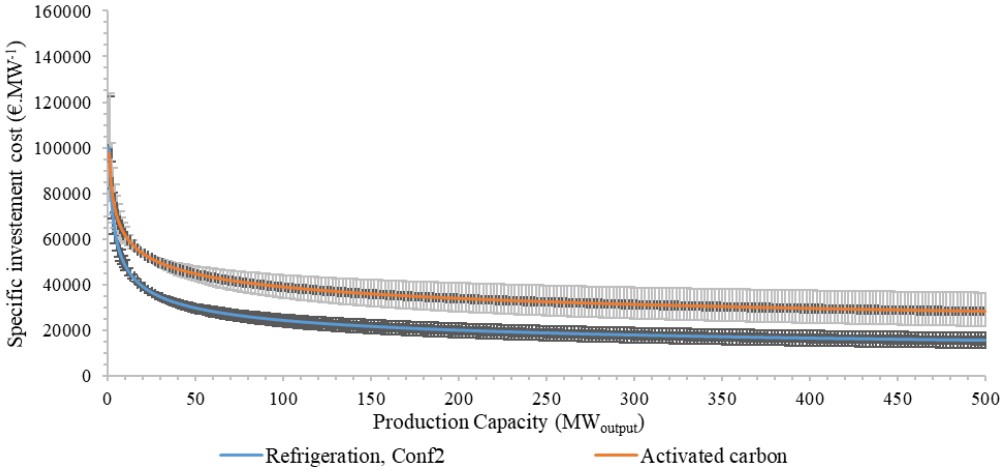

c

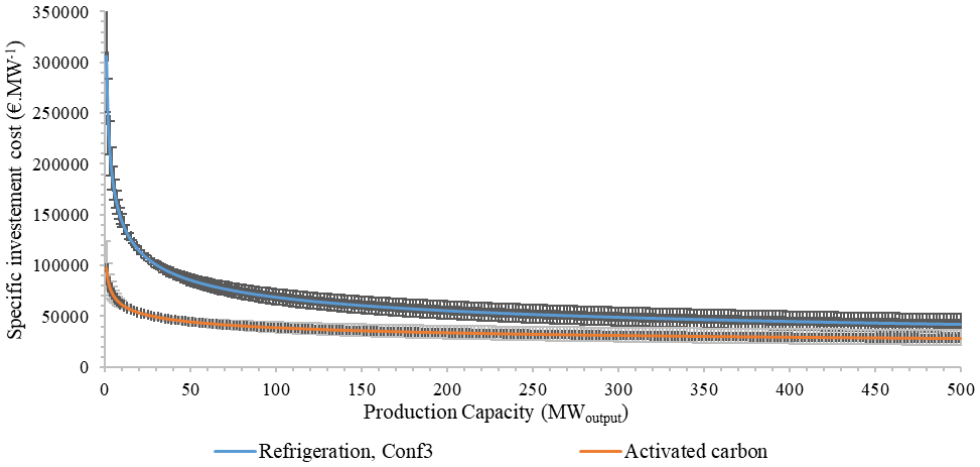

Figure 4-17: Comparison between the $Z_{Inv,spec}$ variation of the tar removal by adsorption, with that of (a) Conf1, (b) Conf2 and (c) Conf3, function of the biomethane production capacity.

It can be seen from Figure 4-15 that the compressors electrical consumption forms around 99% of $\dot{Z}_{op}$, in the three configurations. Therefore, $\dot{Z}_{op}$ strongly depends on C_{elec}, which varies from one country to another. For instance, C_{elec} in the European Union varies from 0.0443 $€.kWh^{-1}$ in Luxembourg to 0.1268 $€.kWh^{-1}$ in the Netherlands [178]. For this purpose, the variation of $\dot{Z}_{op}$, function of C_{elec}, is analyzed in Figure 4-18. It can be seen that $\dot{Z}_{op}$ linearly increases function of C_{elec}, for the three

configurations. In addition, $Conf2$ has the lowest $\dot{Z}_{op}$ followed by $Conf1$, while $Conf3$ has the highest one. Firstly, C_{elec} in Sweden (0.046 €. kWh^{-1} [178]) is considered, since it is the country where the GoBiGas project is developed. This allows to compare $\dot{Z}_{op}$ of the refrigeration system to that of the AC beds from the GoBiGas project. Based on C_{elec} in Sweden, $\dot{Z}_{op}$ of the three selected cases are lower than that of the AC. $\dot{Z}_{op}$ is equal to 10.55, 7.13, and 16.23 €. h^{-1} for $Conf1$, $Conf2$ and $Conf3$, respectively, while that of AC is equal to 17.2 €. h^{-1}. However, Sweden is one of the countries that have the lowest C_{elec}. Therefore, an average C_{elec} of 0.08 €. kWh^{-1} is considered. Based on this price, $\dot{Z}_{op}$ increases and becomes equal to 18.34, 12.40 and 27.84 €. h^{-1} for $Conf1$, $Conf2$ and $Conf3$, respectively. Consequently, the $\dot{Z}_{op}$ of $Conf1$ and $Conf3$ becomes higher than that of the AC. On the contrary, the $\dot{Z}_{op}$ of $Conf2$ remains lower than that of the AC by 28%. Therefore, the best solution for simultaneously reducing Z_{Inv} and $\dot{Z}_{op}$ of the tar treatment unit, consists in using $Conf2$ for the refrigeration cycle instead of the AC beds.

The variation of $\dot{Z}_{op}$, function of the production capacity, is not analyzed since the SF of the consumable is equal to unity. Therefore, the specific operating cost $(\dot{Z}_{op,spec})$, expressed in €. MWh^{-1}, is constant function of the production capacity.

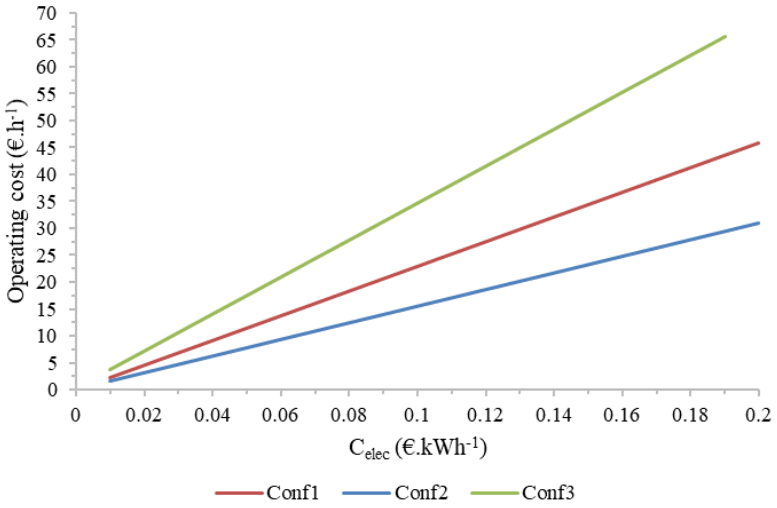

Figure 4-18: Variation of $\dot{Z}_{op}$function of C_{elec}, for the three studied configurations.

Finally, Figure 4-19 presents a comparison between the variation of $\dot{Z}_{Inv} + \dot{Z}_{op}$ of the optimal case for each configuration, function of the biomethane production capacity. As previously mentioned, the comparison does not include $\dot{Z}_{env}$ since it was not considered in the GoBiGas project. The sum of $\dot{Z}_{Inv}$ and $\dot{Z}_{op}$ is considered. It can be seen that the cost rate increases as the biomethane production capacity increases. However, the rate of increase in $Conf3$ is higher than that in $Conf1$ and $Conf2$. In addition, the lowest cost rate is achieved in $Conf2$, as expected from the previous results. The cost rate highly increases in $Conf3$ from 0.024 €. s^{-1} for a production capacity of 20 MW, until reaching 0.105 €. s^{-1} for 500 MW production capacity. Thus, the cost rate is increased by a factor of 4.375. Moreover, the cost rate of $Conf3$ is higher than that of the AC beds. Furthermore, increasing the production capacity from 20 MW to 500 MW increases the cost rate from 0.013 €. s^{-1} to 0.045 €. s^{-1} in $Conf1$, and from 0.0096 €. s^{-1} to 0.039 €. s^{-1} in $Conf2$. Finally, the cost rates of both $Conf1$ and $Conf2$ are lower than that of the AC for the different considered production capacities.

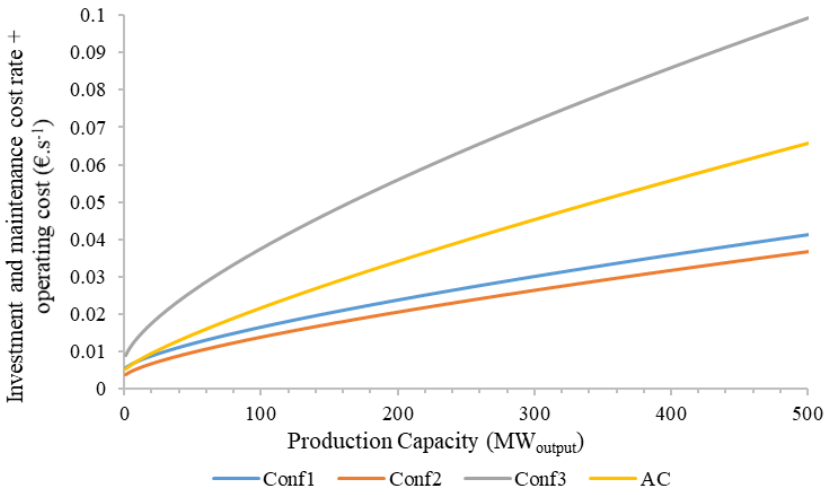

Figure 4-19: Comparison between the variation of $\dot{Z}_{Inv} + \dot{Z}_{op}$ of the optimal case for each configuration, function of the biomethane production capacity.

4.6. Conclusion

In this chapter, a techno-economic analysis is performed in order to assess the feasibility of the proposed tar removal method at low temperatures. Firstly, the economic analysis of the pre-treatment unit is performed. A comparison between the investment and the operating costs of the proposed water-based scrubbers and the traditional oil-based scrubbers, is done for the different sensitivity studies. Three different configurations for the refrigeration system are then proposed in order to reduce the producer gas temperature, and therefore the tar content, to the acceptable level. The study involves energy, exergy, environmental and economic aspects. In the three configurations, the cold of the producer gas leaving the evaporator is integrated in the condenser to reduce the refrigerant temperature after the compression. The first configuration involves the use of nitrogen and methane as refrigerants. In the first two configurations, the producer gas is cooled in two separated refrigeration units, while in the third configuration a single refrigeration unit is considered. In addition, only nitrogen is used as a refrigerant since the throttle valve is replaced by a turbine in the second and third configurations.

A sensitivity analysis is then performed to optimize each configuration. Consequently, several variables are considered to select the optimal operating conditions including T_7, $\dot{m}_r$, HP and LP. The energy analysis showed that the highest COP is achieved in the second configuration while the first configuration yields the lowest COP. According to the exergy analysis, the highest $\eta_{\dot{E}_{tot}}$ is achieved in the first configuration while the lowest one is encountered in the third configuration. In addition, the economic analysis showed that the lowest investment cost is achieved in the first configuration while the lowest operating cost is encountered in the second configuration. Moreover, the environmental analysis showed that the lowest environmental cost is achieved in the second configuration, while the highest one is encountered in the third configuration. Furthermore, the third configuration has the highest total cost rate. Finally, the total cost rate of the second configuration is lower than that of the first one.

The total cost rates of the optimal configurations are compared to that of the AC beds used for the tar removal in the GoBiGas project. It can be deduced from the results, that replacing the RME scrubbers with a water scrubber increases the operating cost, at the optimal operating conditions, from 9.14 to 32.8 €.h^{-1} but it yields a lower producer gas temperature. In addition, the cost of the make-up scrubbing liquid is importantly reduced from 60.04 to 0.83 €.h^{-1}, for P_{ref}=20MW$_{biomethane}$. Therefore, the total operating cost of the scrubbers is reduced by 51.4% while the investment cost remains constant. Moreover, the proposed low temperature process seems to be a promising alternative for the AC beds. In fact,

optimizing the refrigeration cycle and selecting the most suitable configuration (*Conf2*) reduces the investment cost by 27.2% and the operating cost by 27.9%, for P_{ref}=20$MW_{biomethane}$. In total the cost rate of the proposed refrigeration system is lower than that of the AC beds by 6.7% if $Conf1$ is adapted and by 27.4% in case where $Conf2$ is considered.

Chapitre 4 : Etude économique.

1. Introduction

Ce chapitre vise à évaluer l'impact de la nouvelle méthode d'élimination du goudron suggérée sur le coût du processus de conversion de la biomasse en biométhane. L'étude évalue le coût des colonnes d'épuration et de l'unité de réfrigération nécessaires à l'élimination du goudron. Afin de compléter une analyse économique du procédé de traitement du goudron proposé, un procédé de référence doit être considéré. Celui-ci définit les conditions initiales de fonctionnement et les débits des flux, principalement du gaz produit, dans l'analyse. Par conséquent, l'analyse économique est d'abord menée pour une capacité de production de biométhane bien définie. Ensuite, le coût du processus pour différentes capacités de production est calculé à partir du coût du processus de référence, sur la base d'un facteur d'échelle. A cet effet, l'usine GoBiGas est considérée comme le procédé de référence puisqu'il s'agit de la seule usine disponible à l'échelle industrielle, qui transforme la biomasse en biométhane tout en atteignant la teneur en goudron souhaitée. Une évaluation économique détaillée pour l'ensemble de l'usine se trouve dans la littérature [85]. Ce dernier comprend le coût du procédé de traitement de goudron adapté dans l'usine, qui associe une colonne d'absorption à RME à des lits de charbon actif. L'analyse économique dans la littérature est faite pour une usine ayant une capacité de production égale à 20 MW de biométhane. Cette capacité est considérée comme la capacité de production de référence. Elle correspond à une unité de gazéification de biomasse de 32 MWth DFB gazéifieur [98]. Le gazéifieur convertit 150 tonnes sèches de biomasse par jour en 7998 $Nm^3.h^{-1}$ de gaz produit (flux sec).

Puisque cette thèse cible l'élimination de goudron, le coût de cette unité qui inclut les colonnes d'absorption et le cycle de réfrigération est uniquement étudié, alors que le coût des autres unités est considéré constant. Selon GoBiGas, le coût d'investissement de l'étape de prétraitement est égal à 2402 k€ alors que ce celui des lits de charbon active est égal à 1072 k€. En outre, le coût d'exploitation comprend le coût des consommables et plus précisément le prix du RME qui est égal à 64 $€.h^{-1}$, et le coût du charbon actif qui est égale à 17,2 $€.h^{-1}$. Le coût d'électricité n'est pas alors défini par unité, et il est uniquement donné pour l'usine complète.

2. Méthodologie

Le taux de coût total $\left(\dot{Z}_{tot}\right)$ comprend le coût d'exploitation $\left(\dot{Z}_{op}\right)$, le coût environnemental $\left(\dot{Z}_{env}\right)$, ainsi que le taux de coût d'investissement et de maintenance $\left(\dot{Z}_{Inv}\right)$:

$$\dot{Z}_{tot} = \dot{Z}_{Inv} + \dot{Z}_{op} + \dot{Z}_{env} \qquad \text{Eq. 4.1}$$

Le coût d'investissement total du procédé (Z_{Inv}) est égal à la somme des coûts d'investissement de chaque section du procédé j : $Z_{Inv} = \sum_j Z_{Inv,j}$. Les coûts d'investissement pour chaque section sont calculés, en US$, à partir de fonctions trouvées dans la littérature. Cependant, ces fonctions proposées ne sont pas à jour. Pour cela, le coefficient Chemical Engineering Plant Cost Index (CEPCI) [160] est utilisé afin de considérer l'inflation des prix, et pour actualiser les coûts comme suit :

$$Z_{2021} = Z_t \frac{CEPCI_{2021}}{CEPCI_t} \qquad \text{Eq. 4.2}$$

Par la suite, $\dot{Z}_{Inv}$ est calculé pour chaque équipement en fonction de son coût d'investissement, du coefficient de maintenance ($\varphi = 1.06$), du Capital Recovery Factor (CRF) et de la période à pleine charge ($FLH = 8000\ h$) :

$$\dot{Z}_{inv} = \frac{Z_{inv} \times \varphi \times CRF}{FLH \times 3600}$$ Eq. 4.3

Le CRF est calculé en fonction de la durée de vie attendue pour les équipements ($N = 20$) et du taux d'intérêt ($i = 0.1$) comme suit :

$$CRF = \frac{i(1+i)^N}{(1+i)^N - 1}$$ Eq. 4.4

Finalement, $\dot{Z}_{op}$ comprend le coût des consommables, de refroidissement, de chauffage et d'électricité consommée par les pompes et les compresseurs.

3. Epurateurs

3.1. Coût d'investissement

Le coût d'investissement de l'étape de prétraitement proposée comprend le coût de deux colonnes d'absorption, une colonne de régénération, quatre échangeurs de chaleur et trois pompes. Cette configuration est basée sur le procédé OLGA qui utilise le même équipement avec des conditions opératoires différentes. Par conséquent, le coût d'investissement du procédé proposé est similaire à celui du procédé OLGA. Il est rapporté que le coût d'investissement spécifique diminue au fur et à mesure que la taille du processus de gazéification augmente, jusqu'à devenir presque constant à 200 €.Nm^{-3} pour des débits de gaz produit humide supérieurs à 4000 $Nm^3.h^{-1}$ [46]. Ainsi, le coût d'investissement actualisé du système d'épuration d'une usine produisant 20 MW de biométhane, est égal à 3222 k€. Ce prix inclut les coûts indirects et supplémentaires. En revanche, le coût d'investissement actualisé du système d'épuration du GoBiGas est égale à 2612 k€. Cependant, 30% sont ajoutés afin de prendre en compte les coûts indirects et supplémentaires [163]. Le coût d'investissement des colonnes d'absorption du GoBiGas devient alors similaire à celui proposé. Plus précisément, il devient égal à 3396 k€.

3.2. Coût d'exploitation

Les coûts d'exploitation des colonnes d'absorption à l'huile et à l'eau sont évalués. Les coûts d'exploitation du procédé sont principalement déterminés par le coût de consommation de l'agent de lavage et des utilités (Tableau 4.1). Ce dernier est divisé en trois parties différentes : (1) La consommation électrique des trois pompes nécessaires pour la circulation de l'agent de lavage. (2) La quantité de vapeur d'eau nécessaire pour augmenter la température de l'agent de lavage. (3) La quantité de refroidissement et de réfrigération requise pour réduire la température de l'agent de lavage. La variation des coûts d'exploitation des colonnes d'absorption est étudiée en fonction du ratio L/G et de la température de l'gent de lavage dans l'absorbeur.

Tableau 4.1: Prix des différents services.

Service	Electricité	Chaleur	Eau de refroidissement (30°C)	Réfrigération (5°C)
Prix	0.08 €.kWh^{-1}	4 €.GJ^{-1}	0.012 €.m^{-3}	0.15 €.m^{-3}

Premièrement, les pompes ont le coût d'exploitation le plus faible pour tous les colonnes d'absorption, indépendamment des conditions opératoires. Les coûts d'exploitation des pompes, des échangeurs de chaleur de refroidissement et de réchauffement augmentent linéairement en augmentant le ratio L/G et en diminuant la température de l'agent de lavage pour toutes les colonnes d'absorption. De plus, dans les colonnes d'absorption à l'huile, les échangeurs de chaleur de réchauffement ont le coût d'exploitation le plus élevé. Ce dernier forme 50% du coût total d'exploitation qui atteint 14,3 €.h^{-1} pour un ratio L/G de 2,66x10^{-3} $m^3.m^{-3}$ à 60°C, et 11,03 €.h^{-1} pour un ratio L/G de 1,82x10^{-3} $m^3.m^{-3}$ à 40°C.

Pour les colonnes d'absorption à l'eau, le ratio L/G dans le collecteur a un faible impact sur le coût de refroidissement. Au contraire, l'augmentation du ratio L/G dans l'absorbeur augmente considérablement le coût d'exploitation. De plus, la consommation de vapeur pour les échangeurs de chaleur de réchauffement augmente linéairement avec le ratio L/G dans l'absorbeur. D'autre part, réduire la température d'agent de lavage augmente simultanément les consommations de vapeur d'eau, d'eau de refroidissement et de réfrigération. On peut voir qu'opérer à des températures inférieures à 30°C augmente considérablement les coûts de refroidissement et de réfrigération. Il s'agit de la réfrigération supplémentaire nécessaire pour réduire la température de l'eau de 30°C à la température de fonctionnement appropriée. Cependant, la diminution de la température d'eau augmente l'efficacité d'élimination du goudron. Pour une température de 5°C, le coût total des utilités est de 32,8 €.h^{-1}. Enfin, on peut déduire que le coût des utilités des colonnes d'absorption à eau est supérieur à celui des colonnes d'absorption RME. Cependant, la différence entre les prix des liquides de lavage fait des colonnes d'absorption à eau une solution alternative appropriée. Le prix de l'eau dépend du pays considéré. Par exemple, en France, un mètre cube d'eau coûte environ 3,42 € [166]. Alors que le RME est beaucoup plus cher que l'eau. Un mètre cube de RME coûte environ 970 € [167]. Par conséquent, le coût de l'agent de lavage est égal à 60,04 €.h^{-1} et à 0,827 €.h^{-1} pour les colonnes d'absorption à RME et à l'eau, respectivement.

4. Procédé à basse température

Dans cette section, trois systèmes de réfrigération sont comparés en effectuant une analyse énergétique, exergétique et économique pour chaque configuration.

4.1. Configurations étudiées pour l'unité de réfrigération

Le système de réfrigération vise à réduire la teneur en goudron à 1 mg.Nm^{-3}, et donc la température du gaz produit à -110 °C. Cependant, il n'est pas nécessaire que le gaz produit soit à basse température dans le processus de méthanation. A cet effet, le froid du gaz produit est récupéré par son intégration dans le procédé de réfrigération, dans lequel ce froid est utilisé pour abaisser la température du fluide frigorigène après sa compression. Cela diminue le coût et l'énergie requise dans le cycle de réfrigération. Trois configurations sont comparées afin de sélectionner la meilleure, avec les meilleures conditions opératoires. Fig. 4.1 présente les schémas de principe de deux configurations de cycle de réfrigération ($Conf1$ et $Conf3$), alors que $Conf2$ est similaire à $Conf1$ sauf que la vanne d'étranglement est remplacée par une turbine.

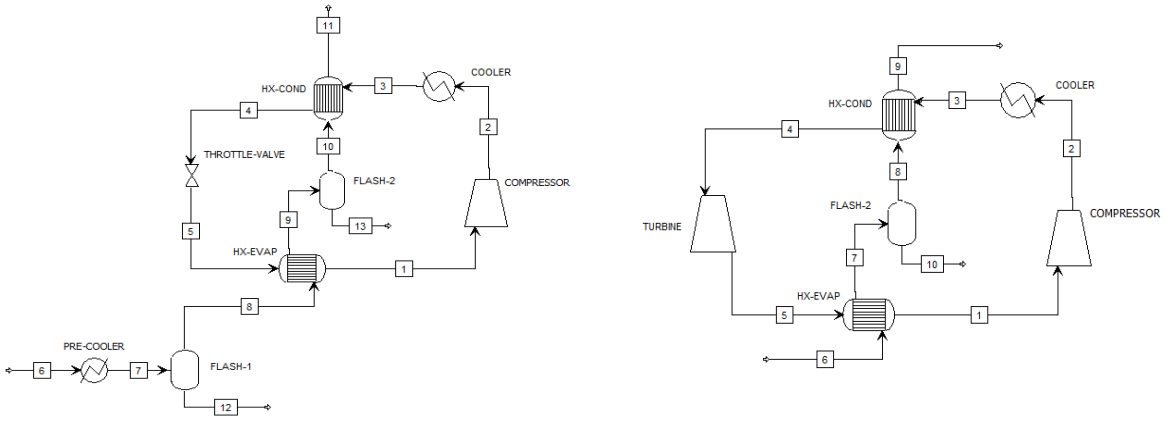

Fig. 4.1: Schéma de principe du cycle de réfrigération pour Conf1 (gauche) et Conf3 (droite).

Pour les trois configurations, le gaz produit froid et propre sortant de l'évaporateur est utilisé afin de refroidir le fluide frigorigène dans le condenseur. De plus, un échangeur de chaleur pour refroidissement

est ajouté dans les trois configurations avant le condenseur afin de réduire la température du fluide frigorigène à 30°C en utilisant l'eau de refroidissement. Dans les deux premières configurations ($Conf1$ et $Conf2$), un cycle de pré-refroidissement (symbolisé par « pre-cooler » dans la Fig. 4.1) est présent afin de réduire la température du gaz produit jusqu'à une température minimale de -50°C et d'éliminer une fraction de goudron et de vapeur d'eau, avant que le gaz sera introduit dans l'évaporateur. Le logiciel BITZER [168] est utilisé pour concevoir le système de réfrigération puisque l'étape de pré-refroidissement est bien développée industriellement. Cela nécessite la définition du fluide frigorigène, du type de compresseur, de la puissance frigorifique, des températures d'évaporation et de condensation. Cependant, cette étape de pré-refroidissement est éliminée de la troisième configuration ($Conf3$). L'azote et le méthane sont testés comme fluide frigorigène dans $Conf1$, alors qu'uniquement l'azote est utilisé dans $Conf2$ et $Conf3$.

4.2. Analyse thermodynamique : énergétique et exergétique

L'analyse énergétique est réalisée afin d'évaluer la puissance du cycle de réfrigération en fonction de plusieurs paramètres. L'analyse exergétique est réalisée afin de calculer la destruction exergétique du cycle. A cette fin, Tableau 4.2 résume les bilans énergétiques et exergétiques des différentes équipements des cycles de réfrigération.

Tableau 4.2: Bilans énergétique et exergétique des différents équipements des cycles de réfrigération.

Equipement	Bilan énergétique	Bilan exergétique
Compresseur	$\dot{W}_{comp} = \frac{\dot{m}_r(h_{2,s} - h_1)}{\eta_{isen,comp}}$	$\dot{E}x_{D,comp} = \dot{m}_r(e\dot{x}_1 - e\dot{x}_2) + \dot{W}_{comp}$
Turbine	$\dot{W}_{turb} = (\dot{m}_r(h_4 - h_5))\eta_{isen,turb}$	$\dot{E}x_{D,turb} = \dot{m}_r(e\dot{x}_4 - e\dot{x}_5) - \dot{W}_{turb}$
Vanne d'étranglement	$h_4 = h_5$	$\dot{E}x_{D,TV} = \dot{m}_r(e\dot{x}_4 - e\dot{x}_5)$
Echangeur de chaleur pour refroidissement	$\dot{Q}_{cooler} = \dot{m}_r(h_2 - h_3)$ $= \dot{m}_{CW} \times Cp_{CW}(T_{CW,out} - T_{CW,in})$	$\dot{E}x_{D,cooler} =$ $\dot{m}_r(e\dot{x}_2 - e\dot{x}_3) + \dot{m}_{CW}(e\dot{x}_{CW,in} - e\dot{x}_{CW,out})$
Condenseur	$\dot{Q}_{cnd} =$ $\begin{cases} Conf1\ and\ Conf2: \\ \dot{m}_{g,10}(h_{11} - h_{10}) = \dot{m}_r(h_3 - h_4) \\ Conf3: \\ \dot{m}_{g,8}(h_9 - h_8) = \dot{m}_r(h_3 - h_4) \end{cases}$	$\dot{E}x_{D,cnd} =$ $\begin{cases} Conf1\ and\ Conf2: \\ (\dot{m}_r e\dot{x}_3 + \dot{m}_g e\dot{x}_{10}) - (\dot{m}_r e\dot{x}_4 + \dot{m}_g e\dot{x}_{11}) \\ Conf3: \\ (\dot{m}_r e\dot{x}_3 + \dot{m}_g e\dot{x}_8) - (\dot{m}_r e\dot{x}_4 + \dot{m}_g e\dot{x}_9) \end{cases}$
Evaporateur	$\dot{Q}_{evap} =$ $\begin{cases} Conf1\ and\ Conf2: \\ \dot{m}_{g,8}h_8 - \dot{m}_{g,9}h_9 = \dot{m}_r(h_5 - h_1) \\ Conf3: \\ \dot{m}_{g,6}h_6 - \dot{m}_{g,7}h_7 = \dot{m}_r(h_5 - h_1) \end{cases}$	$\dot{E}x_{D,evap} =$ $\begin{cases} Conf1\ and\ Conf2: \\ (\dot{m}_r e\dot{x}_5 + \dot{m}_{g.8} e\dot{x}_8) - (\dot{m}_r e\dot{x}_1 + \dot{m}_{g,9} e\dot{x}_9) \\ Conf3: \\ (\dot{m}_r e\dot{x}_5 + \dot{m}_{g,6} e\dot{x}_6) - (\dot{m}_r e\dot{x}_1 + \dot{m}_{g,7} e\dot{x}_7) \end{cases}$
Echangeur de chaleur pour pré-refroidissement	$\dot{Q}_{pre-cool} = \dot{m}_{g,6}h_6 - \dot{m}_{g,7}h_7$	$\dot{E}x_{D,pre-cool} = \dot{m}_{R404A}(e\dot{x}_{R404A,in}$ $- e\dot{x}_{R404A,out})$ $-\left(1 - \frac{T_0}{T_{R404A}}\right)\dot{Q}_{pre-cool}$
Efficacité	$COP =$ $\begin{cases} \frac{\dot{Q}_{evap}}{\dot{Q}_{cnd} + \dot{Q}_{cooler} - \dot{Q}_{evap}}, Conf1 \\ \frac{\dot{Q}_{evap}}{\dot{W}_{comp} - \dot{W}_{turb}}, Conf2\ and\ Conf3 \end{cases}$	$\eta_{\dot{E}_{tot}} =$ $\begin{cases} \frac{\dot{m}_g(e\dot{x}_{g,out} - e\dot{x}_{g,in})}{\dot{W}_{comp}}, Conf1 \\ \frac{\dot{m}_g(e\dot{x}_{g,out} - e\dot{x}_{g,in})}{\dot{W}_{comp} + \dot{W}_{turb}}, Conf2\ and\ Conf3 \end{cases}$

L'exergie d'un flux n ($\dot{ex}_n$) est calculée en fonction de l'enthalpie (h) et l'entropie (s) à son état de référence 0 comme suit :

$$\dot{ex}_n = (h_n - h_0) - T_0(s_n - s_0) \quad \text{Eq. 4.5}$$

4.3. Analyse économique

4.3.1. Coût d'investissement

Le coût d'investissement des différents équipements des cycles de réfrigération sont calculés, en USD, selon les corrélations présentées dans le Tableau 4.3. Un facteur de conversion de $0.85\ €.USD^{-1}$est considéré afin de convertir le coût en euro.

Tableau 4.3: Corrélations pour la prédiction des coûts d'investissement des différents équipements du cycle de réfrigération.

Equipment	Coût d'investissement
Compresseur	$Z_{comp} = 10167{,}5 \times \dot{W}_{comp}$
Vanne d'étranglement	$Z_{TV} = 114{,}5 \times \dot{m}_r$
Turbine	$Z_{turb} = 10167{,}5 \times \dot{W}_{turb}$
Condenseur	$Z_{cnd} = 516{,}621 \times A_{cnd} + 268{,}45$
Evaporateur	$Z_{evap} = 309{,}143 \times A_{evap} + 231{,}915$
Echangeur de chaleur	$Z_{HX} = 130 \times \left(\frac{A_{HX}}{0{,}093}\right)^{0{,}78}$

4.3.2. Coût d'exploitation

Le coût d'exploitation total $(\dot{Z}_{op})$, présenté dans l'Eq. 4.6, inclut la consommation électrique des compresseurs du cycle de réfrigération $(\dot{Z}_{elec,comp,r})$ et du cycle de pré-refroidissement $(\dot{Z}_{elec,comp,pre-cooler})$, aussi bien que la consommation d'eau de refroidissement requise dans l'échangeur de chaleur pour refroidissement $(\dot{Z}_{CW})$. Le coût d'exploitation des compresseurs, défini dans l'Eq. 4.7, est calculé en fonction du coût d'électricité (C_{elec}). Le coût d'eau de refroidissement, défini dans l'Eq. 4.8, est calculé en fonction du prix d'eau (C_{CW}).

$$\dot{Z}_{op} = \dot{Z}_{elec,comp,r} + \dot{Z}_{elec,comp,pre-cooler} + \dot{Z}_{CW} \quad \text{Eq. 4.6}$$

$$\dot{Z}_{elec} = \dot{W} C_{elec} \quad \text{Eq. 4.7}$$

$$\dot{Z}_{CW} = \dot{m}_{CW} C_{CW} \quad \text{Eq. 4.8}$$

4.4. Analyse environnementale : émission de CO_2

En raison de l'intérêt croissant pour la limitation du réchauffement climatique, il est important de considérer la quantité de CO_2 émise afin de sélectionner la configuration de réfrigération appropriée. La quantité de CO_2 annuellement émise $(\dot{m}_{CO_2})$, défini dans l'Eq. 4.9, est calculée en fonction du facteur d'émission $(\mu_{CO_2} = 0{,}4218\ kg.kWh^{-1})$ et de la consommation électrique annuelle (W_{annual}). Ensuite, le taux de coût de pénalité des émissions de CO_2 $(\dot{Z}_{env})$, exprimé par l'Eq. 4.10, est calculé en fonction du coût de la pénalité des émissions de CO_2 $\left(C_{CO_2} = 0{,}076\ €.{kg_{CO_2}}^{-1}\right)$.

$$\dot{m}_{CO_2} = \mu_{CO_2} W_{annual} \quad \text{Eq. 4.9}$$

$$\dot{Z}_{env} = \frac{\dot{m}_{CO_2} C_{CO_2}}{FLH \times 3600} \quad \text{Eq. 4.10}$$

5. Paramètres et contraintes de conception

Afin d'analyser et d'optimiser les différents cycles frigorifiques, une étude paramétrique est complétée. L'objectif de cette étude est d'atteindre la température du gaz produit requise tout en réduisant la consommation d'énergie, la destruction d'exergie, l'impact environnemental et le coût total du procédé. Les paramètres étudiés sont : le flux massique du réfrigérant ($\dot{m}_r$), la haute pression (HP), la basse pression (LP) et la température du gaz produit qui sort de l'étape de pré-refroidissement (T_7). De plus, plusieurs contraintes doivent être considérés, plus précisément : $HP/LP \leq 3$, $T_2 < 150$°C, et un pincement de température égal à 3°C est imposé dans les échangeurs. En outre, plusieurs paramètres sont imposés par les conditions opératoires et le procédé de prétraitement comme le flux massique du gaz produit ($\dot{m}_{g,6} = 1{,}866\ kg.s^{-1}$) et la température de l'échangeur de chaleur pour refroidissement ($T_3 = 30$°C), par exemple.

6. Résultat et discussion

Dans un premier temps, l'impact des différentes variables sur la capacité du cycle de réfrigération à réduire la température du gaz produit est analysé. Tableau 4.4 présente les plages de variation pour chaque paramètre étudié afin d'évaluer l'impact de chacun sur la température du gaz produit après la réfrigération.

Tableau 4.4: Les plages dans lesquelles varient les paramètres considérés pour chaque configuration.

Configuration	**Conf1**		**Conf2**	**Conf3**
Fluide frigorigène	**N_2**	**CH_4**	**N_2**	**N_2**
$LP\ (bar)$	10-30	7-15,5	10-40	10-30
$HP\ (bar)$	15-70	20-46	30-70	30-70
T_7 (°C)	(-35)-(-46)	(-30)-(-35)	(-20)-(-27)	5
$\dot{m}_r\ (kg.s^{-1})$	1,60-2,50	1,11-1,20	2,25-3,00	2,30-3,50

6.1. Coefficient de performance (COP)

Le COP est un paramètre important qui doit être analysé pour sélectionner le cycle de réfrigération approprié. Le COP augmente avec l'augmentation de $\dot{Q}_{evap}$ ou avec la diminution de $\dot{W}_{net}$. $\dot{W}_{net}$ de $Conf2$ est inférieur à celui de $Conf1$ à cause du travail produit par la turbine. Au contraire, $\dot{Q}_{evap}$ augmente de $Conf1$ à $Conf2$ puisque la température du gaz produit entrant dans l'évaporateur augmente, tandis que la même température du gaz produit sortant de l'évaporateur est atteinte. Le remplacement de la vanne d'étranglement par une turbine augmente le COP de $Conf1$ à $Conf2$. La valeur moyenne de COP de la $Conf3$ est 6% supérieure que celle de la $Conf1$, alors qu'elle est 35 % inférieure à celle de $Conf2$.

En $Conf1$, le COP le plus bas de 0,66 est obtenu pour la T_7 la plus basse, alors qu'il augmente jusqu'à 1,61 pour le HP/LP le plus bas. De plus, le remplacement de l'azote par le méthane diminue $\dot{m}_r$ ainsi que $\dot{W}_{net}$. Par conséquent, le COP du groupe frigorifique augmente. Dans $Conf2$, le COP le plus bas de 1,18 est obtenu pour le HP/LP le plus élevé. Le COP le plus élevé de 2,56 correspond au $\dot{m}_r$ le plus bas avec un HP/LP de 1,75 en considérant une T_7 de -27°C. Enfin, le COP de $Conf3$ est quasiment constant autour de 1,2 puisque la variation HP/LP est limitée entre 2,917 et 3.

6.2. Taux du coût total

Le $\dot{Z}_{tot}$ moyen de $Conf2$ est inférieur à celui de $Conf1$. Plus précisément, $\dot{Z}_{tot}$ de $Conf1$ varie entre 0,0105 et 0,0193 €.s^{-1}, tandis que celui de $Conf2$ varie entre 0,008 et 0,0139 €.s^{-1}. $\dot{Z}_{tot}$ augmente

fortement en $Conf3$ et atteint 0,021 €.s^{-1}. On peut voir que dans la plupart des cas considérés dans $Conf1$ et $Conf2$, $\dot{Z}_{op}$ a la part la plus élevée du $\dot{Z}_{tot}$. En moyenne, $\dot{Z}_{op}$, $\dot{Z}_{Inv}$ et $\dot{Z}_{env}$ forment respectivement 50,4%, 30,8% et 28,8% de $\dot{Z}_{tot}$, en $Conf1$. Alors que dans $Conf2$, $\dot{Z}_{op}$, $\dot{Z}_{Inv}$ et $\dot{Z}_{env}$ forment respectivement 43,5%, 41,2% et 15,3% de $\dot{Z}_{tot}$, en moyenne. La part de $\dot{Z}_{Inv}$ augmente dans $Conf2$ alors que celui de $\dot{Z}_{op}$ diminue, du fait du remplacement de la vanne d'étranglement par une turbine. D'une part, Z_{turb} est supérieur à Z_{TV}. D'autre part, la turbine diminue $\dot{W}_{net}$ ainsi que $\dot{Q}_{pre-cool}$. Quant à $Conf3$, $\dot{Z}_{op}$, $\dot{Z}_{Inv}$ et $\dot{Z}_{env}$ forment respectivement 38,8%, 47,7% et 13,5% de $\dot{Z}_{tot}$, en moyenne. De plus, $Conf3$ a le $\dot{Z}_{tot}$ le plus élevé. Ainsi, l'élimination de l'unité de pré-refroidissement en $Conf3$ augmente $\dot{Z}_{tot}$ d'au moins de 10%. Le comportement général des différents coûts peut être résumé comme suit : (1) L'augmentation de $\dot{m}_r$ augmente les dimensions de l'équipement et donc augmente $\dot{Z}_{Inv}$. De plus, $\dot{W}_{comp}$ augmente, et donc $\dot{Z}_{op}$ et $\dot{Z}_{env}$ augmentent. (2) L'augmentation du HP/LP augmente $\dot{W}_{comp}$, et donc $\dot{Z}_{op}$ et $\dot{Z}_{env}$ augmentent. Au contraire, $\dot{Z}_{Inv}$ reste quasiment constant puisque Z_{comp} et Z_{turb} augmentent, tandis que Z_{evap} diminue. (3) Réduire T_7 augmente les différents coûts unitaires de l'étape de pré-refroidissement. Cependant, cela réduit les coûts du cycle de réfrigération en réduisant la température du réfrigérant à l'entrée du compresseur. La variation de $\dot{Z}_{tot}$ est donc dépendante de ces deux unités. (4) La limitation de la température du gaz produit sortant de l'évaporateur à -110°C, diminue $\dot{Z}_{op}$ puisque la température du fluide frigorigène entrant dans le compresseur (T_1) est réduite.

6.2.1. Coût d'investissement

Le Z_{Inv} total moyen de $Conf1$, $Conf2$ et $Conf3$ est égal à 908723 €, 957256 € et 2274278 €, respectivement. Pour toutes les configurations, l'évaporateur a le coût d'investissement le plus élevé. Cela est dû au fait que le coefficient de transfert de chaleur global est trop faible en raison de la formation de givre. La part de l'étape de pré-refroidissement dans Z_{Inv} diminue de 24,43 % en $Conf1$ à 4,88 % en $Conf2$ en raison de la diminution de T_7 comme illustré dans la Fig. 4.2. Z_{cond} est inférieur à $Z_{pre-cool}$ en $Conf1$, alors que c'est l'inverse en $Conf2$. La part moyenne du compresseur dans Z_{Inv} est inférieure à celle du condenseur, et elle est quasi constante autour de 11 %, pour les deux premières configurations. Elle diminue à 6,37% dans la troisième configuration. Parmi tous les composants, le Z_{TV} est le plus bas. Z_{turb} est plus grand que celui de la vanne d'étranglement. Enfin, Z_{cool} est inférieur à 1 % dans les trois configurations.

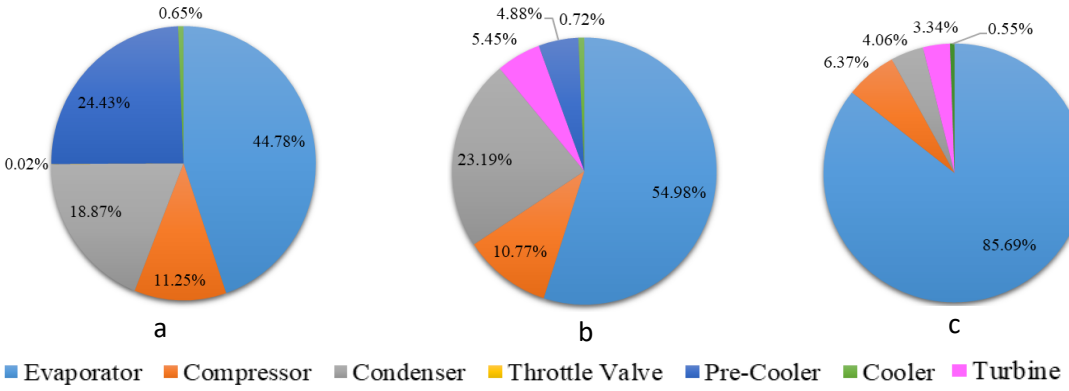

Fig. 4.2: Distribution de Z_{Inv} pour (a) Conf1, (b) Conf2 et (c) Conf3.

6.2.2. Coût d'exploitation

Les $\dot{Z}_{op}$ moyens de $Conf1$, $Conf2$ et $Conf3$ sont respectivement égaux à 25 €.h^{-1}, 18 €.h^{-1} et 29 €.h^{-1}. Le $\dot{Z}_{op}$ de la $Conf2$ est inférieur à celui de $Conf1$ puisque la turbine diminue le $\dot{W}_{net}$ requis, et donne des températures plus basses à la sortie de la turbine (T_5) pour les mêmes HP et LP considérées dans la

vanne. La distribution du $\dot{Z}_{op}$ des différentes configuration est illustrée dans Fig. 4.3 De plus, $\dot{Z}_{elect,comp,r}$ forme respectivement 62,2%, 79,1% et 98,6% de $\dot{Z}_{op}$ dans $Conf1$, $Conf2$ et $Conf3$. Dans $Conf1$ et $Conf2$, $\dot{Z}_{elec,comp,pre-cool}$ est supérieur à $\dot{Z}_{CW}$. Les températures plus basses imposées dans l'étape de pré-refroidissement par l'utilisation de la vanne d'étranglement dans $Conf1$, conduisent à un $\dot{Z}_{elec,comp,pre-cool}$ plus élevé. En outre, $\dot{Z}_{op}$ dans $Conf3$ est d'au moins 16% supérieur à ceux des autres configurations. D'une part, l'élimination de l'étape de pré-refroidissement augmente fortement $\dot{Z}_{CW}$. D'autre part, les HP/LP élevés requis entraînent une consommation électrique plus élevée. Enfin, $\dot{Z}_{env}$ est lié à la consommation électrique. Par conséquent, $Conf2$ a le plus faible impact environnemental, suivi par $Conf1$ et $Conf3$.

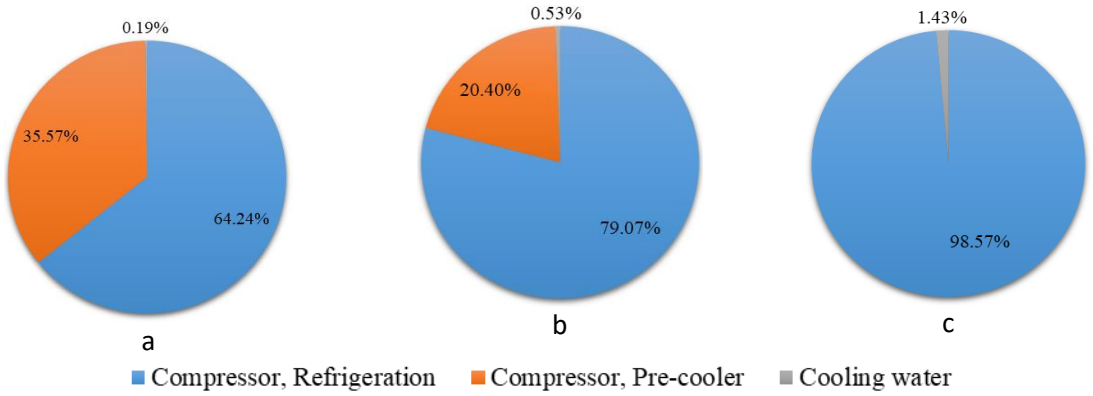

Fig. 4.3: Distribution de $\dot{Z}_{op}$ pour (a) Conf1, (b) Conf2 et (c) Conf3.

6.3. Destruction exergétique $(\dot{E}x_D)$

Les différentes destruction exergétiques ($\dot{E}x_D$) moyennes pour les différents composants des cycles de réfrigération sont illustrées dans la Fig. 4. 4. En général, augmenter T_7 tout en fixant HP/LP diminue l'efficacité exergétique ($\eta_{\dot{E}_{tot}}$).

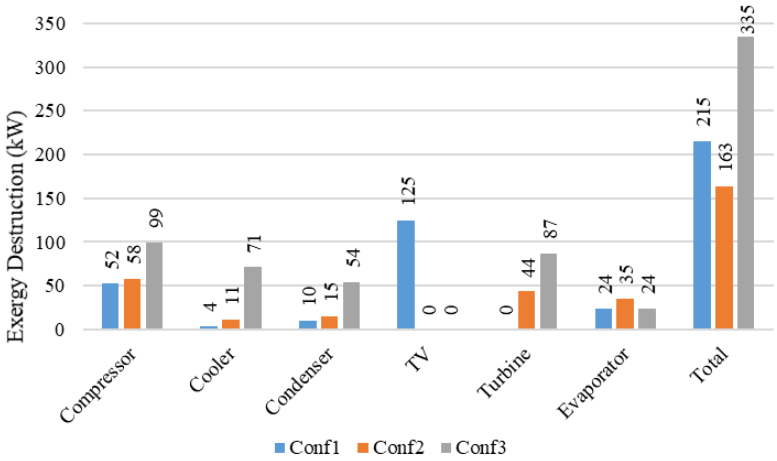

Fig. 4. 4: Comparaison entre les $\dot{E}x_D$ dans les différents composants des systèmes de réfrigération Conf1, Conf2 et Conf3.

Plus précisément, l'augmentation de T_7 augmente $\dot{E}x_{D,evap}$, ce qui conduit à une destruction exergétique totale plus élevée. De plus, augmenter HP/LP tout en fixant les autres variables, réduit fortement $\eta_{\dot{E}_{tot}}$ puisque la $\dot{E}x_D$ dans tous les composants ainsi que le $\dot{W}_{net}$ requis augmentent. De plus, augmenter $\dot{m}_r$ tout en fixant les autres variables réduit $\eta_{\dot{E}_{tot}}$, en particulier lorsqu'une turbine est utilisée à la place d'une vanne d'étranglement.

7. Configurations optimales

En moyenne, $Conf1$ a le $\dot{Z}_{Inv}$ le plus bas, ainsi que le COP le plus bas, alors qu'il a la $\eta_{\dot{E}_{tot}}$ la plus élevée. $Conf2$ a les plus faibles $\dot{Z}_{op}$ et $\dot{Z}_{env}$. Au contraire, il a le COP le plus élevé avec une $\eta_{\dot{E}_{tot}}$ élevée. $Conf3$ a le $\dot{Z}_{Inv}$, le $\dot{Z}_{op}$ et le $\dot{Z}_{env}$ les plus élevés, la $\eta_{\dot{E}_{tot}}$ la plus basse et une valeur de COP modérée. La sélection du cas optimal prend en compte les différents taux de coût, le COP et la $\eta_{\dot{E}_{tot}}$. Dans le meilleur cas, le cas sélectionné doit avoir le $\dot{Z}_{tot}$ le plus bas, le COP le plus élevé et la $\dot{E}x_D$ la plus basse. Cependant, ces conditions ne sont généralement pas remplies dans un seul cas. Les conditions optimales sélectionnées pour chaque configuration sont présentées dans le Tableau 4. 5.

Tableau 4. 5: Les conditions d'opération optimales sélectionnées pour chaque configuration en se basant sur les études paramétriques.

Configuration	**Conf1**	**Conf2**	**Conf3**
Fluide frigorigène	**CH_4**	**N_2**	**N_2**
$LP\ (bar)$	14	40	24
$HP\ (bar)$	30	70	70
T_7 (°C)	-32	-27	5
$\dot{m}_r\ (kg.s^{-1})$	1,11	2,25	3,18

8. Facteur d'échelle

Le coût d'investissement d'une unité (Z_{Inv}) ayant une capacité P est relié au coût de la même unité $(Z_{Inv,ref})$ ayant une capacité de référence P_{ref} selon l'Eq. 4.11. Cette équation reflète la non-linéarité entre le coût et la capacité de l'installation en fonction du facteur d'échelle (SF). Ensuite, le coût d'investissement spécifique est calculé $(Z_{Inv,spec} = Z_{Inv}/P)$.

$$Z_{Inv} = Z_{Inv,ref}\left(\frac{P}{P_{ref}}\right)^{SF} \qquad \text{Eq. 4.11}$$

Une comparaison entre la variation du $Z_{Inv,spec}$ de l'élimination de goudron par adsorption sur des lits de charbon actif avec ceux des cas optimaux sélectionner pour $Conf1$, $Conf2$ et $Conf3$. On constate que le $Z_{Inv,spec}$ total de $Conf1$ et $Conf2$ est inférieur à celui des lits AC, tandis que celui de $Conf3$ est supérieur à celui des lits AC. Les $Z_{Inv,spec}$ des cycles de réfrigération et des lits AC diminuent fortement jusqu'à devenir quasi constant pour des capacités de production supérieures à 200 MW à des valeurs près de 16900, 15550, 44920 et 31000 €.MW^{-1} pour $Conf1$, $Conf2$, $Conf3$ et les lits AC, respectivement.

La variation de $\dot{Z}_{op}$ en fonction du C_{elec}, qui varie d'un pays à l'autre, est étudiée. On peut voir que $\dot{Z}_{op}$ augmente linéairement en fonction de C_{elec}, pour les trois configurations. De plus, $Conf2$ a le $\dot{Z}_{op}$ le plus bas suivi par $Conf1$, tandis que $Conf3$ a le $\dot{Z}_{op}$ le plus élevé. En se basant sur le C_{elec} le plus bas en Suède, $\dot{Z}_{op}$ est égal à 10,55, 7,13 et 16,23 €.h^{-1} pour $Conf1$, $Conf2$ et $Conf3$, respectivement, tandis que celui des lits AC est égal à 17,2 €.h^{-1}. Dans le cas où une valeur moyenne de C_{elec} est considérée (0,08 €.kWh^{-1}), $\dot{Z}_{op}$ augmente et devient égal à 18,34, 12,40 et 27,84 €.h^{-1} pour $Conf1$, $Conf2$ et $Conf3$, respectivement. Par conséquent, $\dot{Z}_{op}$ de $Conf1$ et $Conf3$ devient supérieur à celui de l'AC. Au contraire, $\dot{Z}_{op}$ de $Conf2$ reste inférieur (par 28%) à celui de l'AC.

Finalement, Fig. 4.5 illustre une comparaison entre la variation du $\dot{Z}_{Inv} + \dot{Z}_{op}$ du cas optimal pour chaque configuration en fonction de la capacité de production de biomethane. On constate que le taux du coût augmente au fur et à mesure que la capacité de production de biométhane augmente. Cependant,

le taux d'augmentation dans $Conf3$ est plus élevé que celui dans $Conf1$ et $Conf2$. De plus, le taux du coût le plus bas est obtenu dans $Conf2$, suivi par $Conf1$, puis par les lits AC et enfin $Conf3$ a le taux d coût le plus élevé.

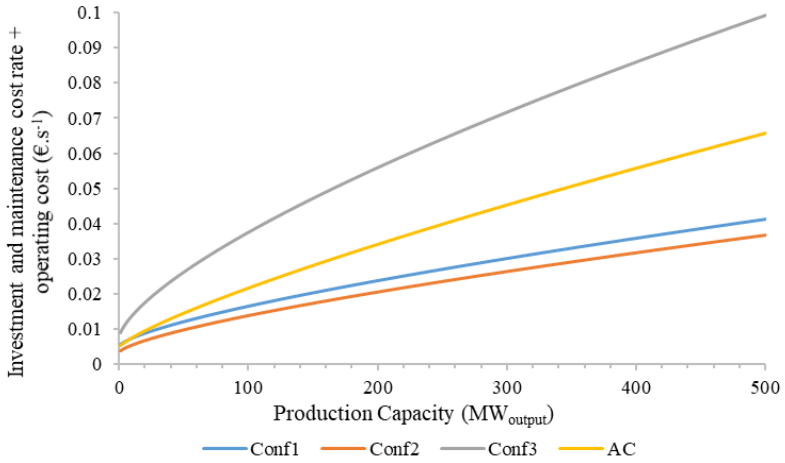

Fig. 4.5: Comparaison entre la variation de $\dot{Z}_{Inv} + \dot{Z}_{op}$ du cas optimal pour chaque configuration en fonction de la capacité de production de biométhane.

9. Conclusion

Dans ce chapitre, une analyse technico-économique est réalisée afin d'évaluer la faisabilité de la méthode d'élimination du goudron proposée à basse température. Les résultats obtenus sont comparés à ceux des lits AC utilisés pour l'élimination du goudron dans le projet GoBiGas. Une analyse de sensibilité est ensuite effectuée pour optimiser chaque configuration. Plusieurs variables sont alors considérées pour sélectionner les conditions opératoires optimales : T_7, $\dot{m}_r$, HP and LP. L'analyse énergétique a montré que le COP le plus élevé est atteint dans $Conf2$ tandis que $Conf1$ donne le COP le plus bas. D'après l'analyse exergétique, le $\eta_{\dot{E}_{tot}}$ le plus élevé est atteint dans $Conf1$ tandis que le $\eta_{\dot{E}_{tot}}$ le plus faible est rencontré dans $Conf3$. De plus, l'analyse économique a montré que le coût d'investissement le plus bas est atteint dans $Conf1$ tandis que le coût d'exploitation le plus bas est rencontré dans $Conf2$. De plus, l'analyse environnementale a montré que le coût environnemental le plus bas est atteint dans $Conf2$, tandis que le plus élevé est rencontré dans $Conf3$. De plus, $Conf3$ a le taux du coût total le plus élevé. Le taux du coût total de $Conf2$ est inférieur à celui de $Conf1$. Finalement, le taux du coût total du cas optimal du cycle de réfrigération est inférieur à celui des lits de charbon actif par 6,7% et par 27,4% pour $Conf1$ et $Conf2$, respectivement.

General Conclusion and Perspectives

Biomass conversion into biofuels and biogas is a promising way for energy and heat generation. However, this application is limited by the tar quantity and quality formed during the conversion process. The knowledge of tar chemical and physical properties is a key factor in developing tar removal/reduction technologies.

Based on the previously described treatment methods, reducing the tar content to 1 $mg.Nm^{-3}$ is a challenging objective that is not yet reached by most of the existing tar treatment methods. In fact, most of the researchers focus on reducing the tar content for the CHP application. In this latter, fewer restrictions are set on the gas quality, while benzene, toluene and xylene compounds are usually denied. It is assumed that these compounds do not affect the process, since the tar dew point is below the lowest operating temperature at atmospheric pressure. However, linking the gasification process to biomethane chemical synthesis requires an extremely high quality, which is not yet reached by most of the existing methods. Based on the state of the art developed in Chapter 1, the main limitations for reaching an extreme clean gas are: limited temperature difference, saturation of the scrubbing medium, saturation of the adsorbent bed, and deactivation of the catalyst by coke deposition.

To overcome these limitations, a solution consists in operating a process at a low temperature, thus ensuring a sufficient temperature difference to condense all the tar components including BTX. This solution is proposed after developing the psychrometric charts for the tar representative components. Those charts reflected that the temperature of the producer gas should be reduce to at least -110°C in order to reach a total tar content lower than 1 $mg.Nm^{-3}$. The suggested low temperature process for tar removal is a non-reactive process that is divided in two main steps. The first one ensures the removal of the heavy tar fraction at ambient temperature before entering the low temperature unit. Within the latter unit, part of the light tar and BTX are removed by simultaneous multi-component condensation and deposition. The condensation and deposition take place over a cold surface by indirect contact heat transfer.

The first unit is formed of two scrubbers placed in series. The use of two different scrubbing liquids: RME and water, is analyzed. Several sensitivity analyses are done in order to select the optimal operating conditions for both scrubbers. The sensitivity studies analyze the impact of the L/G ratio and of the scrubbing liquid temperature on the remaining tar content in the producer gas, and therefore on the tar removal efficiency. Simulations and sensitivity studies of RME and water scrubbers showed that the heavy tar fraction is efficiently reduced in the scrubber for both scrubbing liquids. The overall tar removal efficiency is higher if RME is used as a scrubbing liquid. However, operating with water as a scrubbing liquid leads to lower producer gas temperatures and lower values of water vapor content remaining in the producer gas. Consequently, the use of water as a scrubbing liquid is more suitable for combining the scrubbing process with a simultaneous multi-component deposition/condensation.

The main challenge of the tar removal at low temperature consists in modeling a simultaneous condensation and deposition for several components. When cooling down the gas temperature, benzene and water vapor present in the producer gas undergo a frosting process and they are assumed to form two separate frost layers. In addition, toluene condenses as a liquid film that fills the frost pores. Moreover, a CO_2 frost layer starts to grow for temperatures lower than $-95°C$.

The mathematical model of simultaneous frost growth and condensation is developed on Dymola. Flat plates are considered to validate the scientific aspect of the model by comparing its results with the results of the existing models as well as with the published experimental results. The sensitivity studies

highlighted the impact of several parameters, including the wall temperature, the gas velocity and the heat transfer area, on the low temperature tar removal process. This allows to select the best operating conditions for the tar removal.

In order to explicitly reduce the tar content and therefore implicitly reduce the gas temperature, a high energy consumption is required, which is hard to achieve using a single plate. Therefore, dividing the process into several refrigeration stages can be of great importance in reducing the exergy destruction. For this purpose, multiple plates with decreasing wall temperature were placed in series in order to significantly reduce the producer gas temperature.

On the other hand, reducing the producer gas temperature to -110°C requires an efficient refrigeration system, which is costly. Therefore, integrating the cold of the producer gas to reduce the refrigerant temperature improves the design and the COP, which reduces the total cost of the system. The optimal conditions and configuration are selected based on sensitivity studies. Accordingly, the optimal configuration has a total cost rate lower than that of the activated carbon beds by 27.4%. The activated carbon beds are used in the literature to remove the remaining tar fraction after the scrubbers.

For future work, it is first crucial to develop an experimental setup that allows the visualization of the frosting and condensation behaviors. The experimental study has several objectives. The first one is the validation of the developed model. This imposes the conduction of qualitative and quantitative investigations for benzene, ice deposition and toluene condensation, simultaneously. The frost formation and accumulation should be studied for several operating conditions in order to cover the full low temperature process of tar removal. This indicates that several conditions for inlet gas temperature, refrigerant temperature and inlet gas compositions, should be considered for testing. Knowing the gas inlet composition, the temporal variation of the tar content at the end of the cold plate should be monitored using a gas chromatography. This allows the calculation of the total condensed mass flow rate. In addition, the frost layer thickness can be measured using a depth micrometer with a thermocouple, mounted at the top of the micrometer probe. This measurement method yields the average frost thickness and the frost surface temperature. Therefore, the average frost density can be computed based on the total deposited mass flow rate and the frost thickness. Moreover, the temperature variation of the producer gas and of the refrigerant are measured, function of time, using thermocouples horizontally inserted in the gas passage. This allows the calculation of the heat and mass transfer between the producer gas and the refrigerant. Besides the model validation, the experiment targets the visualization of the condensed phase formation, which is a mixture of solid and liquid. It will also allow assessing if the presence of a certain amount of liquid in the condensed phase facilitates the removal of the formed frost layer. Another point to consider is the impact of the assumptions previously considered, such as the formation of the two separate frost layers where the pores are filled with liquid toluene. Therefore, the experimental setup should be built into a transparent environmental to allow the visualization of the frost formation.

The obtained results are encouraging in terms of tar content reduction efficiency and total cost rate. They prove that the proposed tar treatment method at low temperature is advantageous for biomethane production by catalytic methanation. These promising results open the way for a collaboration with an industrial party. This allows to build a pilot plant that operates with a real producer gas charged with all the impurities, rather than a gas mixture prepared in the laboratory.

An additional point to consider is to analyze several geometries other than flat plates such as tubes in order to assess the impact of the considered geometry on the tar removal efficiency. Therefore, the geometry of the heat exchanger and its type can be optimized based on the obtained results. Moreover,

removing the deposited frost layer to avoid plugging the heat exchanger is essential. This can be done by different methods. One of the method consists in placing an additional heat exchanger in parallel, in order to regenerate the first one by heating it up while keeping a continuous operational mode. This can be done by passing the hot producer gas or flue gas, and therefore internally providing the required heat and eliminating an additional operating cost.

Finally, developing new correlations based on the experiment for the frost density and the frost effective thermal conductivity is of great importance. Since most of the existing correlations are valid for ice frost density and for single component frost layer, developing new correlations that can be applied for a multi-component frost layer will be advantageous. The mathematical model should be then modified in a way to use the new developed correlations. Therefore, a comparison between the model results that are based on the assumption of two frost layers formation and those obtained from the developed new correlations should be performed. This allows to evaluate the impact of the considered assumptions on the heat and mass transfer as well as on the frost growth phenomena.

Conclusion générale et perspectives

La conversion de la biomasse en biocarburants et biogaz est une voie prometteuse pour la production d'énergie et de chaleur. Cependant, cette application est limitée par la quantité et la qualité du goudron formé pendant le processus de conversion. La connaissance des propriétés chimiques et physiques du goudron est un facteur clé pour le développement des technologies d'élimination/réduction du goudron.

En se basant les méthodes de traitement décrites précédemment, réduire la teneur en goudron jusqu'à 1 $mg.Nm^{-3}$ est un objectif ambitieux qui n'est pas encore atteint par la plupart des méthodes de traitement de goudron existantes. Les principales limitations pour atteindre un gaz extrêmement propre sont ; différence de température limitée, saturation de l'agent de lavage, saturation du lit d'adsorbant de charbon actif et désactivation du catalyseur par dépôt de coke. Pour pallier ces limitations, une solution consiste à proposer un procédé d'élimination de goudron à basse température, assurant ainsi un écart de température suffisant pour condenser tous les composants de goudron y compris les BTX. Il s'agit d'un procédé non réactif qui se divise en deux étapes principales. La première assure l'élimination de la fraction lourde de goudron à température ambiante avant d'entrer dans l'unité basse température. Dans la deuxième unité, ce qui reste de la partie légère de goudron et du BTX sont éliminés par condensation et dépôt simultanés. La condensation et le dépôt ont lieu sur une surface froide par transfert de chaleur par contact indirect.

L'enjeu principal de l'élimination de goudron à basse température consiste à modéliser une condensation et un givrage simultanés de plusieurs composants. Lors du refroidissement de la température du gaz, le benzène et la vapeur d'eau présents dans le gaz produit subissent un processus de givrage formant deux couches de givre. Cependant, le toluène se condense sous forme d'un film liquide qui remplit les pores du givre. De plus, une couche de givre de CO_2 commence à se développer pour des températures inférieures à -95°C. Le modèle mathématique de la croissance simultanée du givre et de la condensation est développé sur Dymola. Dans un premier temps, des plaques planes sont envisagées pour le modèle afin de le valider par comparaison avec des modèles existants ainsi qu'avec des expériences publiées. Les études de sensibilité ont mis en évidence l'impact de plusieurs paramètres sur le processus d'élimination du goudron à basse température. Cela permet de sélectionner les meilleures conditions pour l'élimination du goudron.

Afin de réduire la teneur en goudron et donc la température du gaz, une consommation d'énergie élevée est nécessaire, ce qui est difficilement réalisable avec une seule plaque. Par conséquent, diviser le processus en plusieurs étapes de réfrigération peut être d'une grande importance pour réduire la destruction de l'exergie. À cette fin, plusieurs plaques avec une température de paroi décroissante sont placées en série afin de réduire considérablement la température du gaz produit.

D'autre part, réduire la température du gaz produit nécessite un système de réfrigération efficace, ce qui est coûteux. Par suite, l'intégration du froid du gaz produit pour réduire la température du réfrigérant dans le condenseur améliore la conception, le COP et réduit le coût total du système. Les conditions optimales pour chaque configuration sont sélectionnées sur la base des études de sensibilité. Par conséquent, la configuration optimale a un coût total inférieur à celui des lits de charbon actif par 27,4%.

Enfin, dans les travaux futurs, il est crucial de développer un dispositif expérimental permettant de valider les résultats du modèle. L'expérience permettra de visualiser les comportements de givrage et de condensation simultanés, et d'évaluer ainsi l'impact des hypothèses du modèle précédemment discutées.

References

1. Chan FL, Tanksale A. Review of recent developments in Ni-based catalysts for biomass gasification. Renew Sustain Energy Rev. 2014 Oct;38:428–38.

2. Patra TK, Mukherjee S, Sheth PN. Process simulation of hydrogen rich gas production from producer gas using HTS catalysis. Energy. 2019 Apr;173:1130–40.

3. Anis S, Zainal ZA. Tar reduction in biomass producer gas via mechanical, catalytic and thermal methods: A review. Renew Sustain Energy Rev. 2011 Jun;15(5):2355–77.

4. Valderrama Rios ML, González AM, Lora EES, Almazán del Olmo OA. Reduction of tar generated during biomass gasification: A review. Biomass Bioenergy. 2018 Jan;108:345–70.

5. Guan G, Kaewpanha M, Hao X, Abudula A. Catalytic steam reforming of biomass tar: Prospects and challenges. Renew Sustain Energy Rev. 2016 May;58:450–61.

6. de Lasa H, Salaices E, Mazumder J, Lucky R. Catalytic Steam Gasification of Biomass: Catalysts, Thermodynamics and Kinetics. Chem Rev. 2011 Sep 14;111(9):5404–33.

7. Woolcock PJ, Brown RC. A review of cleaning technologies for biomass-derived syngas. Biomass Bioenergy. 2013 May 1;52:54–84.

8. Weston P. Tar Destruction in a Coandă Tar Cracker. University of Sheffield; 2014.

9. Didier B. Biomass for electricity and heating: opportunities and challenges. EPRS Eur Parliam Res Serv. 2015 Sep;8.

10. BP. BP Statistical Review of World Energy 2020. 2020;68.

11. IEA. Total primary energy supply by fuel, 1971 and 2019 [Internet]. World Energy Balances: Overview. 2021 [cited 2021 Aug 25]. Available from: https://www.iea.org/reports/world-energy-balances-overview

12. Phan C, Plouhinec C. Chiffres clés des énergies renouvelables - Édition 2021 [Internet]. Ministère de la transition écologique; 2021 Jul p. 98. Available from: www.statistiques.developpement-durable.gouv.fr

13. ADEME. A 100% renewable gas mix in 2050? [Internet]. 2018 Jan. Available from: www.ademe.fr/mediatheque

14. Sharma A, Pareek V, Zhang D. Biomass pyrolysis—A review of modelling, process parameters and catalytic studies. Renew Sustain Energy Rev. 2015 Oct;50:1081–96.

15. Mai TP, Nguyen DQ. Gasification of Biomass [Internet]. IntechOpen; 2020 [cited 2021 Jun 11]. Available from: https://www.intechopen.com/online-first/gasification-of-biomass

16. Zhang Y, Wan L, Guan J, Xiong Q, Zhang S, Jin X. A Review on Biomass Gasification: Effect of Main Parameters on Char Generation and Reaction. Energy Fuels. 2020 Nov 19;34(11):13438–55.

17. Dong J, Tang Y, Nzihou A, Chi Y, Weiss-Hortala E, Ni M. Life cycle assessment of pyrolysis, gasification and incineration waste-to-energy technologies: Theoretical analysis and case study of commercial plants. Sci Total Environ. 2018 Jun;626:744–53.

18. Shakorfow A. Biomass. Incineration, Pyrolysis, Combustion and Gasification. Int J Sci Res IJSR. 2016 Jul 5;5(7):13–25.

19. Daouk E. Etudes expérimentale et numérique de la pyrolyse oxydante de la biomasse en lit fixe. [France]: Ecole des Mines de Nantes; 2015.

20. Gollakota ARK, Kishore N, Gu S. A review on hydrothermal liquefaction of biomass. Renew Sustain Energy Rev. 2018 Jan;81:1378–92.

21. Nachenius RW, Ronsse F, Venderbosch RH, Prins W. Chapter Two - Biomass Pyrolysis. In: Murzin DY, editor. Advances in Chemical Engineering [Internet]. Academic Press; 2013 [cited 2021 Aug 27]. p. 75–139. (Chemical Engineering for Renewables Conversion; vol. 42). Available from: https://www.sciencedirect.com/science/article/pii/B978012386505200002X

22. Al Arni S. Comparison of slow and fast pyrolysis for converting biomass into fuel. Renew Energy. 2018 Aug 1;124:197–201.

23. Neathery JK. Biomass Gasification. In: Thermochemical Conversion of Biomass to Liquid Fuels and Chemicals [Internet]. 2010. p. 28. (RSC Energy and Environment Series). Available from: https://doi.org/10.1039/9781849732260-00067

24. Couto EA, Pinto F, Varela F, Reis A, Costa P, Calijuri ML. Hydrothermal liquefaction of biomass produced from domestic sewage treatment in high-rate ponds. Renew Energy. 2018 Apr 1;118:644–53.

25. Elliott DC, Biller P, Ross AB, Schmidt AJ, Jones SB. Hydrothermal liquefaction of biomass: Developments from batch to continuous process. Bioresour Technol. 2015 Feb 1;178:147–56.

26. Khonde R, Hedaoo S, Deshmukh S. Prediction of product gas composition from biomass gasification by the method of Gibbs free energy minimization. Energy Sources Part Recovery Util Environ Eff. 2021 Feb 1;43(3):371–80.

27. Bassil G. Gazéification de la biomasse : élimination des goudrons par lavage, étude expérimentale et modélisation [Internet] [Alimentation et Nutrition]. [France]: Université Claude Bernard - Lyon I; 2012. Available from: https://tel.archives-ouvertes.fr/tel-01127492

28. Thunman H, Seemann M, Vilches TB, Maric J, Pallares D, Ström H, et al. Advanced biofuel production via gasification – lessons learned from 200 man-years of research activity with Chalmers' research gasifier and the GoBiGas demonstration plant. Energy Sci Eng. 2018;6(1):6–34.

29. Bermudez JM, Fidalgo B. Production of bio-syngas and bio-hydrogen via gasification. In: Luque R, Lin CSK, Wilson K, Clark J, editors. Handbook of Biofuels Production (Second Edition) [Internet]. Woodhead Publishing; 2016 [cited 2019 May 7]. p. 431–94. Available from: http://www.sciencedirect.com/science/article/pii/B9780081004555000151

30. Alamia A, Larsson A, Breitholtz C, Thunman H. Performance of large-scale biomass gasifiers in a biorefinery, a state-of-the-art reference. Int J Energy Res. 2017;41(14):2001–19.

31. Hasler P, Nussbaumer T. Gas cleaning for IC engine applications from fixed bed biomass gasification. Biomass Bioenergy. 1999;11.

32. van Paasen SVB, Kiel JHA. Tar formation in a fluidised-bed gasifier: Impact of fuel properties and operating conditions. ECN Biomass. 2004;013:58.

33. Vera D, Jurado F, Margaritis NK, Grammelis P. Experimental and economic study of a gasification plant fuelled with olive industry wastes. Energy Sustain Dev. 2014 Dec 1;23:247–57.

34. Gil J, Corella J, Aznar MP, Caballero MA. Biomass gasification in atmospheric and bubbling fluidized bed: Effect of the type of gasifying agent on the product distribution. Biomass Bioenergy. 1999;15.

35. Lv P, Yuan Z, Ma L, Wu C, Chen Y, Zhu J. Hydrogen-rich gas production from biomass air and oxygen/steam gasification in a downdraft gasifier. Renew Energy. 2007 Oct;32(13):2173–85.

36. Schmid M, Beirow M, Schweitzer D, Waizmann G, Spörl R, Scheffknecht G. Product gas composition for steam-oxygen fluidized bed gasification of dried sewage sludge, straw pellets and wood pellets and the influence of limestone as bed material. Biomass Bioenergy. 2018 Oct;117:71–7.

37. Maniatis K, Beenackers AACM. Tar Protocols. IEA Bioenergy Gasification Task. Biomass Bioenergy. 2000;18:1–4.

38. Milne TA, Evans RJ, Abatzaglou N. Biomass Gasifier "'Tars'": Their Nature, Formation, and Conversion [Internet]. 1998 Nov [cited 2018 Dec 19]. Report No.: NREL/TP-570-25357, ON: DE00003726, 3726. Available from: http://www.osti.gov/servlets/purl/3726/

39. Bergman PCA, Paasen SVB van, Boerrigter H. The novel "OLGA" technology for complete tar removal from biomass producer gas. In Strasbourg, France; 2002. p. 10.

40. Li C, Suzuki K. Tar property, analysis, reforming mechanism and model for biomass gasification—An overview. Renew Sustain Energy Rev. 2009 Apr;13(3):594–604.

41. Rapagnà S, Jand N, Kiennemann A, Foscolo PU. Steam-gasification of biomass in a fluidised-bed of olivine particles. Biomass Bioenergy. 2000;11.

42. Qin Y, Huang H, Wu Z, Feng J, Li W, Xie K. Characterization of tar from sawdust gasified in the pressurized fluidized bed. Biomass Bioenergy. 2007 Apr;31(4):243–9.

43. Wang Y, Kinoshita CM. Kinetic model of biomass gasification. Sol Energy. 1993 Jul 1;51(1):19–25.

44. Han J, Kim H. The reduction and control technology of tar during biomass gasification/pyrolysis: An overview. Renew Sustain Energy Rev. 2008 Feb;12(2):397–416.

45. Zwart RWR, Van der Drift A, Bos A, Visser HJM, Cieplik MK, Könemann HWJ. Oil-based gas washing-Flexible tar removal for high-efficient production of clean heat and power as well as sustainable fuels and chemicals. Environ Prog Sustain Energy. 2009 Oct;28(3):324–35.

46. Boerrigter H. "OLGA" tar removal technology Proof-of-Concept (PoC) for application in integrated biomass gasification combined heat and power (CHP) systems. ECN Biomass. 2005;05:58.

47. Phuphuakrat T, Namioka T, Yoshikawa K. Absorptive removal of biomass tar using water and oily materials. Bioresour Technol. 2011 Jan;102(2):543–9.

48. Paethanom A, Nakahara S, Kobayashi M, Prawisudha P, Yoshikawa K. Performance of tar removal by absorption and adsorption for biomass gasification. Fuel Process Technol. 2012 Dec 1;104:144–54.

49. Phuphuakrat T, Namioka T, Yoshikawa K. Tar removal from biomass pyrolysis gas in two-step function of decomposition and adsorption. Appl Energy. 2010 Jul 1;87(7):2203–11.

50. Gateau P, Van Dievoet F, Bouillon V, Vermeersch G, Claude S, Staat F. Environmentally friendly properties of vegetable oil methyl esters. Ol Corps Gras Lipides. 2005 Jul;12(4):308–13.

51. Chen S, Zhao K, Tang Y. Modeling of Biodiesel Production from Rape-Seed Oil and Methanol. In: Proceedings of the 2015 International Symposium on Energy Science and Chemical Engineering [Internet]. Guangzhou City, China: Atlantis Press; 2015 [cited 2021 Mar 18]. Available from: http://www.atlantis-press.com/php/paper-details.php?id=25846103

52. DeVincentis J. Aspen Plus Biodiesel Model. Aspen Technol. 2008;13.

53. Zwart R, Van Der Heijden S, Emmen R, Dall Bentzen J, Ahrenfeldt J, Stoholm P, et al. Tar removal from low-temperature gasifiers. ECN. 2010;73.

54. Bridgwater AV. The technical and economic feasibility of biomass gasif ication for power generation. Biomass Gasif Power Gener. 1995;74(5):631–53.

55. Brandt P, Henriksen U. Decomposition of tar in gas from updraft gasifier by thermal cracking. In: 1st World Conference and Exhibition on Biomass for Energy and Industry [Internet]. Spain: James & James; 2000. p. 4. Available from: http://orbit.dtu.dk/files/3427636/sevilla2000_v8-67.pdf

56. Nunnally T, Tsangaris A, Rabinovich A, Nirenberg G, Chernets I, Fridman A. Gliding arc plasma oxidative steam reforming of a simulated syngas containing naphthalene and toluene. Int J Hydrog Energy. 2014 Aug 4;39(23):11976–89.

57. Fassinou WF, Van de Steene L, Toure S, Volle G, Girard P. Pyrolysis of Pinus pinaster in a two-stage gasifier: Influence of processing parameters and thermal cracking of tar. Fuel Process Technol. 2009 Jan 1;90(1):75–90.

58. Torres W, Pansare SS, Jr JGG. Hot Gas Removal of Tars, Ammonia, and Hydrogen Sulfide from Biomass Gasification Gas. Catal Rev. 2007 Oct 1;49(4):407–56.

59. Tao K, Ohta N, Liu G, Yoneyama Y, Wang T, Tsubaki N. Plasma enhanced catalytic reforming of biomass tar model compound to syngas. Fuel. 2013 Feb 1;104:53–7.

60. Sutton D, Kelleher B, Ross JRH. Review of literature on catalysts for biomass gasification. Fuel Process Technol. 2001 Nov;73(3):155–73.

61. Tomishige K, Asadullah M, Kunimori K. Syngas production by biomass gasification using Rh/CeO2/SiO2 catalysts and fluidized bed reactor. Catal Today. 2004 Jun 1;89(4):389–403.

62. El-Rub ZYKA. Biomass char as an in-situ catalyst for tar removal in gasification systems [Internet] [PhD Thesis]. [The Netherlands]: Twente University; 2008 [cited 2021 Apr 16]. Available from: https://research.utwente.nl/en/publications/biomass-char-as-an-in-situ-catalyst-for-tar-removal-in-gasificati

63. Yung MM, Jablonski WS, Magrini-Bair KA. Review of Catalytic Conditioning of Biomass-Derived Syngas. Energy Fuels. 2009 Apr 16;23(4):1874–87.

64. Xie YR, Shen LH, Xiao J, Xie DX, Zhu J. Influences of Additives on Steam Gasification of Biomass. 1. Pyrolysis Procedure. Energy Fuels. 2009 Oct 15;23(10):5199–205.

65. Hu G, Xu S, Li S, Xiao C, Liu S. Steam gasification of apricot stones with olivine and dolomite as downstream catalysts. Fuel Process Technol. 2006 May 1;87(5):375–82.

66. Pallozzi V, Di Carlo A, Bocci E, Carlini M. Combined gas conditioning and cleaning for reduction of tars in biomass gasification. Biomass Bioenergy. 2018 Feb;109:85–90.

67. Dou B, Gao J, Sha X, Baek SW. Catalytic cracking of tar component from high-temperature fuel gas. Appl Therm Eng. 2003 Dec 1;23(17):2229–39.

68. D'Orazio A, Rapagnà S, Foscolo PU, Gallucci K, Nacken M, Heidenreich S, et al. Gas conditioning in H2 rich syngas production by biomass steam gasification: Experimental comparison between three innovative ceramic filter candles. Int J Hydrog Energy. 2015 Jun 22;40(23):7282–90.

69. Abu El-Rub Z, Bramer EA, Brem G. Experimental comparison of biomass chars with other catalysts for tar reduction. Fuel. 2008 Aug 1;87(10):2243–52.

70. Furusawa T, Tsutsumi A. Comparison of Co/MgO and Ni/MgO catalysts for the steam reforming of naphthalene as a model compound of tar derived from biomass gasification. Appl Catal Gen. 2005 Jan 10;278(2):207–12.

71. Noichi H, Uddin A, Sasaoka E. Steam reforming of naphthalene as model biomass tar over iron–aluminum and iron–zirconium oxide catalyst catalysts. Fuel Process Technol. 2010 Nov 1;91(11):1609–16.

72. Buchireddy PR, Bricka RM, Rodriguez J, Holmes W. Biomass Gasification: Catalytic Removal of Tars over Zeolites and Nickel Supported Zeolites. Energy Fuels. 2010 Apr 15;24(4):2707–15.

73. Pérez-Martínez D, Giraldo SA, Centeno A. Effects of the H2S partial pressure on the performance of bimetallic noble-metal molybdenum catalysts in simultaneous hydrogenation and hydrodesulfurization reactions. Appl Catal Gen. 2006 Nov 23;315:35–43.

74. Myrén C, Hörnell C, Björnbom E, Sjöström K. Catalytic tar decomposition of biomass pyrolysis gas with a combination of dolomite and silica. Biomass Bioenergy. 2002 Sep 1;23(3):217–27.

75. Devi L, Craje M, Thüne P, Ptasinski KJ, Janssen FJJG. Olivine as tar removal catalyst for biomass gasifiers: Catalyst characterization. Appl Catal Gen. 2005 Oct 4;294(1):68–79.

76. Simell PA, Bredenberg JB -son. Catalytic purification of tarry fuel gas. Fuel. 1990 Oct 1;69(10):1219–25.

77. Lu P, Huang Q, Bourtsalas AC, Chi Y, Yan J. Effect of Operating Conditions on the Coke Formation and Nickel Catalyst Performance During Cracking of Tar. Waste Biomass Valorization. 2019 Jan;10(1):155–65.

78. Hervy M, Weiss-Hortala E, Pham Minh D, Dib H, Villot A, Gérente C, et al. Reactivity and deactivation mechanisms of pyrolysis chars from bio-waste during catalytic cracking of tar. Appl Energy. 2019 Mar 1;237:487–99.

79. GRTgaz. Contrat relatif au raccordement d'une installation de production de biométhane et d'injection de biométhane dans le réseau de transport de gas naturel [Internet]. 2018. Available from: http://www.grtgaz.com/fileadmin/clients/producteur_gaz/fr/contrat-raccordement-injection-biomethane-CG.pdf

80. Jensen JH, Poulsen JM, Andersen NU. From coal to clean energy. Nitrogen+Syngas. 2011;5.

81. Rönsch S, Schneider J, Matthischke S, Schlüter M, Götz M, Lefebvre J, et al. Review on methanation – From fundamentals to current projects. Fuel. 2016 Feb 15;166:276–96.

82. Maheut M. Projet GAYA : réalisations et prochaines étapes dans l'industrialisation de la filière biométhane de 2ème génération. GT Injection; 2020; France.

83. Rehling B, Hofbauer H, Rauch R, Aichernig C. BioSNG—process simulation and comparison with first results from a 1-MW demonstration plant. Biomass Convers Biorefinery. 2011 Jul 1;1(2):111–9.

84. Alamia A, Òsk Gardarsdòttir S, Larsson A, Normann F, Thunman H. Efficiency Comparison of Large-Scale Standalone, Centralized, and Distributed Thermochemical Biorefineries. Energy Technol. 2017;5(8):1435–48.

85. Thunman H, Gustavsson C, Larsson A, Gunnarsson I, Tengberg F. Economic assessment of advanced biofuel production via gasification using cost data from the GoBiGas plant. Energy Sci Eng. 2019;7(1):217–29.

86. van der Meijden C, Könemann J-W, Sierhuis W, van der Drift B, Rietveld B. Wood to Bio-Methane demonstration project in the Netherlands. Energy Res Cent Neth ECN. 2013 Jun;13.

87. Rapagnà S, Jand N, Kiennemann A, Foscolo PU. Steam-gasification of biomass in a fluidised-bed of olivine particles. Biomass Bioenergy. 2000 Sep 1;19(3):187–97.

88. Lotfi S, Ma W, Austin K, Kumar A. A wet packed-bed scrubber for removing tar from biomass producer gas. Fuel Process Technol. 2019 Oct 1;193:197–203.

89. Unyaphan S, Tarnpradab T, Takahashi F, Yoshikawa K. An Investigation of Low Cost and Effective Tar Removal Techniques by Venturi Scrubber Producing Syngas Microbubbles and Absorbent Regeneration for Biomass Gasification. Energy Procedia. 2017 May 1;105:406–12.

90. Caprariis B, de Filippis PD, Hernandez AD, Petrullo A, Scarsella M, Verdone N. Use of low cost natural materials for tar abatement process. Chem Eng Trans. 2017 May;57:91–6.

91. Meijden CM van der. The MILENA gasification technology for the production of Bio-Methane. Germany; 2014 p. 30. (ECN Biomass & Energy Efficiency). Report No.: ECN-L--14-0.37.

92. Rabou L. Biomethane in the EDGaR program and at ECN. In Sweden: REGATEC; 2014. p. 6.

93. Thersites: Complete model. [Internet]. [cited 2019 Jul 18]. Available from: http://www.thersites.nl/completemodel.aspx

94. Rabou LPLM, Zwart RWR, Vreugdenhil BJ, Bos L. Tar in Biomass Producer Gas, the Energy research Centre of The Netherlands (ECN) Experience: An Enduring Challenge. Energy Fuels. 2009 Dec 17;23(12):6189–98.

95. Aspen Technology. Aspen Physical Property System: Physical Property Methods. 2013;8(4):250.

96. Phuphuakrat T, Namioka T, Yoshikawa K. Absorptive removal of biomass tar using water and oily materials. Bioresour Technol. 2011 Jan;102(2):543–9.

97. Abu El-Rub Z, Bramer EA, Brem G. Experimental comparison of biomass chars with other catalysts for tar reduction. Fuel. 2008 Aug 1;87(10):2243–52.

98. Thunman H, Seemann M, Vilches TB, Maric J, Pallares D, Ström H, et al. Advanced biofuel production via gasification – lessons learned from 200 man-years of research activity with Chalmers' research gasifier and the GoBiGas demonstration plant. Energy Sci Eng. 2018;6(1):6–34.

99. van Paasen SVB, Cieplik MK, Phokawat NP. Gasification of Non-woody Biomass. Energy research Centre of the Netherlands; 2006 p. 54. (Economic and Technical Perspectives of Chlorine and Sulphur Removal from Product Gas). Report No.: ECN-C-06-032.

100. Hassan S, Zainal ZA, Miskam MA. A Preliminary Investigation of Compressed Producer Gas from Downdraft Biomass Gasifier. J Appl Sci. 2010;10:406–12.

101. Monte MJS, Notario R, Pinto SP, Lobo Ferreira AIMC, Ribeiro da Silva MDMC. Thermodynamic properties of fluoranthene: An experimental and computational study. J Chem Thermodyn. 2012 Jun;49:159–64.

102. de Kruif CG, Kuipers T, van Miltenburg JC, Schaake RCF, Stevens G. The vapour pressure of solid and liquid naphthalene. J Chem Thermodyn. 1981 Nov;13(11):1081–6.

103. Biddiscombe DP, Martin JF. Vapour pressures of phenol and the cresols. Trans Faraday Soc. 1958;54:1316.

104. Jackowski AW. Vapour pressures of solid benzene and of solid cyclohexane. J Chem Thermodyn. 1974 Jan 1;6(1):49–52.

105. Rabou L, Van der Drift A. Benzene and ethylene in Bio-SNG production: nuisance, fuel or valuable products? In Vienna; 2011.

106. Kandula M. Frost growth and densification in laminar flow over flat surfaces. Int J Heat Mass Transf. 2011 Jul;54(15–16):3719–31.

107. Ueda H, Takashima Y. The local growth rate of desublimation on the surface of an annular-tube cold trap. J Chem Eng Jpn. 1976;9(2):121–9.

108. Hendry JR. Computational fluid dynamics modelling of benzene abatement using cryogenic condensation [Internet] [Thesis]. Newcastle University; 2018 [cited 2021 Dec 22]. Available from: http://theses.ncl.ac.uk/jspui/handle/10443/4338

109. Hayashi Y, Aoki A, Adachi S, Hori K. Study of Frost Properties Correlating With Frost Formation Types. J Heat Transf. 1977 May 1;99(2):239–45.

110. Lenic K, Trp A, Frankovic B. Transient two-dimensional model of frost formation on a fin-and-tube heat exchanger. Int J Heat Mass Transf. 2009 Jan;52(1–2):22–32.

111. Brèque F, Nemer M. Frosting modeling on a cold flat plate: Comparison of the different assumptions and impacts on frost growth predictions. Int J Refrig. 2016 Sep;69:340–60.

112. Hermes CJL, Loyola FR, Nascimento VS. A semi-empirical correlation for the frost density. Int J Refrig. 2014 Oct 1;46:100–4.

113. Biguria G, Wenzel LA. Measurement and Correlation of Water Frost Thermal Conductivity and Density. Ind Eng Chem Fundam. 1970 Feb 1;9(1):129–38.

114. Lee K-S, Kim W-S, Lee T-H. A one-dimensional model for frost formation on a cold flat surface. Int J Heat Mass Transf. 1997 Nov;40(18):4359–65.

115. Na B, Webb RL. New model for frost growth rate. Int J Heat Mass Transf. 2004 Feb;47(5):925–36.

116. Ismail KAR, Salinas CS. Modeling of frost formation over parallel cold plates. Int J Refrig. 1999 Aug 1;22(5):425–41.

117. Kim D, Kim C, Lee K-S. Frosting model for predicting macroscopic and local frost behaviors on a cold plate. Int J Heat Mass Transf. 2015 Mar 1;82:135–42.

118. Cui J, Li WZ, Liu Y, Jiang ZY. A new time- and space-dependent model for predicting frost formation. Appl Therm Eng. 2011 Mar 1;31(4):447–57.

119. Armengol JM, Salinas CT, Xamán J, Ismail KAR. Modeling of frost formation over parallel cold plates considering a two-dimensional growth rate. Int J Therm Sci. 2016 Jun;104:245–56.

120. Lee J, Kim J, Kim DR, Lee K-S. Modeling of frost layer growth considering frost porosity. Int J Heat Mass Transf. 2018 Nov;126:980–8.

121. Lee K-S, Jhee S, Yang D-K. Prediction of the frost formation on a cold flat surface. Int J Heat Mass Transf. 2003 Sep;46(20):3789–96.

122. Na B, Webb RL. Mass transfer on and within a frost layer. Int J Heat Mass Transf. 2004 Feb;47(5):899–911.

123. Léoni A, Mondot M, Durier F, Revellin R, Haberschill P. State-of-the-art review of frost deposition on flat surfaces. Int J Refrig. 2016 Aug;68:198–217.

124. Li J-D, Saraireh M, Thorpe G. Condensation of vapor in the presence of non-condensable gas in condensers. Int J Heat Mass Transf. 2011 Aug;54(17–18):4078–89.

125. Rose JW. Film and Dropwise Condensation. In: Handbook of Thermal Science and Engineering [Internet]. Cham: Springer International Publishing; 2018 [cited 2020 Jul 28]. p. 2031–74. Available from: https://doi.org/10.1007/978-3-319-26695-4_50

126. Nasr A. Heat and mass transfer for liquid film condensation along a vertical channel covered with a thin porous layer. Int J Therm Sci. 2018 Feb 1;124:288–99.

127. Zhang Y, Peng XF, Conte I. Heat and Mass Transfer with Condensation in Non-Saturated Porous Media. Numer Heat Transf Part Appl. 2007 Sep 21;52(12):1081–100.

128. Tiwari A. Characterization of mass transfer by condensation on a horizontal plate [Internet]. [France]: Université Blaise Pascal - Clermont-Ferrand II; 2011. Available from: https://tel.archives-ouvertes.fr/tel-00708562

129. Terhan M, Comakli K. Design and economic analysis of a flue gas condenser to recover latent heat from exhaust flue gas. Appl Therm Eng. 2016 May;100:1007–15.

130. Jeong K, Levy EK. Theoretical prediction of sulfuric acid condensation rates in boiler flue gas. Int J Heat Mass Transf. 2012 Dec;55(25–26):8010–9.

131. Chilton TH, Colburn AP. Mass transfer (Absorption) coefficients prediction from data on heat transfer and fluid friction. Ind Eng Chem. 26(11):1183–7.

132. Wang W, Guo QC, Lu WP, Feng YC, Na W. A generalized simple model for predicting frost growth on cold flat plate. Int J Refrig. 2012 Mar;35(2):475–86.

133. Dymola and Modelica Explained [Internet]. Claytex. 2019 [cited 2020 Jul 29]. Available from: https://www.claytex.com/tech-blog/dymola-and-modelica-explained/

134. Mazumder S. The Finite Volume Method (FVM). In: Numerical Methods for Partial Differential Equations [Internet]. 1st ed. Elseveir; 2015 [cited 2020 Jul 29]. Available from: https://www.elsevier.com/books/numerical-methods-for-partial-differential-equations/mazumder/978-0-12-849894-1

135. Jones BW, Parker JD. Frost Formation With Varying Environmental Parameters. J Heat Transf. 1975 May 1;97(2):255–9.

136. Sanders CT. Frost formation: The influence of frost formation and defrosting on the performance of air coolers [Internet] [Ph.D.]. [Netherlands]: Technische Hogeschool, Lab. for Refrigeration; 1974 [cited 2020 Jul 30]. Available from: https://repository.tudelft.nl/islandora/object/uuid%3Ab99381a0-893c-4382-8b14-b1d9bdb370dd

137. Yonko JD, Sepsy CF. An Investigation of the Thermal Conductivity of Frost while Forming on a Flat Horizontal Plate. ASHRAE Trans. 1967;73(2):1.1-1.11.

138. Le Gall R, Grillot JM, Jallut C. Modelling of frost growth and densification. Int J Heat Mass Transf. 1997 Sep;40(13):3177–87.

139. Pursky OI, Sholonko MM. Thermal properties of solid benzene. Ukrayinskij Fyizichnij Zhurnal Kiev. 2004;49(11):1105–11.

140. Shen Y, Xu P, Qiu S, Rao B, Yu B. A generalized thermal conductivity model for unsaturated porous media with fractal geometry. Int J Heat Mass Transf. 2020 May 1;152:119540.

141. Cengel YA, Ghajar AJ. Mass Transfer. In: Heat and Mass Transfer: Fundamentals and Applications. 4th ed. New York: McGraw-Hill Publishing Company; 2011.

142. Noël F, Serra C, Le Calvé S. Design of a Novel Axial Gas Pulses Micromixer and Simulations of its Mixing Abilities via Computational Fluid Dynamics. Micromachines. 2019 Mar 23;10(3):205.

143. Poling B, Prausnitz J, O'Connell J. Diffusion coefficients. In: The properties of gases and liquids. 5th ed. USA: McGraw-Hill; 2001. p. 635–89.

144. Fuller EN, Schettler PD, Giddings JC. A new method for prediction of binary gas-phase diffusion coefficients. Ind Eng Chem. 1966;58(5):18–27.

145. Brian PLT, Reid RC, Shah YT. Frost Deposition on Cold Surfaces. Ind Eng Chem Fundam. 1970 Aug;9(3):375–80.

146. Auracher H. Water vapor diffusion and frost formation in capillaries. In: Bulletin of the international institute of refrigeration. 1972. p. 477–88.

147. Tao Y-X, Besant RW, Rezkallah KS. A mathematical model for predicting the densification and growth of frost on a flat plate. Int J Heat Mass Transf. 1993 Jan 1;36(2):353–63.

148. Holman JP. Empirical and practical relations for forced-convection heat transfer. In: Heat Trandfer. 10th ed. New York: McGraw-Hill; 2010. p. 758.

149. Bergman TL, Incropera FP, DeWitt DP, Lavine AS. Fundamentals of Heat and Mass Transfer. John Wiley & Sons; 2011. 2249 p.

150. Tokura I, Saito H, Kishinami K. Prediction of growth rate and density of frost layer developing under forced convection. Wärme - Stoffübertrag. 1988 Sep 1;22(5):285–90.

151. Lemmon EW, Huber ML, McLinden MO. NIST Standard Reference Database 23: Reference Fluid Thermodynamic and Transport Properties-REFPROP. Gaithersburg: National Institute of Standards and Technology, Standard Reference Data Program; 2013.

152. Haddad S. Controlled Solid-Vapour CO2 phase transitions in methane rich streams applied to biogas upgrading [Internet] [Chemical and Process Engineering]. [France]: Université Paris sciences et lettres; 2019. Available from: https://pastel.archives-ouvertes.fr/tel-03118446

153. Shchelkunov VN, Rudenko NZ, Shostak YV, Dolganin VI. Surface desublimation of caron dioxide from binary gas mixtures. J Eng Phys. 1986;51(6):1432–5.

154. Haddad Sylvain, Rivera-Tinoco Rodrigo, Bouallou Chakib. Modelling of CO2 Frost Formation and Growth on a Flat Plate. Chem Eng Trans. 2019 Oct;76:667–72.

155. Lide DR, editor. CRC Handbook of Chemistry and Physics. Boca Raton, Florida: CRC Press; 2009. 2–65 p.

156. Poling BE, Prausnitz JM, O'Connell JP. Chapter 11: Diffusion coefficients. In: The properties of gases and liquids [Internet]. 5th edition. McGraw-Hill; 2001. p. 803. Available from: 10.1036/0070116822

157. Lee YB, Ro ST. Analysis of the frost growth on a flat plate by simple models of saturation and supersaturation. Exp Therm Fluid Sci. 2005 Jul 1;29(6):685–96.

158. Sanaye S, Shirazi A. Four E analysis and multi-objective optimization of an ice thermal energy storage for air-conditioning applications. Int J Refrig. 2013 May 1;36(3):828–41.

159. Khosravi A, Koury RNN, Machado L. Thermo-economic analysis and sizing of the components of an ejector expansion refrigeration system. Int J Refrig. 2018 Feb 1;86:463–79.

160. CEPCI. The Chemical Engineering Plant Cost Index [Internet]. Chemical Engineering. 2021. Available from: https://www.chemengonline.com/

161. Sanaye S, Emadi M, Refahi A. Thermal and economic modeling and optimization of a novel combined ejector refrigeration cycle. Int J Refrig. 2019 Feb 1;98:480–93.

162. Aminyavari M, Najafi B, Shirazi A, Rinaldi F. Exergetic, economic and environmental (3E) analyses, and multi-objective optimization of a CO2/NH3 cascade refrigeration system. Appl Therm Eng. 2014 Apr 1;65(1):42–50.

163. de Saint Jean M. Étude énergétique et évaluation économique d'une boucle de stockage - déstockage d'énergie électrique d'origine renouvelable sur méthane de synthèse à l'aide d'un convertisseur électrochimique réversible SOEC - SOFC [Internet] [Energie électrique]. [France]: Ecole Nationale Supérieure des Mines de Paris; Available from: https://pastel.archives-ouvertes.fr/tel-01142360

164. Binder M, Kraussier M, Kuba M, Luisser M. Hydrogen from biomass gasification. IEA Bioenergy; 2018 p. 85. Report No.: 33.

165. Turton R, Shaeiwitz JA, Bhattacharyya D, Whiting WB. Analysis, synthesis, and design of chemical processes. 5th edition. Pearson; 2018. 965 p.

166. Eau de Paris. Une eau au juste prix - Eau de Paris [Internet]. 2020 [cited 2021 Mar 28]. Available from: http://www.eaudeparis.fr/leau-au-quotidien/une-eau-au-juste-prix/

167. Neste. Biodiesel prices (SME & FAME) [Internet]. Neste worldwide. 2015 [cited 2021 Mar 28]. Available from: https://www.neste.com/investors/market-data/biodiesel-prices-sme-fame

168. BITZER Software. Germany: BITZER Kühlmaschinenbau GmbH; 2017.

169. Le Froid Pacomark. Catalogue le Froid Refrigeration 2021 [Internet]. 2021. Available from: https://www.lefroid.fr/cataleg/FR/2021_Refrigeration/

170. R404A Gas not allowed after 1st January 2020 [Internet]. [cited 2021 Oct 13]. Available from: https://www.air-conditioning-refrigeration-essex.co.uk/air-con-refrigeration-news/r404a-gas-not-allowed-after-1st-january-2020.html

171. Sayyaadi H, Nejatolahi M. Multi-objective optimization of a cooling tower assisted vapor compression refrigeration system. Int J Refrig. 2011 Jan 1;34(1):243–56.

172. Ahamed JU, Saidur R, Masjuki HH. A review on exergy analysis of vapor compression refrigeration system. Renew Sustain Energy Rev. 2011 Apr 1;15(3):1593–600.

173. Kumar Singh K, Kumar R, Gupta A. Comparative energy, exergy and economic analysis of a cascade refrigeration system incorporated with flash tank (HTC) and a flash intercooler with indirect subcooler (LTC) using natural refrigerant couples. Sustain Energy Technol Assess. 2020 Jun 1;39:100716.

174. Roy R, Mandal BK. Thermo-economic Assessment and Multi-Objective Optimization of Vapour Compression Refrigeration System using Low GWP Refrigerants. In: 2019 8th International Conference on Modeling Simulation and Applied Optimization (ICMSAO). 2019. p. 1–5.

175. Country specific electricity grid greenhouse gas emission factors [Internet]. Carbon Footprint; 2020 Jul p. 12. Report No.: v1.3. Available from: https://www.carbonfootprint.com/

176. Mosaffa AH, Garousi Farshi L. Exergoeconomic and environmental analyses of an air conditioning system using thermal energy storage. Appl Energy. 2016 Jan 15;162:515–26.

177. Engineering ToolBox. Heat Exchanger Heat Transfer Coefficients [Internet]. 2003 [cited 2021 Nov 8]. Available from: https://www.engineeringtoolbox.com/heat-transfer-coefficients-exchangers-d_450.html

178. Alves B. Electricity prices for industries in the European Union in 2020, by country* [Internet]. statista. 2021 [cited 2021 Aug 18]. Available from: https://www.statista.com/statistics/1046605/industry-electricity-prices-european-union-country/

179. Mendes D, Mendes A, Madeira LM, Iulianelli A, Sousa JM, Basile A. The water-gas shift reaction: from conventional catalytic systems to Pd-based membrane reactors-a review. Asia-Pac J Chem Eng. 2010 Jan;5(1):111–37.

Appendices

Appendix A. Computational mass content (*w*) and concentration (*C*) at temperature (*T*) and atmospheric pressure for the different mixtures of tar components in raw gas.

Table A.1, Table A.2, Table A.3, Table A.4, Table A.5 and Table A. 6 present the tar content of fluoranthene, indene, naphthalene, phenol, toluene and benzene, respectively.

Table A.1: Computational mass content (w) and concentration (C) at temperature (T) and atmospheric pressure for the mixture of fluoranthene in raw gas.

T (°C)	$C_{fluoranthene}$ (mg.Nm^{-3})	$w_{fluoranthene}$ (x10^{-5} kg.kg^{-1} raw gas)	T (°C)	$C_{fluoranthene}$ (mg.Nm^{-3})	$w_{fluoranthene}$ (x10^{-5} kg.kg^{-1} raw gas)
120	1950.30	244.24	86	136.62	17.27
118	1719.08	215.32	84	109.78	13.90
116	1511.45	189.34	82	86.88	11.03
114	1325.35	166.06	78	51.31	6.56
112	1158.86	145.23	76	38.00	4.88
110	1010.19	126.63	72	19.20	2.51
108	877.86	110.08	70	13.26	1.76
106	760.38	95.37	66	6.42	0.88
104	656.28	82.35	64	4.61	0.65
102	564.24	70.82	62	3.39	0.48
100	483.03	60.66	60	2.54	0.37
96	348.78	43.85	58	1.94	0.29
94	293.82	36.96	56	1.50	0.23
92	245.83	30.95	54	1.17	0.18
88	167.87	21.18	52	0.93	0.14

Table A.2: Computational mass content (w) and concentration (C) at temperature (T) and atmospheric pressure for the mixture of indene in raw gas.

T (°C)	C_{indene} (mg.Nm^{-3})	w_{indene} (x10^{-5} kg.kg^{-1} raw gas)	T (°C)	C_{indene} (mg.Nm^{-3})	w_{indene} (x10^{-5} kg.kg^{-1} raw gas)
37	839.82	139.19	-1	37.86	6.62
35	721.50	120.28	-3	31.42	5.50
33	619.87	103.89	-5	26.02	4.56
29	457.03	77.31	-7	21.48	3.77
27	392.01	66.58	-9	17.69	3.11
25	335.90	57.25	-11	14.53	2.55
21	245.66	42.13	-13	11.90	2.09
19	209.59	36.05	-17	7.91	1.39
17	178.50	30.77	-19	6.42	1.13
15	151.73	26.22	-21	5.19	0.92
13	128.70	22.28	-23	4.18	0.74
11	108.91	18.89	-27	2.69	0.48
7	77.43	13.47	-29	2.15	0.38
5	65.03	11.33	-33	1.35	0.24
1	45.48	7.94	-36	0.94	0.17

Table A.3: Computational mass content (w) and concentration (C) at temperature (T) and atmospheric pressure for the mixture of naphthalene in raw gas.

T (°C)	$C_{naphthalene}$ (mg.Nm^{-3})	$w_{naphthalene}$ (x10^{-5} kg.kg^{-1} raw gas)	T (°C)	$C_{naphthalene}$ (mg.Nm^{-3})	$w_{naphthalene}$ (x10^{-5} kg.kg^{-1} raw gas)
57	1196.61	179.20	12	33.80	5.86
54	902.32	138.01	9	26.65	4.63
51	691.93	107.84	6	20.93	3.64
48	537.34	85.14	3	16.37	2.86
45	421.21	67.71	0	12.75	2.23
42	332.45	54.12	-3	9.89	1.73
39	263.68	43.40	-6	7.62	1.34
36	209.83	34.87	-9	5.85	1.03
33	167.32	28.04	-12	4.46	0.78
30	133.55	22.54	-15	3.38	0.60
27	106.61	18.10	-18	2.55	0.45
24	85.04	14.52	-21	1.91	0.34
21	67.75	11.62	-24	1.42	0.25
18	53.87	9.28	-27	1.04	0.18
15	42.74	7.38	-28	0.95	0.17

Table A.4: Computational mass content (w) and concentration (C) at temperature (T) and atmospheric pressure for the mixture of phenol in raw gas.

T (°C)	C_{phenol} (mg.Nm^{-3})	w_{phenol} (x10^{-5} kg.kg^{-1} raw gas)	T (°C)	C_{phenol} (mg.Nm$^{-3)}$)	w_{phenol} (x10^{-5} kg.kg^{-1} raw gas)
30	1159.37	195.91	-2	52.52	9.26
28	975.65	165.62	-4	42.05	7.42
26	819.18	139.64	-6	33.54	5.93
24	686.16	117.42	-8	26.63	4.72
22	573.32	98.45	-10	21.06	3.73
20	477.79	82.31	-12	16.58	2.94
18	397.11	68.61	-14	12.99	2.31
16	329.12	57.01	-16	10.13	1.80
14	271.97	47.23	-18	7.86	1.40
12	224.07	39.00	-20	6.07	1.08
10	184.02	32.10	-22	4.66	0.83
8	150.64	26.33	-24	3.56	0.64
6	122.90	21.52	-26	2.70	0.49
4	99.91	17.53	-28	2.04	0.37
2	80.94	14.22	-30	1.53	0.28
0	65.32	11.50	-33	0.99	0.18

Table A.5: Computational mass content (w) and concentration (C) at temperature (T) and atmospheric pressure for the mixture of toluene in raw gas.

T (°C)	$C_{toluene}$ (mg.Nm^{-3})	$w_{toluene}$ (x10^{-5} kg.kg^{-1} raw gas)	T (°C)	$C_{toluene}$ (mg.Nm^{-3})	$w_{toluene}$ (x10^{-5} kg.kg^{-1} raw gas)
-50	1076.46	197.84	-64	44.90	8.41
-51	887.42	163.26	-65	34.25	6.43
-52	728.20	134.10	-66	25.96	4.88
-53	594.70	109.64	-67	19.54	3.68
-54	483.29	89.20	-68	14.61	2.76
-55	390.77	72.20	-69	10.85	2.05
-56	314.32	58.15	-70	8.00	1.52
-57	251.47	46.58	-71	5.85	1.11
-58	200.09	37.11	-72	4.25	0.81
-59	158.31	29.41	-73	3.07	0.59
-60	124.54	23.17	-74	2.20	0.42
-61	97.40	18.15	-75	1.56	0.30
-62	75.71	14.13	-76	1.10	0.21
-63	58.49	10.93	-77	0.77	0.15

Table A. 6: Computational mass content (w) and concentration (C) at temperature (T) and atmospheric pressure for the mixture of benzene in raw gas.

T (°C)	$C_{benzene}$ (mg.Nm^{-3})	$w_{benzene}$ (x10^{-5} kg.kg^{-1} raw gas)	T (°C)	$C_{benzene}$ (mg.Nm^{-3})	$w_{benzene}$ (x10^{-5} kg.kg^{-1} raw gas)
-60	4785.37	918.98	-86	95.58	21.03
-62	3693.72	714.08	-88	66.85	14.96
-64	2835.28	552.02	-90	46.37	10.56
-66	2163.09	424.33	-92	31.90	7.40
-68	1639.42	324.21	-94	21.76	5.15
-70	1233.87	246.13	-96	14.72	3.56
-72	921.84	185.61	-98	9.88	2.44
-74	683.47	139.00	-100	6.58	1.66
-76	502.74	103.36	-102	4.34	1.12
-78	366.80	76.30	-104	2.84	0.75
-80	265.41	55.91	-106	1.85	0.50
-82	190.44	40.66	-108	1.19	0.33
-84	135.49	29.36	-109	0.95	0.26

Appendix B. Water gas shift reaction

Water gas shift reaction (WGSR) is the most used method to increase the H_2/CO ratio prior to methanation. During this reaction, carbon monoxide reacts with steam in presence of a catalyst and it is converted into hydrogen and carbon dioxide. As illustrated in eq. (B-1), WGSR is slightly exothermic, thus it is favored at low temperature. WGSR can be divided into two types: low temperature (LT) and high temperature (HT). The LT process takes place between 150°C and 300°C over Cu/Zn based catalyst, while the HT process takes place between 350°C and 500°C over Fe/Cr based catalyst. Although HT catalyst has a high resistance to poisoning, Fe/Cr catalyst is poisoned by sulfur and chloride if present in high concentrations. Cu based catalysts are less resistant to poisoning. They are also unstable at high temperatures and they will be deactivated due to thermal sintering. The highest operating temperature that Cu/Zn based catalyst could withstand is 300°C. In industrial applications, the process is generally divided into two stages: a high temperature WGSR followed by a LT one. An intercooler is placed after the HT reactor to cool the gas stream to the suitable temperature of the LT reactor. Figure B.1 depicts the conventional two stages process for WGSR. The ratio of H_2O/CO should be higher than 1 (up to 3) in order to obtain a high CO conversion.

$$CO + H_2O \leftrightarrow CO_2 + H_2 \qquad \Delta H_r = -41\ kJ.mol^{-1} \tag{B-1}$$

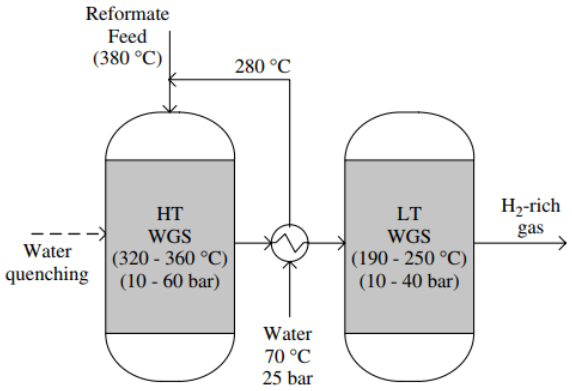

Figure B.1: Two stages water gas shift reaction [179].

Based on thermodynamic equilibrium, the equilibrium constant K_p of the WGSR is calculated according to eq. (B-2). The latter expresses K_p as function of temperature in Kelvin. K_p calculated from eq. (B-2) is plotted against the temperature in Figure B.2. It is clear that the reaction is favored at low temperature. Another expression of the equilibrium constant is shown in eq. (B-3), where y_i is the mole fraction of the component i at the inlet of the reactor and $X_{CO,eq}$ is the equilibrium conversion of CO [179]. After calculating K_p from eq. (B-2), CO conversion can be calculated form eq. (B-3) for a well-defined inlet gas composition. The impact of CO_2 initial content on the conversion of the reaction can also be assessed by varying the gas composition and solving eq. (B-3) for CO conversion.

$$K_p = exp\left(\frac{4577.8}{T} - 4.33\right) \tag{B-2}$$

$$K_p = \frac{\left(y_{CO_{2,in}} + y_{CO_{in}} X_{CO,eq}\right)\left(y_{H_{2,in}} + y_{CO_{in}} X_{CO,eq}\right)}{\left[y_{CO_{in}}\left(1 - X_{CO,eq}\right)\right]\left(y_{H_{2O,in}} - y_{CO_{in}} X_{CO,eq}\right)} \tag{B-3}$$

To analyze the impact of the initial composition and more specifically of CO_2 concentration on the CO conversion, three different initial compositions are considered. Table B.1 summarizes the initial molar

fraction of the different considered cases. In the first case, the same content shown in Table 2-3, which corresponds to the producer gas initial composition, is considered. The second case corresponds to the producer gas composition obtained after the pre-treatment unit (cf. Table 2-6). In case 2, steam is added in a stoichiometric ratio with the CO since its content was reduced in the scrubbers. The third case corresponds to a lower CO_2 initial content since part of the CO_2 is removed by frosting over the cold plates. Similarly to case 2, a stoichiometric H_2O initial content is considered in case 3.

Table B.1: Initial gas composition for each case expressed in mole fraction.

	Case 1	Case 2	Case 3
H_2	0.265	0.306	0.298
CO_2	0.132	0.152	0.077
CO	0.159	0.182	0.177
H_2O	0.319	0.182	0.177
H_2/CO	1.667	1.681	1.667
H_2/CO_2	2.006	2.016	3.890

As seen in Figure B.2, the highest CO conversion is achieved in case 1 where the H_2O is in excess. Moreover, a lower content of CO_2 in the initial gas feed (case 3) increases the CO conversion. The aim of the WGSR resides in adjusting the H_2/CO and H_2/CO_2 ratios. Thus ensuring the stoichiometry of the methanation reactions, and avoiding an excess of CO_2 that should be removed after the methanation. Table B.2 shows that even for the highest CO conversion, the ratio of H_2/CO_2 will be lower than 4. The highest ratio is equal to 2.25 and it is reached for the lowest CO_2 initial content. Thus, in all cases, a certain amount of CO_2 will remain in the gas after water gas shift reaction, which requires an additional elimination step prior or after the methanation. For certain types of methanation reactors, a ratio taking into account at the same time CO and CO_2 content is considered. This ratio should have a value around 3 and it is expressed as $(H_2 - CO_2)/(CO + CO_2)$. This ratio is usually considered since the methanation from carbon monoxide is the predominant reaction.

Table B.2: Variation of H_2/CO and H_2/CO_2 ratios, function of the temperature and the initial gas composition.

	Case 1		Case 2		Case 3	
Temperature (°C)	200	400	200	400	200	400
CO conversion	0.978	0.746	0.857	0.503	0.874	0.565
H_2/CO	119.80	9.49	17.76	4.39	20.28	5.16
H_2/CO_2	1.42	1.53	1.50	1.63	1.96	2.25

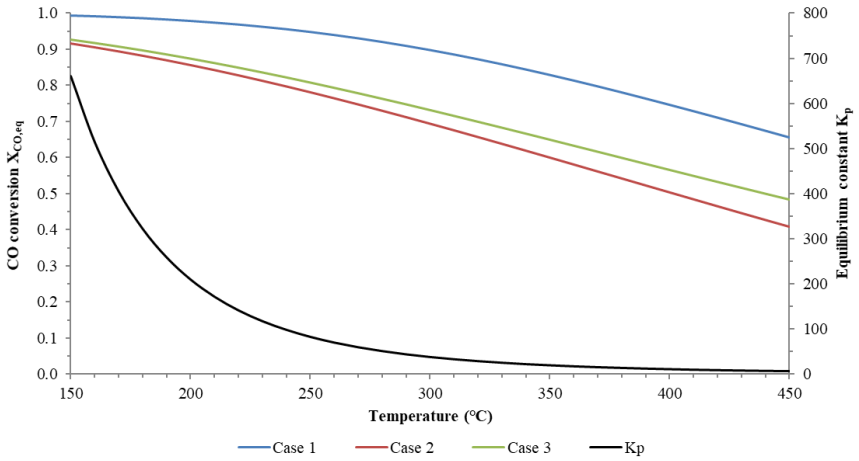

Figure B.2: Variation of K_p and $X_{CO,eq}$, function of temperature.

Appendix C. Sensitivity analysis for the number of meshing

In order to assess the impact of the number of meshes (M_c) on the results of the 1D model, a sensitivity study is conducted by varying the value of M_c. Five different values of M_c are considered:10, 20, 30, 40 and 50. The model was conducted for Case 1 in Table 3-4. A comparison between the results as function of the number of meshes is illustrated in Figure C.1. The main results considered are the frost thickness, the frost surface temperature and the frost density. It can be seen from the figures, that the impact of the number of meshes does not affect importantly the results. The variations in results are lower than 1%. Since no important variations is encountered, the number of meshing was limited to 50 meshes.

A

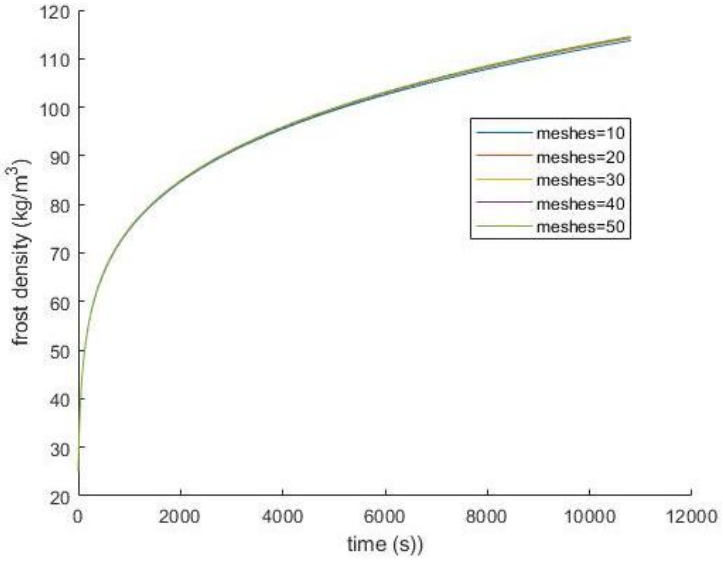

B

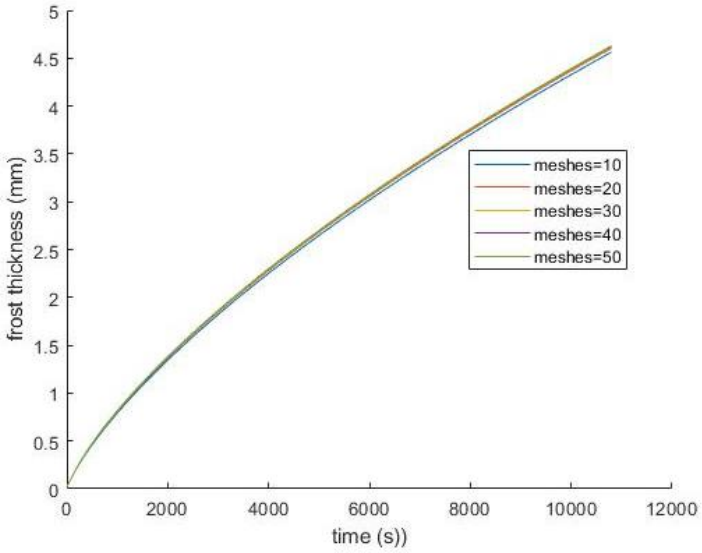

C

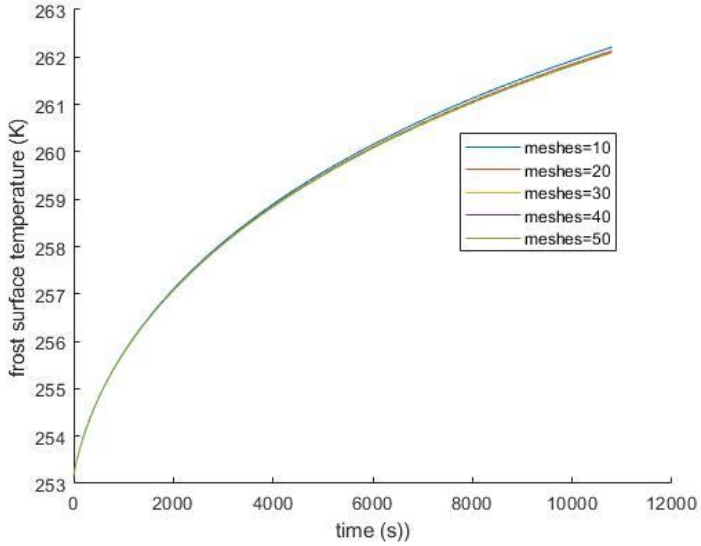

Figure C.1: Comparison between the variation of A) frost density, B) frost thickness and C) frost surface temperature function of time for different values of M.

Appendix D. Refrigerants P-h diagrams

The P-h diagrams of nitrogen and methane are illustrated in Figure D.1 and Figure D.2, respectively.

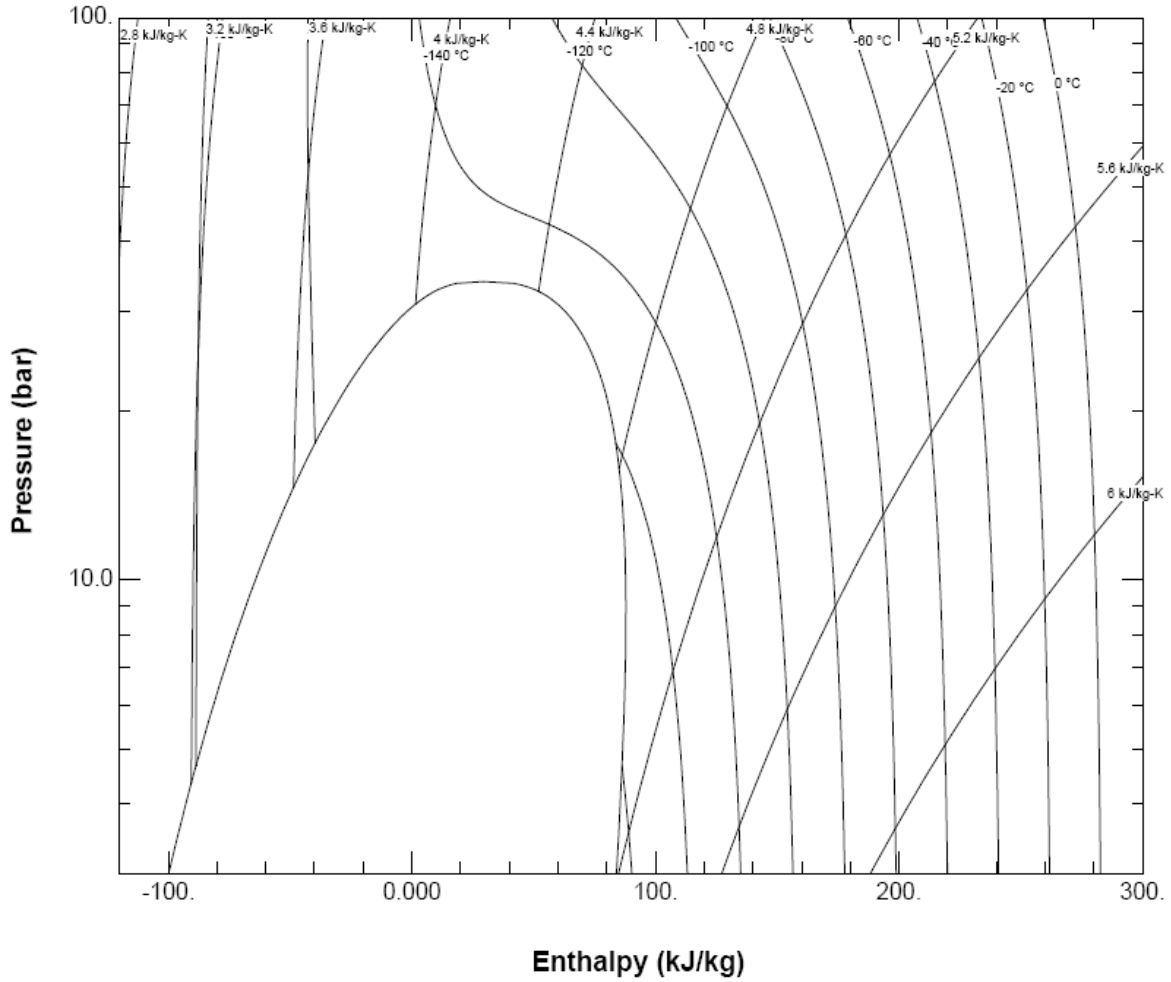

Figure D.1: P-h diagram of nitrogen [151].

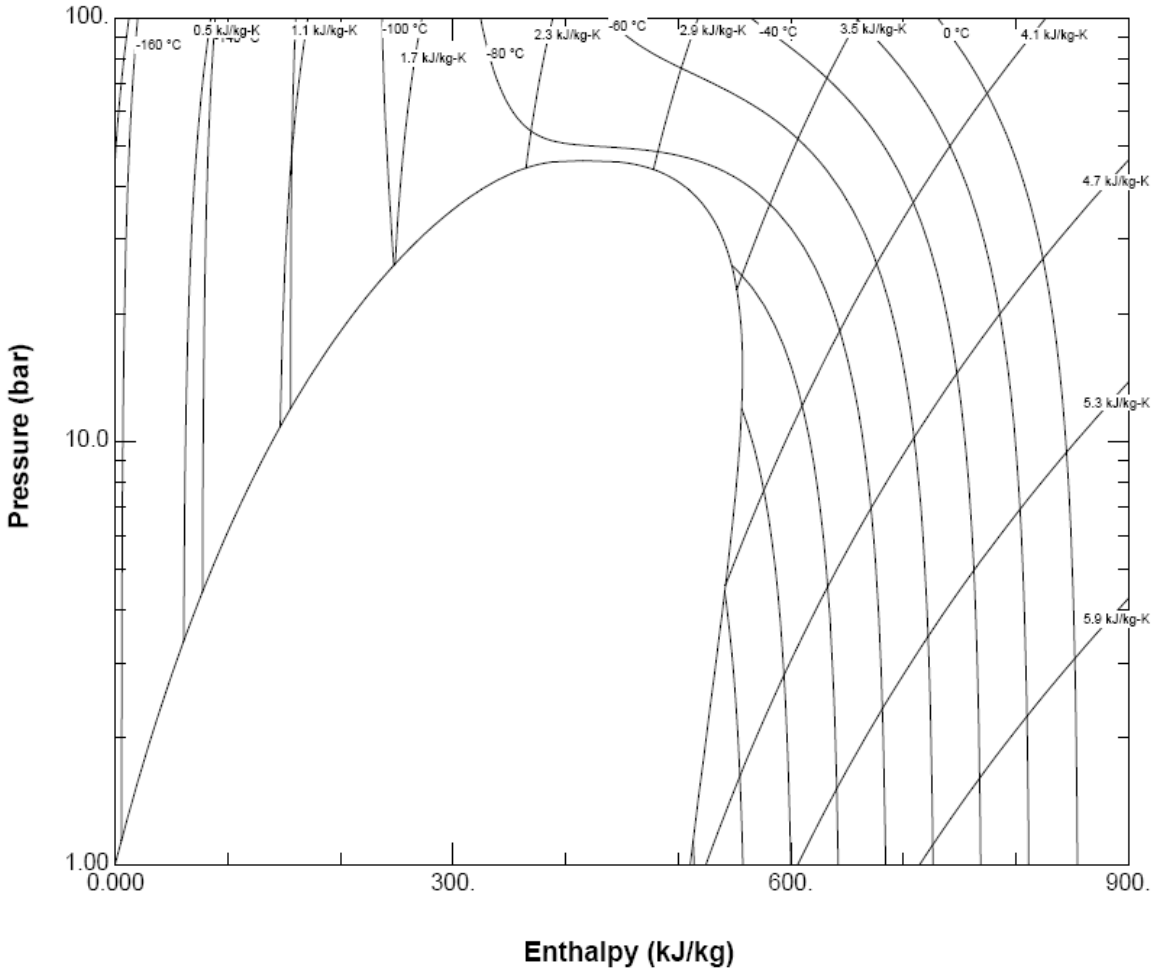

Figure D.2: P-h diagram of methane [151].

RÉSUMÉ

Cette thèse porte sur le procédé de traitement de goudrons qui permet la conversion du gaz produit issu de la gazéification de la biomasse en méthane par une méthanation catalytique. Pour cela, la teneur en goudrons (y compris pour les BTX) doit être réduite à 1 $mg.Nm^{-3}$. Les procédés de traitement de goudron présentent à ce jour un fardeau économique et une pénalité énergétique. Des diagrammes psychrométriques sont alors développés pour les composants représentatifs du goudron dans le gaz produit : une température de -110°C est nécessaire pour atteindre la teneur en goudron acceptable. Des procédés à basse température pour l'élimination du goudron sont proposés. Cependant, le gaz doit être prétraité dans deux colonnes d'absorption où l'eau est l'agent de lavage afin de réduire sa température, son taux d'humidité et la fraction en goudron lourd. Seuls le benzène et le toluène restent dans le gaz produit après les colonnes d'absorption. Ensuite, le gaz s'écoule sur des plaques refroidies sur lesquelles un dépôt/ condensation a lieu. Au-dessous de 5°C, le benzène forme une couche de givre poreuse tandis que le toluène se condense sous forme liquide. L'élimination de goudron à basse température induit le givrage de la vapeur d'eau restant dans le gaz produit en plus du givrage du CO_2 en dessous de -95°C. Les résultats de simulation ont permis d'analyser l'impact des conditions opératoires sur l'élimination des goudrons et de préciser l'énergie requise pour l'élimination du goudron. Enfin, une analyse technico-économique a montré que l'élimination du goudron à basse température est une solution prometteuse. Le taux du coût total du système frigorifique proposé est réduit en intégrant le froid du gaz produit dans le cycle de réfrigération. Ainsi, cette thèse établit les bases d'une nouvelle méthode d'élimination des goudrons à basse température.

MOTS CLÉS

Traitement de goudron, gazéification de la biomasse, équilibre entre phases, procédés à basse température, croissance du givre, condensation, méthanation.

ABSTRACT

This thesis focuses on the tar treatment process that enables the conversion of the producer gas obtained from biomass gasification into methane through a catalytic methanation. To do so, the tar content (including BTX) should be reduced to 1 $mg.Nm^{-3}$. Tar treatment processes present to date an economic burden and an energy penalty. Consequently, psychrometric charts are developed for the tar representative components in the producer gas. Based on the charts, a temperature of -110°C is required to reach the acceptable tar content. Therefore, low temperature processes for tar removal are proposed. However, the gas should be pre-treated in two water-based scrubbers in order to reduce its temperature, its moisture content and its heavy tar fraction. Only benzene and toluene remain in the producer gas after the scrubbers. Afterwards, the gas flows over cooled plates over which a simultaneous deposition/condensation takes place. Below 5°C, benzene forms a porous frost layer while toluene condenses as a liquid. The tar removal at low temperatures, induces the water vapor frosting remaining in the producer gas in addition to CO_2 frosting below -95°C. The simulation results allowed to analyze the impact of the operating conditions on the tar removal and the required energy for tar removal. Finally, a techno-economic analyses showed that tar removal at low temperature is a promising solution. The total cost rate of the proposed refrigeration system is reduced by integrating the cold of the producer gas in the refrigeration cycle. Hence, this thesis establishes the basis of a new method for tar removal at low temperatures.

KEYWORDS

Tar treatment, biomass gasification, phase equilibrium, low temperature process, frost growth, condensation, methanation.